Investigations into Homogeneous Electrocatalytic H_2 Production and NO_2^- Reduction Using a Variety of 3d Transition Metal Complexes

Joshua Brown

A Thesis Submitted in Partial Fulfilment
of the Requirements for the Degree of

Doctor of Philosophy in Chemistry

Department of Chemistry and Biomolecular Science
Faculty of Science
University of Ottawa

Abstract

Investigations into the homogeneous electrocatalytic capabilities and functionality of several 3d transition metal complexes for the generation of hydrogen and ammonia are presented herein. This research utilizes electrochemical, spectroscopic, and computational simulation techniques to probe the redox activity of organometallic complexes, identifying the active catalyst species and evaluating their catalytic capability. Co, Ni, and Fe are the selected metal centers used in each of the multidentate ligand systems. Non-innocent ligand contributions have been explored for each complex, uncovering a spectrum of participation within the catalytic mechanism across the catalogue of complexes, ranging from inert to intrinsically involved. Overall, this work aims to identify complexes capable of catalytic reduction reactions, evaluate their selectivity and kinetics, and elucidate details of their catalytic mechanisms.

Acknowledgements

First and foremost, I would like to thank my thesis supervisor, Darrin Richeson, for all the support, direction, and knowledge he has provided me throughout my time as both an undergraduate and graduate student. Darrin's dedication to my research and overall development as a scientist helped foster my competence and confidence, ultimately allowing me to complete this research.

Establishing my knowledge in electrochemistry would have been much more challenging without the help of Wendy Pell, the next person I'd like to thank. You always made time to answer my complicated questions in electrochemistry and beyond; I will always appreciate that.

Along the way, I was lucky enough to work alongside many friends and colleagues from the Richeson group, providing me with further motivation and support. Special thanks to Gyan, Yasmeen, Patrick, Sarah, Sara, Vince, Somayeh, Jon, Jake, and Eman. I would also like to thank Émilien and Eneko, for their hard work assisting in the lab with my research.

Thank you to my family for your constant support and encouragement. Mom, Dad, and brother David, you've always been unwavering with your confidence in me. Without your constant encouragement, completing this work would not have been possible.

Finally, I'd like to thank my soon to be wife, Valerie, for putting up with my irregular schedule and constant rambling about experiments that didn't work or data that I couldn't seem to make sense of. Having you to come home to has gotten me through many frustrating days and nights working in the lab, over the past several years.

Table of Contents

List of Figures

List of Tables

List of Schemes

List of Abbreviations

ΔE	Potential separation between peak cathodic and anodic current
ΔG	Change in relative Gibbs free energy
τ	Tau parameter (describes geometry of 5-coordinate complex)
AA	Acetic acid
ACN	Acetonitrile
Bpca	Bis(2-pyridylcarbonyl)amine) when ligand coordinated to a metal
BSSE	Basis set superposition error
BSIE	Basis set incompleteness error
CCDC	Cambridge Crystallographic Data Centre
CE	Counter electrode (CE)
CI	Central imide structure in bpca ligand
Cp	Cyclopentadienyl
CPE	Controlled potential electrolysis
CoPN3RP	$Co(\kappa^3\text{-}2,6\text{-}\{Ph_2PNR\}_2(NC_5H_3))Br_2$
CV	Cyclic voltammogram (CV)
DFT	Density functional theory
DCM	Dichloromethane
DMF	Dimethylformamide
$E_{1/2}$	Half-wave potential
E_{cat}	Reduction potential of catalyst
EDG	Electron donating group
EDTA	Ethylenediamine tetraacetic acid
EWG	Electron withdrawing group
$Fc^{+/0}$	Ferrocene/ferrocenium redox couple
Fc/Fc^+	Ferrocene/ferrocenium redox couple
FE	Faradaic efficiency
FOWA	Foot-of-the-wave analysis
GC	Glassy carbon
GC/MS	Gas chromatography/mass spectrometry
GC-TCD	Gas chromatography – Thermal conductivity detector
Hbpca	Bis(2-pyridylcarbonyl)amine) as a free ligand
HF	Hartree-Fock
HOMO	Highest occupied molecular orbital
I_a	Peak anodic current
I_{cat}	Catalytic current (Catalyst current in the presence of substrate)

I_c	Peak cathodic current
LSV	Linear scan voltammetry
LUMO	Lowest unoccupied molecular orbital
MO	Molecular orbital
MOPS	4-morpholinepropanesulfonic acid
MPc	Metal phthalocyanine
NiPc	The complex 1,4,8,11,15,18,22,25-octabutoxyphthalocyanine Ni(II)
NMR	Nuclear magnetic resonance spectroscopy
Pc	Phthalocyanine
PCET	Proton coupled electron transfer
PCM	Polarizable continuum model
PN3RP	2,6-$\{Ph_2PNR\}_2(NC_5H_3)$ ligand (R = H or Me)
PXRD	Powdered x-ray diffraction
RE	Reference electrode (RE)
SCE	Saturated calomel electrode
SC-XRD	Single crystal X-ray diffraction
SEC	Spectroelectrochemical
SEM	Scanning electron microscopy
SOMO	Singly occupied molecular orbital
SP	Square pyramidal (molecular geometry)
TBAHFP	Tetra-N-butylammonium hexafluorophosphate
TBP	Trigonal bipyramidal (molecular geometry)
TD-DFT	Time dependant density functional theory
TEM	Tunneling electron microscopy
TEA	Triethylamine
TEOA	Triethanolamine
TFA	Trifluoroacetic acid
TFE	Trifluoroethanol
THF	Tetrahydrofuran
TOF	Turnover frequency
UV-vis	Ultraviolet-visible spectroscopy
WE	Working electrode
XPS	X-ray photoelectron spectroscopy
ZnPc	The complex 1,4,8,11,15,18,22,25-octabutoxyphthalocyanine Zn(II)

Chapter 1: Introduction

1.1 – Value-added Products and Green Energy Production

Dependence on petroleum reserves to supply industry and generate energy sources has deteriorated into an unsustainable predicament leading to environmental decay.[1–3] Alternative routes to synthetic feedstocks and energy sources are crucial in moving toward a balanced industrialized society.[4,5] Establishing effective and efficient processes capable of remediating waste chemicals into something useful is an especially significant contribution to sustainable and responsible chemical practices.

Greenhouse gases are common targets for chemical remediation to value added products. CO_2 reduction is the most prominently studied example, commonly being transformed into CO, MeOH, or formic acid.[5] NO_x gasses like N_2O and NO are some examples that have been investigated to a lesser degree, for generation of ammonia.[6] The nitrogen cycle contains other non-gaseous targets, like NO_2^- and NO_3^-, which are also reduced to produce ammonia. Each of these pathways carries a varying degree of environmental benefits depending on the detriment of the waste and the value of the product, but understanding how each reaction can be catalyzed contributes to our fundamental knowledge of the area. Ideally, a lower energy catalytic process would be developed to replace the Haber-Bosch process for ammonia generation, as this process is very energy intensive – using more than 1% of worldwide energy output each year.[2–4]

Sustainable generation of green energy requires a full evaluation of the chemical cycle responsible for energy production. When energy is generated from combustion of a molecule, where the molecule came from, and the products of its combustion both must be considered to ensure the overall process adheres to green chemistry principles.

Hydrogen combustion is a clean process because it generates energy with a sole chemical product of water. Unfortunately, the most common method used to source H_2 is steam reforming from methane, which is energy intensive and generates CO_2 as a byproduct.[1] Electrolysis of water to generate H_2 negates the generation of CO_2 as a by-product, but still remains an energy intensive process and too expensive to rely on, in its current form.[7] Electrocatalytic water splitting has been an active area of investigation over the past several decades to address this issue.[1,7,8]

Whether the targeted substrate for the production of a value-added product is something environmentally detrimental, like CO_2 and NO_2^-, or benign, like water for H_2 generation, both still contribute meaningfully to the advancement of sustainable industrial processes. Often these processes can be in competition with one another and follow similar catalytic cycles. Investigating the larger, more complex catalytic cycles like nitrite reduction are often informed by our understanding of shorter, simpler cycles, like hydrogen generation.

1.2 - Organometallic Complexes: History, Electrochemical Investigations, and Catalysis

This investigation intends to apply the unique and versatile redox properties of organometallic complexes to perform electrocatalysis. The discovery of organometallic complexes perplexed the scientific community for many years before technological advancements allowed the true nature of interactions between metals and organic matter to be revealed. Before the advent of sophisticated NMR analysis and X-ray crystallography, early chemists had to rely on little more than their senses and some rudimentary chemical intuition to elucidate structural details.[9,10] Important theories

regarding the nature of bonding interactions arose from the 19th century struggle with this new, strange, and non-obvious class of molecules – organometallic complexes.[11]

Broadly speaking, organometallic complexes are defined as molecules that contain at least one bond between organic carbon and metals or metalloids. This classification is often expanded to include any class of compound with an organic ligand bonded with a Lewis acid.[9] Many of the compounds that fit in this broadened definition bond through a nitrogen or phosphorus. Similarities in reactivity and structural details between this expanded class of complexes and the more stringent classification justify the expansion.

1.2.1 - Early investigations and discovery

Early work in this field was slow and sporadic, beginning in the early 1700s, with the synthesis of Prussian blue.[12] Classically, this molecule is not defined as an organometallic complex, because the carbon in CN is not regarded as organic; therefore, it does not satisfy the more stringent definition.[9] Regardless, the first documented metal-carbon bond warrants some discussion. It was synthesized first in 1706 by paint maker, Johann Jacob Diesbach by mixing hydrogen peroxide with ferricyanide.[12] This era of scientific inquiry into the nature of matter predates most modern theories and represents some of the purest examples of the scientific method. All observable faculties of reason were applied to understand what was occurring, from sight to scent. Diesbach didn't know the concept of catenation, or crystal field theory, or even the term, "ligand." The area of study had not yet been established that would be required to fully understand Prussian blue, nevertheless, it made contributions to countless works of art through the 18th century.

The first example of an organometallic complex that adheres to the more strict interpretation of the term's definition is potassium trichloro(ethylene)platinate(II) hydrate, classically known as Zeise's salt.[13,14] Specific details regarding the structure of this complex would remain somewhat of a mystery until crystallography was introduced in the 20th century, but Ziese was able to identify its composition. William Christopher Ziese was able to prepare his molecule in 1827 by mixing $PtCl_4$ with boiling ethanol, eliminating a chloride and coordinating ethylene.[14] The proposed structure was often criticized, but was generally accepted by 1868, when a different synthetic route to Zeise's salt was accomplished using ethylene instead of ethanol. Studying the structure of this complex would eventually revolutionize our understanding of possible bonding interactions between sp^2 carbons and metal centers.

Further discoveries and advancements in organometallic chemistry started to occur more frequently through the 19th century and into the 20th century. Some notable early examples include the first organozinc and organotin complexes in 1849 and 1863, respectively.[9] This era was marked by the expansion and establishment of our understanding of possible organometallic structures. Sandwich compounds were one of the most significant developments to come out of this expansion. These structures contained cyclopentadienyl groups coordinated above and below a metal center, creating the image of a sandwich.[9,15] The first example demonstrating the bonding capabilities of cyclopentadienyl groups occurred in 1901 with the discovery of potassium cyclopentadienyl.[9] The "sandwich" structure could not be confirmed until ferrocene was first synthesised in 1951 when more sophisticated X-ray crystallography was available.

Understanding the bonding interactions present in ferrocene significantly contributed to our modern understanding of ligand field theory.[15] Ferrocene is still a significant molecule in electrochemistry, acting as a reliable internal reference potential for cyclic voltammetry in organic solvents and even performing electrocatalysis, efficiently oxidizing ammonia.[10,16]

Following the development and widespread application of modern crystallographic and spectroscopic analysis techniques, the field of organometallic chemistry exploded. Chemists were no longer required to speculate on chemical structures, the technology had finally caught up with the synthetic capabilities. With these newfound capabilities, structure function relationships could be constructed, and these compounds started to become useful.

1.2.2 - Advancements in bonding theories

New models describing what governs the interactions observed in organometallic chemistry were necessary following their identification. Previous rules and models in main group chemistry were insufficient to explain the observed structures.[9,11] Valence bond theory was effective in describing organic molecules and simple inorganic structures but struggled to fully describe the electron configuration of metallic complexes, especially transition metals. Parsing the structural reality of complexes like Zeise's salt and ferrocene with some overarching bonding theory resulted in several new guiding principles like the 18-electron rule and even established the most sophisticated bonding model devised in chemistry, molecular orbital theory. The following are some examples

of bonding rules and theories that resulted from interpretation of organometallic structures.[13,14]

18-electron rule: Investigations of transition metal complexes with carbonyl groups lead to the establishment of this effective rule, that proved to be predictive for the stability of many transition metal complexes. The rule posits that organometallic complexes that place 18-electrons in the valence shell of the central metal, leave the orbitals fully occupied and are likely to be stable. There are exceptions to the rule, but overall, this configuration is optimal. For transition metal chemists, counting electrons has become second nature when determining if a proposed structure will be stable.[17]

Crystal field theory and ligand field theory: These theories both use geometric arguments and explain the relationship between d-electron, coordination number, and electron geometry. Ligand theory is a more in-depth adaptation of crystal field theory that addresses coordination with ligand systems that share delocalized electrons with the metal center.[18]

Crystal field theory operates in a crystal lattice with the metal in its center. Each ligand coordinated to the metal center is treated as a point charge. The degree by which the point charge is repelled by the d-orbitals of the metal center depends on their positioning in the crystal lattice.[11,18] When a point charge overlaps significantly with a specific d-orbital, that d-orbital is considered higher energy and has a lesser chance of being occupied. Occupied orbitals have minimal overlap with point charges in the crystal lattice. For example, molybdenum hexacarbonyl has a d-electron count of d^6. The direct overlap

with the d_{z^2} and $d_{x^2-y^2}$ atomic orbitals of Mo causes these orbitals (E_g) to be higher in energy, leaving the d_{xy}, d_{xy}, and d_{yz} (t_{2g}) fully occupied, as shown in Figure 1.1.

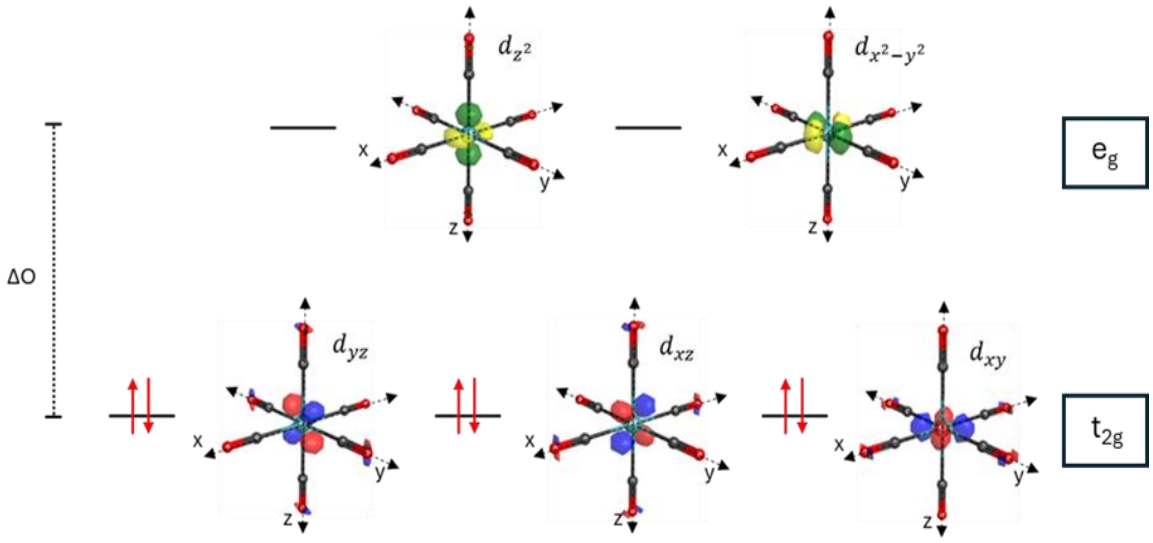

Figure 1.1: d-Electron splitting diagram and associated molecular orbitals for $Mo(CN)_6$.

The ligand contributions to this structure expand beyond simple point charges. The CN ligand can perform pi back bonding through its unoccupied pi orbitals, which further affects the energy levels of each orbital displayed in Figure 1.1, increasing ΔO. Several non-bonding orbitals from the CN ligands also exist in between the e_g and t_{2g} levels, which were omitted for clarity.

Molecular orbital theory: Early bonding theories, like valence bond theory, imagined electrons as being localized around each atom, occupying bonds with adjacent atoms. MO theory alters this approach, by imagining the electrons to be delocalized in an isosurface surrounding the structure.[11] The electrons stored in the orbitals in Figure 1.1 are equally likely to be found in all parts of the isosurfaces displayed in each of the MOs. The shapes of the MOs are established jointly through consideration of the relative energy levels of

atomic orbitals and their symmetry relative to one another; overlap of the atomic orbitals is required to establish an MO. Atomic orbitals that are closer in energy to the newly formed MO, contribute more of their own character than the atomic orbital with a larger energy difference. Investigation into the electrochemistry of ferrocene in the 1950s was an early and significant example demonstrating the effectiveness of MO theory, greatly popularizing the theory.[19] The stability in the structure of ferrocene, as seen in Figure 1.2a could not be easily justified by any of the early bonding theories. MO theory showed that the delocalized electrons contained in the pi-orbitals of the cyclopentadienyl rings, as shown in Figure 1.2b, could interact with the atomic orbitals of iron, allowing this strange structure to be stabilized.

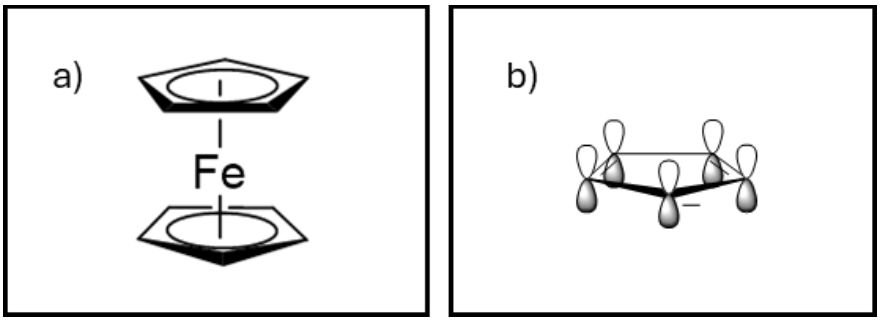

Figure 1.2: a) A line drawing depicting the structure of ferrocene b) Atomic orbital contributions to the MO of the Cp ring.

Studying the interactions between matter and electricity has taken many forms over the past several centuries. The definitions and terminology described by Michael Faraday in the early 1800s have been refined since, but still stand as the basis for modern investigations.[20] Electrochemical investigations have made significant contributions to understanding the redox activity of organometallic molecules. Studying the

electrochemistry of ferrocene marks the beginning of the systematic description of redox characteristics for organometallic complexes.[10] Ferrocene became a standard potential for investigating other complexes in organic solvents. The stable and reversible nature of the ferrocene/ferrocenium redox event allows the complex to be added as an internal standard during cyclic voltammetry to determine the redox potentials of other complexes.[10] In most cases ferrocene is inert and unreactive, having no influence on the structure of complexes being investigated. Establishing a standard potential that could be referenced in organic solvents helped to expand this area of study to complexes that are insoluble in water, which applies to many organometallic molecules.[21]

Electrochemical investigations of organometallic complexes accelerated after the studies involving sandwich molecules. Insights into the nature of redox chemistry and specific mechanism for electron transfers were elucidated.[10] Catalytic detection and evaluation were brought to the forefront of this analysis technique. Analysis methods like foot-of-the-wave analysis allowed for the generation of kinetic information to be accessible through simple voltammetry, even correcting for mitigating effects like substrate depletion or catalyst deactivation.[22] What began as a rudimentary technique to determine redox potentials has developed into an in-depth evaluation of the how and why in redox chemistry. Linking electrochemical analysis with density functional theory (DFT) calculations further enhanced the capacity of this technique by offering some insight into the identity of molecular orbitals that would be filled or become unoccupied during a redox event. For example, the simple calculation displayed in Figure 1.1 suggests that an electron is removed from a t_{2g} orbital during an oxidation process. This has

implications into the charge of the central atom, as well as the magnetic properties of the material. This calculation could be run again with one less electron in a doublet state, generating a proposed structure of the oxidized species. Examining the MOs of the oxidized species would demonstrate how the structure adjusts to fit the new electronic configuration, utilizing the principles of MO theory and crystal field theory.

1.2.3 – Development of organometallic catalysis

Organometallic complexes have become ubiquitous in the world of catalysis. Their ability to stabilize multiple oxidation states makes them particularly apt at completing a catalytic cycle. The earliest examples of catalysis were heterogeneous in nature, generally using small amounts of pure metals. The famous French chemist, Paul Sabatier, uncovered such a reaction for the hydrogenation of several organic compounds using finely cut up metals. This instance marks the beginning of the journey from bulk metals to homogeneous catalysis.[23] Sabatier's idea to increase surface area by using the smallest possible pieces was eventually brought to its extreme, through the establishment of molecular catalysis. Organometallic complexes were first observed to operate as molecular catalysts in the 1950s, when various aluminum alkyl complexes were demonstrated to act as cocatalysts for the polymerization of alkenes. The Ziegler-Natta catalysts, established by Karl Ziegler and further developed and popularized by Giulio Natta, revolutionized the polymer industry, allowing for generation of isotactic polypropylene.[24] Organometallic catalysts continued to make significant advancements to science and society over the next several decades at an accelerated rate. Hydrogenation, cross-coupling reactions, and metathesis

are just a few examples of significant reactions made more accessible by organometallic catalysts.[25]

The trajectories of organometallic catalysis and electrochemistry significantly overlapped following the discovery and study of sandwich molecules. Though electrocatalysts did exist before this, efforts made into the study of molecules like ferrocene resulted in the establishment of analytical techniques that could effectively assess and benchmark electro-redox catalysts. Moving into the 1960s and 1970s, hydrogen generation from water and CO_2 reduction began to gain prominence as targets for electrocatalytic studies.[26] These investigations continue to garner significant interest, as both play a part in addressing current environmental threats. Some other prominent targets for homogeneous electrocatalysis include reduction of NO_x compounds, oxidation of water, and oxidation of ammonia. Each of these targets has their own challenges but they share the same general form. For each target, the catalyst must have a redox event in the appropriate potential range, and the target must chemically interact with the catalyst. Details about the order of these operations, overpotentials required for catalysis to occur, and overall catalytic efficiencies can all be determined through the strategic use and combination of electrochemical techniques.[22]

1.3 – Practical Homogeneous Electrocatalysis

Modern homogeneous electrocatalytic studies utilize many of the same electrochemical techniques to detect substrate turnover and evaluate their catalysts. Valuable information can be garnered regarding efficiency and functionality by applying these techniques in conditions with and without substrate (catalytic and non-catalytic,

respectively).[21,27,28] In non-catalytic environments, fundamental redox information can be obtained. How many redox events are there? Are the events reversible? At what potential does the complex lose or gain electrons? How many electrons are passed in the process? These are just some of the questions that can be answered in non-catalytic environments.[21] Catalytic environments screen complexes for catalytic activity and have broader variance in their systems to be navigated. The pH, strength of solvent coordination, choice of electrolyte, and concentration of substrate can all affect the performance of the catalyst during its evaluation.[29,30] For H_2 generation and NO_2^- reduction, pH is an especially important parameter to optimize.

Initial assessment for potential catalysts generally begins in non-catalytic environments. Determining the redox potentials for a complex establishes which substrate could be viable catalytic targets.[31] Once it is established that a catalyst has a redox potential in an appropriate region, then catalytic environments can be explored for detection and evaluation. Just a couple of quick voltammetry experiments can signify a positive hit worthy of further exploration.

1.3.1 – The electrochemical cell

Multiple forms of electrochemical experimentation can be performed using the same general equipment.[21] The powerhouse of the operation is a potentiostat, which supplies the electricity through an arrangement of circuits, strategically wired to allow interpretation of the flow of electrons within the electrochemical cell. The electrochemical cell is composed of 3 electrodes: the working electrode (WE), the counter electrode (CE), and the reference electrode (RE). In the context of homogeneous

electrochemistry, the working electrode plays host to the electron transfer process being investigated.[28] The eventual output data portrays the transactions that occur at the WE. Glassy carbon is a very common choice of material for the WE. Completion of the circuit is assured through the CE. The CE must readily conduct the charge transferred through the chemical cell, meaning it must have a larger surface area than the WE. Carbon rods or platinum mesh are popular material choices used for the CE.[21,27] The RE acts to set the potential in reference to another redox process. In aqueous solvents, Ag/AgCl is a common redox couple choice. Ag/AgCl electrodes contain a miniature electrochemical cell, separated from the bulk material by a frit. The solvent and electrolyte make up the remaining components, which allow electrochemical cells to function. The solvent brings the analyte and electrolyte into the homogeneous phase and the electrolyte allows for the charge to be transferred through the bulk solution, from the WE to the CE.

1.3.2 - Investigative methods and metrics

Several forms of voltammetry and coulometry can be performed using the simple cell described previously. Each technique has their own purpose and can generate a variety of important catalytic metrics. The techniques pertinent to this work and related metrics are described below.

Cyclic voltammetry (non-catalytic): Performing a cyclic voltammogram (CV) involves selecting a potential range to scan through and the rate at which the scan will be performed, also known as the 'scan rate.' Initial investigation for a complex with unknown redox activity would generally involve a moderate scan rate (0.1V/s) and a range close to the edges of the solvent window. Each solvent has a different window, based on what

potential solvent molecule is reduced and oxidized. When a potential scan approaches the edge of a solvent window, reduction or oxidation of the solvent causes the current to spike as electrons are rapidly added or removed, dwarfing the flow of electrons caused by the analyte. This highlights the importance of selecting an appropriate solvent for each investigation. Acetonitrile is an excellent choice for performing CVs in organic solvents, as it offers a large operating range in both the anodic and cathodic directions.[21,27,28]

Once the initial scans are completed and the redox events are located, more directed scans can be chosen to isolate redox events. Consider the scan of ferrocene displayed in Figure 1.3, the image on the left (1.3a) displays how the potential changes over time. In this case, the entire scan is completed in less than 20 seconds, starting at 0.53V, switching potential direction at -0.48V, and finishing at the starting potential at 0.53V. Potential sweeps in this direction (in the negative direction) are referred to as cathodic sweeps, when the direction of the potential sweep is reversed, they are denoted as anodic sweeps.[21] Figure 1.3b displays the accompanying CV. The shape of this figure is indicative of a reversible process. The 1-electron process is not associated with any significant structural rearrangements, meaning the electron can be added or removed in a similar manner. For a redox event to be 'reversible' the peak cathodic current (i_c) and peak anodic current (i_a) must have the same absolute value.[21,27] The second, and final criteria for a reversible process involves the separation of peaks (ΔE). This criterion is dependant on the choice of solvent. In water, a reversible 1-electron process must have a ΔE of 59mV. Variance in mass transport constants in different solvents results in some variance in this value. For this reason, reversibility is often predicated on how closely the ΔE value

conforms to that of ferrocene in the same environment, since the $Fc^{+/0}$ redox couple is a well established, reversible, 1-electron process.

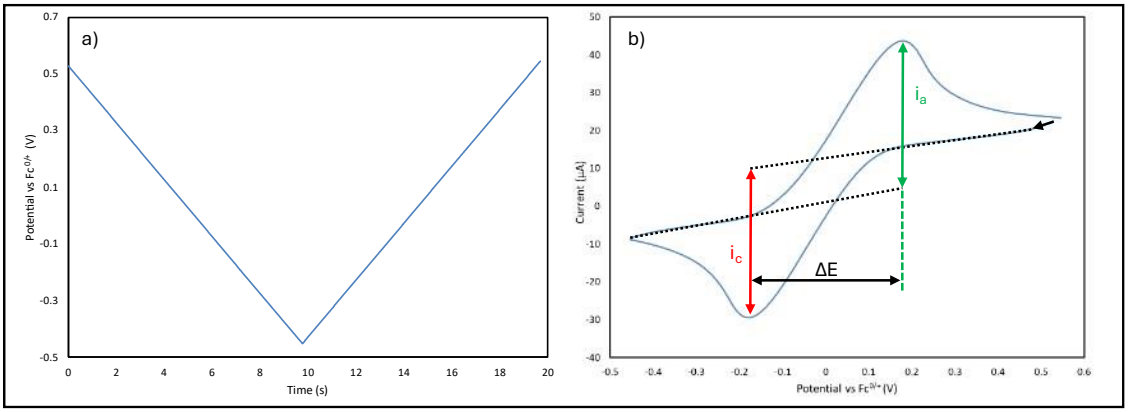

Figure 1.3: a) Potential versus time graph for a cyclic voltammogram of ferrocene b) cyclic voltammogram of the ferrocene/ferrocenium redox event in THF at a scan rate of 0.1V/s.

Scan rate dependence investigations using cyclic voltammetry are necessary to provide support for the homogeneous nature of the redox activity. According to the Randles-Sevcik equation (eq. 1.1), the square root of the scan rate should be directly proportional to the observed peak current. Instances where this relationship is not linear could indicate heterogeneous processes or the occurrence of a chemical change through a redox process.[21]

$$i_p = 0.446nFAC^0\left(\frac{nF\nu D_0}{RT}\right)^{\frac{1}{2}} \qquad \text{(eq. 1.1)}$$

i_p=peak current value (A), n=number of electrons, F=faraday constant (A·mol^{-1}), A= area of electrode (cm^2), C^0= bulk concentration of analyte (mol·cm^{-3}), ν=scan rate (V·s^{-1}), D_0=diffusion constant (cm^2·s^{-1}), R=gas constant (J·mol^{-1}K^{-1}), T=temperature (K)

Cyclic voltammetry (catalytic): Exploring the catalytic capability of a complex involves the implementation of cyclic voltammetry in a catalytic environment.[28,31] Once the general electrochemical behaviour of the complex has been investigated, the pertinent redox events can be screened for catalytic activity. There are two main indicators of catalytic activity, enhancement at the redox event and disappearance of the return process. For example, CoPN3HP was investigated in Chapter 2 for electrocatalytic proton reduction. When CoPN3HP is exposed to acetic acid, the once reversible event completely changes shape, as displayed in Figure 1.4.[28]

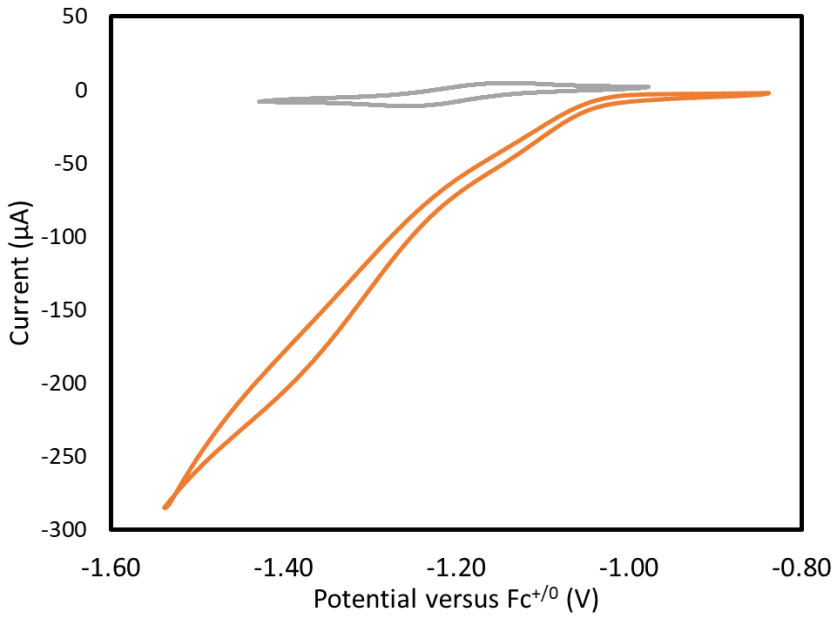

Figure 1.4: CV of 1mM CoPN3HP in acetonitrile with 0.1M TBAHFP electrolyte without acetic acid (grey) and with added acetic acid (orange).

The reduction peak current of the event is significantly enhanced, and the return oxidation completely disappears. The enhancement is a result of the catalyst facilitating electron transfer into the product. The protons are acting as an electron sink, performing

turnovers of the catalytic cycle. Disappearance of the return oxidation further substantiates this claim, since completion of the catalytic cycle brings the catalyst back to its initial state, before an electron is added to it.

Linear scan voltammetry (LSV) and the dip test:

Performing LSV requires similar considerations to CV, the scan rate and range must be selected. The key difference here, is that there is no return scan. For LSV, the reversal of the scan direction does not occur. The associated potential-time relationship would simply appear like the first half of the function observed in Figure 1.3a. In the context of homogeneous catalysis, LSV is commonly employed in an experiment known as a dip test, to support the presumption of a homogeneous process by demonstrating that the material does not become adsorbed to the electrode surface. During this process, several (5-50) sequential scans are performed in a catalytic environment. Next, the electrode is removed and rinsed with the solvent. The newly rinsed electrode is then placed into a new solution that contains the substrate, but no catalyst. Instances where some catalytic features are still observed in the solution containing no catalyst suggest that some of the catalyst may have formed a coating on the electrode, ultimately indicating a heterogeneous process. If no catalytic features are observed and the scan rate dependence investigated through CV indicates a diffusion-controlled process, sufficient evidence for a homogeneous process can be presumed.[32]

Controlled potential electrolysis (CPE):

Observation of enhanced current during voltammetry experiments indicates catalysis but does not confirm it. Bulk experiments must be performed to generate enough catalytic

product to be detected and quantified. CPE is performed based on the information gained during voltammetry. This experiment requires setting of the potentiostat at a specific potential for a set amount of time, supplying the catalyst with an appropriate voltage to perform catalysis.[33] The potential is strategically set to overlap sufficiently with the indicated enhancement, while remaining less than the potential at which the substrate may undergo a redox process at the electrode on its own. Depending on the product, different detection techniques can be used. Some examples include GC-TCD, various NMR analyses, or redox titration. The efficiency of the process can be evaluated through calculating of the 'Faradaic efficiency' which is calculated according to eq. 1.2.[34]

$$FE = \frac{\#\ electrons\ consumed}{\#\ electrons\ provided} \cdot 100\% \qquad \text{(eq. 1.2)}$$

The number of electrons consumed is determined based on the number of electrons required to generate the product from the substrate. The number of electrons provided is based on the total charge transferred through the electrochemical cell over the electrolysis process. Effective catalysts should be close to 100%. Poor performance based on this metric could indicate that the catalyst decays over the reaction time.[35]

1.3.3 - Spectroelectrochemistry

Combining spectroscopy and electrochemistry allows for some revelation into the excited states and electronic structures of the products generated following a redox process. Examining the CV of a redox process can direct the chosen potentials which are stepped through during the spectroscopic measurements. Ideally, the first few chosen potentials will begin at the start of the redox couple and step towards the peak current. For these

experiments, multiple potentials are chosen for consecutive CPE experiments. Each potential is held for a short period of time, and an absorbance spectrum is collected.[36] The obtained data for these experiments can be presented in a variety of ways. When each stepped potential is displayed consecutively, the peaks associated with the species before the reduction event will begin to shrink, and new peaks for the species present after the redox event will grow.[37] The presence of isosbestic points throughout this transition period can indicate a clean transition from one species to another, suggesting that no significant chemical alteration occur after the reduction event. This methodology can be implemented in a non-catalytic environment to better understand the redox behaviour of the complex itself. It can also be used to detect intermediate species in a catalytic environment, helping to probe for mechanistic details.[38]

1.4 - Establishing Mechanistic Insights

Elucidating mechanistic details regarding a catalytic cycle can be achieved through the joint application of a variety of electrochemical, spectroscopic, and computational methods.[39] Understanding the order in which steps occur and their overall functionality can help optimize the environment, promoting catalysis and directing the design of future catalysts. Homogeneous electrocatalytic hydrogen generation and nitrite reduction each occur through a wide range of mechanisms. Overall, more research has been completed for hydrogen production, but recently investigations into nitrite reduction electrocatalysis have become increasingly prevalent.[2] Many of the same complexes explored for these substrates are capable of catalyzing both reaction pathways. Proton reduction occurs in a larger variety of environments, ranging in pH, solvent choice, and in the presence or

absence of a buffer. While there have been reports of nitrite-reducing electrocatalysts demonstrating capabilities in a range of pH's, most works find that the presence of a buffer is necessary.[40]

1.4.1 - H_2 evolution

Generation of hydrogen from a proton source requires the addition of two protons and two electrons. Water is the most used substrate generally observed in proton electrocatalytic reduction. Electrolyzing water is often referred to as "water splitting." The concept of water splitting involves the production of both oxygen and hydrogen, at the anodic and cathodic electrodes, respectively.[41] Generation of hydrogen from a proton source addresses one half of that redox equation, as displayed in scheme 1.1.

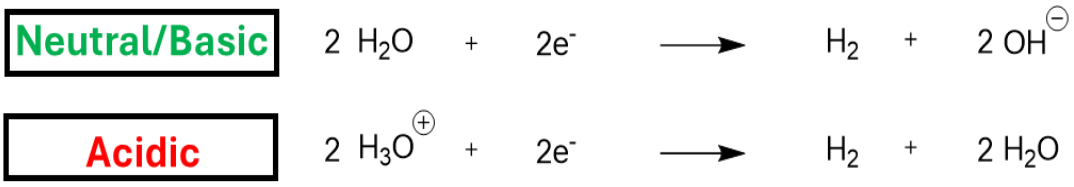

Scheme 1.1: Chemical equations for water reduction in basic/neutral and acidic conditions.

Determining how these simple reactions are facilitated electrocatalytically can be a complex and meticulous process. The order in which the electrons or protons are added, whether the protons are added through intra- or intermolecular interactions, and the process which ultimately releases the hydrogen atom from the catalyst are just some of the details in the mechanism that can be elucidated.[7] The specific details for each mechanism are not bifurcated, as Scheme 1.1 appears to imply. The potential required to

generate hydrogen from a proton source is inversely proportional to the pH of the environment. Electrocatalysts aim to generate hydrogen in any pH environment at a potential less than what would be required at the electrode.[42]

The relationship between pH and the potential requirements can be most readily applied to aqueous environments, but the trend still stands in organic solvents. Interpretation of pH in organic solvents varies significantly from solvent to solvent. Water is as easily protonated as deprotonated, generating a symmetrical and predictable pH scale. Organic solvents don't have the same relationship with acid/base chemistry. Recognition of the pH dependence on reduction potential can be more reliably and practically communicated by referring to the pK_a of the proton source, rather than the pH of solution, allowing the values to be qualitatively normalized, for comparison.

When investigating proton reduction catalysts, establishing the order in which the protons and electrons are added is often used to characterize the mechanism. This nomenclature associates four letters to each mechanism, two of the letters represent electron-transfer processes (E) and another two document a chemical step (C), referring to a protonation.[22,31,43] When this system was developed, the presumed mechanisms occurred through the generation of a metal hydride, that was either protonated to release hydrogen, or interacted with another hydride species in a homolytic process. Regardless of these early assumptions, this nomenclature remains relevant, bolstered by the establishment of foot-of-the-wave analysis (FOWA) proposed by Costentin and Savéant. This technique allowed for the effective benchmarking of catalysts, while also providing direction in determining order of operations for E and C processes. For example,

a proton reduction catalyst that is reduced, then protonated, then reduced, then protonated to ultimately release H_2 would be denoted as an ECEC mechanism. Many different metal-ligand combinations have been established to effectively produce hydrogen from a variety of proton sources.[22,31]

FOWA was developed for electrocatalytic H_2 generation but has since been broadened to collect kinetic information for other substrate targets, like CO_2 or NO_2^- reduction. This technique becomes useful when varying the scan rate of a CV cannot achieve the "S-shaped" curve indicative of substrate saturation that traces itself during the return oxidation. FOWA uses the region of the voltametric scan at the very beginning of a catalytic curve, where substrate-initiated enhancement is observed. By studying this initial part of the curve, FOWA can extract kinetic information about the catalytic process. Near the start of the catalytic curve, mitigating factors like catalyst deactivation or substrate depletion are not present. Ultimately, this technique avoids underestimating the kinetics of the reaction. FOWA represents an important analytical tool in electrochemistry, allowing researchers to obtain more accurate kinetic data for various electrocatalytic processes. This is particularly valuable in fields such as renewable energy research, where understanding the kinetics of hydrogen generation or CO_2 reduction is crucial for developing efficient catalysts and processes. [22,31]

1.4.2 – Nitrite reduction

Electrocatalytic reduction of nitrite to generate ammonia requires more chemical steps than producing hydrogen from water, making the overall mechanism more complex.[44]

One implication of the complexity of nitrite reduction is that there are several other possible products when it is reduced, as displayed in scheme 1.2.[2]

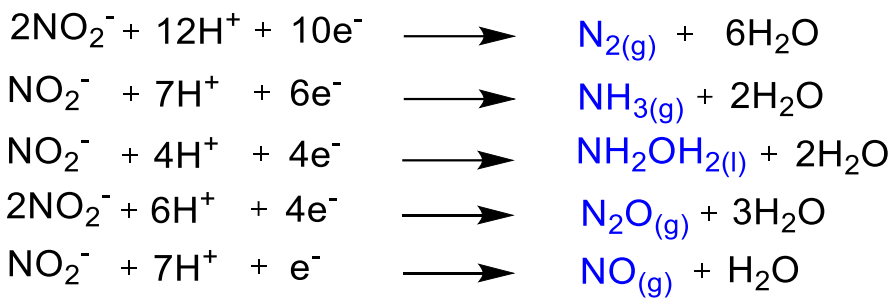

Scheme 1.2: Reduction products of nitrite with varying number of reduction and protonation processes. Intended reduction products are displayed in blue.

The first reduction product, nitrogen gas, represents the complete reduction of nitrite. This reaction requires the greatest amount of energy and is uncommonly observed in electrocatalysis. The next two products, ammonia and hydroxylamine, are the two main products found in the studies investigated herein. Ammonia undergoes another protonation in solution to become ammonium, in this scenario. Nitrous oxide and nitric oxide are two gaseous products that are often detected in catalytic trials.[2]

The pH dependence for electrocatalytic NO_2^- has a range of effects on catalytic products and competing reactions. In acidic aqueous environments with pH<2, NO_2^- undergoes a protonation process to begin, meaning that catalytic processes act on HNO_2 as the substrate. This alteration affects both the capacity of molecular catalysts to coordinate through the nitrogen, and shifts the actual redox potential required to reduce the substrate. [40,45,46]Additionally, in an acidic environment, hydrogen generation becomes more prominent as a competing reaction pathway. Coordinating through oxygen instead

of nitrogen tends to direct the generation of $N_2O_{(g)}$ as the catalytic product, rather than NO, NH_2OH, or NH_3.[47]

Performing nitrite reduction in a neutral/basic environment allows the substrate to participate as NO_2^-, meaning it can interact with molecular catalysts through the oxygen or the nitrogen. There are a variety of mechanistic pathways that can occur following the coordination of NO_2^-. The variance in functionality can largely be accredited to the diversity in surrounding ligand structures and the many possible ways in which these structures can interact chemically, or electronically with the coordinated NO_2^- substrate throughout the catalytic cycle. Many of the proposed mechanisms with similar catalytic abilities mimic enzymatic production of ammonia (Figure 1.5).[48]

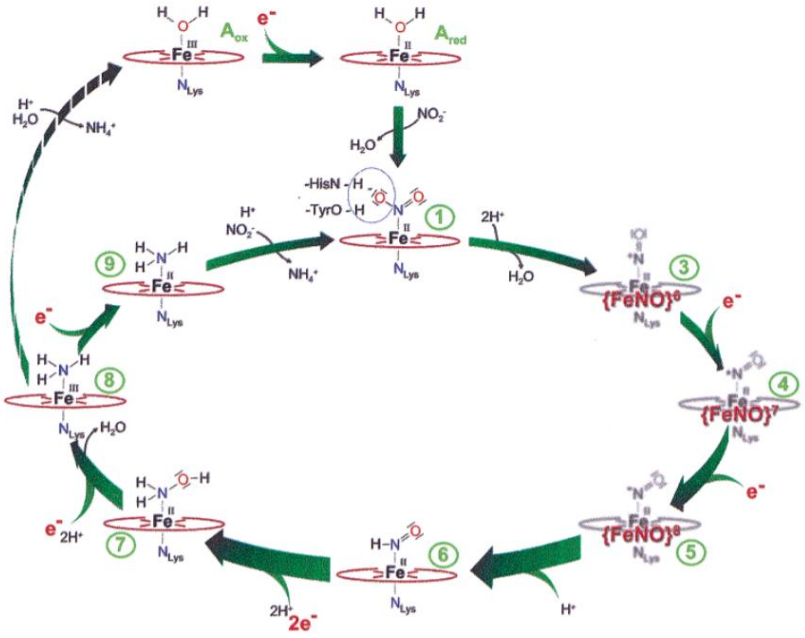

Figure 1.5: Proposed mechanism for the enzymatic production of ammonia from nitrite for Cytochrome c Nitrite Reductase. Reprinted with permission from {J Am Chem Soc. 2002, 124, 39, 11737-11745} Copyright {2024} American Chemical Society.

During the completion of the catalytic cycle, several proton-coupled electron transfer (PCET) steps are completed. In Figure 1.5, from steps 6 to 7, two PCET steps are proposed. These steps are not likely concerted, it is more likely that one step induced the other.[49] Reducing a complex can alter the pK_a of active protonation sites on ligand structures, which in the case of enzymes, includes amino acid sites.[48] The reverse is also true; protonation can alter the redox potential of a catalyst. Considering the changing pK_a and reduction potential throughout the catalytic cycle adds complexity to elucidating mechanistic details, but ultimately generates a more thorough understanding of each catalyst's functionality.

1.5 - Application of DFT

Proposing mechanistic pathways for any catalytic cycle requires clear experimental evidence but can be supported through the application of density functional theory (DFT). Over the past several decades, DFT analysis has become increasingly accessible to chemists as a tool to support their experimental claims.[50–52] Using this technology, reaction steps can be simulated through the optimization of proposed structures, demonstrating the relative Gibbs free energy between each step. For each simulated structure, molecular orbitals can also be investigated, displaying their shape and location (Figure 1.1). Several spectra can also be generated from each structure, including absorption spectra, that can readily be compared to obtained UV-vis spectroscopy measurements.[37]

The structure of computational methods can be broken down into two main layers. The first of these layers is the choice of functional, or level of theory. This layer can be thought

of as a sort of 'function of functions.' Ultimately, this layer looks to represent the self consistent field encompassing the behaviour of each individual electron and their interactions. Many attempts have been made to accurately and efficiently represent the interaction of these functions. The pathways that represent these attempts can be broken down into two main classifications; functionals based entirely on the wave functions of individual atoms, denoted as Hartree-Fock (HF), and functionals based on electron density (DFT). The most effective functionals to date combine these approaches, amalgamating the strengths of each viewpoint to optimize accuracy and efficiency.[50,51]

The second layer completing the design of a computational method is the basis set. These functions are meant to represent the individual functions of atomic orbitals. The basis set for each atom are combined in a linear combination to generate the overall molecular orbital. The simplest representation for a basis set would describe all atomic orbitals for a molecule in which electrons reside. Adding more functions to describe each atomic orbital in a molecular structure allows for a more detailed representation of the molecular orbital, based on their bonding interactions. Effective modulation of orbital size based on these interactions can be achieved by inclusion of polarization functions in each basis set. Polarization functions are representations of p- or d-orbitals with principal quantum numbers one higher than the valence electrons of a structure. Care needs to be taken when increasing the overall number of functions that make up basis sets, as the computational time scales exponentially with the number of functions. With added functions, a point will be reached where the increase in computational accuracy suffers

diminishing returns, causing the computational time to soar past practical considerations.[50,51]

Designing a computational strategy to effectively simulate a proposed structure or generate excited states, requires the consideration of two competing factors: accuracy of results and computational cost. Applying the most complex functionals and robust basis sets, generally results in more accurate values. However, computational power and processor time limitations can make completion of these calculations impossible. B3LYP is a common functional choice for optimization and energy calculations for a wide variety of molecular structures. The standard B3LYP functional incorporates aspects of DFT and HF into a hybrid functional that is often used as a benchmark to evaluate the accuracy of other functionals. Choice of functional is dependent on the size of the molecule and type of atoms being investigated. When transition metal complexes are being studied, a class of functionals known as the "Minnesota functionals" are commonly employed. The MO6L functional is an electron density based functional that includes no HF character which has been shown to effectively calculate reaction energies of organometallic complexes with relatively low computational cost. Choice of basis set depends on the type of calculation being performed. Structural optimization and vibrational frequency calculations require less refinement; therefore, fewer functions need to be included to establish the molecular structure. Basis sets like def2-SVP (split-valence with polarization) can efficiently generate accurate structures. When calculating the energetics of a process, more functions are required for each atomic orbital to generate accurate results. Moving to def2-TZVP or def2-QZVP will return more accurate results. In some instances, increasing the

polarization consideration for an orbital is necessary, selecting basis sets with an additional P at the end of their name implies a more significant correction.[50,51]

Despite the application of best computational practices, some errors can remain, affecting the accuracy of a calculation. Basis set incompleteness error (BSIE) and basis set superposition error (BSSE) are two examples of errors that must be addressed. BSIE implies that the selected basis set is insufficient or not flexible enough to represent the molecular system. What results is a crude interpretation of a molecular structure, drastically miscalculating its energy. Corrections for this error can involve the inclusion of additional polarization functions or increasing the number of functions that describe atomic orbitals. In instances where additional functions would increase the computational time to unsustainable levels, larger atoms can be specifically targeted, allowing smaller atoms to remain with the original basis set.[50]

BSSE involves the unintended overlap and interaction of atomic orbitals that should not electronically interact, but do so anyway during a calculation, due to their proximity. The erroneous interactions result in an artificially lowered energy value, causing the calculations to underestimate molecular energy. Identifying the erroneous interaction and strategically breaking the molecule into separate sections and recomputing is one technique that can be employed. This is known as the 'counterpoise' correction. This method can identify the magnitude that the energy is lowered by the unintended overlap. Introducing a dispersion correction factor built into the initial computation, like the D3 Grimme's correction, is a simple method that can be used on its own, or in tandem with the counterpoise correction. This correction considers the intermolecular interactions

that would prevent the unintended lending of atomic orbital functions between atoms that are not actually covalently bonded.[50]

Consistent application of functionals, basis sets, and overall corrections to the computational method must occur throughout the entire process for energy differences, like relative Gibbs free energy, to be compared between structures. Consistency in computational methodology assures that apples are not being compared to oranges. Different basis sets can be used to optimize structure and calculate energies; however, the same process must occur when computing the next structure in a mechanistic pathway. It is also important to ensure that balanced chemical equations are being used to guide the overall process.

1.6 - Ligand Contributions: Developing Perspectives

Perspectives on ligand contributions to electro-redox catalysts have greatly shifted throughout the development of this field of study. Early investigations focused on the utilization of precious metals like platinum, which were already capable of stabilizing multiple redox potentials.[25] The focus for these mechanisms was on the metal, when mechanisms were proposed. 3d transition metals are smaller, meaning they need some assistance with stabilization when moving through multiple oxidation states; their smaller, less diffuse orbitals cannot as effectively stabilize the charge associated with high oxidation states.[53] Once more interest was garnered surrounding the function of ligands, the extent of their participation was shown to vary greatly from complex to complex. What resulted was a continuum of ligand contributions, from mechanisms involving no

ligand interaction with the substrate, all the way to mechanisms where the ligand seems to do the entire job.

1.6.1 – Metal-centered reactions

Reaction mechanisms in which the metal seems to be the sole participant for electro-redox catalysts are most commonly seen in catalysts which contain transition metals after the 3d metals; however, some examples do exist from the 3d metals. In these instances, the ligand essentially acts only to bring the metal into solution with the substrate. Upon identifying a redox active event, all, or the majority, of the electron density storage associated with the change in oxidation state are attributed to the metals. Additionally, interactions between the substrate and catalyst exclusively occur through the metal. One example of this is [cobalt(III)bis(1,4,7)triazacyclodecane]. This complex was demonstrated to perform hydrogen evolution in buffered solutions with pH's ranging from 2.7 to 10.3. The mechanism for this reaction proposed multiple pathways, outlined in scheme 1.3.[54]

$$Co(III)\text{-}H + H^+ \longrightarrow Co(III) + H_2 \qquad (1)$$

$$Co(III)\text{-}H \longrightarrow Co(II) + 1/2\ H_2 \qquad (2)$$

Scheme 1.3: Catalytic pathways for hydrogen generation from cobalt(III) bis(1,4,7) triazacyclodecane hydride. Reprinted with permission from {Polyhedron. 1998 17:4535-4541} Copyright {2024} Elsevier.

The first pathway indicates a heterolytic route, where the hydride species is protonated to release one equivalent of H_2. The second pathway requires the interaction of two M-H

species, following a homolytic process, releasing half an equivalent of H_2. In both cases, the mechanism proceeds through the formation of a metal hydride. Formation of the hydride is induced by added electron density on the metal center following a reduction event which increases the pK_a of the metal center, allowing for protonation to occur. That added density then shifts towards the proton to generate a hydride. The ligand appears to play a minimal role in the interaction, apart from providing the appropriate structure allowing the complex to be water soluble and perhaps some minor electronic tuning, resulting in the required reduction potential to achieve catalysis. Overall, the metal takes on the bulk of the responsibility to achieve catalysis, storing the electron density, attracting the proton, facilitating the reaction, and releasing the product.

1.6.2 – Redox-active ligands

Pairing electrochemical investigations with DFT simulation revealed a larger than expected participation in electron storage in ligand systems when used to analyze transition metal complexes with ligands containing substantial sp_2 character. Ligands containing pyridine-like structures are endowed with the appropriate energy levels in their electronic structure and symmetry to significantly overlap with the valence orbitals of 3d transition metals. The result of this is an overall electronic structure in which valence electrons and low energy unoccupied orbitals are composed of combined orbitals with significant ligand contribution. This allows the ligand to act as an electron reservoir, stabilizing the increased electron density associated with reduction processes to then be utilized in such a fashion that the delocalized electrons are directed towards the substrate during catalytic turnover.[53,55]

In a paper published by Chang et al., electrocatalytic CO_2 reduction from an iron (II) complex with a connected-pyridine ligand system was presented. This work was able to identify the essential electronic contributions from the ligand to achieve catalytic turnover for CO_2 reduction. This investigation displayed the cooperativity between the metal and ligand by a comparison study, with a similar iron complex containing an analogue of the ligand that has a symmetry that significantly restricts the formation of MOs with contributions from the metal and the ligand. Additionally, an analogue for each of these complexes was investigated, replacing the metal with zinc. These complexes are summarized in Figure 1.6.[56]

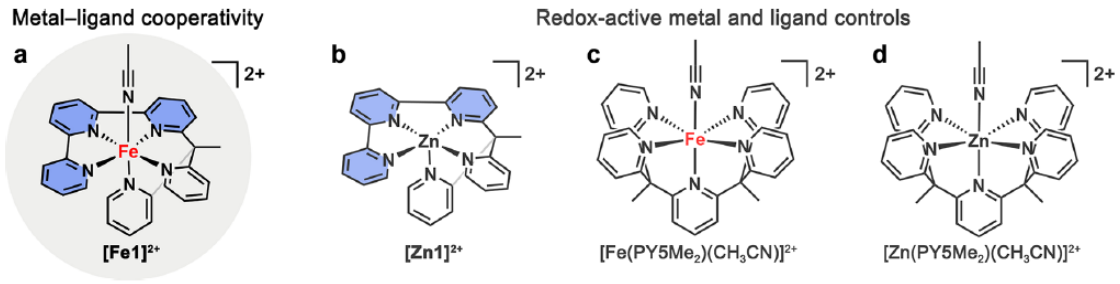

Figure 1.6: Structures of target molecules demonstrating metal-ligand cooperativity and their respective control complexes. Reprinted with permission from {J. Am. Chem. Soc. 2020, 142, 20489−20501}. Copyright {2024} American Chemical Society.

The target complex in this investigation was the only one capable of reducing CO_2. The inability of the Zn complexes to perform catalytic turnover can be attributed to the redox-inert metal center. The lack of catalytic activity from the control species is due to the symmetry restriction, isolating the electron density in the electronic structure either entirely on the metal, or entirely on the ligand. It is not enough to simply include a redox

active ligand in these species, there needs to be MOs generated that contain significant character from the ligand and the metal center to facilitate the storage of the electrons in the ligand, and then the transfer of them through the metal center, to the substrate.

1.6.3 – Chemically active ligands

Introducing ligand systems that can help delocalize electron density and stabilize homogeneous organometallic complexes results in a marked perturbation of the acid/base chemistry of the ligand system; especially with ligands that contain pyridine-like structures. The reverse relationship is also true; when a basic site on a ligand structure is protonated, the redox activity can be greatly affected.[39] These facts add another layer of complexity to many electrocatalytic mechanisms that must undergo protonation steps throughout their cycle. In many cases, protonation sites can act as a proton shuttle, storing protons to be used intramolecularly throughout a catalytic cycle. These sites can be implemented strategically when altering the design of a complex. Long carbon chains with high degrees of freedom containing active proton shuttles at their ends, known as "hangman groups", can be implemented to direct proton transfer to the active site of a catalyst. One study by Dey et al. investigated the implementation of pendant bases as hangman groups on an iron(II) porphyrin complex to improve electrocatalytic H_2 generation from water. In this study, the performance of the catalyst was greatly improved when hangman groups are present, owing to the quicker kinetics associated with intramolecular protonation compared to the typical intermolecular pathway.[57] This is a very deliberate example to improve the output of a known catalyst, utilizing a ligand system for its specialized acid/base chemistry. At multiple points through the catalytic

pathway of nitrite reduction, PCET steps are described.[29,48] These processes can most effectively be facilitated when protons are available, intramolecularly. Catalysts with ligands containing active redox and acid/base chemistry support the interaction with the substrate to the metal center. Protons and electrons may be collected or stored by the ligand structure, but the metal center seems to be the focal point directing the transfer processes, although some recent works have demonstrated electrocatalytic capabilities absent any metal contributions at all.[58]

1.6.4 – Ligand-centered reactions

At the end of the contribution continuum from the ligand in organometallic complexes towards electro-redox catalysis, lie mechanisms that seem to operate with minimal metal participation.[58] In these mechanisms, the substrate physically interacts with the ligand, which then fully facilitates completion of the catalytic cycle. These pathways display a wide variety of mechanistic details because of the structural diversity among the involved ligands. In 2017, Grapperhaus et al. published a paper demonstrating ligand-centered hydrogen generation using the copper complex of diacetyl-bis(N-4-methyl-3-thiosemicarbazone).[32] The proposed mechanism (Figure 1.7) flipped the more prominently explored narrative of ligands acting as electron reservoirs upside down. In this mechanism, the central Cu(II) becomes reduced to Cu(I), but the proton does not interact with the metal center; instead, the metal acts as the electron reservoir, transferring the charge to the ligand following a tautomerization process, moving protons to the opposite side of the ligand, to adjacent sites, evolving hydrogen.

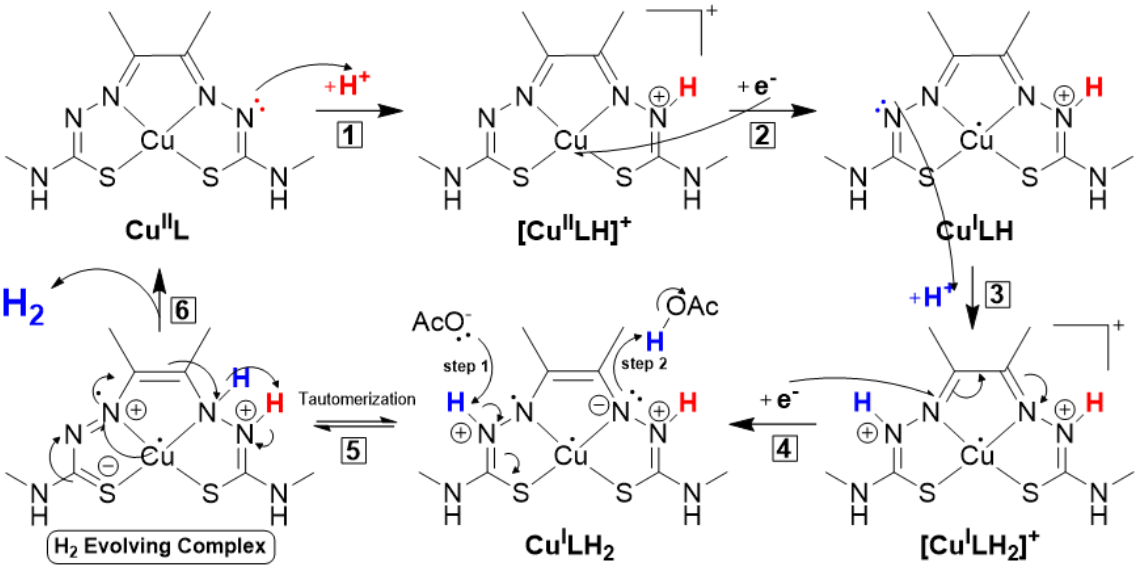

Figure 1.7: Proposed Mechanism of Hydrogen Evolution by [Cu(II)diacetyl-bis(N-4-methyl-3-thiosemicarbazone)]. Redesigned with permission from {Inorg. Chem. 2017, 56, 11254−11265} Copyright {2024} American Chemical Society.

The contribution continuum was further exaggerated to its absolute limit in a paper published in 2018 by Villagrán et al. that showed electrocatalytic turnover for H_2 generation from p-toluenesulfonic acid using a metal-free porphyrin ligand.[59]

Overall, electrocatalytic turnover can occur through an ever-expanding array of pathways. Our increased understanding of the different roles the metal and ligand can play can help direct the future design of improved catalysts. Many different structural and electronic considerations must be made when altering a catalyst to improve its efficacy. Even minor alteration of structural features can shift redox potentials and modulate the acid/base chemistry of a complex that may be pivotal in facilitating a specific complex's catalytic pathway. Exploring the catalytic capabilities for a class of complexes can be best achieved through the strategic alteration of structures that vary important attributes, in a series.

Varying electron withdrawing character and metal selection to shift redox potentials, switching out protonation sites that change their pK_a, and exploring size differences to modulate steric hindrance, are all important aspects to consider when generating a series of complexes for investigation. Each substrate target requires a delicate balance of all these attributes and careful evaluation of catalytic properties to discover the optimal catalyst structure in any given environment.

1.7 - Project Summary and Motivation

Throughout the remainder of this thesis, four homogeneous electrocatalytic investigations are described, all utilizing 3d transition metals coordinated to multidentate ligands. In Chapters 2 and 3, hydrogen generation is targeted. In Chapters 4 and 5, ammonia generation from nitrite is studied. Chapters 2,3, and 4 represent works that have been published in peer reviewed journals, whereas Chapter 5 represents a broader exploration of catalytic detection. For each chapter, the experimental, computational, and authorship contributions are stated prior to the main content.

The intention of Chapter 2 was to probe the mechanism of two CoPN3RP complexes, exploring substrates with a range of pK_a's. This work was published in 2021 in ChemSusChem and was based on previous work from the Richeson group that investigated the same complexes as water reduction electrocatalysts. Through a combination of electrochemical studies and DFT evaluation, two pathways were identified, from two different redox events.

During Chapter 3, **NiPc** was investigated for its unique redox activity that was determined to be mostly from the ligand. DFT simulation of the valence electronic structure displayed

minimal contributions from the metal. Spectroelectrochemistry was also implemented in catalytic and non-catalytic environments to gain insight into the acid/base chemistry of the ligand through reduction processes. The H_2 generation capabilities were also evaluated over a range of TEA concentrations as a means of varying the relative pH of the system. This work was published in Dalton Transactions in 2024.

Nitrite reduction was explored in Chapters 4 and 5 from two different classes of compounds. Chapter 4 involved an extensive DFT analysis coupled with complete electrochemical investigations. This work was published in ChemCatChem in 2023. Chapter 5 explores several complexes of $M(bpca)_2$ as electroredox catalysts for several substrates (H_2O, CO_2, NH_3), eventually settling on NO_2^- reduction. These chapters demonstrate catalytic performance in the greenest possible solvent, water. Finally, in Chapter 6 our results are compared to the current state of the art and associated future studies are proposed.

1.8 – References

1 C. J. Okere and J. J. Sheng, *Int J Hydrogen Energy*, 2023, **48**, 38188–38222.

2 X. Zhang, Y. Wang, Y. Wang, Y. Guo, X. Xie, Y. Yu and B. Zhang, *Chem Commun*, 2022, **58**, 2777–2787.

3 G. Qing, R. Ghazfar, S. T. Jackowski, F. Habibzadeh, M. M. Ashtiani, C. P. Chen, M. R. Smith and T. W. Hamann, *Chem Rev*, 2020, **120**, 5437–5516.

4 J. H. Yang, M. Peng, D. D. Zhai, D. Xiao, Z. J. Shi, S. Yao and D. Ma, *ACS Catal*, 2022, **12**, 2898–2906.

5 G. Wang, J. Chen, Y. Ding, P. Cai, L. Yi, Y. Li, C. Tu, Y. Hou, Z. Wen and L. Dai, *Chem Soc Rev*, 2021, **50**, 4993–5061.

6 Y. K. Park and B. S. Kim, *Chem Eng J*, 2023, 461.

7 S. Anwar, F. Khan, Y. Zhang and A. Djire, *Int J Hydrogen Energy*, 2021, **46**, 32284–32317.

8 C. Deng, C. Y. Toe, X. Li, J. Tan, H. Yang, Q. Hu and C. He, *Adv Energy Mater*, 2022, **12**, 1-34.

9 J. S. Thayer, *Adv Organomet Chem*, 1975, **13**, 1–45.

10 W. E. Geiger, *Organometallics*, 2007, **26**, 5738–5765.

11 G. Frenking and N. Fröhlich, *Chem Rev*, 2000, **100**, 717–774.

12 M. R. Singh and A. Sharma, *Hist Sci Technol*, 2024, **14**, 213–235.

13 R. A. Love, T. F. Koetzle, G. J. B Williams, L. C. Andrews and R. Bau, *Inorg Chem*, 1975, **14**, 2653–2656.

14 L. B. Hunt, *Plat Met Rev*, 1984, **28**, 76–86.

15 H. Werner, *Angew Chem Int Ed*, 2012, **51**, 6052–6058.

16 R. Borougeni, C. Greene, J. A. Bertke and T. H. Warren, *ChemRxiv*, 2019, 1–11.

17 W. B., *J Chem Ed*, 2005, **82**, 28.

18 J. Griffith and L. Orgel, *Q Rev, Chem Soc*, 1957, **11**, 381–393.

19 J. W. Linnett, *Trans Faraday Soc*, 1956, **52**, 904–912.

20 M. Faraday, *Philos Trans R Soc London*, 1834, **124**, 77–122.

21 N. Elgrishi, K. J. Rountree, B. D. McCarthy, E. S. Rountree, T. T. Eisenhart and J. L. Dempsey, *J Chem Educ*, 2018, **95**, 197–206.

22 C. Costentin and J. Savéant, *ChemElectroChem*, 2014, **1**, 1226–1236.

23 M. Che, *Catal Today*, 2013, 218–219, 162–171.

24 A. Klaue, M. Kruck, N. Friederichs, F. Bertola, H. Wu and M. Morbidelli, *Ind Eng Chem Res*, 2019, **58**, 886–896.

25 M. Sauthier, P. Zinck and A. Mortreux, *Comptes Rendus Chimie*, 2010, **13**, 304–314.

26 P. Banoth, C. Kandula and P. Kollu, in *ACS Symposium Series*, American Chemical Society, 2022, vol. 1432, pp. 1–37.

27 G. A. Mabbott, *J Chem Educ*, 1983, **60**, 697–702.

28 E. S. Rountree, B. D. McCarthy, T. T. Eisenhart and J. L. Dempsey, *Inorg Chem*, 2014, **53**, 9983–10002.

29 J. G. Woollard-Shore, J. P. Holland, M. W. Jones and J. R. Dilworth, *Dalton Trans*, 2010, **39**, 1576–1585.

30 T. Lazarides, T. McCormick, P. Du, G. Luo, B. Lindley and R. Eisenberg, *J Am Chem Soc*, 2009, **131**, 9192–9194.

31 C. Costentin, S. Drouet, M. Robert and J. M. Savéant, *J Am Chem Soc*, 2012, **134**, 11235–11242.

32 A. Z. Haddad, S. P. Cronin, M. S. Mashuta, R. M. Buchanan and C. A. Grapperhaus, *Inorg Chem*, 2017, **56**, 11254–11265.

33 I. O. Shotonwa, O. Ejeromedoghene, A. O. Adesoji and S. Adewuyi, *Catal Commun*, 2023, 179.

34 O. R. Luca, J. D. Blakemore, S. J. Konezny, J. M. Praetorius, T. J. Schmeier, G. B. Hunsinger, V. S. Batista, G. W. Brudvig, N. Hazari and R. H. Crabtree, *Inorg Chem*, 2012, **51**, 8704–8709.

35 N. Dutta, D. Bagchi, G. Chawla and S. C. Peter, *ACS Energy Lett*, 2024, **9**, 323–328.

36 A. M. Lines, Z. Wang, S. B. Clark and S. A. Bryan, *Electroanalysis*, 2016, **28**, 2109–2117.

37 T. C. Gunaratne, A. V. Gusev, X. Peng, A. Rosa, G. Ricciardi, E. J. Baerends, C. Rizzoli, M. E. Kenney and M. A. J. Rodgers, *J Phys Chem A*, 2005, **109**, 2078–2089.

38 P. Ślęczkowski, *Int J Mol Sci*, 2023, **24**, 6924-6936.

39 N. Elgrishi, B. D. McCarthy, E. S. Rountree and J. L. Dempsey, *ACS Catal*, 2016, **6**, 3644–3659.

40 S. E. Braley, H. Y. Kwon, S. Xu, E. Z. Dalton, E. Jakubikova and J. M. Smith, *Inorg Chem*, 2022, **61**, 12998–13006.

41 X. Li, L. Zhao, J. Yu, X. Liu, X. Zhang, H. Liu and W. Zhou, *Nanomicro Lett*, 2020, **12**, 1–29.

42 B. D. McCarthy, D. J. Martin, E. S. Rountree, A. C. Ullman and J. L. Dempsey, *Inorg Chem*, 2014, **53**, 8350–8361.

43 C. P. Andrieux, J. M. Dumas-Bouchiat and J. M. Savieant, *J Electroanal Chem*, 1980, **113**, 1-18.

44 D. Lancon, K. M. Kadish, H. Barley, K. Takeuchi, W. R. Murphy, Jr, T. J. Meyer, A. A. Diamantis, T. Meyer, G. E. Cabaniss and R. W. Linton, *J Am Chem Soc,* 1986, **108**, 5876-5885.

45 J. R. Stroka, B. Kandemir, E. M. Matson and K. L. Bren, *ACS Catal*, 2020, **10**, 13968–13972.

46 M. H. Barley, K. Takeuchi, W. R. Murphy and T. J. Meyer, *Chem Commun*, 1985, 507–508.

47 G. Yang, P. Zhou, J. Liang, H. Li and F. Wang, *Inorg Chem Front*, 2023, **10**, 4610–4631.

48 O. Einsle, A. Messerschmidt, R. Huber, P. M. H. Kroneck and F. Neese, *J Am Chem Soc*, 2002, **124**, 11737–11745.

49 R. Tyburski, T. Liu, S. D. Glover and L. Hammarström, *J Am Chem Soc*, 2021, **143**, 560–576.

50 M. Bursch, J.M. Mewes, A. Hansen and S. Grimme, *Angew Chem Int Ed*, 2022, **61**, 1–27.

51 A. M. Teale, T. Helgaker, A. Savin, C. Adamo, B. Aradi, A. V. Arbuznikov, P. W. Ayers, E. J. Baerends, V. Barone, P. Calaminici, E. Cancès, E. A. Carter, P. K. Chattaraj, H. Chermette, I. Ciofini, T. D. Crawford, F. De Proft, J. F. Dobson, C. Draxl, T. Frauenheim, E. Fromager, P. Fuentealba, L. Gagliardi, G. Galli, J. Gao, P. Geerlings, N. Gidopoulos, P. M. W. Gill, P. Gori-Giorgi, A. Görling, T. Gould, S. Grimme, O. Gritsenko, H. J. A. Jensen, E. R. Johnson, R. O. Jones, M. Kaupp, A. M. Köster, L. Kronik, A. I. Krylov, S. Kvaal, A. Laestadius, M. Levy, M. Lewin, S. Liu, P. F. Loos, N. T. Maitra, F. Neese, J. P. Perdew, K. Pernal, P. Pernot, P. Piecuch, E. Rebolini, L. Reining, P. Romaniello, A. Ruzsinszky, D. R. Salahub, M. Scheffler, P. Schwerdtfeger, V. N. Staroverov, J. Sun, E. Tellgren, D. J. Tozer, S. B. Trickey, C. A. Ullrich, A. Vela, G. Vignale, T. A. Wesolowski, X. Xu and W. Yang, *Phys Chem Chem Phys*, 2022, **24**, 28700–28781.

52 N. Mardirossian and M. Head-Gordon, *Mol Phys*, 2017, **115**, 2315–2372.

53 Q. Pan, L. Freitag, T. Kowacs, J. C. Falgenhauer, J. P. Korterik, D. Schlettwein, W. R. Browne, M. T. Pryce, S. Rau, L. González, J. G. Vos and A. Huijser, *Chem Commun*, 2016, **52**, 9371–9374.

54 R. Abdel-Hamid, H. El-Sagher, A. M. Abdel-Mawgoud and A. Nafady, *Polyhedron*, 1998, **17**, 3435–3441.

55 F. V Lovecchio, E. S. Gore and D. H. Busch, *J Am Chem Soc*, 1974, **96**, 3109–3118.

56 J. S. Derrick, M. Loipersberger, R. Chatterjee, D. A. Iovan, P. T. Smith, K. Chakarawet, J. Yano, J. R. Long, M. Head-Gordon and C. J. Chang, *J Am Chem Soc*, 2020, **142**, 20489–20501.

57 S. Bhunia, A. Rana, S. Hematian, K. D. Karlin and A. Dey, *Inorg Chem*, 2021, **60**, 13876–13887.

58 G. G. Luo, H. L. Zhang, Y. W. Tao, Q. Y. Wu, D. Tian, and Q. Zhang, *Inorg Chem Front*, 2019, **6**, 343–354.

59 Y. Wu, N. Rodríguez-López and D. Villagrán, *Chem Science*, 2018, **9**, 4689–4695.

Chapter 2: Elucidating Two Distinct Pathways for Electrocatalytic Hydrogen Production Using Co (II) Pincer Complexes

2.1 – Preamble and Statement of Contributions

The content describe in this chapter was published in ChemSusChem in 2021. It can be accessed through the following link: **https://doi.org/10.1002/cssc.202102542**

The experimental and computational data were generated by Josh Brown, except for the crystallography data, which were collected and processed by Jeffry Ovens. Preliminary drafts were completed by Josh Brown, and further edits by Darrin Richeson and Josh Brown.

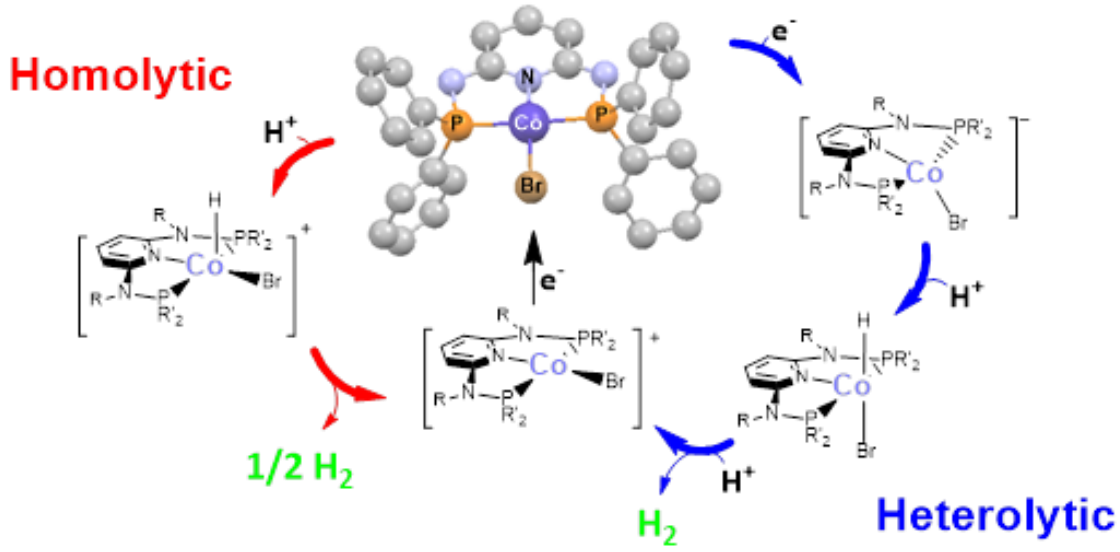

2.2 – Abstract

Hydrogen gas is a sustainable energy vector with a sole combustion product of water. As a result, efforts to catalyze H_2 production are pertinent and widespread. The electrocatalytic H_2 generating capabilities of two Co^{II} complexes, [Co(κ^3-2,6-{Ph_2PNR}$_2$(NC_5H_3))Br_2] R = H (***I***) R = Me (***II***) are presented for a variety of proton sources including trifluoroacetic acid (TFA), acetic acid (AA) and trifluoroethanol (TFE). Cyclic voltammetry (CV) and controlled potential electrolysis (CPE) demonstrated that electrocatalysis from **I** and **II** occurs at two different potentials and is associated with different reduction processes. Computational analysis (DFT) provided insight into the identities of the catalyst and support two distinct reaction pathways for electrocatalytic proton reduction. Specifically, stronger acids (e.g. AA, TFA) proceed at -1.31 to -1.45V through a M(I)/ M(III) pathway while sources with higher pK_a values (e.g. TFE, H_2O) generate hydrogen at -2.4V via M(0)/M(II) ligand-assisted metal centered reduction.

2.3 – Introduction

Growing environmental damage caused by anthropogenic climate change, coupled with the depletion of fossil fuel reserves, has generated intense research interest into the catalytic production of clean burning and sustainable fuel sources such as hydrogen, an energy dense fuel source that has a sole combustion product of water.[1] Noble metals, like platinum, are known to effectively catalyze the reduction of water to produce hydrogen gas.[2] However, such catalysts, due to overall low abundance and high cost, do not provide an environmentally balanced avenue. Compounds composed of economical, earth-abundant metals are essential for the practical application of H_2 generating

electrocatalysts.[3,4] Furthermore, molecular complex catalysts for hydrogen generation are attractive due to the ability to modify supporting ligands and more directly probe mechanisms. Numerous ligand frameworks have been explored with various 3d transition metal centers.[4–10] Tri- or tetradentate ligands can improve the overall stability of the complexes by compensating for the weakened metal ligand coordination present in 3d transition metals, relative to their heavier congeners.[11,12] Pincer ligands are a particular class of rigid, planar, tridentate ligands that are known to modulate the electronic structure of 3d transition metal complexes to form effective proton reduction electrocatalysts.[7,11–17]

While water is the ideal hydrogen source for use in these catalytic systems, exploring substrates across a range of pK_a values would allow for further exploration into the functionality of these complexes and elucidate important fundamental features of their catalytic mechanism.[18] For example, proton reduction electrocatalysts generally operate more efficiently for H_2 in more acidic environments. Elucidating mechanistic differences for H_2 generating electrocatalysts on substrates of different acid strength will inform the trajectory of future research and direct catalyst selection based on the target environment.

Studies of some Co-based hydrogen evolution catalysts performed in organic media have shown that the pK_a of the proton donor and even added buffer can influence the catalyst performance and kinetics of hydride formation.[19–21] In the case of Co(II) dimethylglyoximato complexes, the pathway for H_2 formation was influenced by the applied potential and the acid strength of the proton source.[22]

We previously demonstrated that [Co(κ^3-2,6-{Ph_2PNMe}$_2$(NC_5H_3)Br_2] **II** was capable of efficiently producing H_2 from the reduction of water at a potential of -2 V vs $Fc^{+/0}$.[7] In an effort to more thoroughly probe the mechanism and reactivity of these Co(II) PN3RP pincer species, we now report on catalyst variation and alternative hydrogen sources by examining the catalytic abilities of [Co(κ^3-2,6-{Ph_2PNH}$_2$(NC_5H_3)Br_2] (***I***) and [Co(κ^3-2,6-{Ph_2PNMe}$_2$(NC_5H_3)Br_2] (***II***) with acetic acid (AA), trifluoroacetic acid (TFA), and trifluoroethanol (TFE).

2.4 – Results and Discussion

The direct reaction of the neutral tridentate ligands, 2,6-{Ph_2PNR}$_2$(NC_5H_3) (R = H, Me; PN3PR) with Co(II) bromide at room temperature, in toluene, under nitrogen led to direct synthesis of [Co(κ^3-2,6-{Ph_2PNR}$_2$(NC_5H_3)Br_2] (R = H, **I;** R = Me, **II**).[7] An instant color change was noted upon mixing and the corresponding product was isolated by filtration (Figure 2.1).

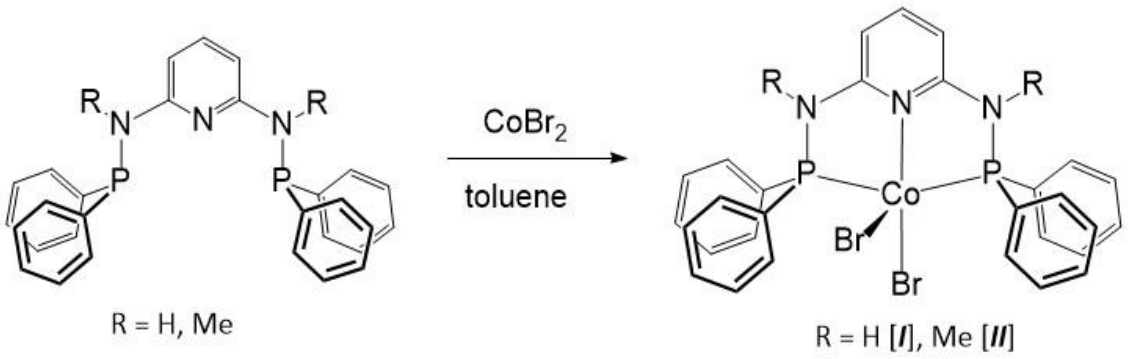

Figure 2.1: Reaction scheme for the preparation of [Co(κ^3-2,6-{Ph_2PNH}$_2$(NC_5H_3)Br_2] (I) and [Co(κ^3-2,6-{Ph_2PNMe}$_2$(NC_5H_3)Br_2] (II).

These complexes can be crystallized from CH_2Cl_2 and we previously confirmed the single crystal X-ray structure of **II** as a square-based pyramidal low spin d^7 Co^{II} center.[7] The basal plane was defined by a tridentate PN3RP ligand and one of the bromo ligands (Br_{bas}). The second bromo group occupied the apical position (Br_{ap}) and Co-Br_{ap} exhibited a bond distance 0.17Å longer than Co-Br_{bas} suggesting a weaker more labile interaction. Consistent with this proposition, crystallization of **I** and **II** from acetonitrile solutions yielded dark purple crystals that when subjected to single crystal X-ray analysis yielded the structures shown in Figure 2.2. In acetonitrile the complexes appear to autoionize, leading to replacement of the apical bromide with acetonitrile. A similar feature was observed in tetrahydrofuran (Figure 2.3). The lability is consistent with d^7 electronic configuration and with our previously reported observations.[7] The X-ray analysis confirms the five-coordinate structures with the planar tridentate PN3PR ligation, with a single bromo ligand in the site *trans* to the N-pyridyl. The acetonitrile ligand occupies the apical site (Figures 2.2, 2.3, Tables 2.1-2.3).

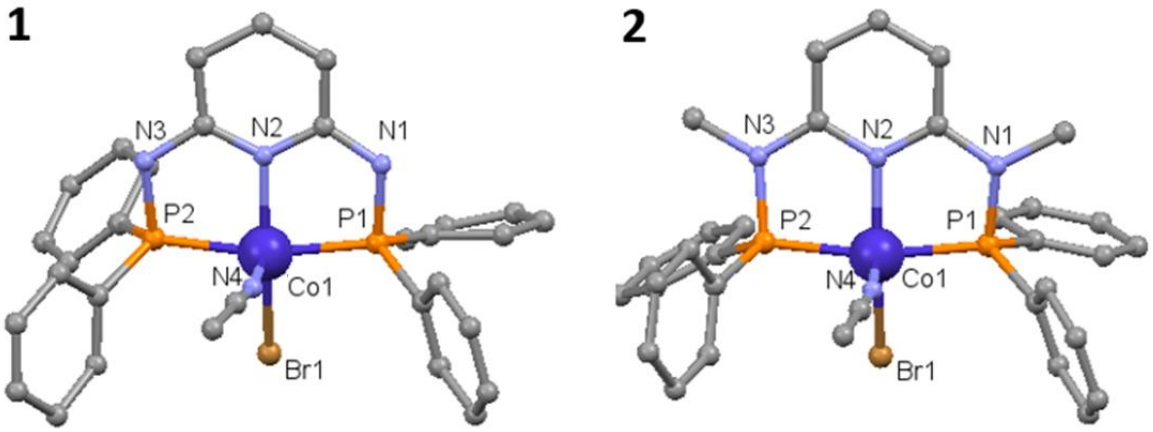

Figure 2.2: SC-XRD structure of $[Co(\kappa^3\text{-}2,6\text{-}\{Ph_2PNH\}_2(NC_5H_3)Br(NCCH_3)]^+$ and $[Co(\kappa^3\text{-}2,6\text{-}\{Ph_2PNMe\}_2(NC_5H_3)Br(NCCH_3)]^+$ obtained from acetonitrile. Hydrogens atoms and counterions have been omitted for clarity.

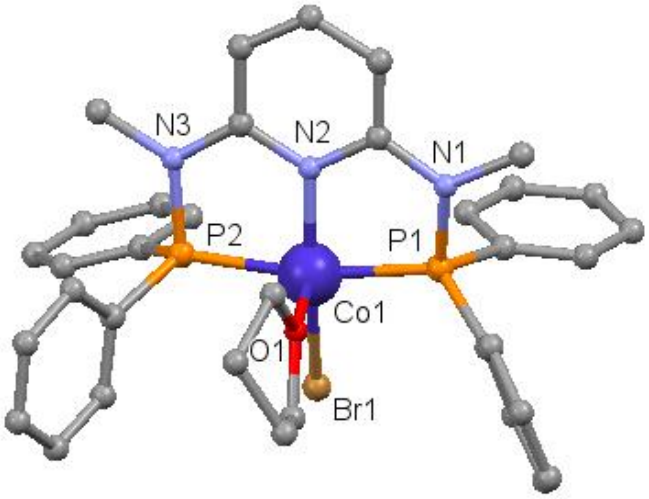

Figure 2.3: SC-XRD structure of $[Co(\kappa^3\text{-}2,6\text{-}\{Ph_2PNMe\}_2(NC_5H_3)Br(THF)]^+$ obtained when II was crystallized from THF. Hydrogen atoms and counter anion omitted for clarity.

Table 2.1: Crystal data and structure refinement for [Co(κ³-2,6-{Ph₂PNMe}₂(NC₅H₃)Br(NCCH₃)]⁺.

	[Co(κ³-2,6-{Ph₂PNMe}₂(NC₅H₃)Br(NCCH₃)]⁺
empirical formula	$C_{66}H_{62}Br_6Co_3N_{10}P_4$
formula weight ($g \cdot mol^{-1}$)	1775.38
crystal system	monoclinic
space group	$P\,2_1$
a (A)	9.066(7)
b (A)	31.47(2)
c (A)	12.540(9)
α (deg)	90
β (deg)	100.755(8)
γ (deg)	90
V (A^3)	3515(4)
Z	2
T (K)	200(2)
ρ_{calcd} ($g \cdot cm^{-3}$)	1.670
μ (mm^{-1})	4.246
$2\theta_{max}$ (deg)	50.000
total/unique reflections	27850/12218
Reflections [$I_o \geq 2\sigma(I_o)$]	6196
R_1, wR_2 [$I_o \geq 2\sigma(I_o)$]	0.0851, 0.1787
goodness of fit	1.006

Table 2.2: Crystal data and structure refinement for [Co(κ³-2,6-{Ph₂PNH}₂(NC₅H₃)Br(NCCH₃)]⁺.

	[Co(κ³-2,6-{Ph₂PNH}₂(NC₅H₃)Br(NCCH₃)]⁺
empirical formula	$C_{35}H_{35}Br_4Co_2N_5P_2$
formula weight ($g \cdot mol^{-1}$)	1025.12
crystal system	monoclinic
space group	$P\,2_1/c$
a (A)	9.2071(11)
b (A)	25.203(3)
c (A)	18.712(2)
α (deg)	90
β (deg)	103.106(4)
γ (deg)	90
V (A^3)	4228.8(9)
Z	4
T (K)	200(2)
ρ_{calcd} ($g \cdot cm^{-3}$)	1.610
μ (mm^{-1})	4.669
$2\theta_{max}$ (deg)	50.484
total/unique reflections	48797/9372
Reflections [$I_o \geq 2\sigma(I_o)$]	5628
R_1, wR_2 [$I_o \geq 2\sigma(I_o)$]	0.0460, 0.0865
goodness of fit	1.010

Table 2.3: Crystal data and structure refinement for [Co(κ³-2,6-{Ph₂PNMe}₂(NC₅H₃)Br(THF)]⁺.

	[Co(κ³-2,6-{Ph₂PNMe}₂(NC₅H₃)Br(THF)]⁺
empirical formula	$C_{39}H_{45.85}Br_4Co_2N_3O_{2.43}P_2$
formula weight ($g \cdot mol^{-1}$)	1094.92
crystal system	monoclinic
space group	$P\ 2_1/c$
a (A)	9.3129(17)
b (A)	26.071(4)
c (A)	17.760(3)
α (deg)	90
β (deg)	96.658(3)
γ (deg)	90
V (A^3)	4282.9(13)
Z	4
T (K)	200(2)
ρ_{calcd} ($g \cdot cm^{-3}$)	1.698
μ (mm^{-1})	4.619
$2\theta_{max}$ (deg)	50.484
total/unique reflections	57659/8935
Reflections [$I_o \geq 2\sigma(I_o)$]	5743
R_1, wR_2 [$I_o \geq 2\sigma(I_o)$]	0.0464, 0.0949
goodness of fit	1.023

A simple metric, the "tau" parameter, has been used to categorize five coordinate structures as trigonal bipyramidal (TBP) (τ=1) or square pyramid (SP) (τ= 0).[23] Complexes **I** and **II** yielded τ values of 0.14 and 0.08, respectively, consistent with the SP assignment. The bonding parameters were similar and consistent with reported [Co(κ^3-2,6-{Ph_2PNMe}$_2$(NC_5H_3)Br_2][7] as well as two recently reported PN3RP complexes of Co(II), [Co(κ^3-2,6-{Ph_2PNH}$_2$(NC_5H_3))Cl_2] (τ = 0.0063) and the triazine-centered complex [Co(κ^3-2,6-{iPr_2PNH}$_2$($N_3C_3H_2Me$))Cl_2] (τ = 0.11).[24] Other related structurally characterized species include the cationic bis(acetonitrile) complex [Co(κ^3-2,6-{Ph_2PNH}$_2$(NC_5H_3)($NCCH_3$)$_2$]$^{2+}$ and a square planar cationic species [Co(κ^3-2,6-{$^tBu_2PNH$}$_2$(NC_5H_3)Br]$^+$.[24,25]

Electrochemical characterization

Electrochemical characterization was performed for both complexes in acetonitrile using a glassy carbon (GC) working electrode, Pt counter electrode, and an Ag wire pseudo-reference electrode. After completing the CV, ferrocene was added to the solution and voltages were referenced to the reversible ferrocene/ferrocenium ($Fc^{+/0}$) redox couple. The resulting cyclic voltammograms for **I** and **II** are displayed in Figure 2.4.

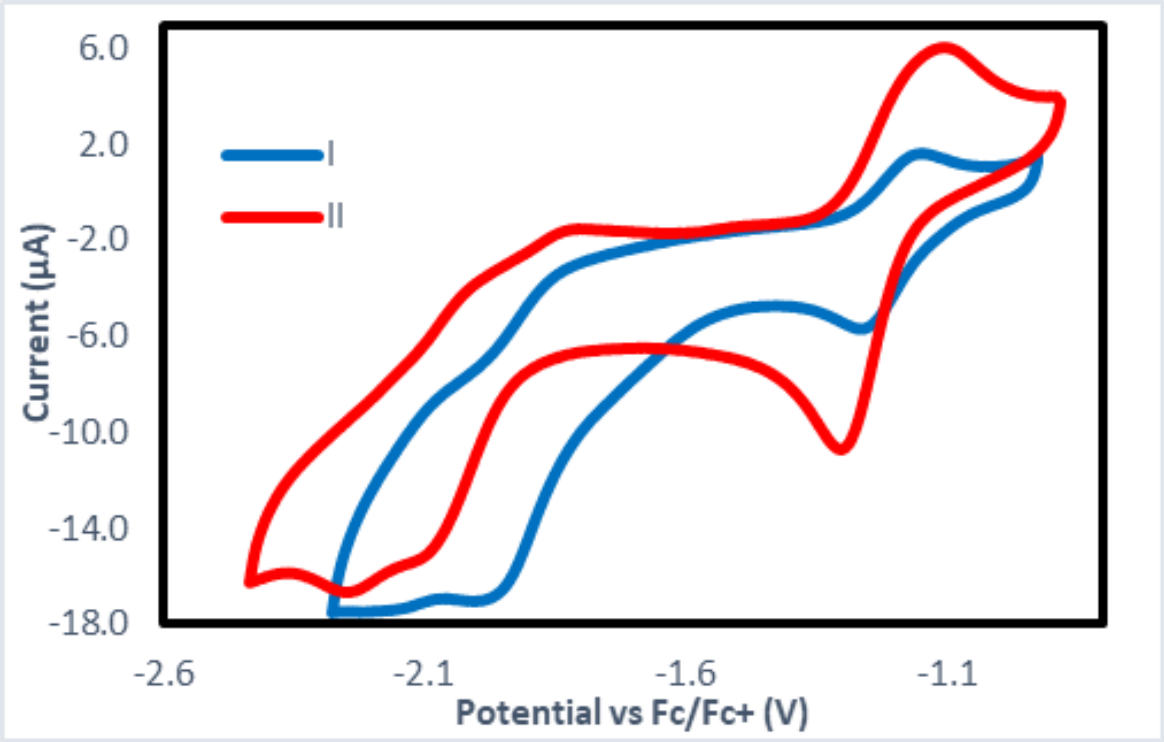

Figure 2.4: Cyclic voltammograms for 1mM of I (blue) and II (red) obtained in acetonitrile in 0.1M TBAHFP as the electrolyte using a GC working electrode. Scans were performed at 100mV/s starting with a cathodic sweep between -0.9V and -2.4V. Potentials were referenced to $Fc^{+/0}$.

Complex **II** displayed its first reduction event at -1.29V (all potentials referenced to $Fc^{+/0}$). This is slightly more negative than that observed for complex **I**, which displayed a reduction at -1.26V. These reduction events were isolated and the CV data of **I** and **II** confirmed reversible redox events (Figure 2.5).

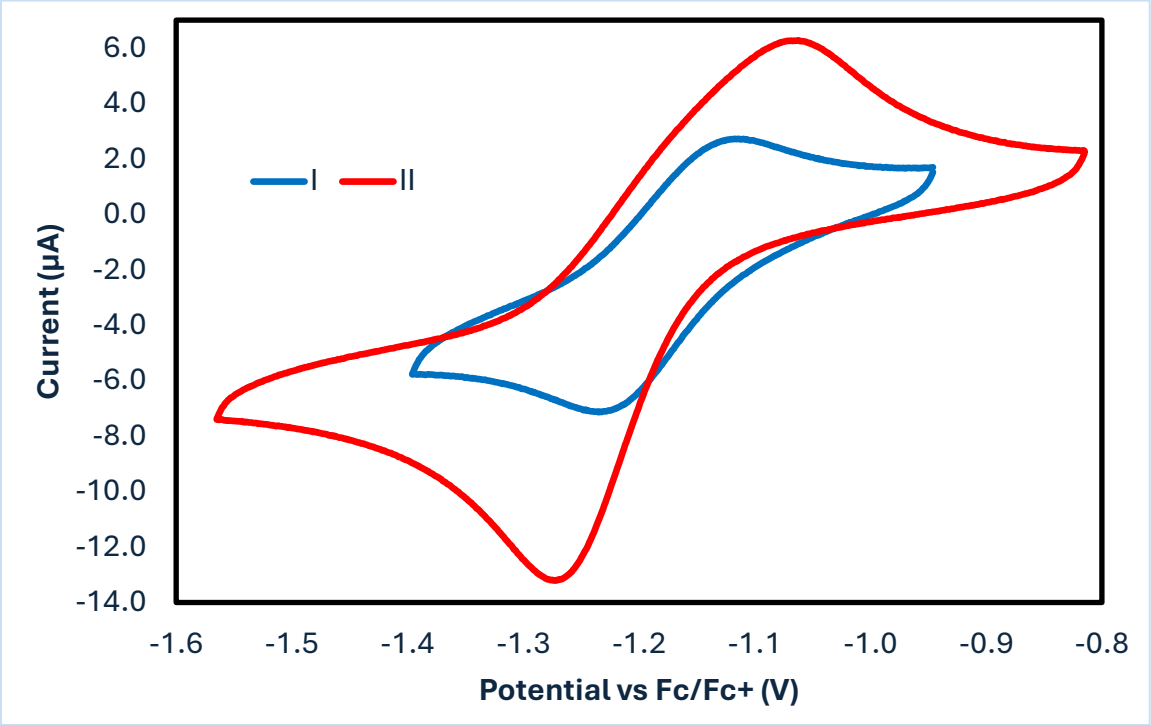

Figure 2.5: Cyclic voltammograms for 1mM of I (blue) and II (red) obtained in acetonitrile in 0.1M TBAHFP as the electrolyte using a GC working electrode. Scans were performed at 100mV/s starting with a cathodic sweep between -0.8V and -1.55V for II and -1V and -1.45V for I targeting the Co(II)/Co(I) reduction event.

These redox events were further examined using varied scan rates (Figures 2.6, 2.7) and a plot of (scan rate)$^{1/2}$ *versus* current displayed a linear relationship consistent with a diffusion-controlled process.[26]

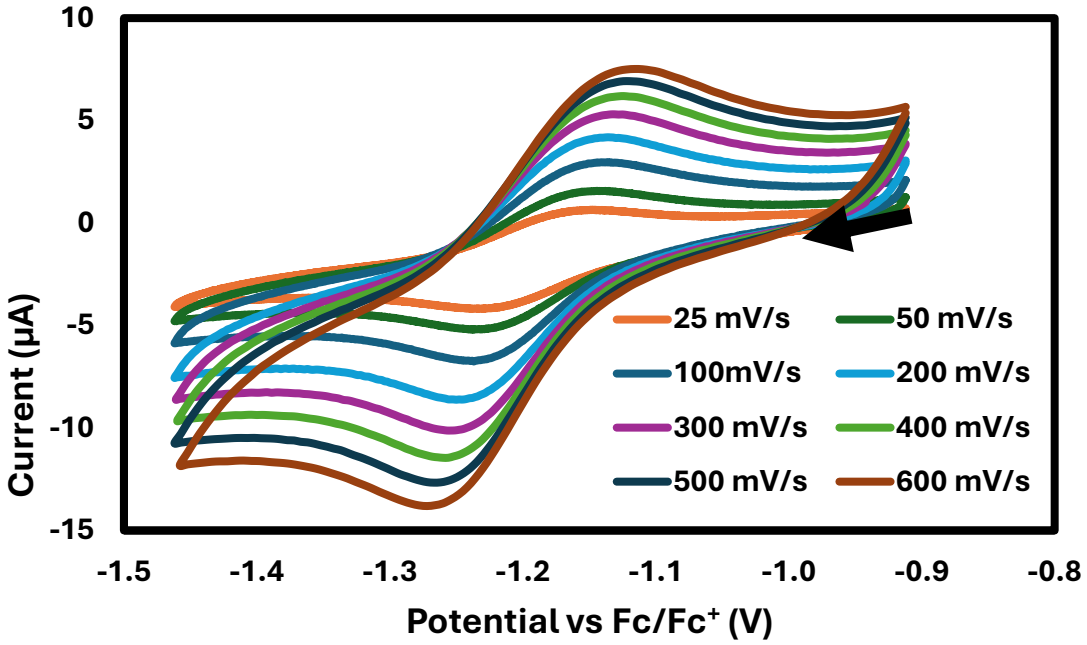

Figure 2.6: Cyclic voltammogram of the first reduction event between Co(II) and Co(I) for 1mM of I in acetonitrile with 0.1M TBAHFP.

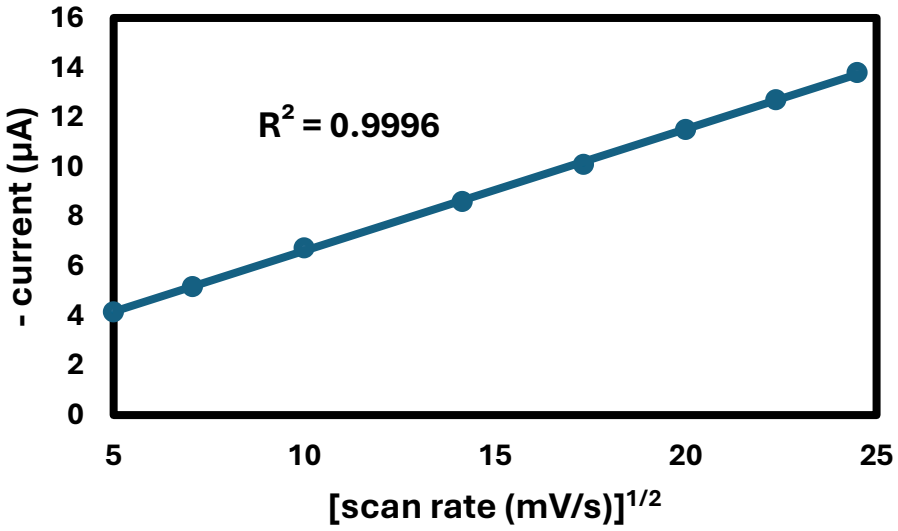

Figure 2.7: Plot of the peak current observed at different scan rates as a function of the square root of the scan rate data from Fig. 2.6. Data were fitted with a linear regression.

At more cathodic potentials, both **I** and **II** display two further reductions. Complex **II** undergoes two consecutive reduction events at -2.1V and -2.23V vs $Fc^{+/0}$. Similarly, **I** displays two consecutive events at -2.0V and -2.15V vs $Fc^{+/0}$. These events are irreversible. Furthermore, these reduction events displayed linear (scan rate)$^{1/2}$ *versus* current dependence, again indicative of diffusion processes.[7]

In order to further elucidate the nature of the observed redox events for **I** and **II**, computational analysis (DFT) of these two compounds and their reductions was performed using the M06L functional.[27] Geometry optimization and frequency analysis were performed using the def2-SVP basis set and energy calculations were then performed with the def2-TZVP basis set and using the PCM for solvation in acetonitrile. The initial optimization was carried out on low spin Co^{II} centers, using crystal structure data as the starting geometry.[7] In the case of **II** the resulting geometric structure was in excellent agreement with the experimental structure. Very similar results were obtained for the calculations on **I** (Figure 2.8, Tables 2.4, 2.5). The frontier orbitals, focusing on the Co-centered d-orbitals were as anticipated for a square pyramidal ligand field (Figure 2.9). The SOMO was a σ* interaction between the apical bromo ligand (Br_{ap}) and N_{py} (orbital contributions 0.46 (Co), 0.36 (Br_{ap})). The Co contribution to this molecular orbital was derived from the dz^2 orbital. The LUMO, while empty, involved contributions from Co dx^2-y^2 and σ* contributions form N_{py}, the two PPh_2 groups and Br_{bas} (orbital contributions 0.42 (Co), 0.23 (P), 0.11 (Br_{bas})). The remaining lower energy (SOMO-1, SOMO-2 and SOMO-4) occupied orbitals were derived from Co dyz, dxz and dxy. The Co-Br σ* nature of the SOMO was consistent with the lability of Br_{ap}.

Complex **I** consisted of a square-based pyramidal species [Co(κ^3-2,6-{Ph_2PNH}$_2$(NC_5H_3)Br_2] (**I**). The descriptions for the computational results on this material are based on the orientation relative to the Cartesian axes shown in Figure 2.8. The orbital array is defined using the z-axis perpendicular to the CoP_2NBr plane. Consistent with a d^7 Co(II) center in a square based pyramid ligand field, the bromo ligands are in the apical position (Br_a) and in the basal plane (Br_b) with the Npy and the two coordinated P centers.

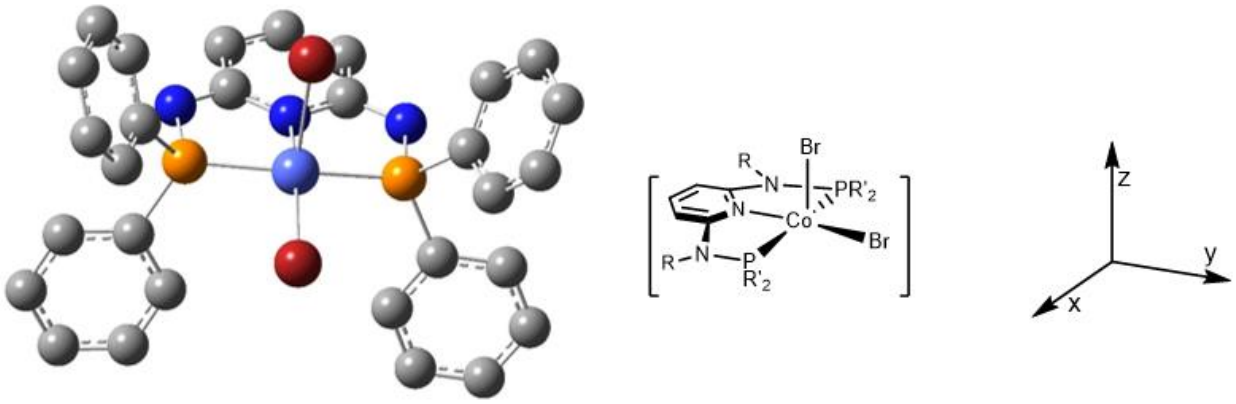

Figure 2.8. DFT optimized structure of [Co(κ^3-2,6-{Ph_2PNH}$_2$(NC_5H_3)Br_2] [I] using the MO6L functional and def2-TZVP basis set in acetonitrile (PCM). Hydrogen atoms are eliminated for clarity. Frequency analysis confirmed that the optimized structure was a minimum with no imaginary frequencies.

Table 2.4. Comparison of selected structural parameters of the single crystal X-ray diffraction structure of [Co(κ^3-2,6-{Ph_2PNH}$_2$(NC_5H_3)Br_2] [I] and the computed complex (MO6L, def2-TZVP) using the PCM model for solvation with acetonitrile as the solvent.

Bond	Experimental	Computed Distance MO6L/def2-TZVP
Co-N_{py}	1.950	1.985
Co-P	2.181	2.213
Co-P	2.199	2.213
Co-Br_a	-*	2.622
Co-Br_b	2.348	2.432

*This complex autoionizes in acetonitrile

Table 2.5. Summary of Co-centered bonding for [Co(κ ^{3}-2,6-{Ph_2PNH}$_2$$NC_5H_3$)$Br_2$] (I). Values for bond length, overlap populations and Mayer bond order indices are from the MO6L/def2-TZVP/PCM (acetonitrile) calculation.

Bond	Length(Å)	Overlap Population	Mayer Bond order
Co-N_{py}	1.985	0.1935484	0.5573863
Co-P	2.213	0.2734356	0.8379806
Co-Br_a	2.622	0.1465955	0.4810572
Co-Br_b	2.432	0.2226827	0.6957958

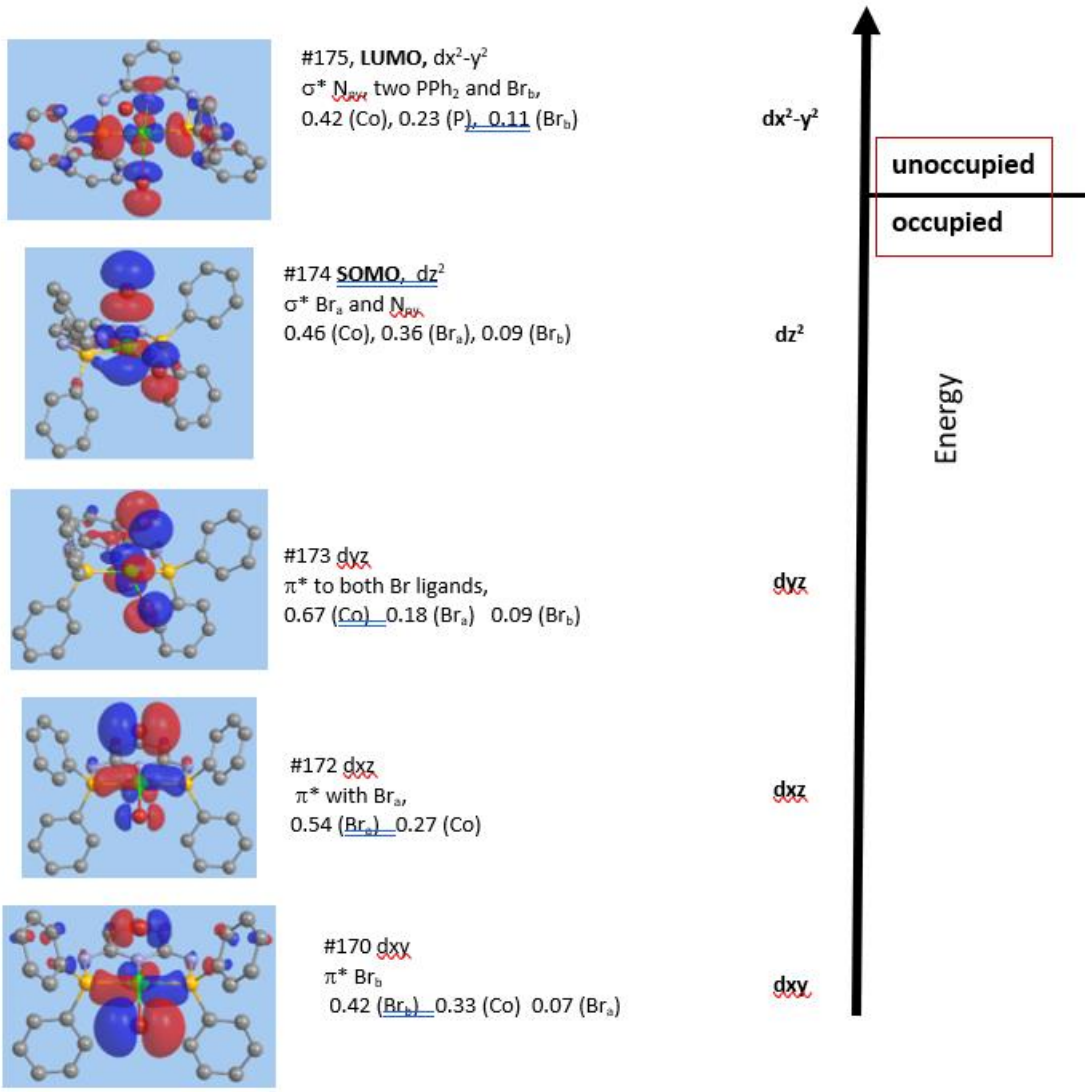

Figure 2.9. Selected, Co-centered molecular orbitals obtained for [Co(κ³-2,6-{Ph₂PNH}₂NC₅H₃)Br₂] (I) using the MO6L functional, def2-TZVP basis set and PCM model for solvation in acetonitrile. Major fragment orbital contributions were obtained from the Chemissian program. Viewing at 0.03 isosurface, with hydrogen atoms omitted for clarity, these are views of the alpha orbitals.

The addition of one electron to **I** was next examined using the same computational optimization approach. Consistent with the computed electronic structure for **I**, this electron populated the dz^2 σ* molecular orbital to generate a d^8 complex. In fact, during the optimization process, the apical Br_{ap} ligand dissociated. As a result, this ligand was removed for the complete optimization that resulted in a neutral square planar d^8 complex [Co(κ^3-2,6-{Ph_2PNH}$_2$$NC_5H_3$)Br] **A** as represented in Figure 2.10 (Table 2.6). The resulting frontier orbitals were consistent with a d^8 Co(I) in a square planar ligand field. The LUMO was constituted from the Co dx^2-y^2 that was σ* in nature. The HOMO was a nonbonding dz^2 based orbital. The lower energy (HOMO-1 to HOMO-3) molecular orbitals were Co centred dyz, dxz and dxy, respectively (Figure 2.11).

The first reduction event adds one electron to **I.** Based on the electronic structure for **I**, this electron would populate the dz^2 that is σ* to Br_a . As expected, the computational optimization led to loss of the apical Br_a ligand resulting in a neutral square planar d^8 complex [Co(κ^3-2,6-{Ph_2PNH}$_2$$NC_5H_3$)Br] **A**. The result of the successful optimization was the square planar neutral species shown in Figure 2.10. The orientation of the complex relative to the Cartesian coordinates was the same as for starting material **I**. The orbital array that is centered on Co remained consistent with the starting material.

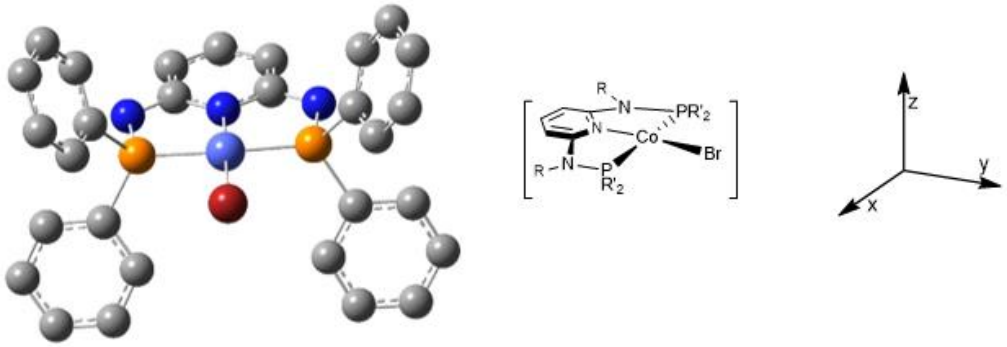

Figure 2.10. DFT optimized for the addition of a single electron to I and loss of bromo ligand as bromide to give the neutral species, [Co(κ^3-2,6-{Ph$_2$PNH}$_2$NC$_5$H$_3$)Br] A. Hydrogen atoms are eliminated for clarity. Frequency analysis confirmed that the optimized structure was a minimum with no imaginary frequencies.

Table 2.6. Summary of Co-centered bonding for [Co(κ ^{3}-2,6-{Ph$_2$PNH}$_2$NC$_5$H$_3$)Br] (A). Values for bond length, overlap populations and Mayer bond order indices are from the MO6L/def2-TZVP/PCM (acetonitrile) calculation.

Bond	Length(Å)	Overlap Population	Mayer Bond order
Co-N	1.922	0.2091657	0.6167812
Co-P	2.142	0.3216326	0.9893058
Co-P	2.142	0.3215385	0.9893945
Co-Br	2.412	0.1852295	0.6079362

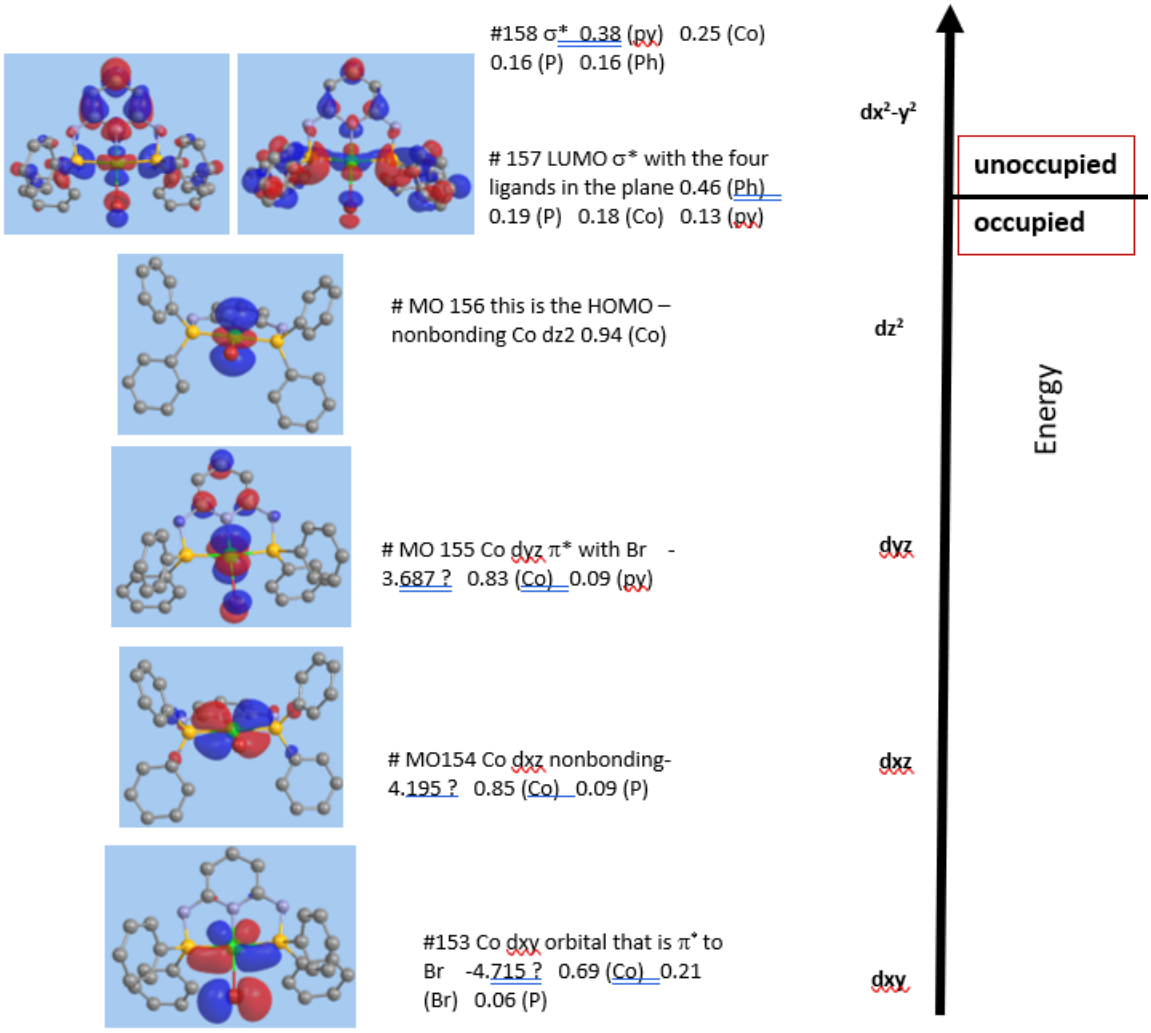

Figure 2.11. Selected, Co-centered molecular orbitals obtained for the first reduction of complex I [Co(κ ^{3}-2,6-{Ph_2PNH}$_2$$NC_5H_3$)Br] (A) using the MO6L functional, def2-TZVP basis set and PCM model for solvation in acetonitrile. Major fragment orbital contributions were obtained from the Chemissian program. Viewing at 0.03 isosurface, with hydrogen atoms omitted for clarity.

The addition of an electron to [Co(κ^3-2,6-{Ph_2PNH}$_2$$NC_5H_3$)Br] **A** leads to the proposed d^9 anion, [Co(κ^3-2,6-{Ph_2PNH}$_2$$NC_5H_3$)Br]$^-$ (**A**$^-$) depicted in Figure 2.12. On the basis of the

optimized structure of [Co(κ^3-2,6-{Ph_2PNH}$_2$$NC_5H_3$)Br] **A** the added electron would be placed in the LUMO, a σ* orbital, to yield a triplet anion.

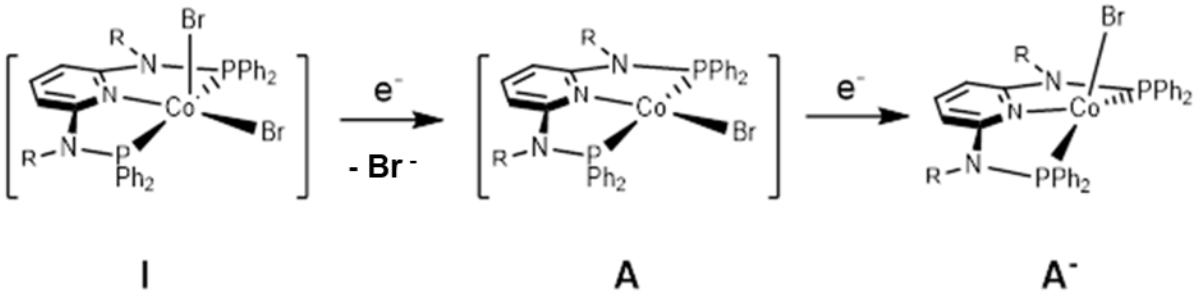

Figure 2.12. Structures and compound labeling scheme for the two reduction processes of compound I to give A and A$^-$.

After addition of an electron to **A** followed by optimization, the resultant structure demonstrated substantial structural changes with the most obvious being deviation of the Co geometry from square planar. In particular, in the optimized structure of **A**$^-$, the bromo ligand was out of the PN3PCo plane as shown in Figure 2.13. There was a concurrent increase in the Co-Br bond length and decrease in the Co-Br bond order (Table 2.8) and Co center moved out of the plane resulting in a P-Co-P angle of 134.7° (from 170.6° in [Co(κ^3-2,6-{Ph_2PNH}$_2$$NC_5H_3$)Br] **A**).

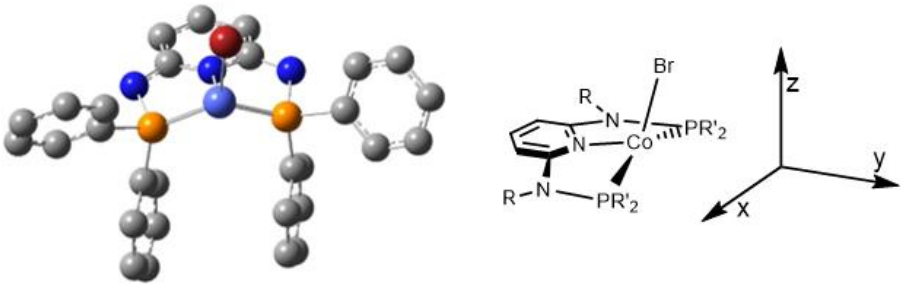

Figure 2.13. DFT optimized structure for the complex [Co(κ³-2,6-{Ph₂PNH}₂NC₅H₃)Br]⁻ (A⁻) using the MO6L functional and def2-TZVP basis set. Frequency analysis confirmed that the optimized structure was a minimum with no imaginary frequencies. Hydrogen atoms are eliminated for clarity. The associated drawing provides the orientation of the Cartesian axes used in the discussion of this complex and is similar to that used throughout the computational presentation.

Table 2.7. Summary of Co-centered bonding for [Co(κ³-2,6-{Ph₂PNH}₂NC₅H₃)Br]⁻ (A⁻). Values for bond length, overlap populations and Mayer bond order indices are from the MO6L/def2-TZVP/PCM (acetonitrile) calculation.

Bond	Length(Å)	Overlap Population	Mayer Bond order
Co-N	2.028	0.1413986	0.4237472
Co-P	2.112	0.3127625	1.0871712
Co-P	2.100	0.3307708	1.1864667
Co-Br	2.534	0.1343911	0.4006373

Since the optimized complex **A**⁻ no longer displayed metal-ligand bonding oriented along the orthogonal axes, the molecular orbitals of **A**⁻ exhibited additional orbital mixing of the frontier/Co-centered orbitals (Figure 2.11). The SOMO for **A**⁻ remained σ* in character and based on Co dx^2-y^2 (contributions 0.54 (Co) 0.23 (P)). The SOMO-1 (52% Co) retained

the dz^2 character but because of the structural changes from **A**, this molecular orbital became σ^* for Co-Br. These results lay the groundwork for our examination of the electrocatalytic abilities of **I** and **II.**

We previously demonstrated that Co^{II} complexes supported with a PN3RP pincer framework, such as $[Co(\kappa^3\text{-}2,6\text{-}\{Ph_2PNMe\}_2(NC_5H_3)Br_2]$ (**II**), provided unprecedented catalysts for generating H_2 from H_2O at the second reduction event (e.g. -1.9 V *vs* $Fc^{+/0}$) with excellent efficiency and rate.[7] These catalysts showed 96% Faradaic efficiency with water or saturated aqueous saline. With a goal of more thoroughly probing the mechanism for this electrocatalysis we examined variation of the proton source using acetic acid (AA), trifluoroacetic acid (TFA), and trifluoroethanol (TFE). This began by examining the addition of AA to 1.0mM solutions of **I** and **II**. As seen in Figure 2.14, both complexes exhibited significant current enhancement in the presence of AA, indicative of catalysis. Furthermore, the corresponding return oxidation events were absent, as expected for redox catalysis.[20]

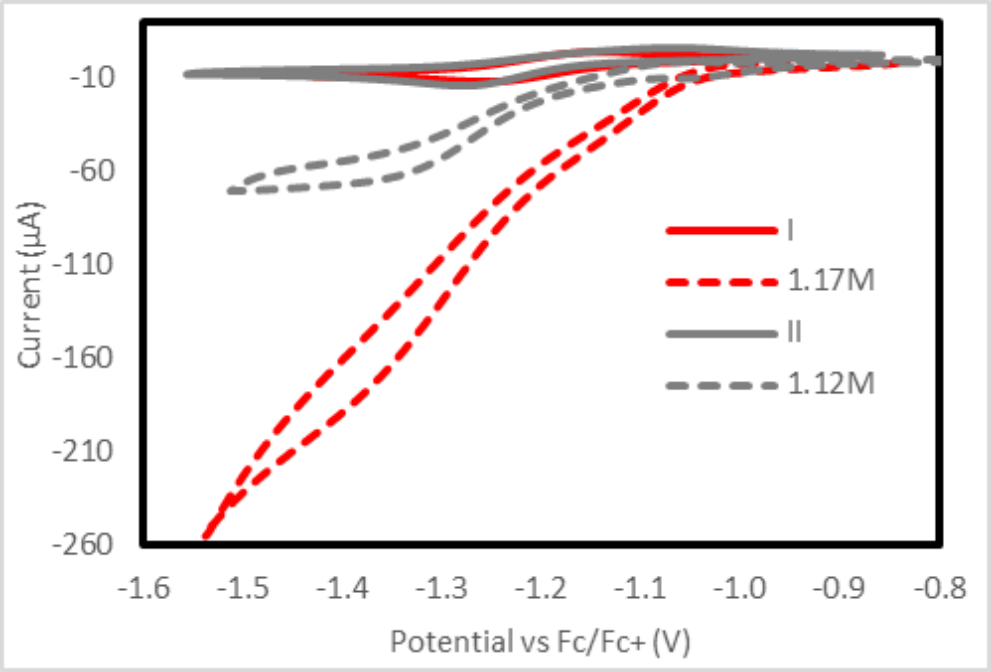

Figure 2.14. Cyclic voltammogram demonstrating catalytic enhancement at the Co(II)/Co(I) reduction event for 1mM of I and II in the presence of acetic acid (AA). Solution contained 0.1M TBAHFP as the electrolyte with a 1mm GC working electrode and a scan rate of 100mV/s.

The onset potential for the catalytic event was determined by identifying the inflection point, which corresponds to the region on the curve where the rate of electron transfer is maximized, before the reaction kinetics are controlled by the diffusion of substrate towards the electrode.[28] The derivatives were determined by the method of first principles (Figures 2.15, 2.16). For complex **I** the onset potential for the reduction of acetic acid was determined to be -1.31V vs $Fc^{+/0}$. This value was only 50mV beyond the reversible redox event for **I**.

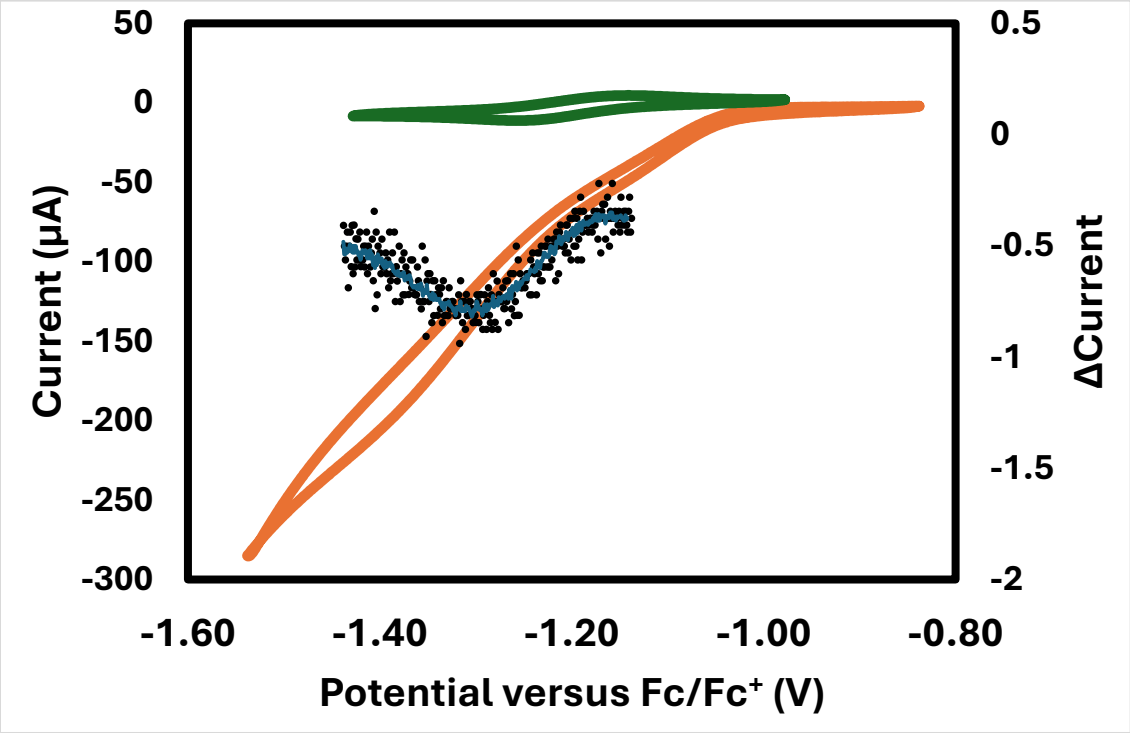

Figure 2.15: Orange curve – Cyclic voltammogram demonstrating catalytic enhancement at the Co(II)/Co(I) reduction event for 1mM of I in the presence 0.97M acetic acid. 0.1M TBAHFP is present as the electrolyte with a 1mm glassy carbon working electrode and a scan rate of 100mV/s. Black markers represent the method of first principles applied to the orange curve. Minima denote an inflection point in the catalytic curve, indicating the associated onset potential and current enhancement for its respective acid concentration. The blue trend line is the moving average of black markers with a period of 5.

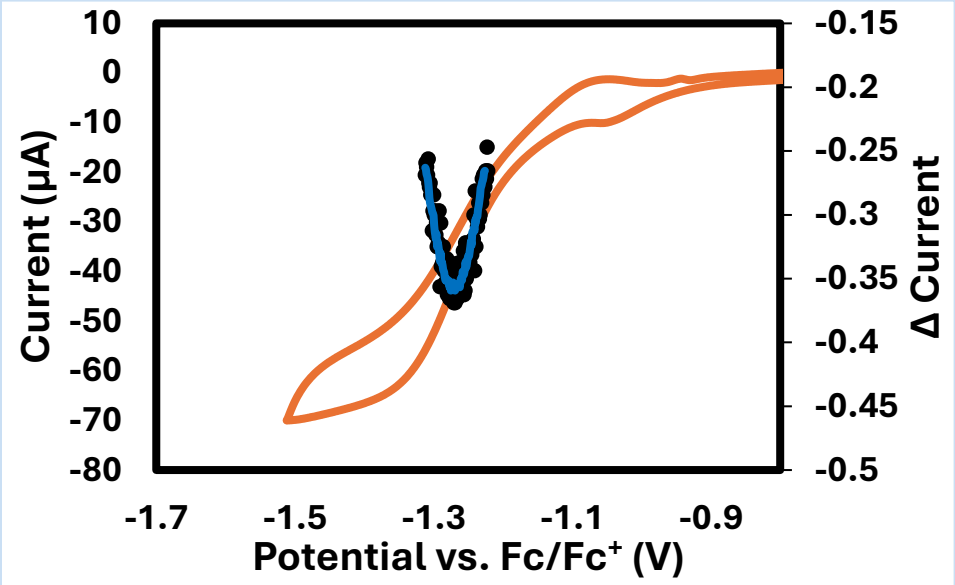

Figure 2.16: Cyclic voltammogram demonstrating catalytic enhancement at the Co(II)/Co(I) reduction event for 1mM of II in the presence 1.14M acetic acid. 0.1M TBAHFP is present as the electrolyte with a 1mm glassy carbon working electrode and a scan rate of 100mV/s. Black markers represent the method of first principles applied to the orange curve. Minima denote an inflection point in the catalytic curve, indicating the associated onset potential and current enhancement for its respective acid concentration. The blue trend line is the moving average of black markers with a period of 5.

The homogeneous catalysis behavior of **I** and **II** was supported by several control experiments. Repeated linear sweep voltammetry measurements of the catalyst/substrate systems were carried out to confirm catalytic current enhancement. Following these sweeps, the electrode was removed, carefully rinsed with clean solvent, and placed into a new solution containing only substrate. Voltammetry measurements on these catalyst free systems did not exhibit any electrochemical events, indicating that the

catalyst had not deposited on the electrode. In addition, following bulk electrolysis measurements, CV measurements were performed on the reaction mixture. These measurements displayed no new redox events and current enhancements occurred at identical potentials before and after bulk electrolysis was performed. These measurements indicated that the catalyst had not transformed during electrolysis.

Using the onset potential, the overpotential for acetic acid reduction with catalyst **I** was determined. Homoconjugation is known to be a factor leading to an underestimation of the overpotential when dealing with high acid concentrations in acetonitrile.[29] This occurs when the conjugate base interacts through the proton of the acid at the surface of the electrode, effectively decreasing the apparent pK_a and decreasing the potential required to reduce the protons.

Accounting for homoconjugation can be achieved by considering the association constant for the formation of the homoconjugation product and the concentration of H_2 dissolved in the acetonitrile when computing the theoretical reduction potential. The theoretical reduction potential can be calculated using eq. 2.1. In this equation, $E^o_{H^+/H_2}$ is the potential required to produce hydrogen in acetonitrile, pK_a is for the proton source, ε_D is the relative diffusion rate of products to reactants, K_c is the rate constant for the formation of the homoconjugation product ($10^{3.9}$ for acetic acid), C_0 is the concentration of proton source, and $C^o_{H_2}$ is the maximum concentration of H_2 in solution.[29] The overpotential is then calculated by taking the difference between the onset potential and the computed theoretical reduction potential.[29,30] For complex **I**, the overpotential for

acetic acid reduction was determined to be 80mV. Complex **II** was slightly less effective and operated at an overpotential of 140mV.

$$E^{T}_{1/2(AH/AHA^{-})} = E^{o}_{H^{+}/H_2} - \frac{2.303RT}{F}pK_a + \varepsilon_D + \frac{RT}{2F}\ln(K_c^2 C_0 C^{o}_{H_2}) \qquad \text{(eq. 2.1)}$$

Having established the onset potential and corresponding overpotentials for AA with each catalyst, the performance and efficiencies of each catalyst were evaluated. The effects of changing acetic acid concentration are displayed in Figure 2.17a for 1mM of **I**. The current enhancement at the inflection point of 1.31V vs $Fc^{+/0}$, increases, approximately linearly, until saturation is reached. Background reduction of AA at the GC electrode only appears at -2.18V and had no effect on these measurements (Figure 2.18).

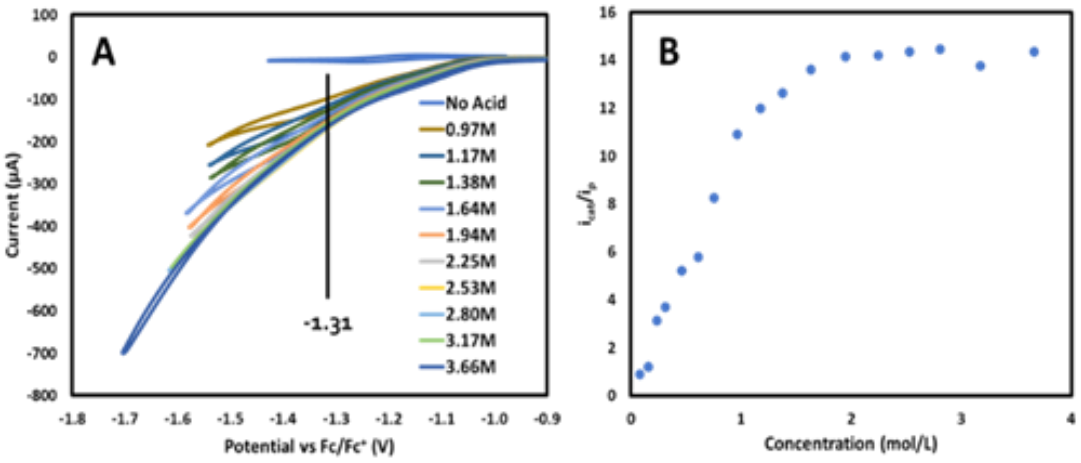

Figure 2.17. (A) Cyclic voltammogram demonstrating catalytic enhancement at the Co(II)/Co(I) reduction event for 1mM of I in the presence of increasing acetic acid concentration. Measurements were with 0.1M TBAHFP using a 1mm GC working electrode at 100mV/s. (B) Plot of the ratio of the catalytic current (i_{cat}) at -1.31V to the peak current of the first reduction event in the absence of acid (i_p) as a function of the concentration of acetic acid.

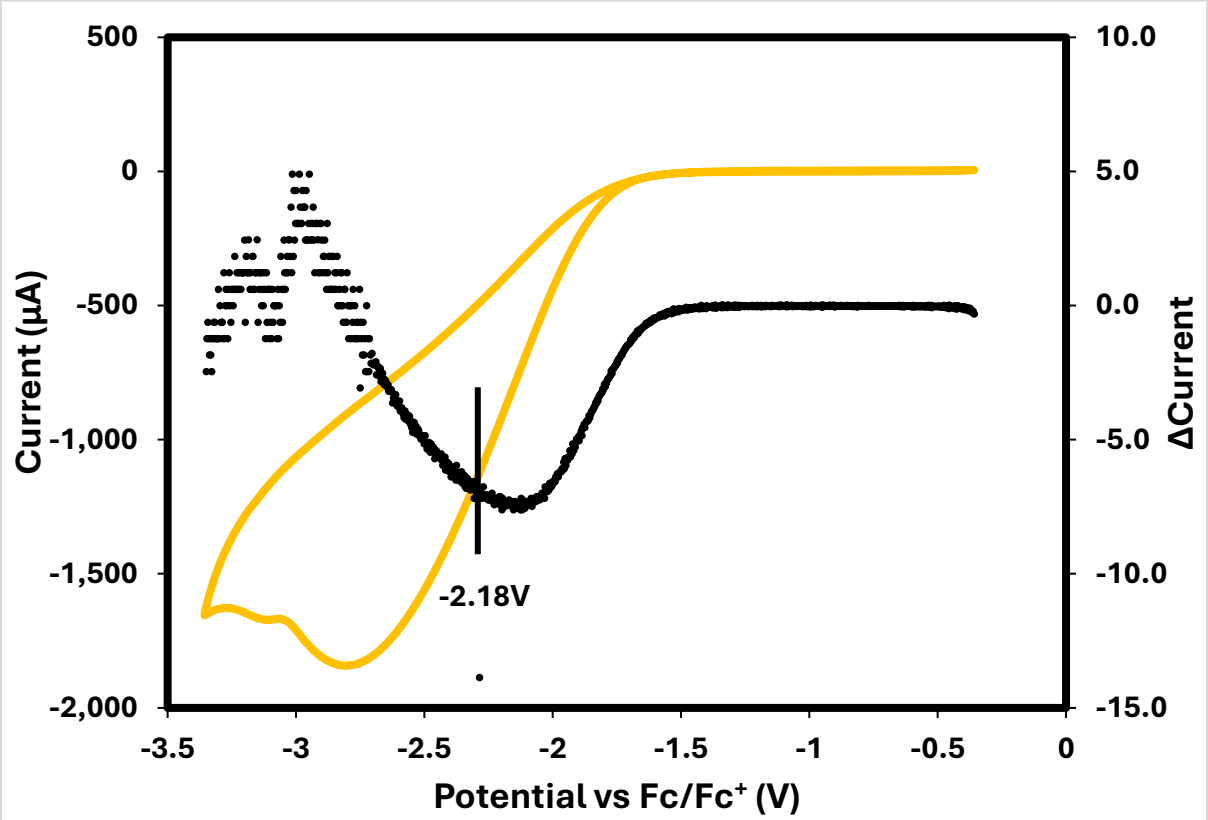

Figure 2.18: Cyclic voltammogram demonstrating the enhancements related to the reduction of the acetic acid by the glassy carbon electrode (orange). Solution contains 0.1M TBAHFP, and 1M acetic acid. The CV was performed at a scan rate of 100mV/s. Black markers represent the method of first principles applied to the orange curve. Minima denote an inflection point in the catalytic curve, indicating the associated onset potential and current enhancement for its respective acid concentration.

Evaluating the current enhancement values (i_{cat}) at -1.31V relative to the acid free reduction current for **I** (i_p) against the acid concentration gave the results displayed in Figure 2.17b. Initially, the enhanced current increased linearly until saturation was achieved at approximately 2M acetic acid. These data can be used to evaluate reaction rates of the overall catalytic cycle. When the reaction rate becomes independent of the

acid concentration, a saturated rate is achieved, and the reaction shifts to a pseudo-zero order rate. This relationship can be expressed in terms of turnover frequency (TOF) using eq. 2.2.[31,32] A similar set of experiments were also performed with catalyst complex **II**, yielding analogous observations (Figures 2.19, 2.20). Using this approach, catalyst **I** exhibited a TOF for hydrogen production from acetic acid of -1.31V of 40 s^{-1} while **II** gave a TOF at -1.35V of 20 s^{-1} (Tables 2.8, 2.9).

$$\frac{i_{cat}}{i_p} = \frac{2}{0.446}\sqrt{\frac{RT(TOF)}{Fv}} \qquad \text{(eq. 2.2)}$$

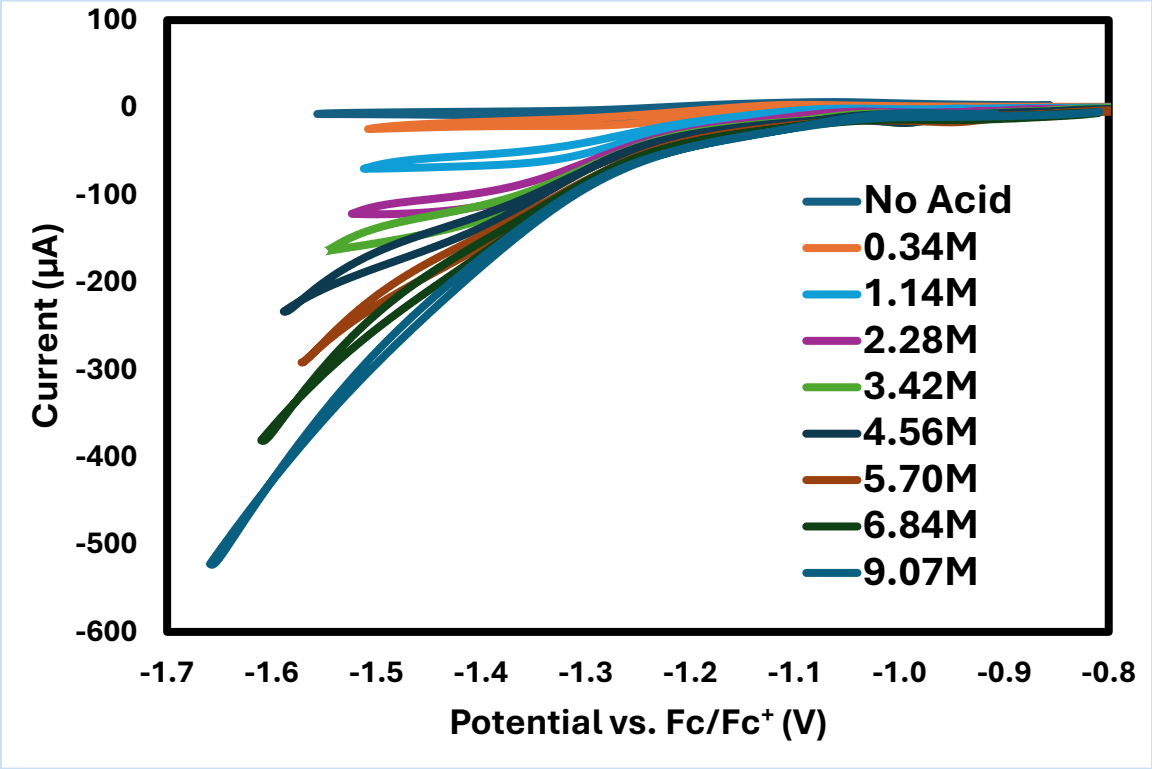

Figure 2.19: Cyclic voltammogram demonstrating catalytic enhancement at the Co(II)/Co(I) reduction event for 1mM of II in the presence of increasing acetic acid concentration. 0.1M TBAHFP is present as the electrolyte using a 1mm glassy carbon working electrode. Scans were performed at 100mV/s.

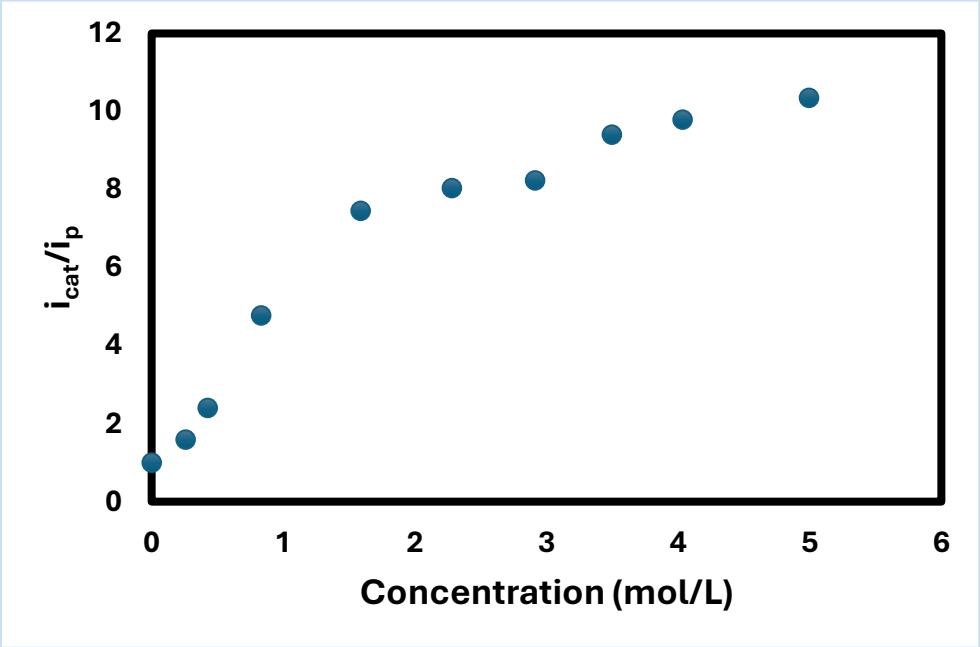

Figure 2.20: Plot of the ratio of the catalytic current (i_{cat}) at its inflection point to the peak current of the first reduction event in the absence of acid (i_p) as a function of the concentration of acetic acid. The solution contained 1mM of II and 0.1M TBAHFP in acetonitrile, the scan rate was 100 mV/s, and the working electrode was glassy carbon.

Table 2.8: Catalytic capability data for 1mM of I. Potentials and turnover frequencies determined through cyclic voltammetry with increasing acid concentration. Faradaic efficiencies were determined in 1 hour controlled potential coulometry experiments using a gas chromatograph for hydrogen detection.

Substrate	Inflection Point (V)	Overpotential (mV)	TOF (s^{-1})	Faradaic Efficiency
Acetic acid	-1.31	80	40	89%
Trifluoroacetic acid	-1.38	730	2740	85%
Trufluoroethanol	-2.4	230	780	82%

Table 2.9: Catalytic capability data for 1mM of II. Potentials and turnover frequencies determined through cyclic voltammetry with increasing acid concentration.

Substrate	Inflection Point (V)	Overpotential (mV)	TOF (s^{-1})
Acetic acid	-1.35	140	20
Trifluoroacetic acid	-1.45	820	1390
Trifluoroethanol	-2.45	280	280

With a pK_a in acetonitrile of 12.7, trifluoroacetic acid (TFA) is considerably more acidic than AA (pK_a = 22.3). The catalytic H_2 generation from TFA was next explored using a parallel set of conditions and analysis. The catalytic enhancement in reduction for complexes **I** and **II** (Figures 2.21, 2.22) was clearly observed and using the inflection points in these curves, the onset potentials for TFA reduction were determined to be -1.38V for **I** and -1.45V for **II**.

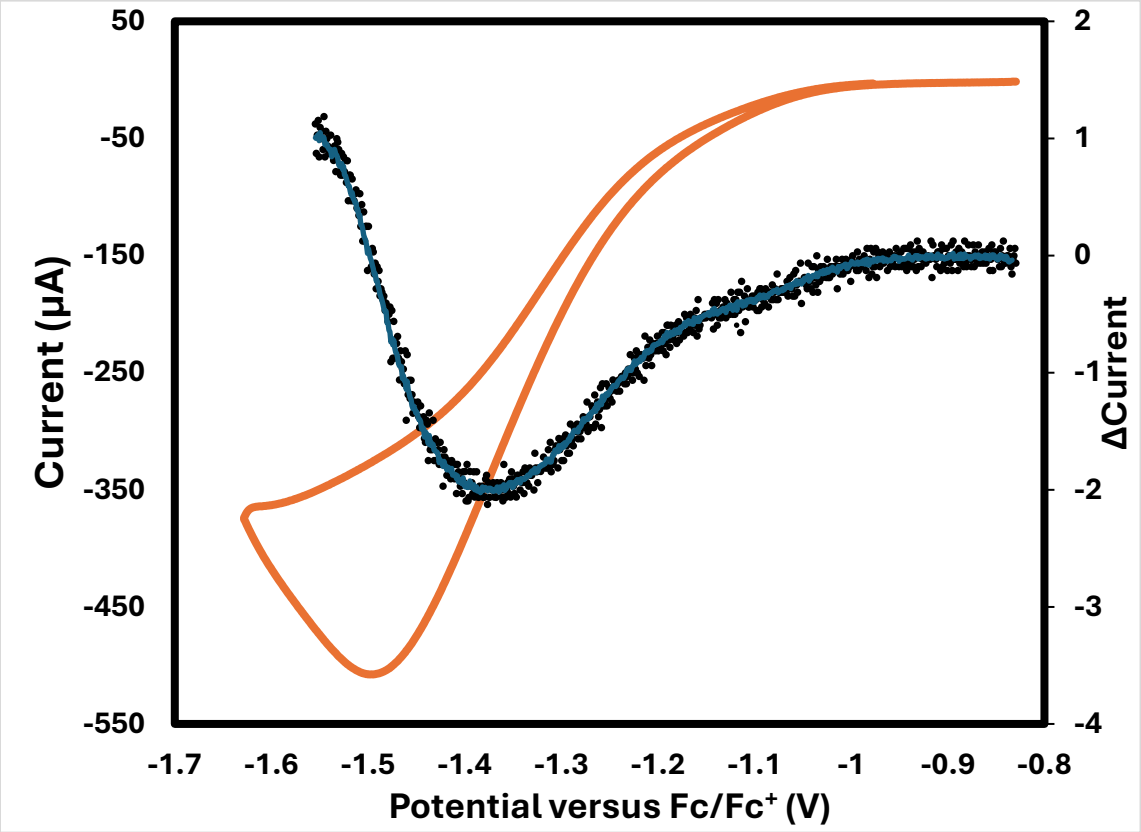

Figure 2.21: Cyclic voltammogram demonstrating catalytic enhancement at the Co(II)/Co(I) reduction event for 1mM of I in the presence 0.063M trifluoroacetic acid (orange). 0.1M TBAHFP is present as the electrolyte with a 1mm glassy carbon working electrode. Scan was performed at 100mV/s. Black markers represent the method of first principles applied to the orange curve. Minima denote an inflection point in the catalytic curve, indicating the associated onset potential and current enhancement for its respective acid concentration. The blue trend line is the moving average of black markers with a period of 5.

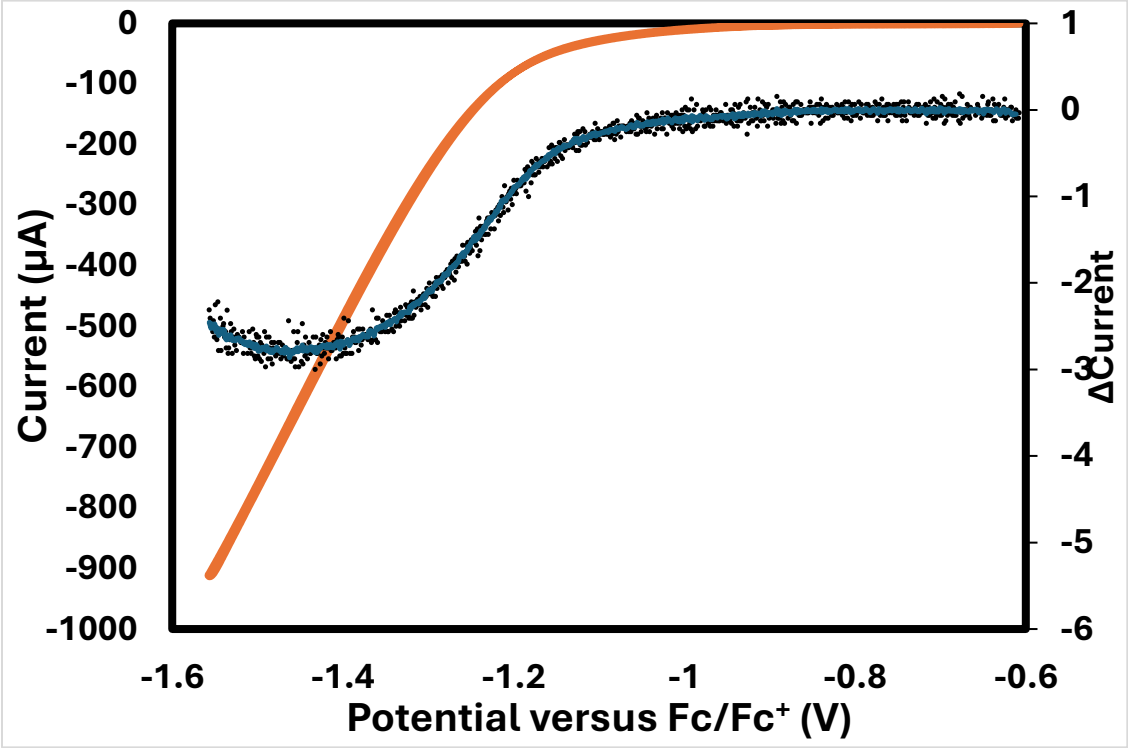

Figure 2.22: Cyclic voltammogram demonstrating catalytic enhancement at the Co(II)/Co(I) reduction event for 1mM of II in the presence 0.19M TFA. 0.1M TBAHFP is present as the electrolyte with a 1mm glassy carbon working electrode and a scan rate of 100mV/s. Black markers – First principles of orange curve representing the change in current enhancements. Black markers represent the method of first principles applied to the orange curve. Minima denote an inflection point in the catalytic curve, indicating the associated onset potential and current enhancement for its respective acid concentration. The blue trend line is the moving average of black markers with a period of 5.

Like AA, this correlates with the first reduction of catalysts **I** and **II**. Using eq 1 and a K_c of $10^{3.7}$ for TFA, for the formation of the homoconjugation product,[30] these values correspond to overpotentials of 730mV for complex **I** and 820mV for **II**. The effect of

increasing TFA concentration on the catalytic current, i_{cat}, and the TFA concentration dependence of i_{cat}/i_p were also measured for both **I** and **II** (Figures 2.23, 2.24, 2.25, 2.26). The application of eq. 2.2 to this data led to catalytic turnover frequencies for hydrogen production from TFA of 2740s^{-1} and 1390s^{-1} for **I** and **II**, respectively. The discrepancy in the performance between AA and TFA is as expected based on the pK_a of the acids and suggests a protonation reaction is the rate limiting step of the catalytic cycle. The Faradaic efficiencies of **I** for hydrogen generation using AA and TFA as the substrate were 89% and 82%, respectively.

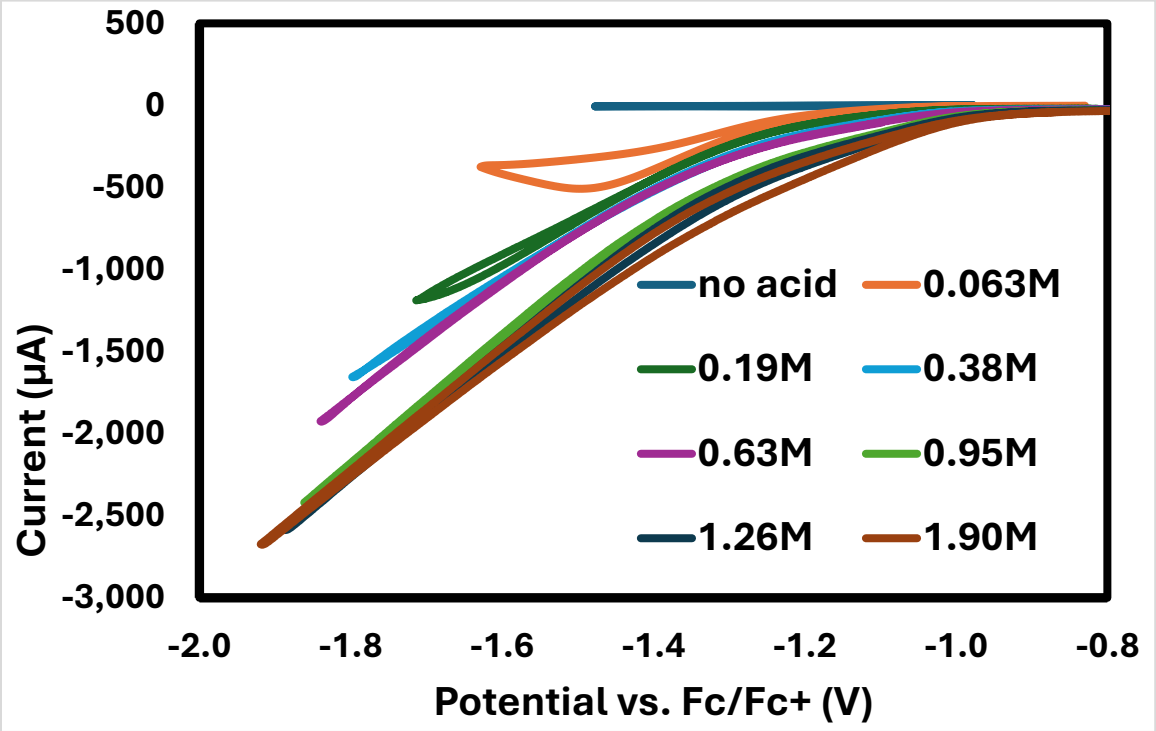

Figure 2.23: Cyclic voltammogram demonstrating catalytic enhancement at the Co(II)/Co(I) reduction event for 1mM of I in the presence of increasing trifluoroacetic acid. 0.1M TBAHFP is present as the electrolyte using a 1mm glassy carbon working electrode. Scans were performed at 100mV/s.

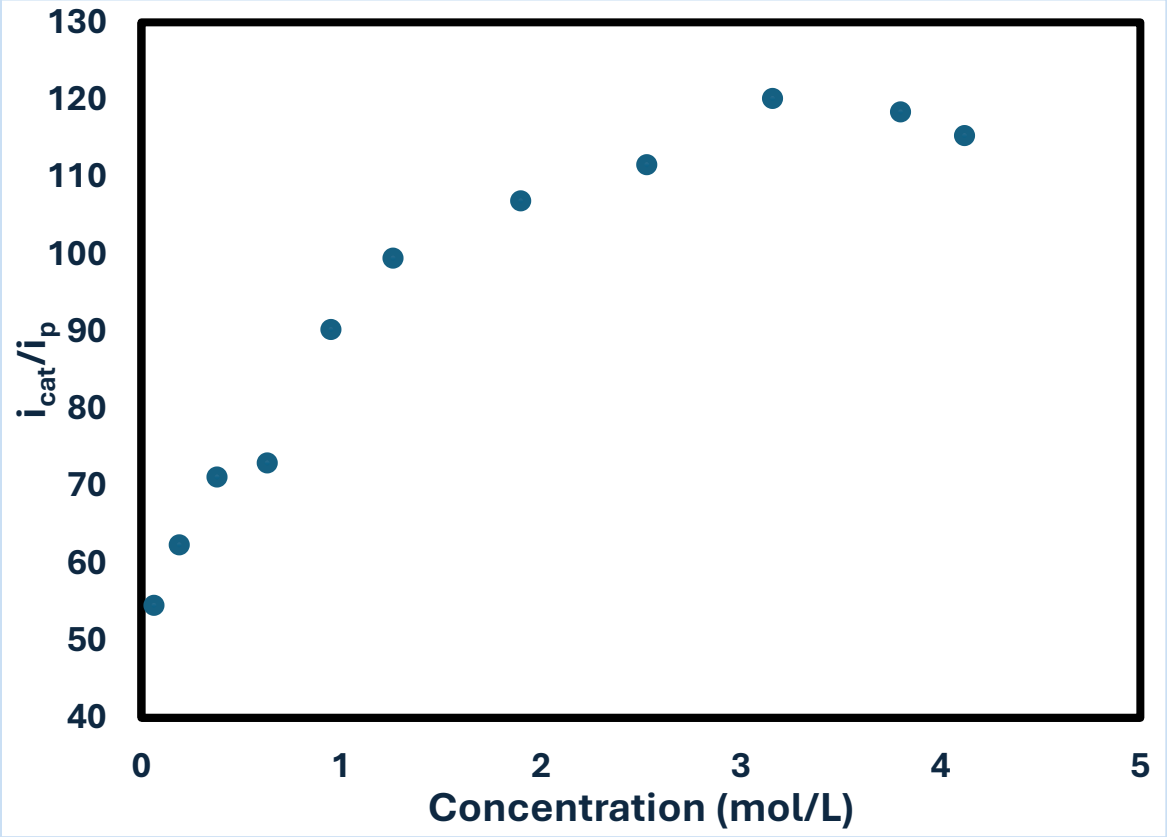

Figure 2.24: Plot of the ratio of the catalytic current (i_{cat}) at its inflection point to the peak current of the first reduction event in the absence of acid (i_p) as a function of the concentration of trifluoroacetic acid. The solution contained 1mM of I and 0.1M TBAHFP in acetonitrile, the scan rate was 100 mV/s, and the working electrode was glassy carbon.

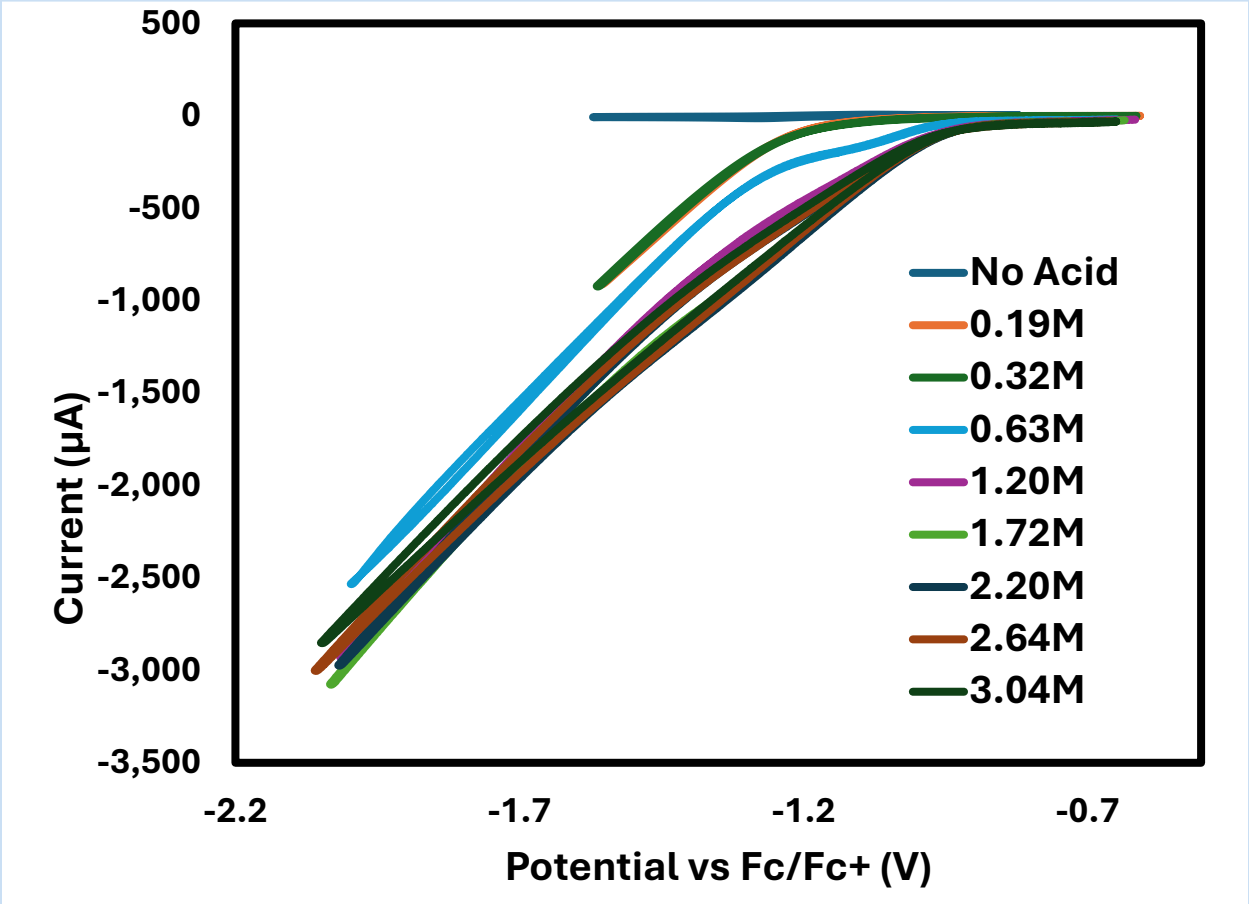

Figure 2.25: Cyclic voltammogram demonstrating catalytic enhancement at the Co(II)/Co(I) reduction event for 1mM of II in the presence of increasing trifluoroacetic acid concentration. 0.1M TBAHFP is present as the electrolyte using a 1mm glassy carbon working electrode. Scans were performed at 100mV/s.

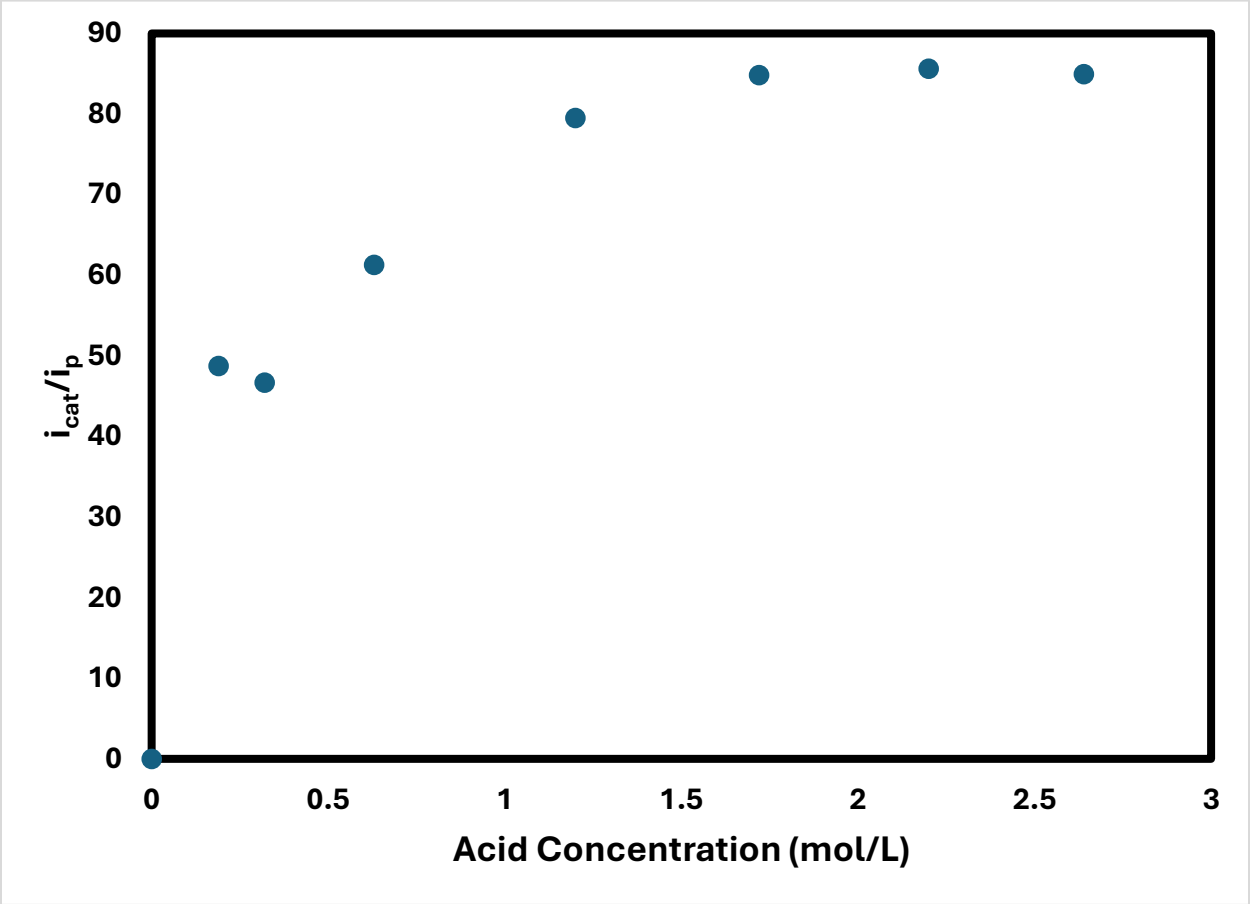

Figure 2.26: Plot of the ratio of the catalytic current (i_{cat}) at its inflection point to the peak current of the first reduction event in the absence of acid (i_p) as a function of the concentration of trifluoroacetic acid. The solution contained 1mM of II and 0.1M TBAHFP in acetonitrile, the scan rate was 100 mV/s, and the working electrode was glassy carbon.

After having explored acids as substrates for hydrogen production with catalysts **I** and **II**, a proton source with larger pK_a, more similar to water in acetonitrile, was targeted. We had established that hydrogen production from water occurred at the second reduction potential and wished to expand the analysis to a substrate that would function as a hydrogen source at the second reduction event.[7] Trifluoroethanol (TFE) with a reported

pK_a of 35.4 in acetonitrile was chosen for this application.[33] As expected, when TFE was the proton source, catalyst **I** showed enhancement at -2.40V (overpotential 230mV) while with **II** this occurred at -2.45V (overpotential = 280mV), these values correlate with the second reduction peak for both complexes (Figures 2.27, 2.28). Again, complex **I** displayed a larger saturation in i_{cat}/i_p than **II** which corresponded to a higher TOF of $780s^{-1}$ compared to the TOF for **II** of 280 s^{-1} (Figures 2.29, 2.30, Tables 2.9, 2.10). Bulk electrolysis using 1mM of **I** at a potential of -2.40V vs $Fc^{+/0}$ yielded production of hydrogen gas with a Faradaic efficiency of 82%. Blank experiments omitting catalyst produced no hydrogen gas.

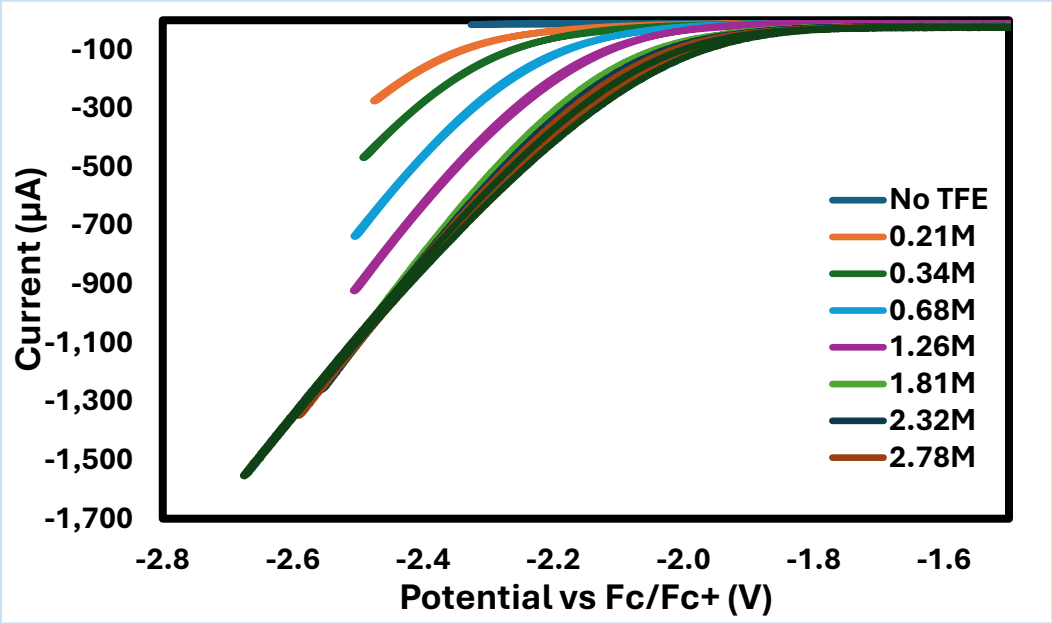

Figure 2.27: Cyclic voltammogram demonstrating catalytic enhancement at the reduction event associated with reduction of the complex at -2V and -2.15V for 1mM of I in the presence of increasing trifluoroethanol concentration referenced to the Fc/Fc^+. 0.1M TBAHFP is present as the electrolyte using a 1mm glassy carbon working electrode. Scans were performed at 100mV/s.

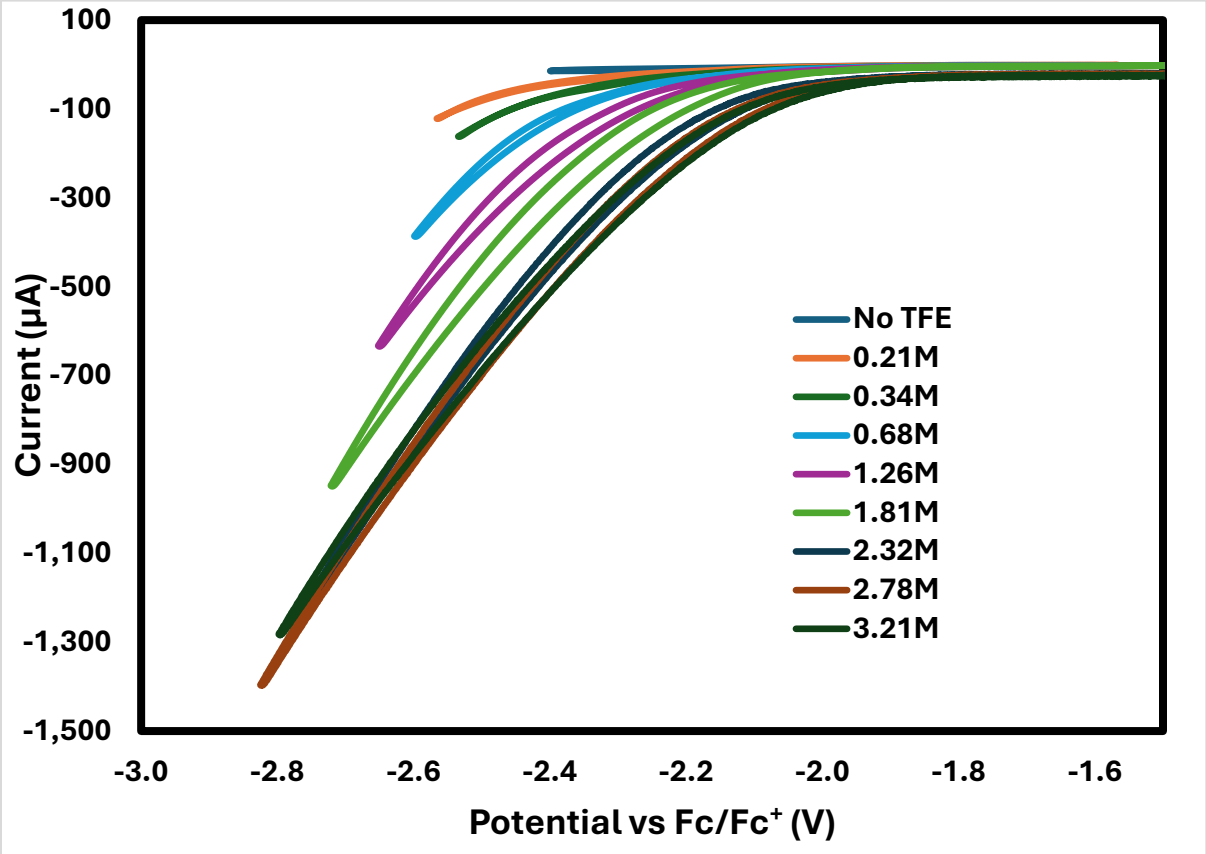

Figure 2.28: Cyclic voltammogram demonstrating catalytic enhancement at the reduction event associated with sequential reduction of the ligands at -2.1V and -2.23V for 1mM of II in the presence of increasing trifluoroethanol concentration. 0.1M TBAHFP is present as the electrolyte using a 1mm glassy carbon working electrode. Scans were performed at 100mV/s.

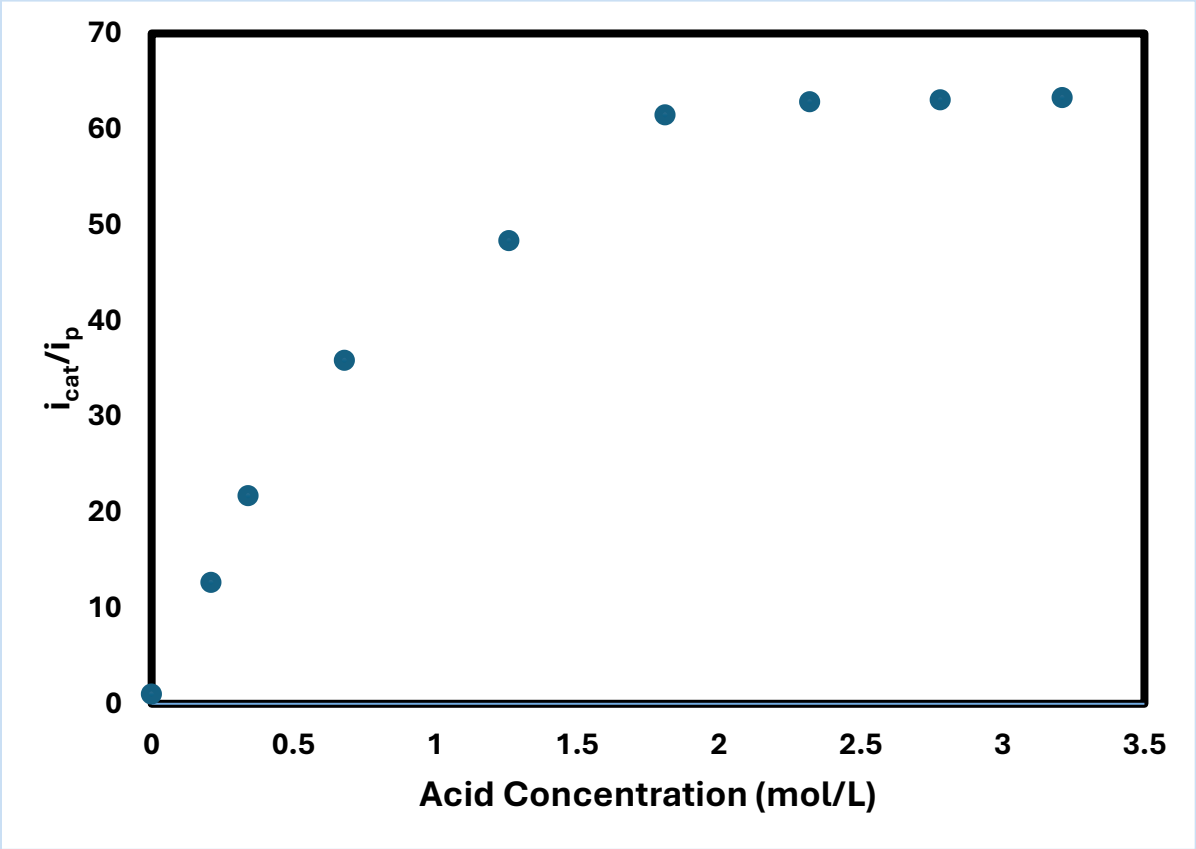

Figure 2.29: Plot of the ratio of the catalytic current (i_{cat}) at its inflection point to the peak current of the first reduction event in the absence of acid (i_p) as a function of the concentration of trifluoroethanol. The solution contained 1mM of I and 0.1M TBAHFP in acetonitrile, the scan rate was 100 mV/s, and the working electrode was glassy carbon.

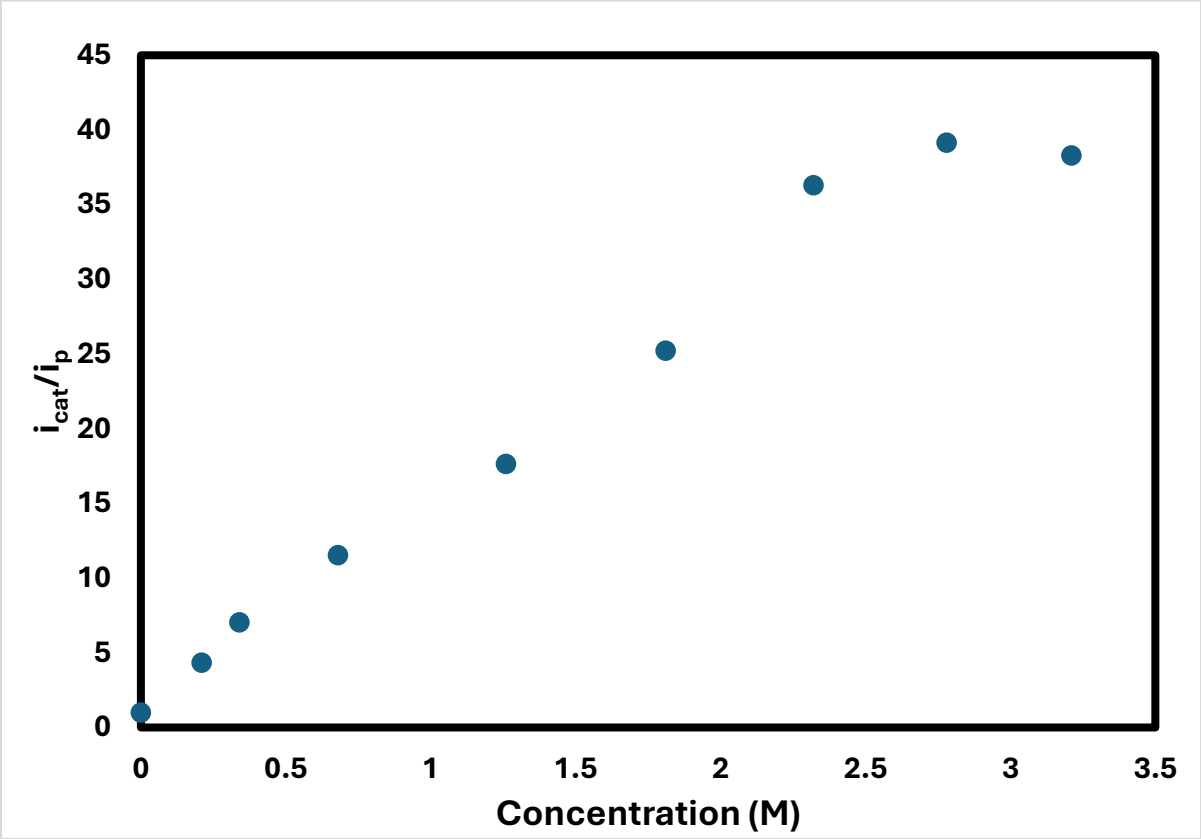

Figure 2.30: Plot of the ratio of the catalytic current (i_{cat}) at its inflection point to the peak current of the first reduction event in the absence of acid (i_p) as a function of the concentration of trifluoroethanol. The solution contained 1mM of II and 0.1M TBAHFP in acetonitrile, the scan rate was 100 mV/s, and the working electrode was glassy carbon.

Our observations clearly indicate that hydrogen generation from [Co(κ^3-2,6-{^{t}Bu$_2$PNR}$_2$(NC$_5$H$_3$)Br$_2$] occurs at two different potentials with what appears to correlate with acidity of the substrate. This prompted a return to examining the electronic structures of the reduced species **A** and **A**$^-$.

The two acids (AA and TFA) displayed catalytic hydrogen generation that appeared at the first reduction for **I** and **II**. Recall that the computational results for the first reduction resulted in a neutral square planar d^8 complex [Co(κ^3-2,6-{Ph_2PNH}$_2$$NC_5H_3$)Br] **A**. The HOMO of this species was a nonbonding electron pair in a Co centered dz^2 orbital. Addition of a proton to this site would lead to a cationic complex. After a proton was added to **A**, a DFT optimization and a frequency analysis was carried out to obtain a proposed structure. The result was a Co complex [Co(κ^3-2,6-{Ph_2PNH}$_2$$NC_5H_3$)Br(H)]$^+$ (**CoIII-H$^+$**) with a square based pyramidal structure and the PN3RP and bromo ligands in the basal plane and a hydride ligand located in the apical position (Figure 2.31).

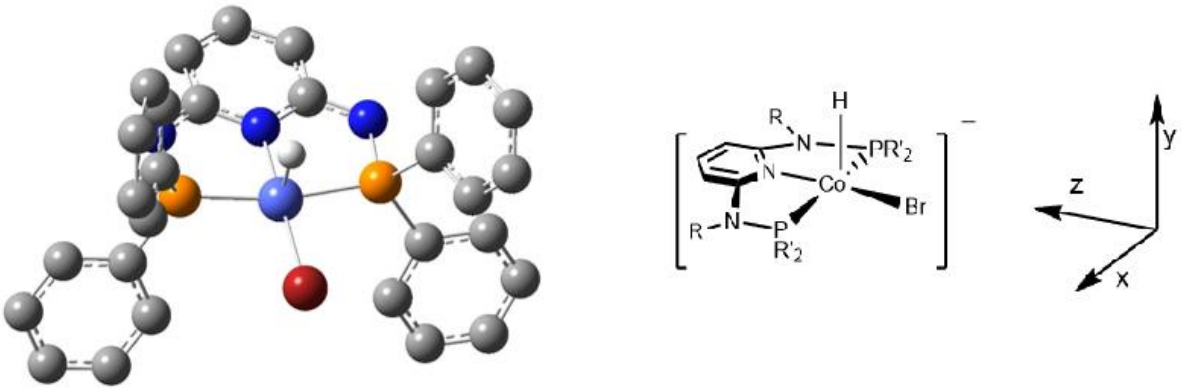

Figure 2.31. DFT optimized structure for the complex [Co(κ^3-2,6-{Ph_2PNH}$_2$$NC_5H_3$)Br(H)]$^+$ (CoIII-H) using the MO6L functional and def2-TZVP basis set. Frequency analysis confirmed that the optimized structure was a minimum with no imaginary frequencies. Hydrogen atoms are eliminated for clarity. The associated drawing provides the orientation of the Cartesian axes used in the discussion of this complex and is similar to that used throughout the computational presentation.

Interestingly, the orientation of the orbital array now has the z-axis oriented along the Br-Co-N_{py} vector. Through orbital analysis and electron counting, the Co center can be assigned an oxidation state of Co(III) with unoccupied molecular orbitals derived from Co dx^2-y^2 (LUMO+1) and dz^2 (LUMO) orbitals (Figure 2.32). The molecular orbitals involving Co dyz, dxy and dxy are occupied as expected for a d^6 Co center. The dyz and dxy based orbitals participate in Co-Br σ* interactions while the dxy Co orbital is nonbonding to the ligand array.

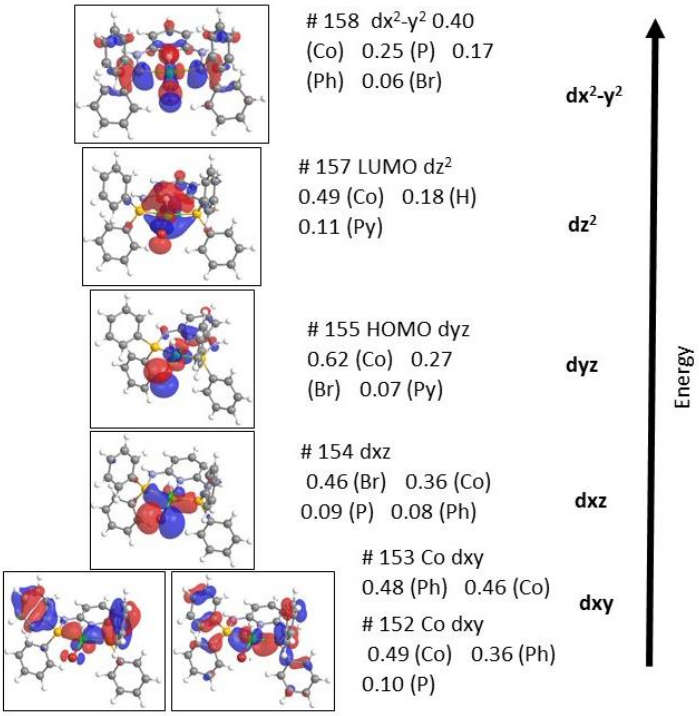

Figure 2.32. Selected Co-centered molecular orbitals obtained for the first reduction and protonation of complex I , [Co(κ³-2,6-{Ph_2PNH}$_2$$NC_5H_3$)Br(H)]⁺ (CoIII-H). Obtained using the MO6L functional, def2-TZVP basis set and PCM model for solvation in acetonitrile. Major fragment orbital contributions were obtained from the Chemissian program. Viewing at 0.03 isosurface.

In contrast, the reduction in trifluoroethanol and water occurred at the second reduction event for $[Co(\kappa^3\text{-}2,6\text{-}\{Ph_2PNR\}_2NC_5H_3)Br_2]$ complexes. The much stronger reducing agent $[Co(\kappa^3\text{-}2,6\text{-}\{Ph_2PNH\}_2NC_5H_3)Br]^-$ **A**$^-$ is also expected to be a stronger base. Furthermore, the SOMO is predominantly Co $dx^2\text{-}y^2$ and oriented for proton attack approximately trans to the N_{py} (Figure 2.33).

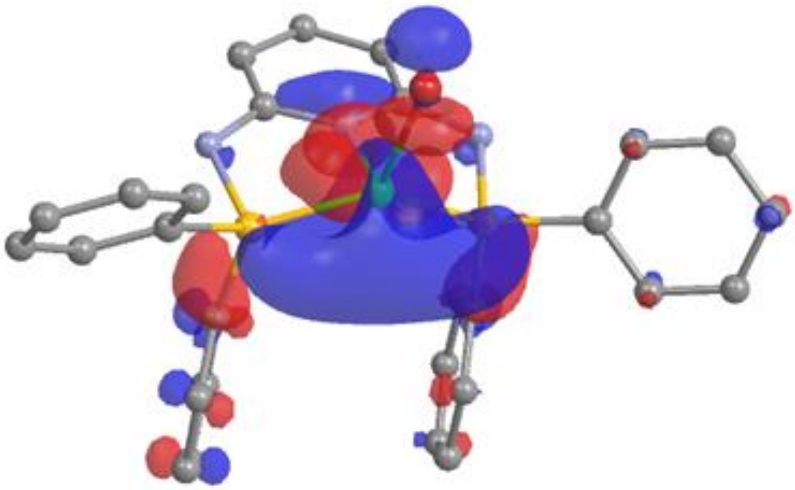

Figure 2.33: Cobalt centered SOMO for A$^-$. Orbital contributions 0.54 (Co), 0.23 (P), 0.13 (Ph), 0.06 (py). Hydrogen atoms omitted for clarity.

This is the logical position for protonation of **A**$^-$ and a proton was added to this site and the resultant cation was optimized. The result was a Co complex **CoII-H** (Figure 2.34) with a square pyramidal structure, however, surprisingly, the basal plane was now defined by the two coordinated P centers, the bromo and the hydride ligands. In **CoII-H**, the z-axis was aligned along the Co-N_{py} vector as shown in Figure 2.34. The proton abstraction results in the Co center now being assigned an oxidation state of Co(II) and a d^7 configuration with SOMO centered in the Co dz^2 orbital and a LUMO derived from $dx^2\text{-}y^2$

orbitals. The molecular orbitals involving Co dyz, dxy and dxy are occupied as expected for a d^7 Co center. The dyz and dxy based orbitals are Co-Br σ* while the dxz Co orbital is nonbonding to the ligand array as shown in Figure 2.35.

The doubly reduced species $[Co(\kappa^3\text{-}2,6\text{-}\{Ph_2PNH\}_2NC_5H_3)Br]^-$ **A**$^-$ is more basic and a stronger reducing agent. Also recall that the SOMO is predominantly Co $dx^2\text{-}y^2$ and oriented for proton attack approximately trans to the $N_{py.}$ A proton was added to this site and this cation was optimized and frequency analysis indicated a minimum energy structure. The result is a Co complex **CoII-H** (Figure 2.32) with a square based pyramidal structure, however the basal plane is now defined by the two P centers, the bromo and hydride ligands. The z-axis is aligned along the Co-N_{py} vector as shown in Figure 2.32. The Co center can now be assigned an oxidation state of Co(II) with the SOMO centered in the Co dz^2 orbital and a LUMO derived from $dx^2\text{-}y^2$ orbitals. The molecular orbitals involving Co dyz, dxy and dxy are occupied as expected for a d^7 Co center. The dyz and dxy based orbitals are Co-Br π* while the dxz Co orbital is non-bonding to the ligand array.

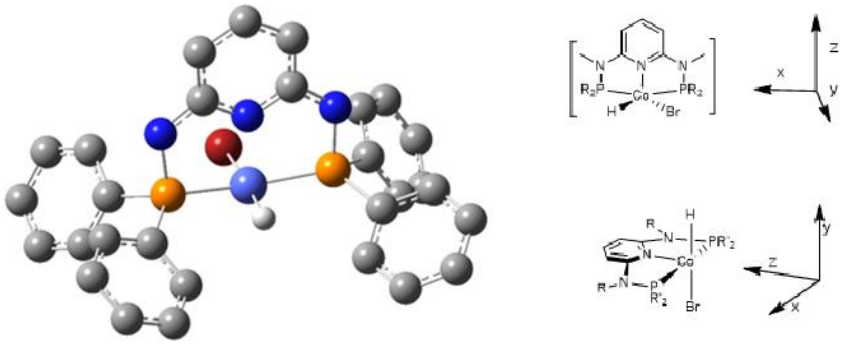

Figure 2.34. DFT optimized structure for the complex [Co(κ^3-2,6-{Ph_2PNH}$_2$$NC_5H_3$)Br(H)] (CoII-H) using the MO6L functional and def2-TZVP basis set. Frequency analysis confirmed that the optimized structure was a minimum with no imaginary frequencies. Hydrogen atoms are eliminated for clarity. The associated drawing provides the orientation of the Cartesian axes used in the discussion of this complex and is similar to that used throughout the computational presentation.

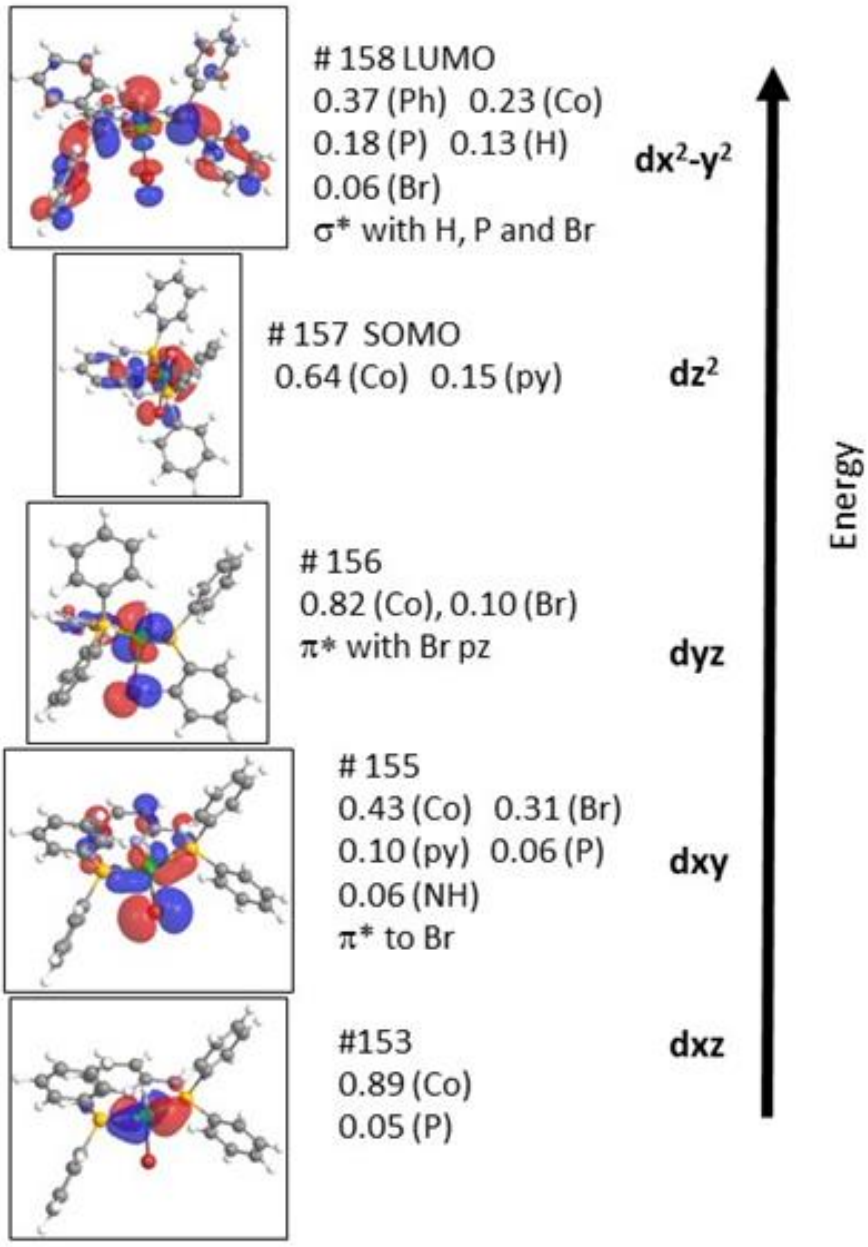

Figure 2.35: Selected Co-centered molecular orbitals obtained for the addition of a proton to the second reduction of complex I, [Co(κ³-2,6-{Ph₂PNH}₂NC₅H₃)Br(H)] (CoII-H). Obtained with the MO6L functional, def2-TZVP basis set and PCM model for solvation in acetonitrile. Major fragment orbital contributions were obtained from the Chemissian program. Viewing at 0.03 isosurface.

This combination of computational and experimental results suggests that complexes **I** and **II** operate via two distinct mechanisms depending on the substrate employed. A proposed mechanism is depicted in Figure 2.36. Both routes begin with the initial reduction of the Co^{II}, d^7 starting material to yield a d^8 square planar Co^{I} species, **A**. With stronger acids, complex **A** accepts a proton from the substrate to yield **CoIII-H**, a Co(III) hydride which can undergo a bimolecular reductive elimination to close the cycle and return to a d^7 starting material. However, a heterolytic pathway involving protonation of this species and release of H_2 cannot be excluded. On the other hand, with weakly acidic substrates such as trifluoroethanol and water, complex **A** is not sufficiently basic to abstract a proton from the substrate. Thus, a second reduction is necessary, yielding an anionic d^9 Co^0 intermediate $\mathbf{A}^-$. This more basic complex can then undergo protonation to produce **Co(II)-H**, a Co^{II} hydride that is now basic enough to react with the weaker acid, producing H_2, regenerating the Co^{II}, d^7 starting material to close the cycle.

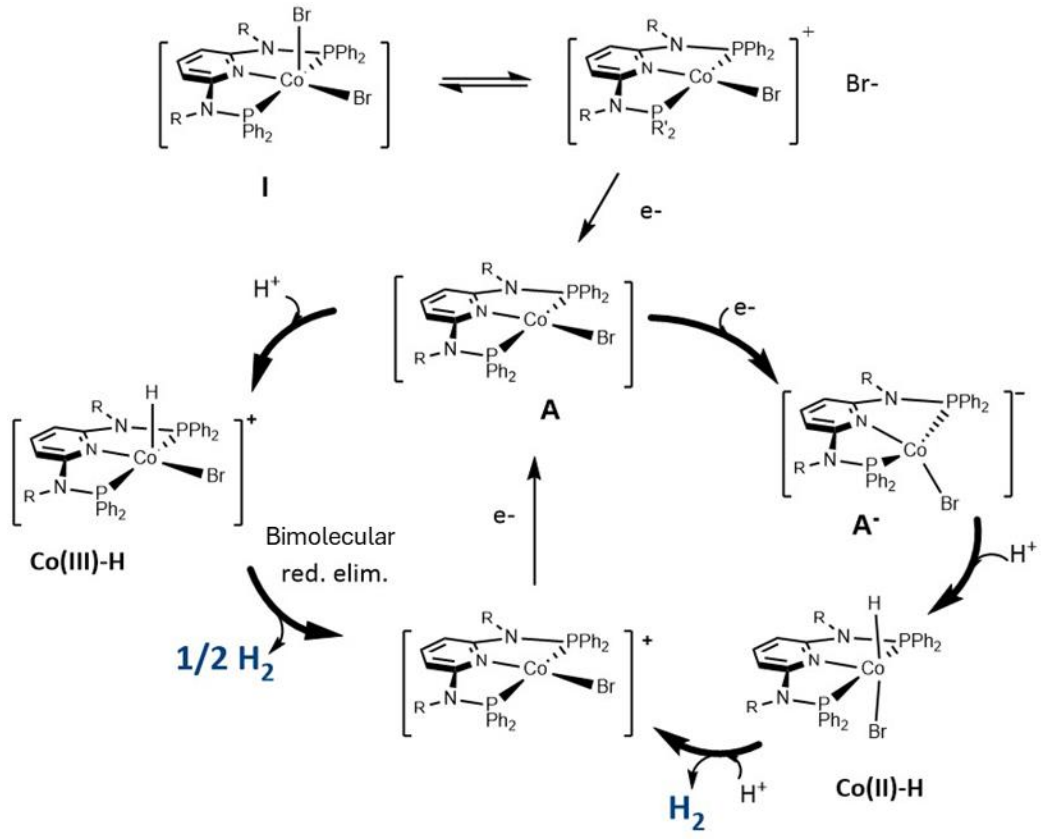

Figure 2.36: Proposed hydrogen evolution catalytic pathways for [Co(κ³-2,6-{Ph₂PNR}₂(NC₅H₃)Br₂]. A homolytic path for strong acids (left) employs a Co(I)/Co(III) while a heterolytic path for weak acids (right) uses a Co(0)/Co(II) route.

2.5 – Conclusion

Fundamental and practical features for the electrocatalytic hydrogen generation from unique, air-stable Co species, [Co(κ^3-2,6-{Ph_2PNR}$_2$(NC_5H_3)Br_2] have been revealed and presented. These species were previously demonstrated to function with neutral water as a substrate. The mechanism of this process has now been more thoroughly revealed by employing a range of substrates with varying pK_a values. These Co^{II} complexes are functional catalysts for efficient H_2 production at two different cathodic potentials. Using

acidic substrates, hydrogen is produced at a potential corresponding to the first reduction of the pincer-supported Co^{II} catalysts. More negative potentials were required for substrates with larger pK_a values, such as trifluoroethanol and H_2O. These experimental results are supported by DFT computational analysis that suggests two distinct reaction pathways for electrocatalytic proton reduction. Specifically, with stronger acids and lower reduction potentials, hydrogen is produced through a Co^{I}/Co^{III} homolytic pathway. With sources having higher pK_a values, catalysis operates at more negative cathodic potentials and follows a heterolytic Co^{0}/Co^{II} route. Our continuing explorations focus on the effects of ligand variation on this process and on efforts to use water as a substrate and solvent.

2.6 – Experimental Section

General methods. Reactions were performed in a glovebox under a nitrogen atmosphere, with the exception of ligand synthesis, which was performed using standard Schlenk techniques under a flow of N_2. All solvents were sparged with nitrogen and then dried by passage through a column of activated alumina using an apparatus purchased from Anhydrous Engineering. Deuterated solvents were dried using activated molecular sieves. All other chemicals were purchased from Sigma-Aldrich and used without further purification. Dried acetonitrile was purchased from Sigma-Aldrich and stored on molecular sieves in a glovebox. The ligand bis(diphenylphosphino)-2,6-di(methylamino)pyridine (PN3RP) was synthesized according to literature procedures.[34]

Synthesis of [Co(κ^3-2,6-{Ph_2PNH}$_2$(NC_5H_3)Br_2] (I)

A solution of ligand N,N'-bis(diphenylphosphino)-2,6- diaminopyridine (0.475 g, 1.0 mmol) in 15 mL of toluene was added to $CoBr_2$ (0.219 g, 1.0 mmol) in a glove box. The

reaction mixture was stirred for 16h at room temperature under N_2. The resulting mixture was then kept in the refrigerator overnight. The resulting dark brown precipitate was removed by filtration to generate the complex.

Synthesis of [Co(κ^3-2,6-{PhPNMe}2(NC_5H_3)Br_2] (II)

A solution of ligand N,N'-bis(diphenylphosphino)-2,6- di(methylamino)pyridine (0.505 g, 1.0 mmol) in 15 mL of toluene was added to $CoBr_2$ (0.219 g, 1.0 mmol) in a glove box. The reaction mixture was stirred for 16h at room temperature under N_2. The resulting mixture was then kept in the refrigerator overnight. The resulting dark brown precipitate was removed by filtration to generate the complex.

DFT calculations

Computations were performed using the WebMO interface with the Gaussian software package. Initial molecular structures were created from crystal structures that were then physically altered on WebMO for intermediate species. Structural optimization was completed with the M06L functional with the def2-SVP basis set. Vibrational frequencies with the same level of theory and basis set were calculated to verify there were no negative vibrational modes and thus the structures were the minimum energy structures, rather than a saddle point. Molecular energy and orbital calculations were completed using the M06L function with the def2-TZVP basis set. The molecular orbitals were analyzed using the Chemissian software package.

Electrochemistry

All cyclic voltammetry experiments were carried out in a three-neck flask, sealed under nitrogen. Samples were prepared in a glove box and sealed before removing for

measurement. Cyclic voltammetry was performed using a PGZ301 Voltameter (Radiometer Analytical) potentiostat . For bulk electrolysis a VersaSTAT 3 (Princeton Applied Research) potentiostat was used. A conventional three electrode system was employed. A glassy carbon electrode (diameter = 0.4 cm) was used as the working electrode, a Pt wire as the counter electrode, and an Ag wire was used as a pseudo-reference electrode. For bulk electrocatalytic reduction experiments, a glassy carbon rod (diameter = 0.4 cm; length 2 cm) was used as the working electrode, a coiled Pt wire as the auxiliary electrode, and an Ag wire was used as a pseudo-reference electrode. Ferrocene was added as an internal reference after purging with N_2 and measured before and after water addition. Tetra-n-butylammonium hexafluorophosphate (TBAHFP), the supporting electrolyte, was purchased directly from Sigma Aldrich. The electrolyte solution, 0.1 M TBAHFP in CH_3CN, was saturated with N_2 by assembling the cell in the glovebox. The concentration of catalyst was 1mM in each experiment. For cyclic voltammetry, 20mL of acetonitrile was used; for bulk experiments 15mL of acetonitrile was used. First principles of the enhancements were computed to demonstrate the inflection point as a minimum value, shown in figure 5 as the blue moving average with a period of 5 over the black dot first principal points.[29] Hydrogen production was measured using an Agilent 7820A gas chromatograph equipped with a thermal conductivity detector (TCD) using an Agilent select permanent gases column. The amount of H_2 was determined using a calibration curve.

2.7 – References

1 T. R. Cook, D. K. Dogutan, S. Y. Reece, Y. Surendranath, T. S. Teets and D. G. Nocera, *Chem Rev*, 2010, **110**, 6474–6502.

2 M. Wang, L. Chen and L. Sun, *Energy Environ Sci*, 2012, **5**, 6763–6778.

3 T. Wang, H. Xie, M. Chen, A. D. Aloia, J. Cho, G. Wu and Q. Li, *Nano Energy*, 2017, **42**, 69–89.

4 V. S. Thoi, Y. Sun, J. R. Long and C. J. Chang, *Chem. Soc. Rev.*, 2013, **42**, 2388–2400.

5 V. Artero, M. Chavarot-Kerlidou and M. Fontecave, *Angew Chem, Int Ed*, 2011, **50**, 7238–7266.

6 P. Du and R. Eisenberg, *Energy Environ Sci*, 2012, **5**, 6012.

7 G. K. Rao, W. Pell, B. Gabidullin, I. Korobkov and D. Richeson, *Chem Eur J*, 2017, **23**, 16763–16767.

8 S. Kaur-Ghumaan, P. Hasche, A. Spannenberg and T. Beweries, *Dalton Trans*, 2019, **48**, 16322–16329.

9 Z. Xiao, M. Natarajan, W. Zhong and X. Liu, *Electrochim Acta*, 2020, **340**, 135998.

10 K. E. Dalle, J. Warnan, J. J. Leung, B. Reuillard, S. Karmel, Isabell and E. Reisner, *Chem Rev*, 2019, **119**, 2752–2875.

11 S. Inoue, Y.-N. Yan, K. Yamanishi, Y. Kataoka and T. Kawamoto, *Chem Commun*, 2020, **56**, 2829–2832.

12 S. Ding, P. Ghosh, A. M. Lunsford, N. Wang, N. Bhuvanesh, M. B. Hall and M. Y. Darensbourg, *J Am Chem Soc*, 2016, **138**, 12920–12927.

13 B. D. Stubbert, J. C. Peters and H. B. Gray, *J Am Chem Soc*, 2011, **133**, 18070–18073.

14 W. Schirmer, U. Florke and H.-J. Haupt, *Z. Anorg. Allg. Chem.*, 1987, **545**, 83–97.

15 W. Schirmer, U. Florke and H.-J. Haupt, *Z. Anorg. Allg. Chem.*, 1989, **574**, 239–255.

16 Ö. Öztopcu, C. Holzhacker, M. Puchberger, M. Weil, K. Mereiter, L. F. Veiros and K. Kirchner, *Organometallics*, 2013, **32**, 3042–3052.

17 M. Nippe, R. S. Khnayzer, J. A. Panetier, D. Z. Zee, B. S. Olaiya, M. Head-Gordon, C. J. Chang, F. N. Castellano and J. R. Long, *Chem Sci*, 2013, **4**, 3934–3945.

18 B. D. McCarthy, D. J. Martin, E. S. Rountree, A. C. Ullman and J. L. Dempsey, *Inorg Chem*, 2014, **53**, 8350–61.

19 N. Elgrishi, B. D. McCarthy, E. S. Rountree and J. L. Dempsey, *ACS Catal*, 2016, **6**, 3644–3659.

20 J. L. Alvarez-Hernandez, A. E. Sopchak and K. L. Bren, *Inorg Chem*, 2020, **59**, 8061–8069.

21 E. S. Rountree, D. J. Martin, B. D. Mccarthy and J. L. Dempsey, *ACS Catal*, 2016, **6**, 3326–3335.

22 C. Baffert, V. Artero and M. Fontecave, *Inorg Chem*, 2007, **46**, 1817–1824.

23 A. W. Addison, T. N. Rao, J. Reedijk, J. van Rijn and G. C. Verschoor, *Dalton Trans*, 1984, 1349.

24 S. Rosler, J. Obenauf and R. Kempe, *J Am Chem Soc*, 2015, **137**, 7998.

25 D. W. Shaffer, I. Bhowmick, A. L. Rheingold, C. Tsay, B. N. Livesay, M. P. Shores and J. Y. Yang, *Dalton Transactions*, 2016, **45**, 17910–17917.

26 N. Elgrishi, K. J. Rountree, B. D. McCarthy, E. S. Rountree, T. T. Eisenhart and J. L. Dempsey, *J Chem Educ*, 2018, **95**, 197–206.

27 Y. Minenkov, A. Singstad, G. Occhipinti and V. R. Jensen, *Dalton Trans*, 2012, **41**, 5526–5541.

28 E. S. Rountree, B. D. McCarthy, T. T. Eisenhart and J. L. Dempsey, *Inorg Chem*, 2014, **53**, 9983–10002.

29 A. M. Appel and M. L. Helm, *ACS Catal*, 2014, **4**, 630–633.

30 V. Fourmond, P.-A. Jacques, M. Fontecave and V. Artero, *Inorg Chem*, 2010, **49**, 10338–10347.

31 D. H. Pool and D. L. Dubois, *J Organomet Chem*, 2009, **694**, 2858–2865.

32 U. J. Kilgore, J. A. S. Roberts, D. H. Pool, A. M. Appel, M. P. Stewart, M. R. Dubois, W. G. Dougherty, W. S. Kassel, R. M. Bullock and D. L. Dubois, *J Am Chem Soc*, 2011, **133**, 5861–5872.

33 Y. C. Lam, R. J. Nielsen, H. B. Gray and W. A. Goddard, *ACS Catal*, 2015, **5**, 2521–2528.

34 S. R. M. M. de Aguiar, B. Stöger, E. Pittenauer, M. Puchberger, G. Allmaier, L. F. Veiros and K. Kirchner, *J Organomet Chem*, 2014, **760**, 74–83.

Chapter 3: Exploring Ligand-Centered Electrocatalytic H_2O Reduction: Hydrogen Generation with a Soluble Ni(II) Octabutoxyphthalocyanine Complex

3.1 – Preamble and Statement of Contributions

The content described in this chapter was published in Dalton Transactions in 2024. It can be accessed through the following link: **https://doi.org/10.1039/D4DT01419G**

All experimental and computational data were generated and initially interpreted by Josh Brown. Preliminary drafts were completed by Josh Brown and the manuscript was further edited by Darrin Richeson and Josh Brown.

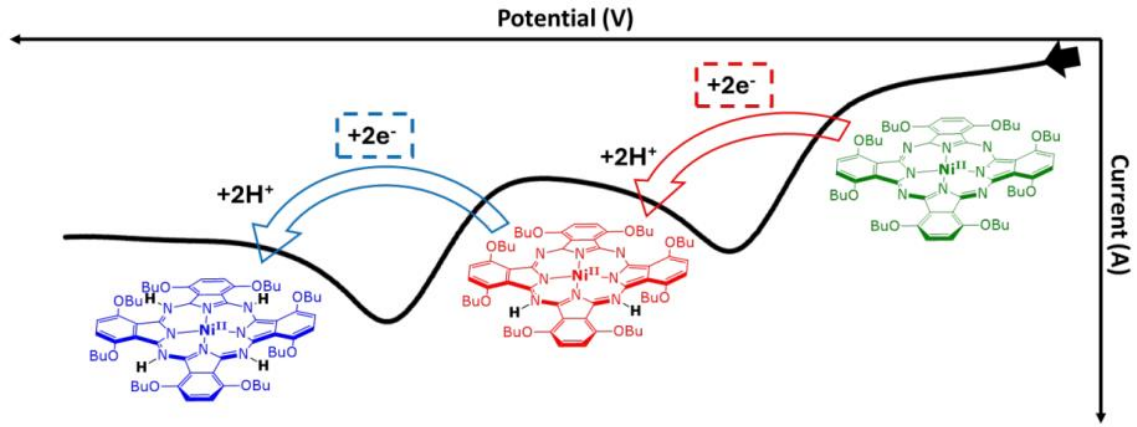

3.2 – Abstract

Herein, a nickel (II) octabutoxyphthalocyanine complex demonstrating ligand-centered redox activity and pH dependence is reported and investigated as an electrocatalyst for hydrogen evolution from water. Spectro- and electrochemical methods were implemented to further elucidate the nature of the pH dependence and catalytic mechanism. Ligand contributions towards the redox chemistry were identified through several analyses, ultimately aligning the catalytic activity of the molecule with these attributes.

3.3 – Introduction

Overreliance on fossil fuels for the generation of energy and material goods has resulted in significant, large-scale environmental damage.[1–4] Addressing the growing environmental burden requires green alternatives to energy production and the synthesis of industrially important chemicals. Hydrogen is a central chemical for both of these aspects but is still produced through inefficient and polluting means.[5,6] Therefore, homogeneous electrocatalytic water reduction for the generation of hydrogen is a topical and significant area of research. Early work in this field employed precious metals as catalysts, but recently less toxic and more sustainable metals have been sought, replacing expensive heavy metals with more earth-abundant 3d transition metals.[6–8] Proposed mechanisms for these complexes can vary but commonly proceed through the formation of a metal hydride that can then either be protonated or undergo M-H homolysis to release hydrogen.[9–11] Recently, redox, and chemically active ligands have been shown to

play an important role in these mechanisms, often acting as electron reservoirs or proton shuttles.[8,12–15]

Phthalocyanines (Pc) are a highly symmetrical, planar, tetradentate, macrocyclic group of ligands with stable electrochemical behaviour that includes several reversible redox events.[13,15–17] Additionally, two potential protonation sites have been identified in this structure, including the coordinated isoindole nitrogen centres (coor-N) and the bisecting/linking nitrogen groups (bi-N).[13,18] These attributes have made Pc ligands good candidates for electrocatalysis for a variety of targets, including water reduction.[19] The majority of research performed using Pc complexes has been in the heterogeneous phase, largely due to solubility issues.[20,21] In this report the homogeneous electrocatalytic hydrogen evolution abilities of Ni(II) octabutoxyphthalocyanine (**NiPc**) (Figure 3.1) along with electrochemical and spectroelectrochemical (SEC) characterization, are reported.[22] Opportune energetics for metal and ligand contributions to the orbital array of **NiPc** generate an electronic structure containing two degenerate HOMO's, resulting in stable catalytic function, even after several reduction processes. This interplay demonstrates the significance of the ligand in catalysis, beyond structural support or assistance in solubility. Coupled with these features are the unique ability of this complex to display non-innocent proton transfer routes that are described herein.

3.4 – Results and Discussion

NiPc was prepared according to literature protocol by the direct reaction of $Ni(OAc)_2$ and the 1,4,8,11,15,18,22,25-octabutoxy-phthalocyanine-H_2 ligand in refluxing dimethylformamide (DMF) for 5 hours under nitrogen. The addition of excess water precipitated the product as green microcrystals, which were then washed with cold ethanol and dried in vacuo overnight.

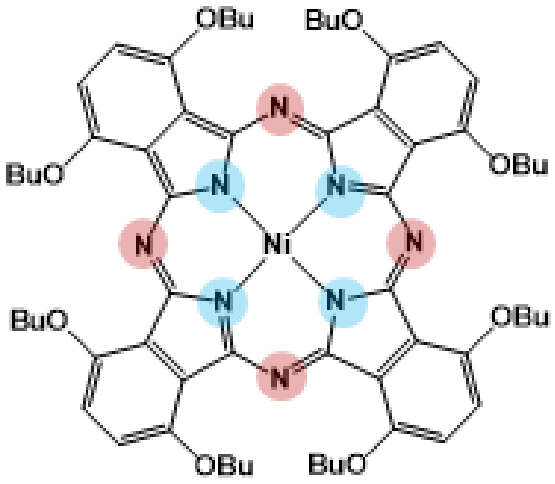

Figure 3.1: Structural representation of planar Ni(II) 1,4,8,11,15,18,22,25-octabutoxyphthalocyanine, NiPc. coor-N centres highlighted in blue and bi-N in red.

Cyclic voltammograms (CVs) of **NiPc** were collected in dichloromethane (DCM) for initial characterization. Two reversible events were observed in a cathodic sweep with $E_{1/2}$ values of -1.46V and -1.85V vs $Fc^{+/0}$ (Figure 3.2). The scan rate (n) dependence of these two reduction events (Figure 3.3) showed a linear relationship for peak current (i_p) *vs.* $n^{1/2}$ (Figures 3.4, 3.5), consistent with diffusion-controlled processes according to the Randles-Ševčík equation.[23]

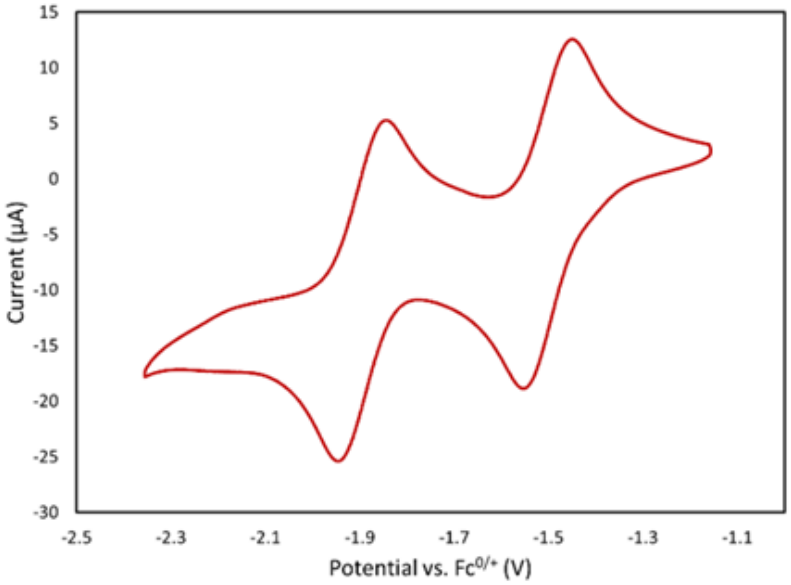

Figure 3.2: CV of 1mM NiPc in CH_2Cl_2 scanned between -1.15V and -2.35V with a scan rate of 0.1V/s and electrolyte (TBAHFP) concentration of 0.1M.

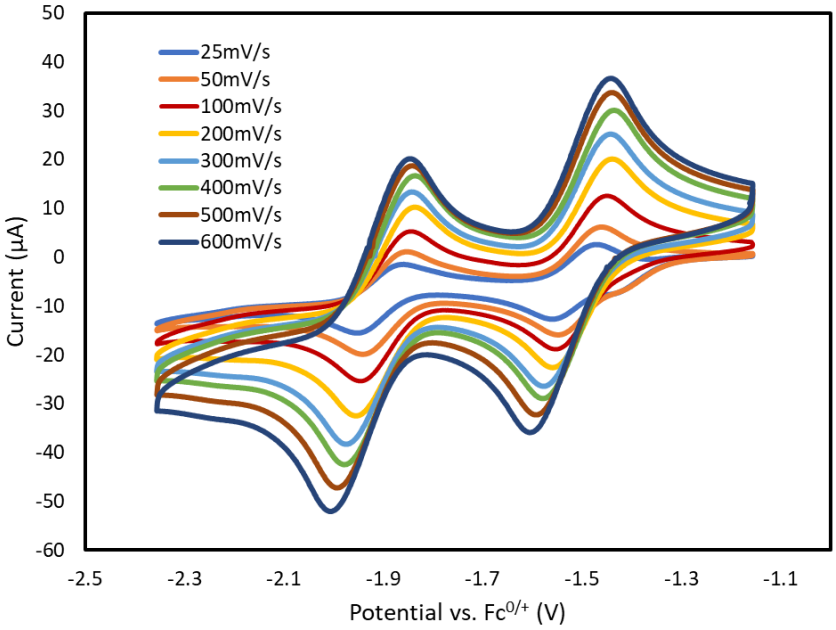

Figure 3.3: CV of 0.5mM NiPc in DCM scanned between -1.15V and -2.35V with a varying scan rate and electrolyte (TBAHFP) concentration of 0.1M.

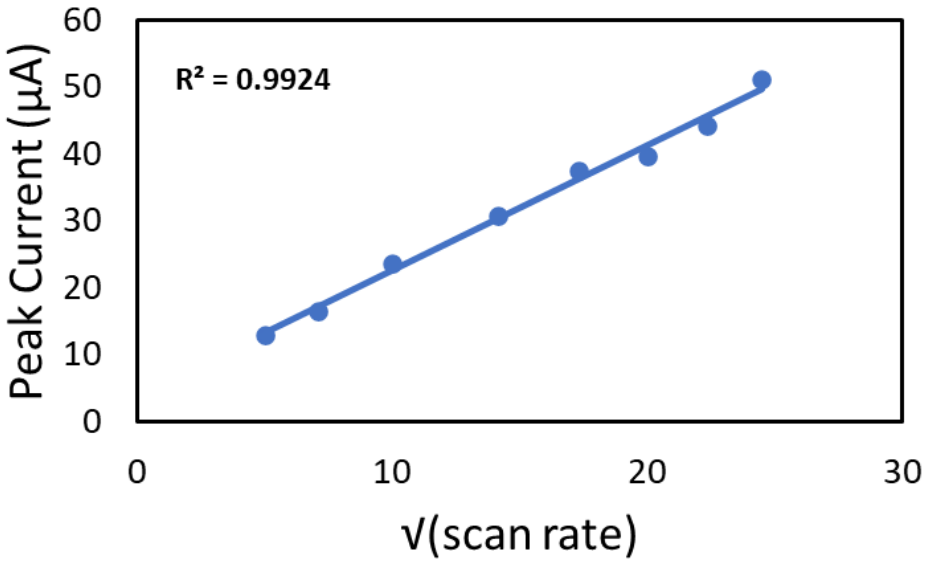

Figure 3.4: Plot of the reduction peak current value from Figure 3.3 as a function of the square root of the scan rate at the first redox event (-1.55V vs $Fc^{+/0}$).

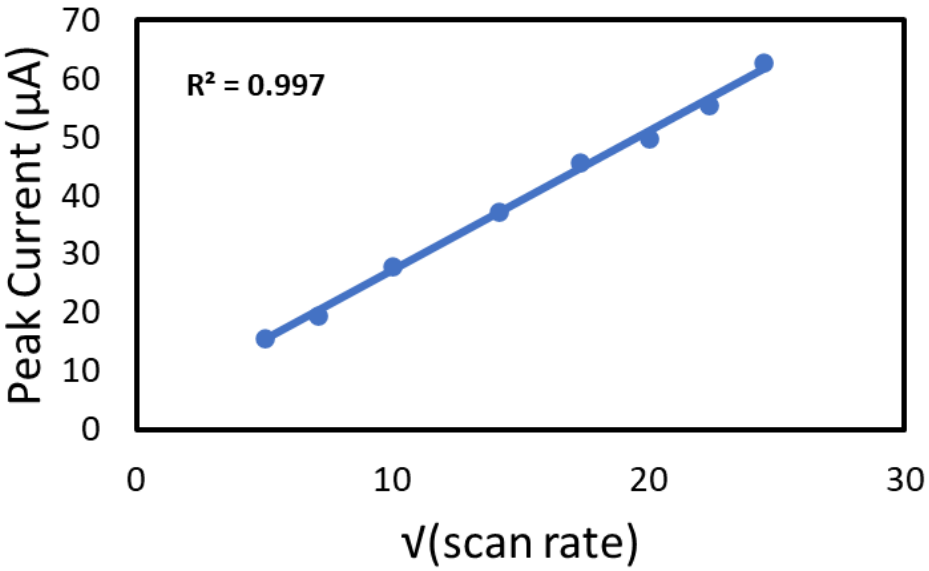

Figure 3.5: Plot of the reduction peak current value from Figure 3.3 as a function of the square root of the scan rate at the second redox event (-1.95V vs $Fc^{+/0}$).

Further examination of the redox events in Figure 2 revealed peak separations (ΔE_p) of only 0.174V. This value was half of the accepted, one-electron $Fc^{+/0}$ redox event, examined in the same environment (Figure 3.6). This indicates that the two observed redox events constitute two-electron processes.[24] Furthermore, when the first redox event at $E_{1/2}$= -1.46V was isolated and measured in mixed THF/water solvent, two distinctive reduction events were clearly resolved at n < 0.1V/s (Figure 3.7). This provides further support that the two reductions of **NiPc** observed in CH_2Cl_2 are two-electron processes, corresponding to reduction of **NiPc** to **$NiPc^{2-}$** and **$NiPc^{4-}$**, respectively.

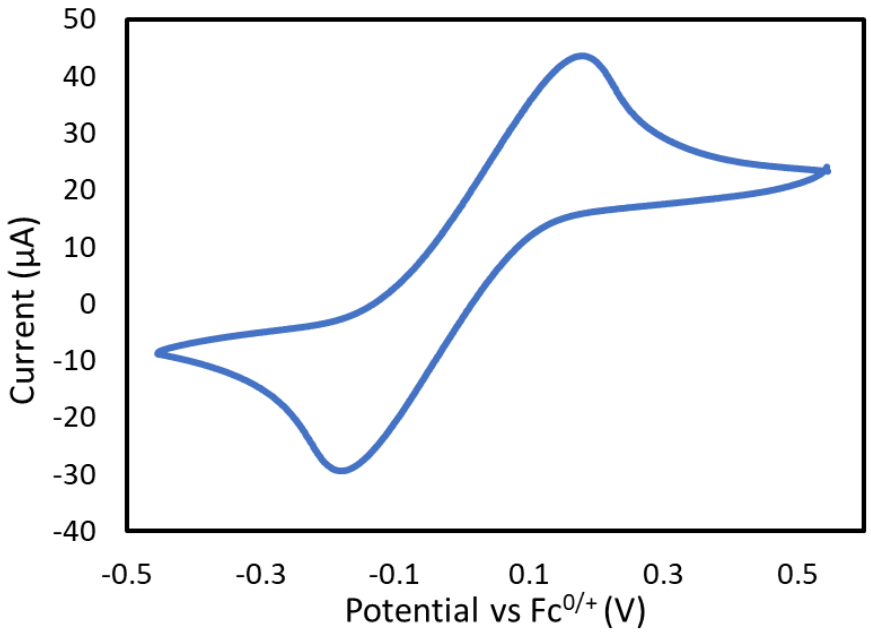

Figure 3.6: CV of 0.5mM Ferrocene in DCM scanned between 0.45V and -0.5V with a scan rate of 0.1V/s and electrolyte (TBAHFP) concentration of 0.1M.

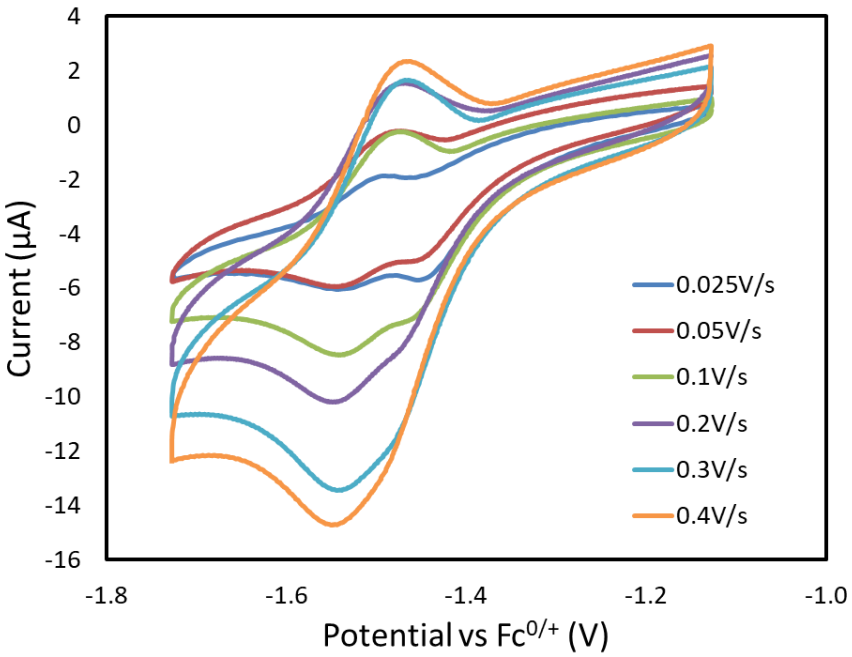

Figure 3.7: CV of 0.5mM NiPc in THF with a water concentration of 9.25M scanned between -1.15V and -1.75V with a varying scan rate and electrolyte (TBAHFP) concentration of 0.1M.

Density functional theory (DFT) optimizations were performed on the **NiPc**, **NiPc^{2-}**, and **NiPc^{4-}** species to elucidate their electronic features. The resulting molecular structure and selected frontier MOs for neutral **NiPc** are depicted in Figure 3.8. The highest occupied molecular orbital (HOMO) is dominated by a p-orbital localized on the isoindole units of the ligand. The two lowest unoccupied molecular orbitals (LUMO) (MO 307, 308) for **NiPc** are composed of two degenerate ligand-centred p-orbitals that are orthogonal in symmetry and have only 2-3% contribution from the Ni centre. These molecular orbitals (MOs) are the likely site for the observed reduction events. Further TD-DFT analysis of **NiPc** produced an excellent match with experimental UV-vis data (Figure 3.9) supporting our computational analyses.

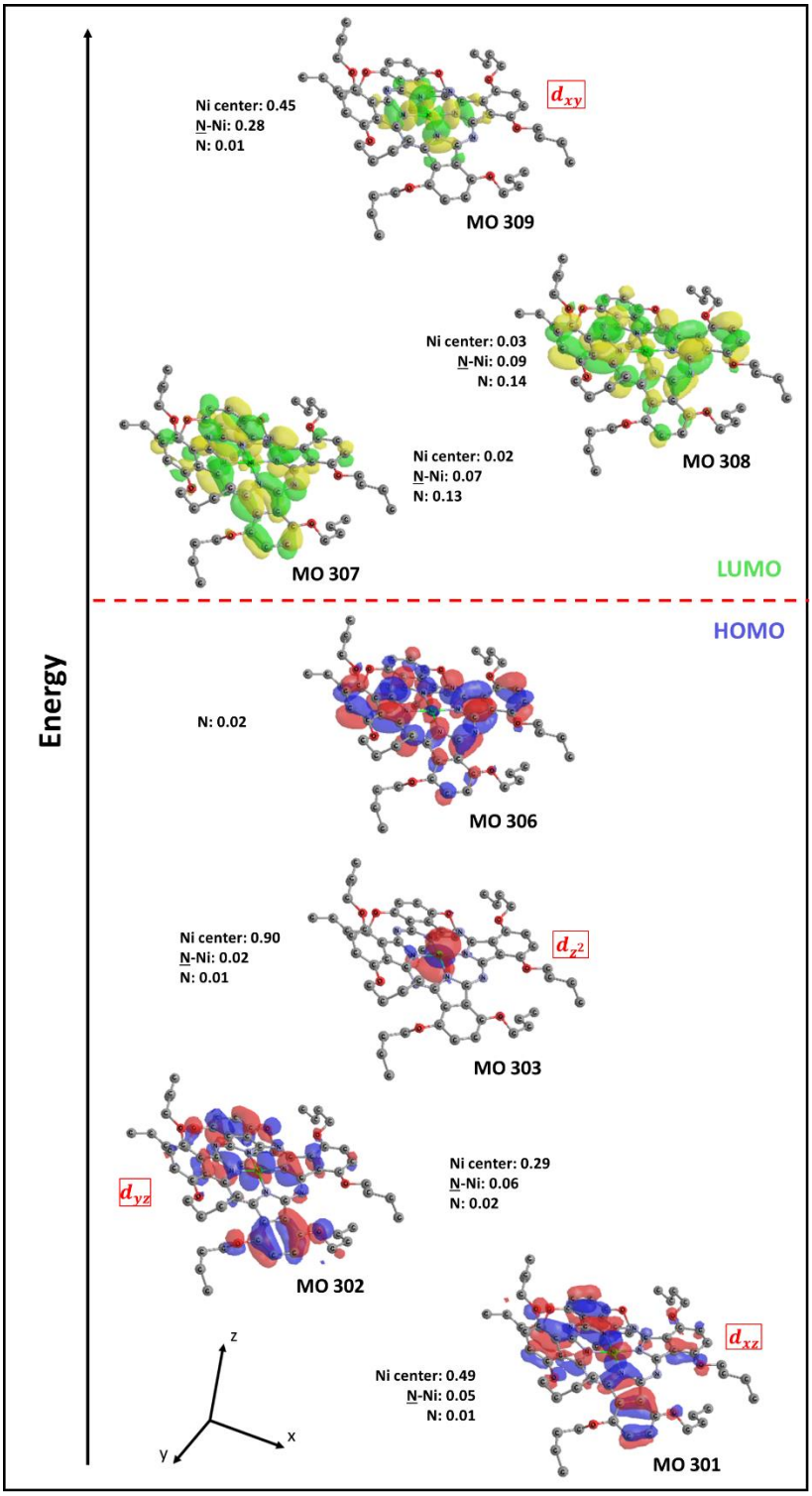

Figure 3.8: Selected molecular orbitals of NiPc in a singlet state calculated at the M06L level of theory with def2-TZVP basis set.

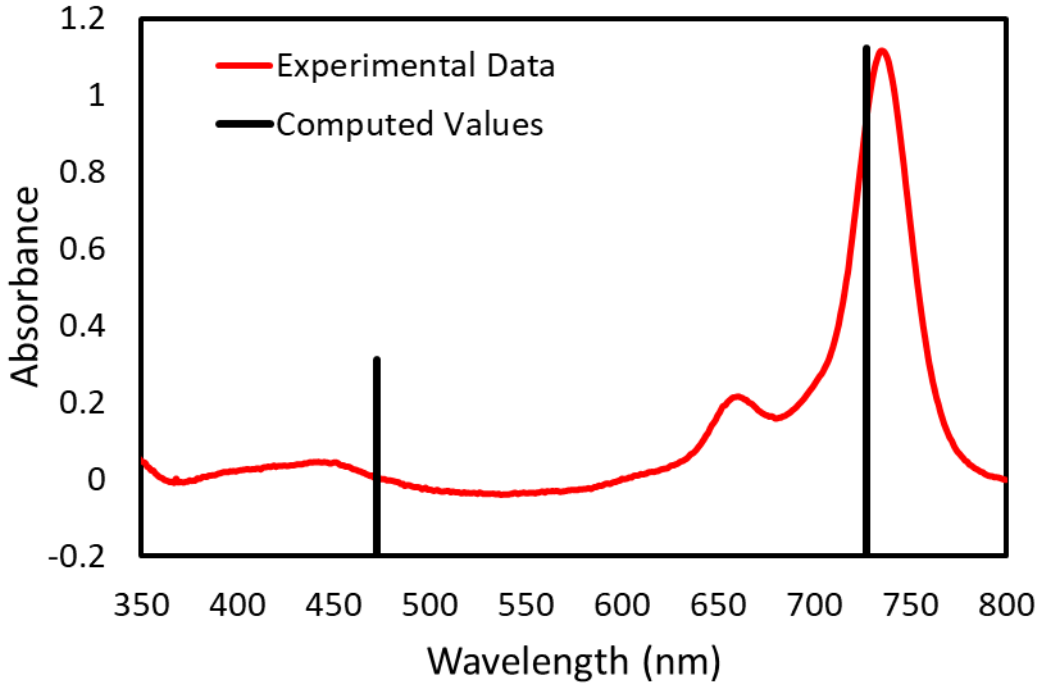

Figure 3.9: UV vis spectrum (red curve) of 0.017mM NiPc in DCM scanned between 800nm and 350nm. Computed values (TD-DFT) for electronic transitions of NiPc at the B3LYP level of theory with def2-TZVP basis set are shown as black lines.

The first two-electron reduction event for **NiPc** at $E_{1/2}$= -1.46V produces **NiPc**$^{2-}$ which could have either a singlet or triplet spin state and, therefore, both were computationally optimized as depicted in Figures 3.10 and 3.11, respectively. The triplet state was slightly favoured (ΔG = -0.89kcal/mol) over the singlet, corresponding to single occupation of the degenerate MOs 307 and 308 of **NiPc**.

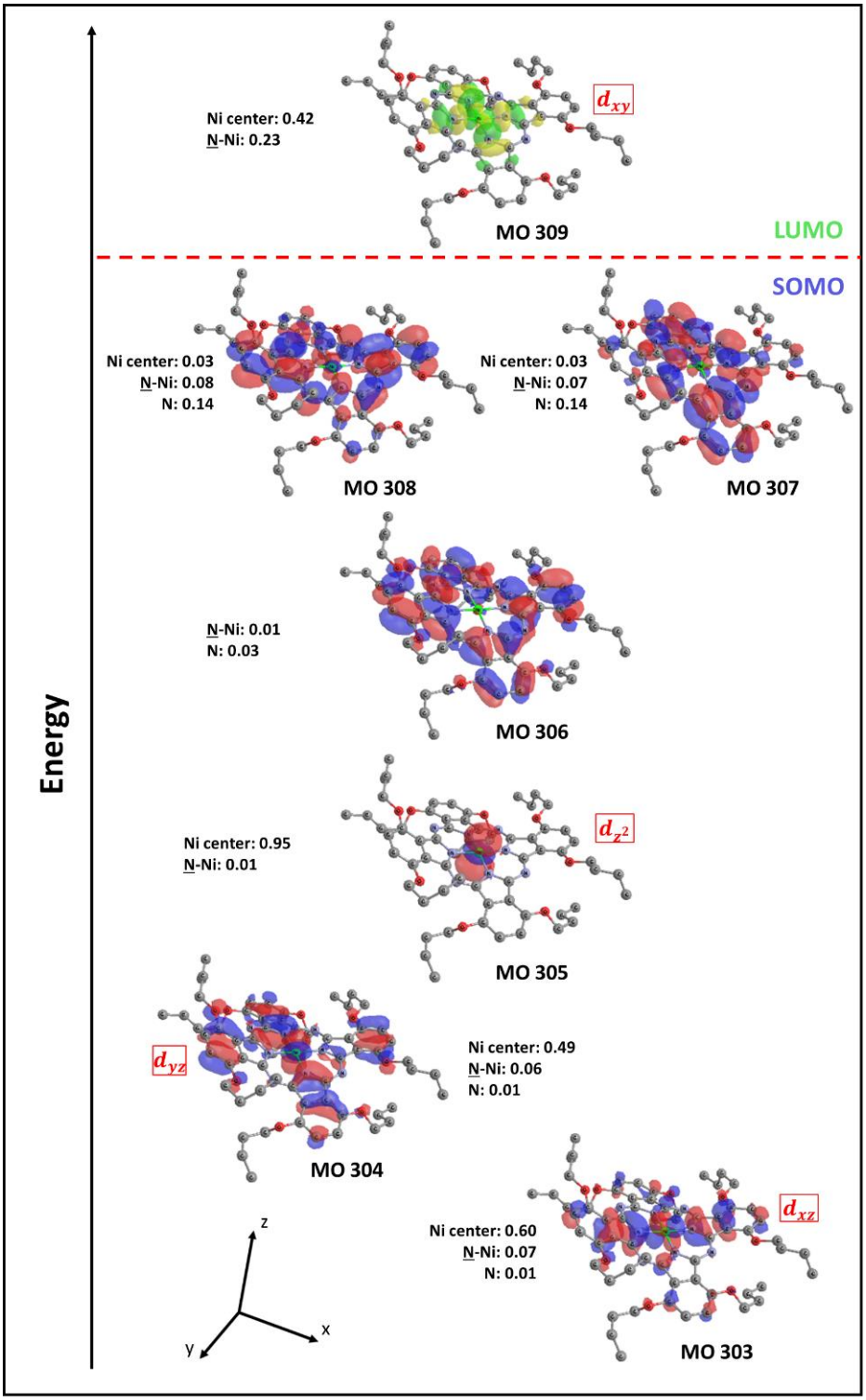

Figure 3.10: Selected molecular orbitals of $NiPc^{2-}$ in a triplet state calculated at the M06L level of theory with def2-TZVP basis set.

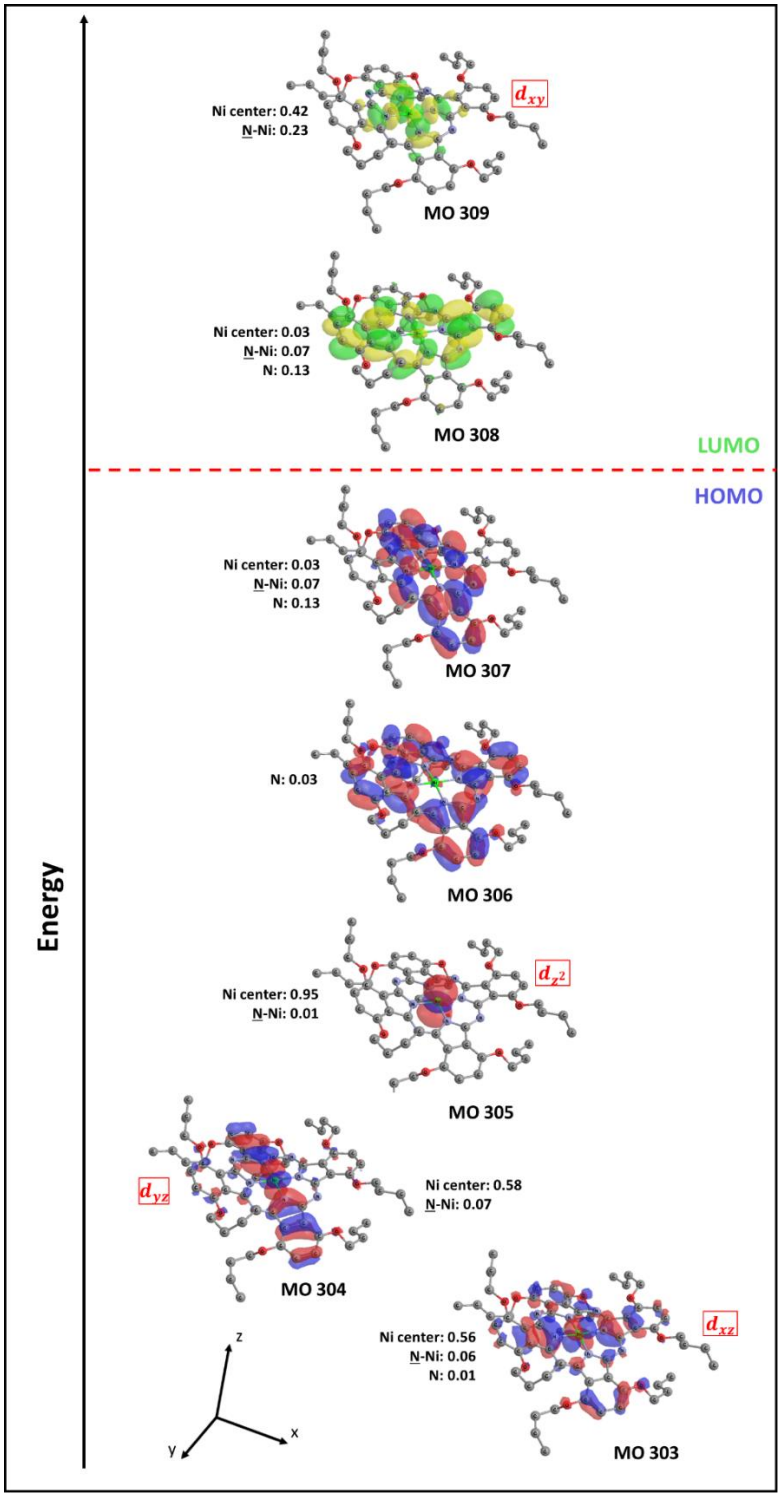

Figure 3.11: Selected molecular orbitals of $NiPc^{2-}$ in a singlet state calculated at the M06L level of theory with def2-TZVP basis set.

Experimental support for this observation was provided by a combination of SEC analysis and TD-DFT calculations that were carried out for the reduction of **NiPc** to **NiPc^{2-}**. During SEC, the major UV-vis absorbance of **NiPc** at 750nm decreased in intensity with cathodic applied potentials beyond -1.17V vs $Fc^{+/0}$. At cathodic potentials beyond the first reduction, between -1.47V and -1.57V, the absorbances for the **NiPc** at 447nm and 750nm further decrease, and three new absorbances at 815nm, 625nm, and 580nm began to appear. Clear isosbestic points were observed at 428nm, 493nm, 690nm, and 800nm, suggesting a clean transition from **NiPc** to **NiPc^{2-}** (Figure 3.12). A comparison of these data with the TD-DFT calculations on **NiPc^{2-}** was most consistent with generation of both singlet and triplet states (Figure 3.13). For example, the absorbances computed for the **NiPc^{2-}** triplet state (615, 640, 784 and 788 nm) correlated with the new absorbances at 625nm and 815nm observed in the SEC data. Furthermore, the new absorbance at 580 nm was supported by a calculated absorbance for singlet state **NiPc^{2-}** at 550 nm as shown in Figure 3.13.

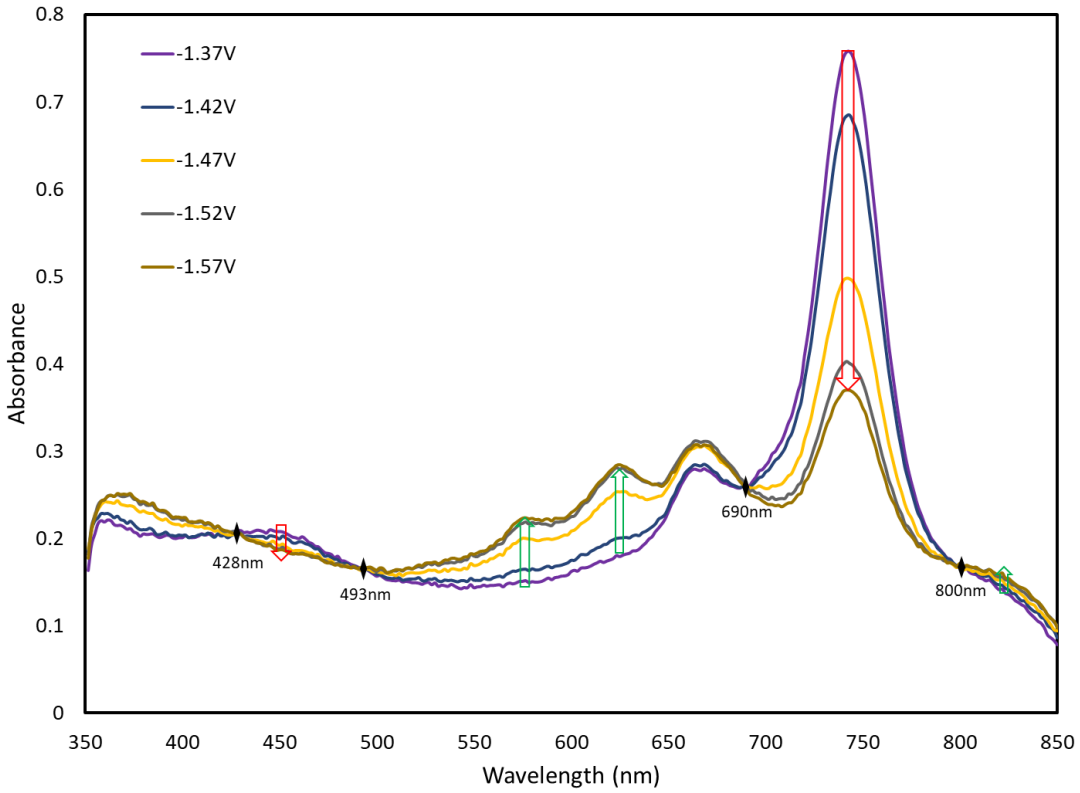

Figure 3.12: UV-vis spectra of 0.017mM NiPc in DCM. Multiple spectra were collected with an applied potential, starting at –1.12V and stepping by 0.05V until -1.62V vs $Fc^{+/0}$. The isosbestic points at 428, 493, 690 and 800 nm are indicated. The increasing (green arrow) and decreasing (red arrow) absorbances are shown.

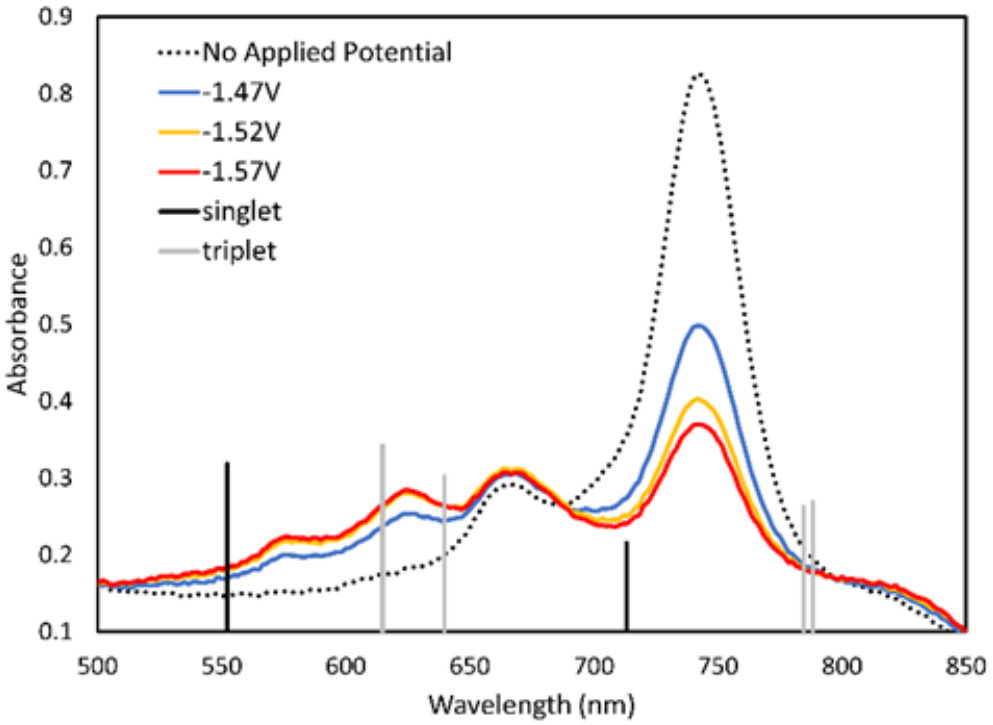

Figure 3.13: SEC analysis of 0.5mM NiPc between -1.47V and -1.57V. The TD-DFT calculated absorbances of $NiPc^{2-}$ singlet state (black lines) and triplet state (gray lines) are shown.

The second reduction event would add two electrons to **$NiPc^{2-}$**, filling the degenerate ligand-based orbitals, and generating singlet **$NiPc^{4-}$**. The results of the computational analysis of this compound and selected frontier orbitals are summarized in Fig. 3.14. The degenerate HOMOs of **$NiPc^{4-}$** are comprised of the p-orbitals on the Pc ligand. The LUMO contains σ^* interactions of the ligand with the Ni centre, with 37% contribution coming from the $d_{x^2-y^2}$ orbital.

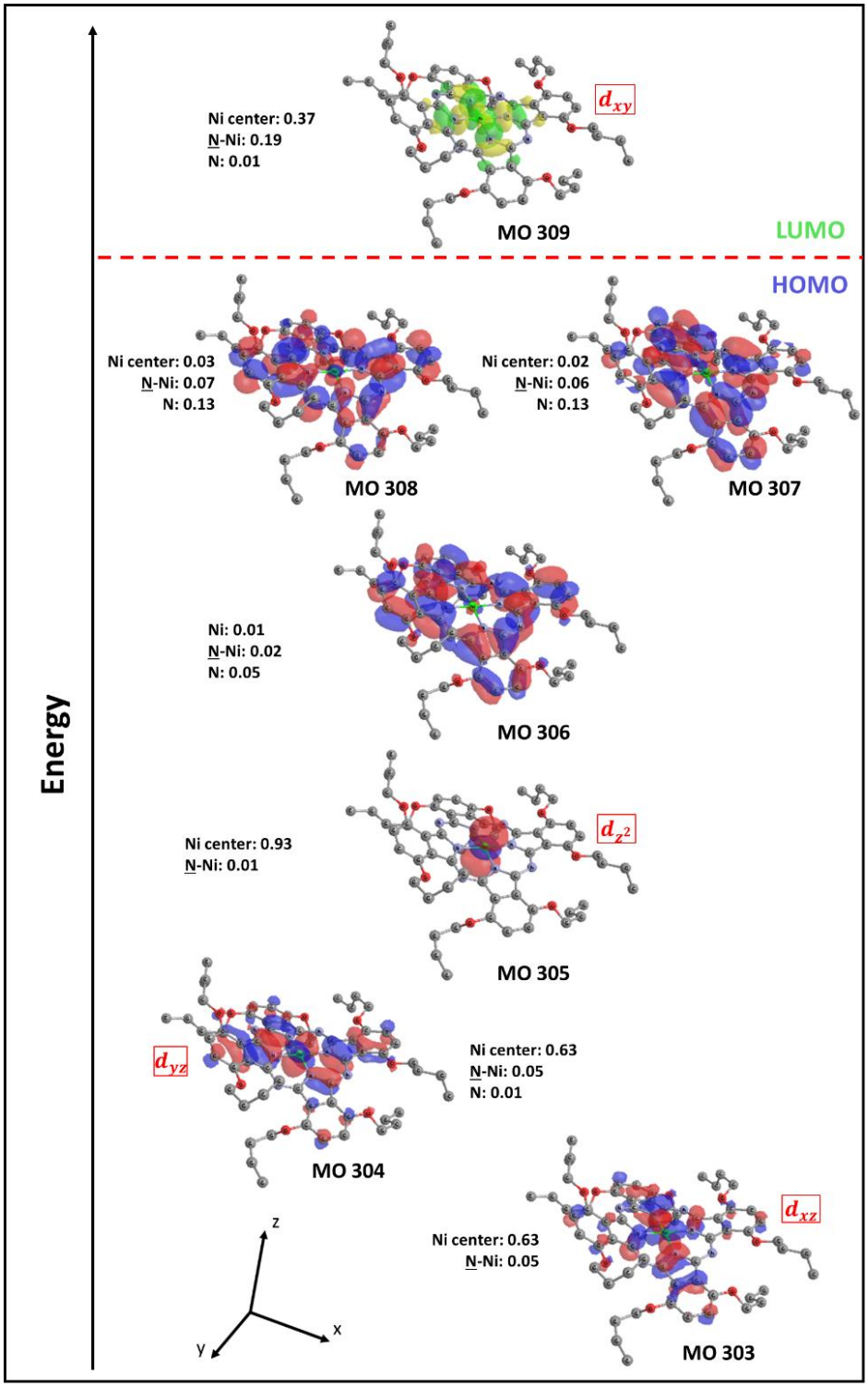

Figure 3.14: Selected molecular orbitals of $NiPc^{4-}$ in a singlet state calculated at the M06L level of theory with def2-TZVP basis set.

Catalytic studies for water reduction and hydrogen evolution were performed in tetrahydrofuran (THF) solution due to significant miscibility limitations between water and DCM. CVs of the parent, **NiPc**, displayed identical redox potentials as those observed in dichloromethane (Figure 3.15). CVs and bulk electrolysis experiments were performed to examine the effect of increased water concentration and to quantify hydrogen production. Investigations into the effect of pH on proton reduction catalysis were completed by repeating the CVs and bulk electrolysis at different concentrations of triethylamine (TEA) as a means of varying the pH to examine the functionality of the catalyst in different pH regions. CVs were recorded in cathodic sweeps between -1.14V and -2.4V vs $Fc^{+/0}$.

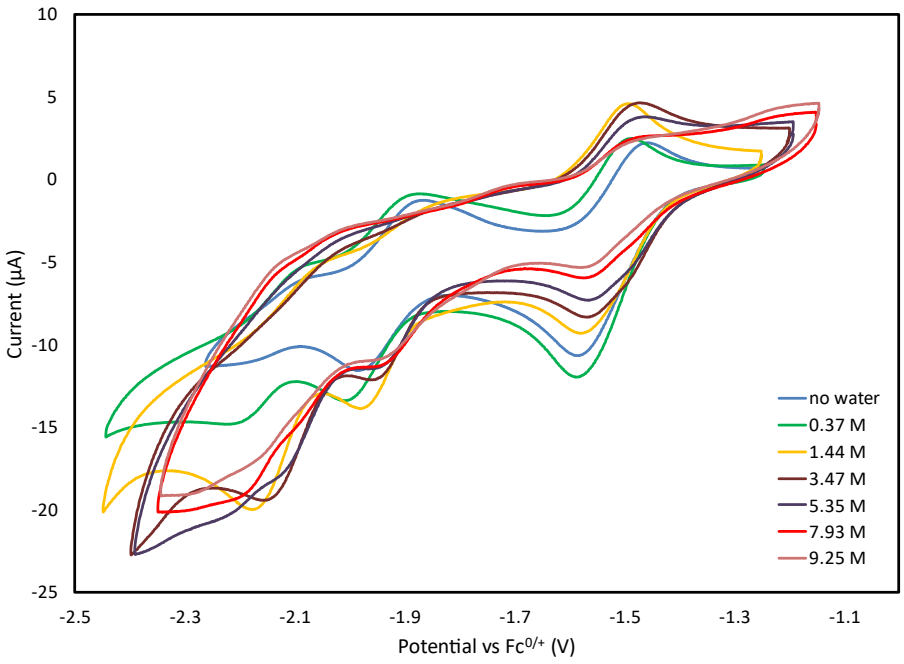

Figure 3.15: The effect of added water on the CVs of 0.5mM NiPc in THF with 0.1M electrolyte (TBAHFP). The CVs was scanned between -1.1V and -2.45V with increased water concentration as shown in the legend.

Signatures for catalysis were observed by enhanced current at the second redox event, splitting the event into sequential reductions, and elimination of the return oxidation (Figure 3.15). Water additions were further performed with TEA concentrations of 0.05M and 0.2M (Figures 3.16, 3.17). No current enhancements were observed when similar electrochemical measurements were performed with free Pc ligand, thus demonstrating the necessity of the nickel metal centre (Figure 3.18).

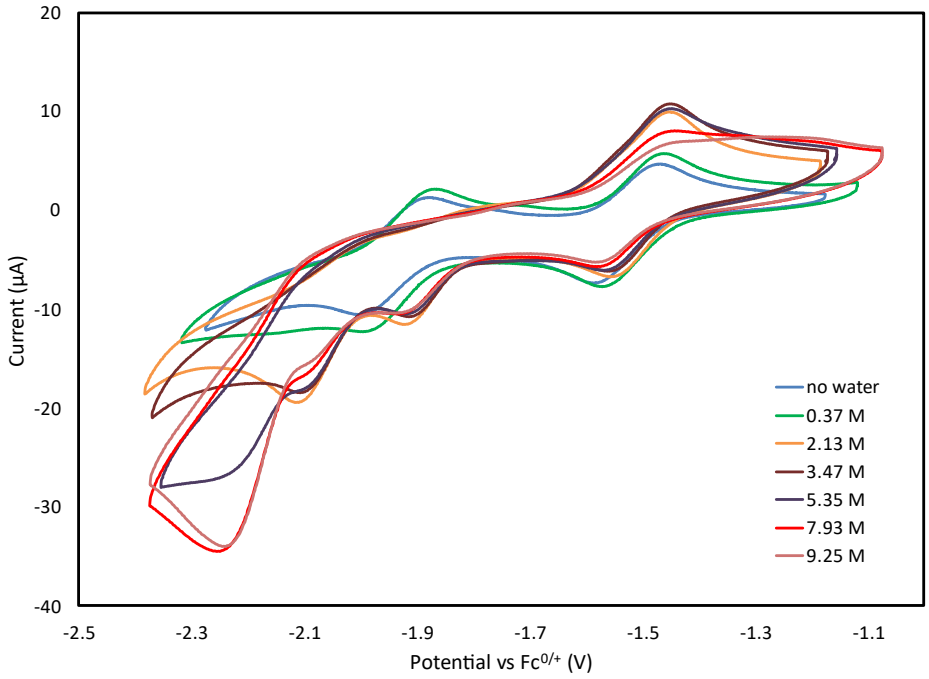

Figure 3.16: The effect of added water on the CVs of 0.5mM NiPc in THF with 0.1M electrolyte (TBAHFP) and 0.05M TEA. The CV was scanned between -1.1V and -2.45V with increased water concentration as shown in the legend.

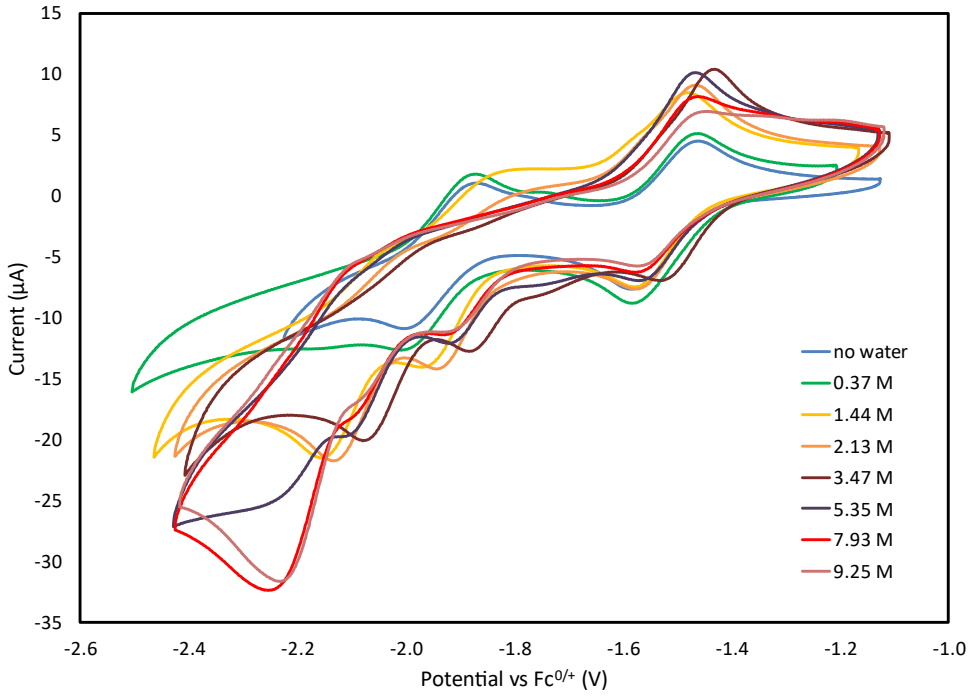

Figure 3.17: The effects of added water on CVs of 0.5mM NiPc in THF with 0.1M electrolyte (TBAHFP) and 0.2M TEA. The CV was scanned between -1.1V and -2.45V with increased water concentration as shown in the legend.

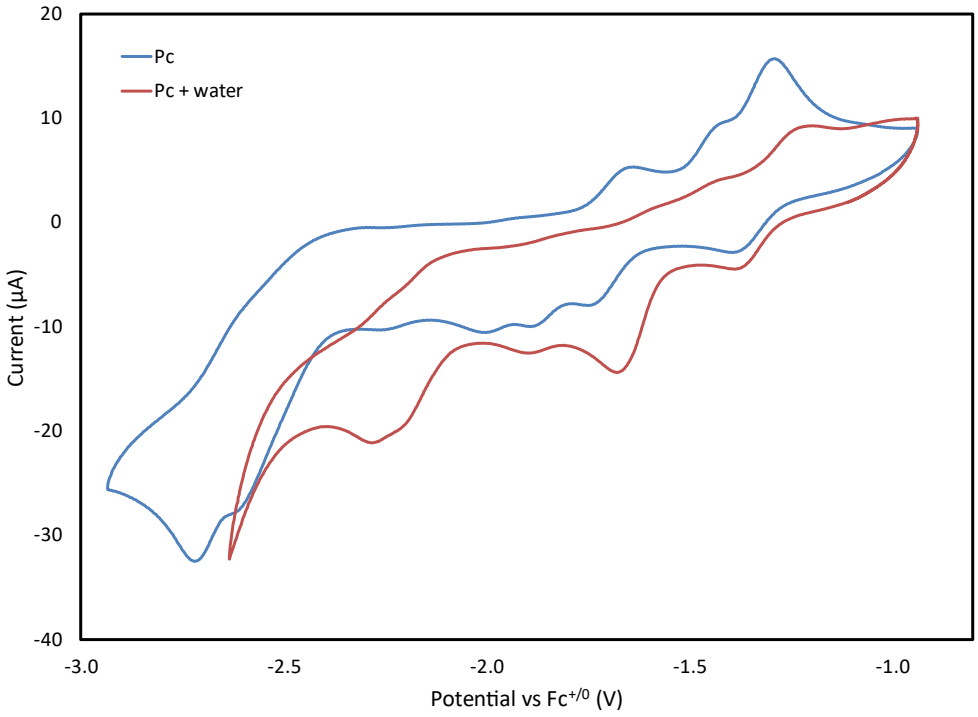

Figure 3.18: CV of 0.5mM Pc ligand in THF scanned between -1.1V and -2.9V (blue curve). The red curve shows the same sample with added [H_2O] of 9.25M scanned from -1.1V to -2.6V.

Homogeneous catalytic activity was supported by a dip test showing the elimination of catalytic enhancement when the electrode was rinsed with THF and placed in a new solution in the absence of **NiPc** (Figure 3.19). Additionally, scan rate dependence studies were performed under a catalytic environment that demonstrated a linear relationship between the square root of the scan rate and the current at the inflection point as expected for a diffusion-controlled process (Figures 3.20, 3.21).

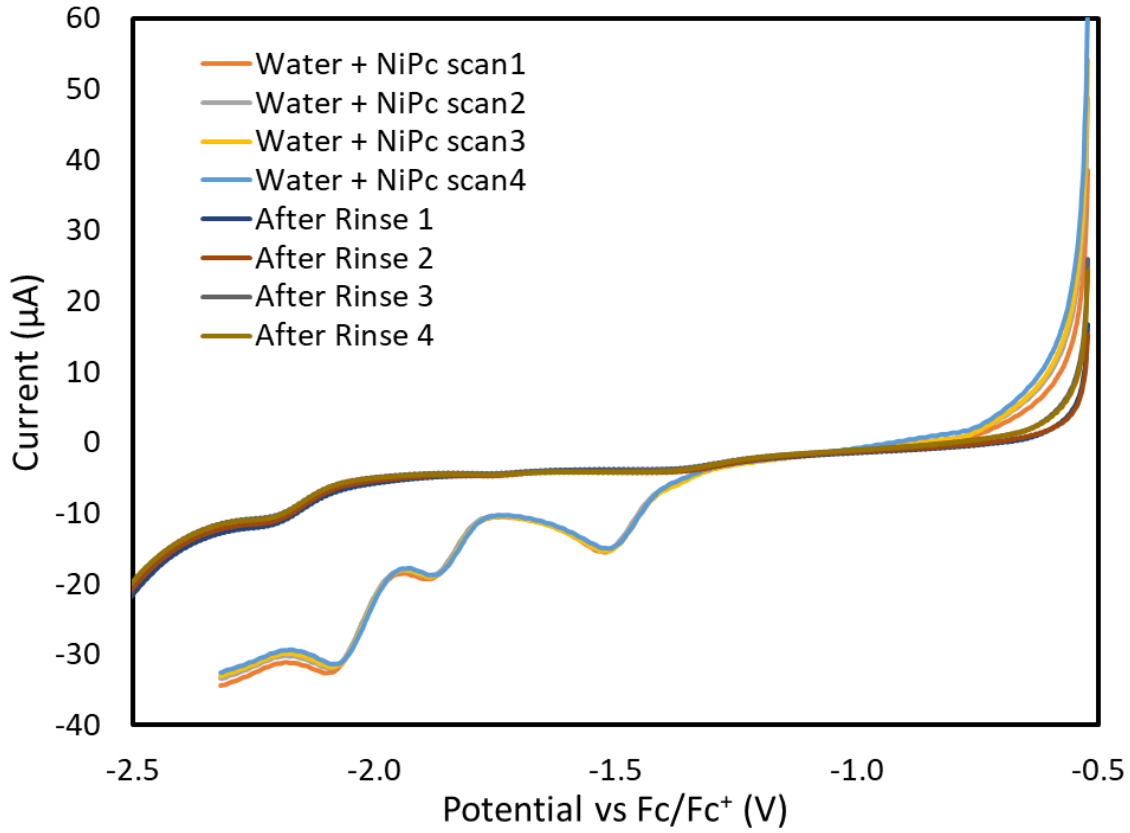

Figure 3.19: Linear sweep voltammograms of 0.5mM NiPc in THF with a water concentration of 6.53M before and after solvent rinse. Scans performed from -0.5V to -2.3V volts before rinse and -0.5V to -2.5V after rinse.

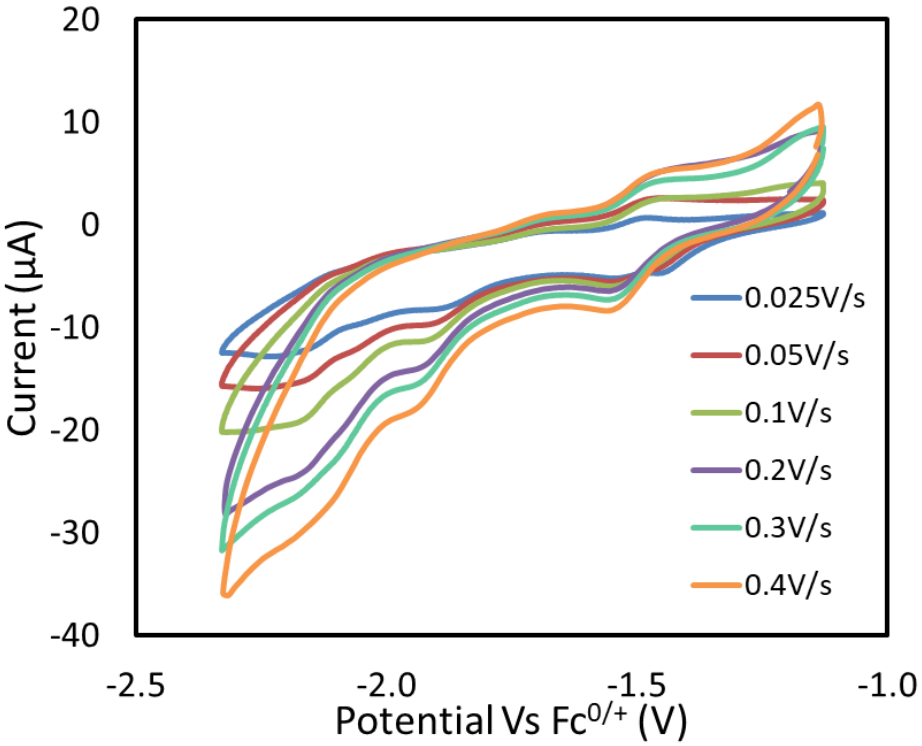

Figure 3.20: CV of 0.5mM NiPc in THF scanned between -1.15V and -2.35V with a varying scan rate and electrolyte (TBAHFP) concentration of 0.1M and water concentration of 9.25M.

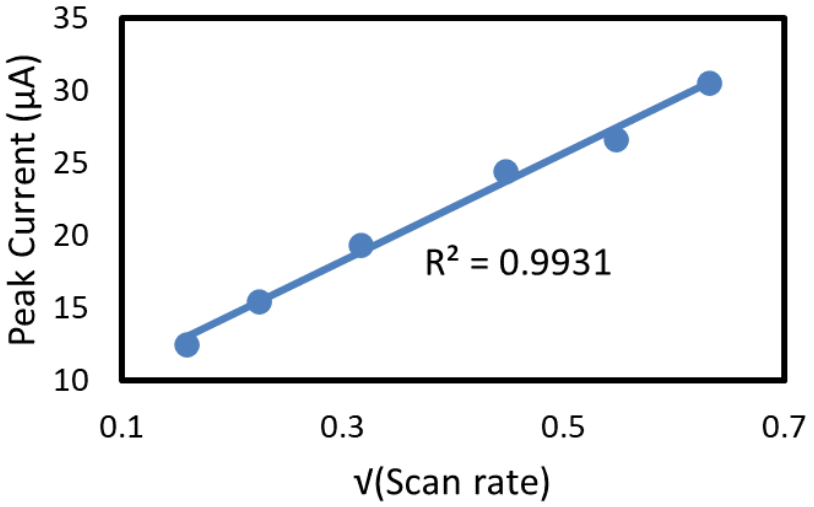

Figure 3.21: Plot of the reduction peak current value from Figure 3.20 as a function of the square root of the scan rate at the catalytic redox event (-2.1V vs $Fc^{+/0}$).

Kinetic evaluation for the catalytic activity of **NiPc** was performed through a foot-of-the-wave analysis (FOWA) with the same TEA concentrations as the bulk electrolysis experiments and this allowed evaluation of the turnover frequency (TOF) under these conditions.[25,26] The pertinent graphical analyses used to establish TOFs for **NiPc** at TEA concentrations of 0M, 0.05M, and 0.2M are displayed in Figures 3.22, 3.23, and 3.24, respectively.

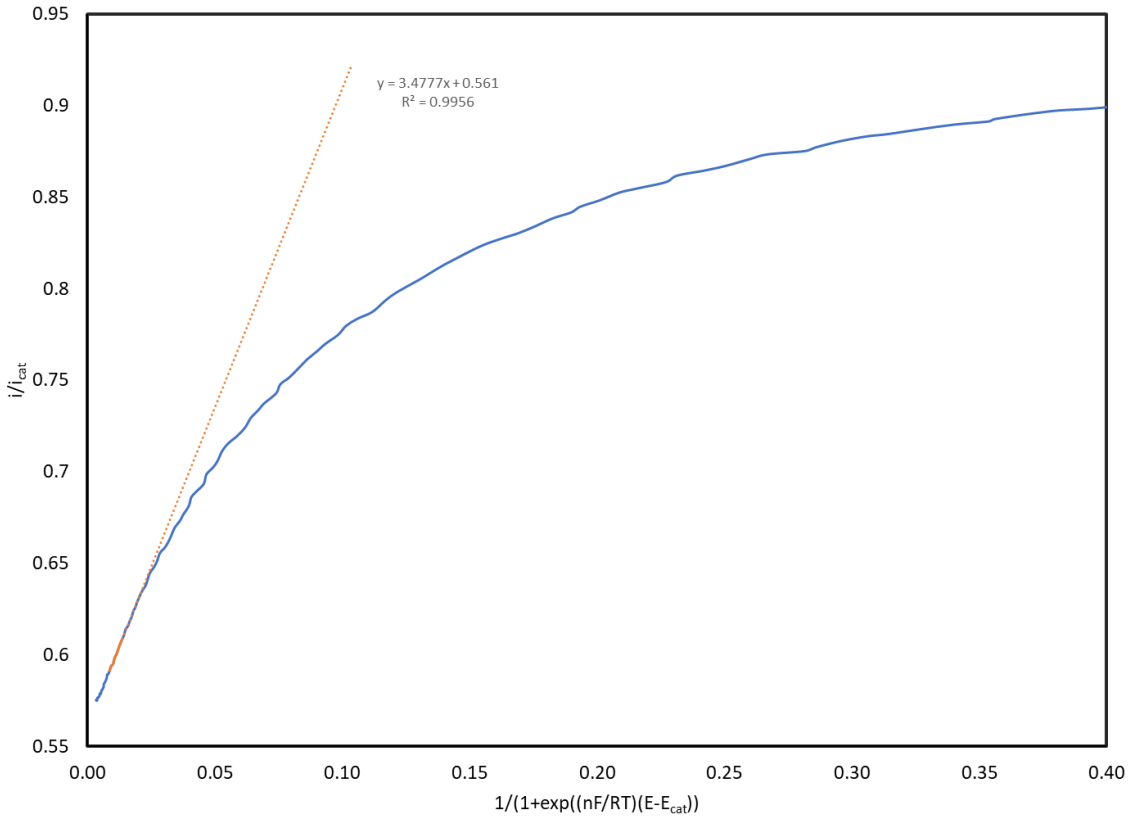

Figure 3.22: FOWA for NiPc with no added TEA. The orange line represents the slope, given by 2.24v $RT(TOF)\ n'Fv$ with n' = 2 for the reduction of water to H_2. The equation for the line is given in the figure.

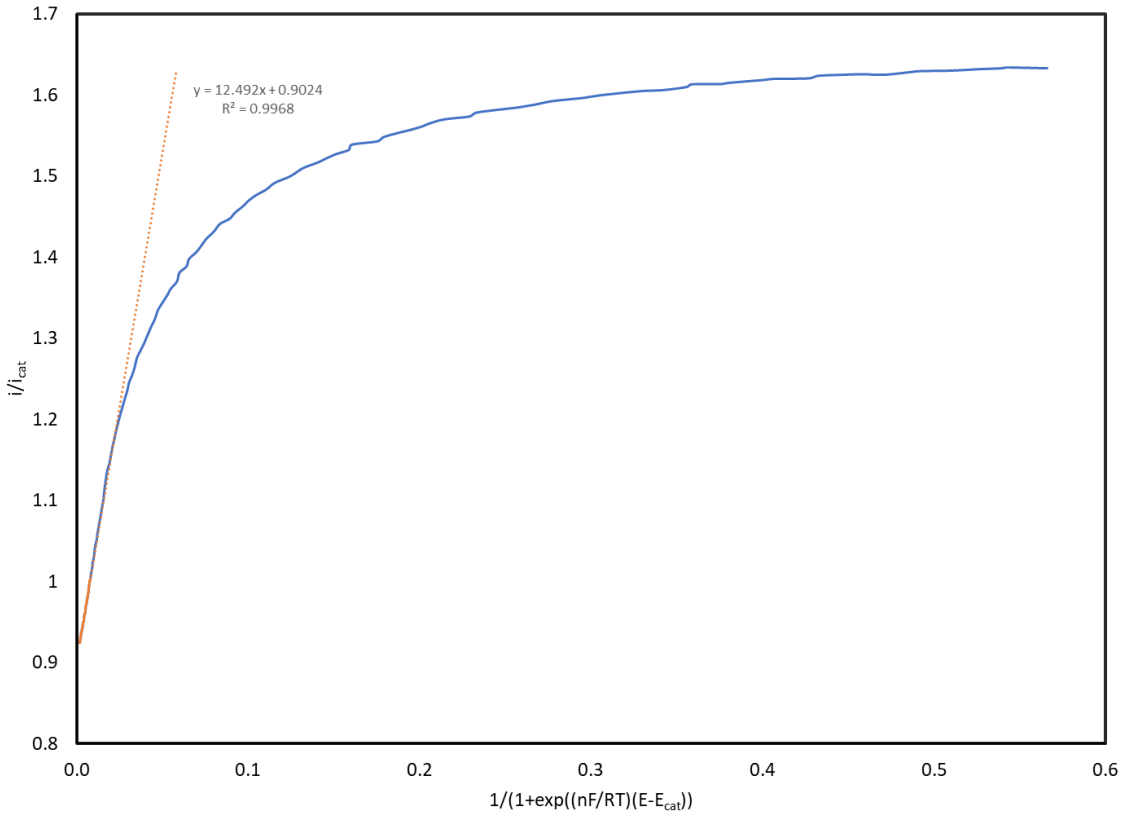

Figure 3.23: FOWA for NiPc with a TEA concentration of 0.05M. The orange line represents the slope, given by 2.24V $\frac{RT}{(TOF)\,n'Fv}$ with n' = 2 for the reduction of water to H_2. The equation for the line is given in the figure.

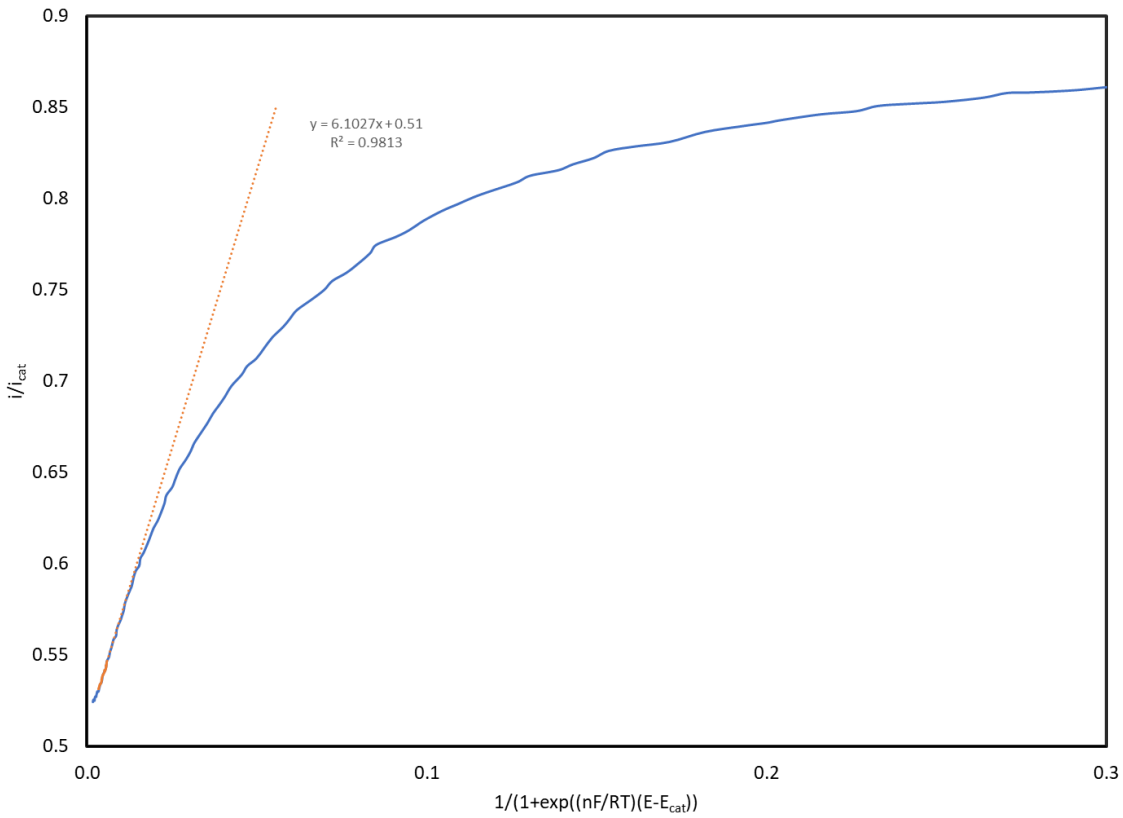

Figure 3.24: FOWA for NiPc with a TEA concentration of 0.2M. The orange line represents the slope, given by 2.24v $RT(TOF)\ n'Fv$ with n' = 2 for the reduction of water to H_2. The equation for the line is given in the figure.

Similar, to the bulk electrolysis, catalysis with no added TEA gave the lowest TOF of 4.7 s^{-1}. With 0.2M and 0.05M added TEA, TOFs of 14.4 s^{-1} and 60.5 s^{-1} were obtained. These results demonstrate the important interplay between the reactivity and stability that can occur through perturbation of pH. Increasing the alkalinity of the environment improves the stability and reactivity of the catalyst initially, but eventually hinders the catalytic activity with additional TEA. This relationship was further supported by the amount of H_2

generated (Table 3.1) in the bulk experiments, the 0.05M TEA environment generated 13.61µmol versus the 0.2M environment, which produced 7.92µmol of H_2.

Table 3.1: Results for bulk 2-hour electrolysis experiments performed at -2.15V vs $Fc^{+/0}$.

Trial [TEA]	Electrons Passed (mol)	H_2 generated (mol)	FE*
0M	17.29	6.01	69%
0.05M	37.73	13.61	72%
0.2M	17.84	7.92	89%

*FE was calculated by dividing the total moles of H_2 produced (quantified by GC-TCD) by the theoretical H_2. Theoretical H_2 was derived from the total charge collected in the bulk electrolysis and then corrected by subtracting 3 electrons associated with priming **NiPc** that are not involved in the catalysis.

Increased catalytic activity in the presence of a base (i.e. TEA) is unusual, since more acidic protons require a lower potential to reduce.[27] The presence of TEA at low concentrations likely scrubs the proton from the protonated bi-N site, allowing the sequential PCET steps to occur that are required for H_2 production. Increased concentration of TEA eventually succumbs to the trend of a higher required overpotential for proton reduction in more alkaline environments. As shown in Table 3.1, bulk electrolysis experiments gave improved catalysis in the presence of TEA. Similarly, FE values were 69%, 72%, and 89% with increasing TEA concentration, performed with 2-hour run times.

To interrogate the mechanistic aspects of catalytic water reduction by **NiPc** several SEC experiments, supplemented with DFT analysis, were carried out. These experiments were performed to identify the nature of the compounds that are

formed following multiple reductions and protonation steps. These data help elucidate the overall functionality of **NiPc** and the role of the potential protonation sites.[28] SEC investigations were performed in THF with an added water concentration of 9.25M (Figure 3.25).

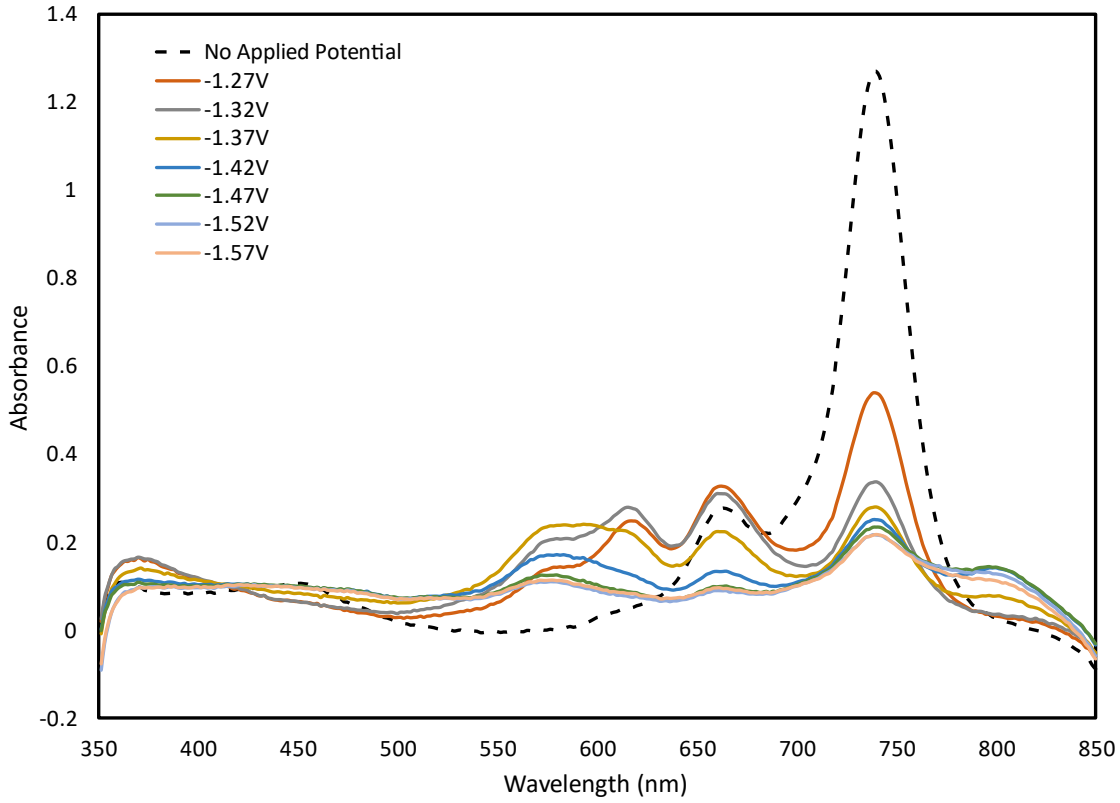

Figure 3.25: UV-vis spectra of 0.017mM NiPc in THF with a water concentration of 9.25M. Multiple spectra were collected with an applied potential, starting at -1.27V and stepping by 0.05V until -1.57V vs $Fc^{+/0}$.

The experiment was carried out with stepped potentials spanning the first reduction event. Importantly, the isosbestic points identified in the absence of water (Figure 3.12) were no longer present in these spectra (Figure 3.25) indicating that a simple reduction from **NiPc** to **$NiPc^{2-}$** no longer occurred when water was

present. A new absorption peak is observed in the presence of water (Figure 3.26) at 595nm when the stepped potentials are at values of -1.37V and -1.42V, that was not observed during the anhydrous studies. TD-DFT calculations support the assignment of this peak to a singly reduced and singly protonated **NiPc-H** species (absorbance peak at 629nm) and further support the existence of **NiPc-H** occurring in a narrow potential range. These SEC observations fit well with the scan rate dependence investigation (Figure 3.7) observed at the first redox event where two distinct reduction events appeared at scan rates below 0.1V/s. The overlapping of these sequential reduction events suggest that after **NiPc-H** is generated, a rapid PCET occurs, generating **NiPc-H_2**.

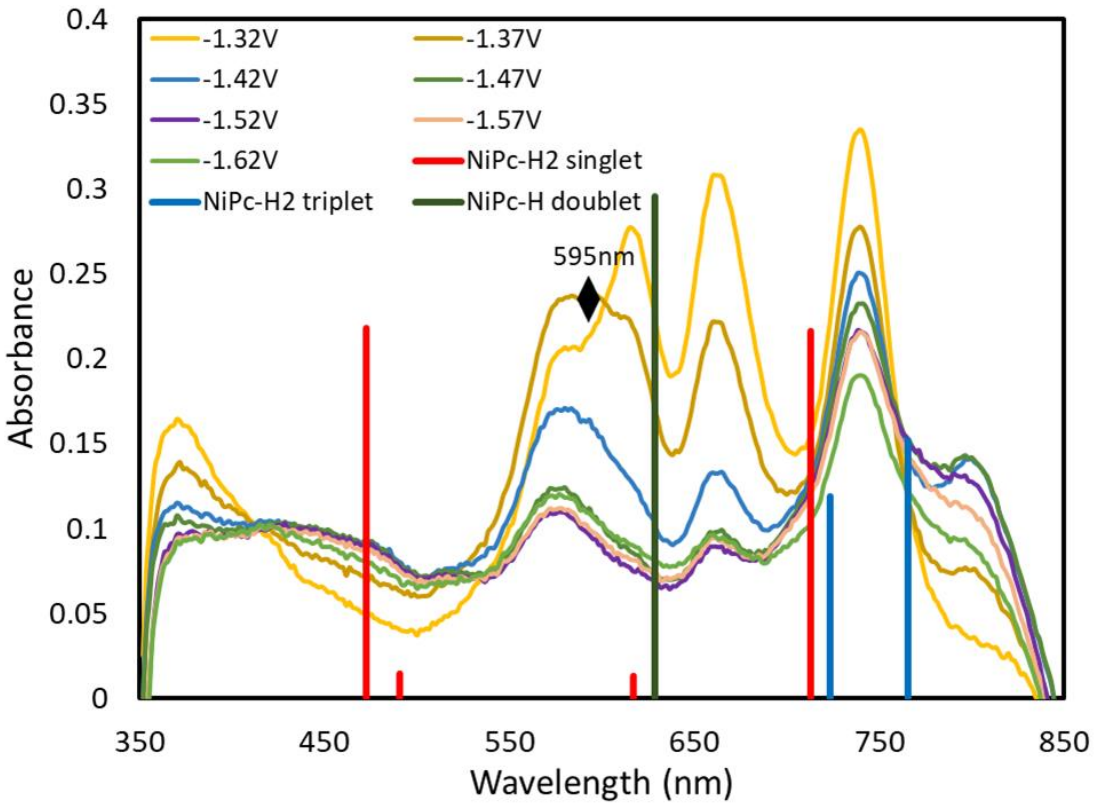

Figure 3.26: UV-vis spectra of 0.017mM NiPc in THF with a water concentration of 9.25M. Multiple spectra were collected with an applied potential, starting at -1.32V and stepping by 0.05V until -1.62V vs $Fc^{+/0}$. DFT simulation of the singlet and triplet states for NiPc-H_2 and NiPc-H doublet are included at the B3LYP level of theory and def2-TZVP basis set.

Further investigations into the pH sensitivity among the possible protonation sites of **NiPc** were performed by obtaining CVs and UV-vis absorbance spectra in the presence of acetic acid (AA) or trifluoroacetic acid (TFA). Additions of AA to **NiPc** followed by a cathodic sweep (Figure 3.27) showed a separation of the first reduction event ($E_{1/2}$ = -1.46V) into two reduction events and loss of the corresponding return oxidation peak. The onset potential of the CV obtained in the

presence of acid was shifted to a less negative potential by 150mV, suggesting that ligand protonation occurs before reduction and disappearance of the return oxidation supports a chemical step. The addition of acid to **NiPc** also caused a colour change in the solution, from green to purple. This colour change was investigated using UV-vis spectroscopy in the presence of TFA. Importantly, the addition of TFA to CV measurements of **NiPc** produced very similar observations, as shown in Figure 3.28. These data were then compared to DFT calculations for **NiPc** protonated at the coor-N site (**NiPc-H$^+$**). Figure 3.29 documents the close correspondence for the calculated **NiPc-H$^+$** electronic transitions and the experimental data.

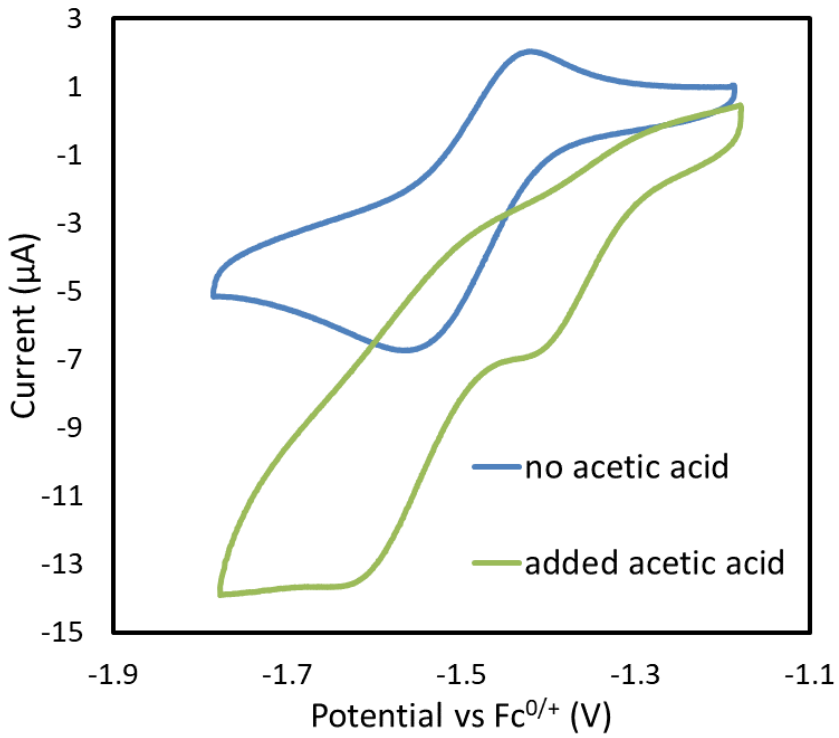

Figure 3.27: CV of 0.5mM NiPc in DCM scanned between -1.18V and -1.77V (blue curve). A similar CV with an added acetic acid concentration of 0.13M (green curve).

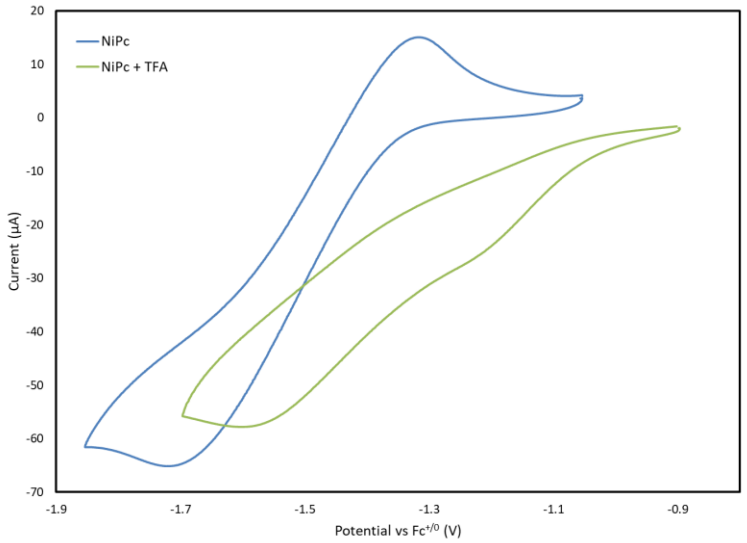

Figure 3.28: CV of 0.5mM NiPc in THF (blue curve) and a similar CV with an added trifluoroacetic acid (TFA) at 20mM concentration (green curve).

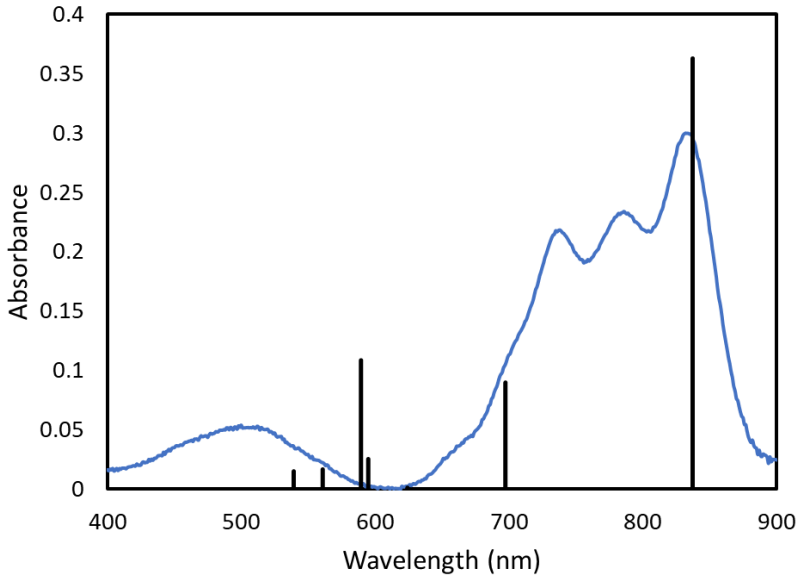

Figure 3.29: Absorbance spectrum of 0.017mM NiPc in DCM scanned between 800nm and 400nm with addition of 1eq of TFA. The TD-DFT calculated values for the electronic transitions of NiPc-H^+ at the B3LYP level of theory with def2-TZVP basis set are shown as black lines at 838, 687, and 589nm.

DFT structural optimization of **NiPc-H$^+$** demonstrated an interesting increase in the angle between the isoindole plane and the plane containing the four coor-N and nickel. The parent **NiPc** species showed a slight out-of-plane alignment of these groups with an angle of 16.5° which increased to 36.4° upon protonation (Figures 3.30, 3.31). Protonation of the coor-N site partially releases it from Ni(II) coordination and allows the isoindole plane to rotate to reduce steric interactions. Addition of TEA immediately reverses the transformation, scrubbing off the proton and regenerating the green **NiPc** complex.[29] Isosurface plots for the MOs of **NiPc-H$^+$** are shown in Figure 3.32. The degeneracy of the LUMO^{-1} and LUMO^{-2} orbitals (MO307 and MO308 in Figure 3.8) for **NiPc** is removed following the protonation, due to the symmetry disruption of the nearly identical orthogonal MOs.

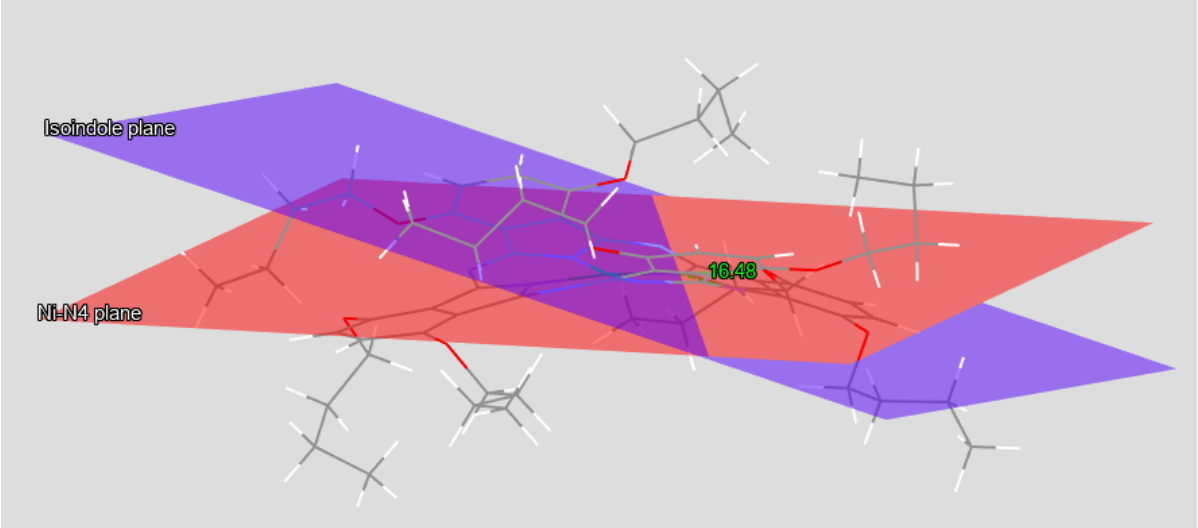

Figure 3.30: Wire plot of NiPc calculated with the M06L functional and the def2-SVP basis set. The Isoindole plane is defined as the planar surface that contains all atoms in the selected isoindole group. The Ni-N4 plane intersects with the Isoindole plane at the coordinated nitrogen atom containing the four coordinated nitrogen and the nickel metal center.

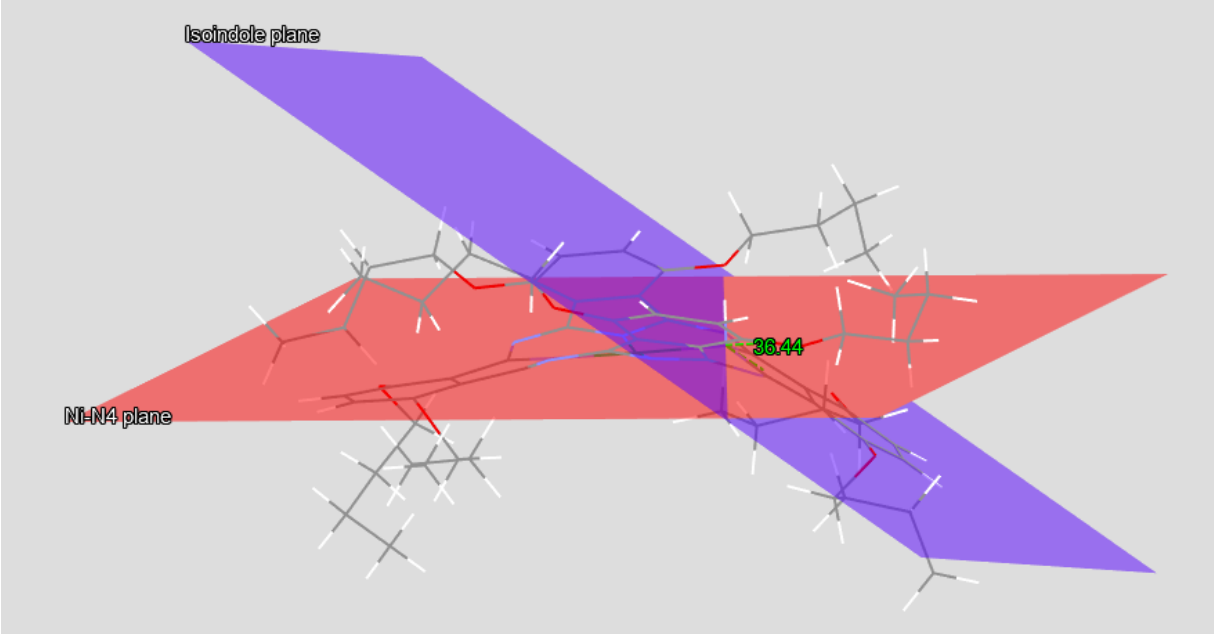

Figure 3.31: Wire plot of NiPc protonated on a coor-N center (NiPc-H$^+$); simulation calculated with the M06L functional and the def2-SVP basis set. The Isoindole plane and Ni-N4 plane are defined in the same way as figure 26, centered at the protonated Coor-N.

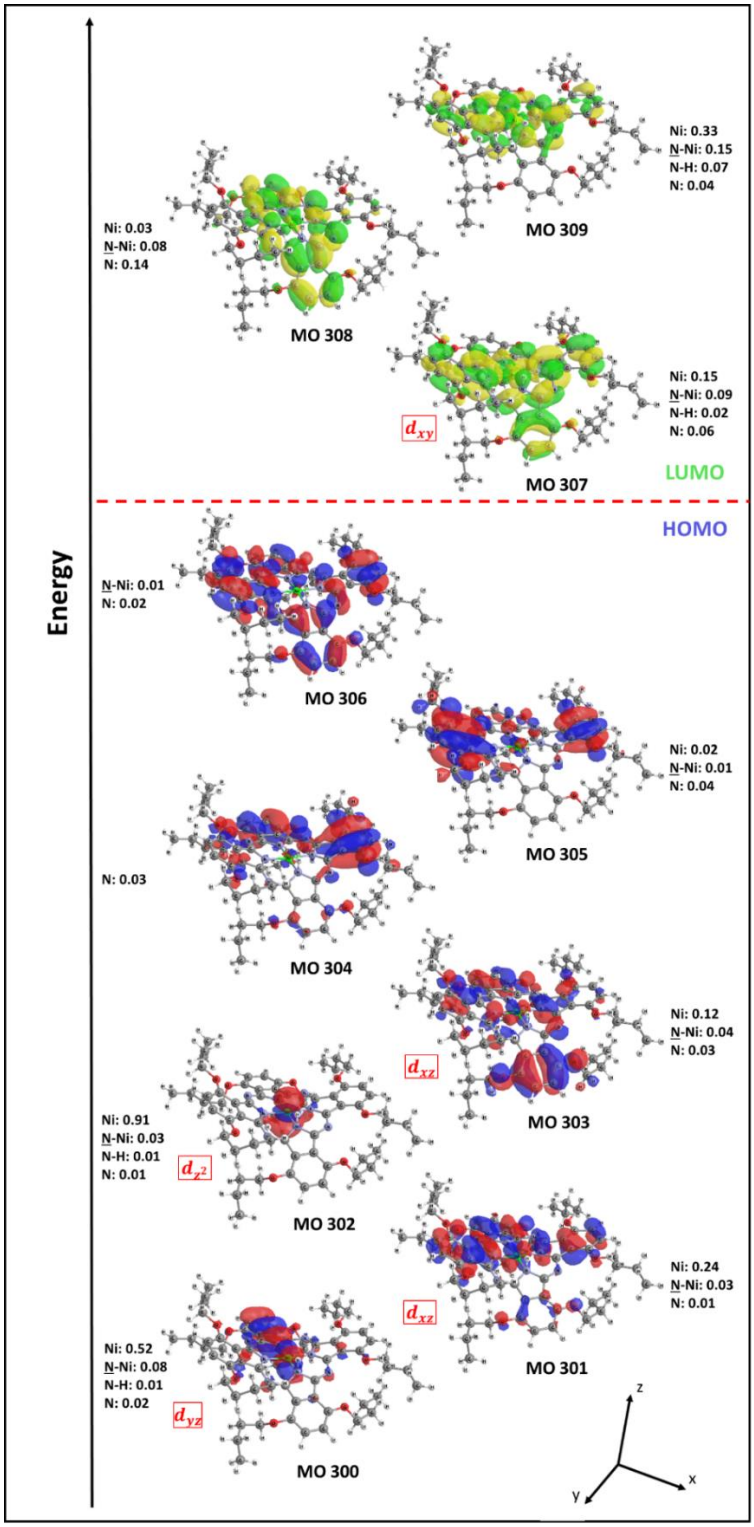

Figure 3.32: Selected molecular orbitals of NiPc-H⁺ in a doublet state computed at the M06L level of theory with def2-TZVP basis set.

Details of the electrocatalytic water reduction mechanism were revealed through experimental data and DFT simulation. Most proton reduction investigations suggest a metal-centred approach for hydrogen generation occurring through a metal hydride intermediate; this work proposes a ligand centred mechanism.[9] The presence of water during the cathodic sweep supplies a proton source to **NiPc**, pairing two protonation steps with the concerted dual reduction of the complex that places the bulk of the electron density on the ligand. This added charge increases the likelihood of protonation occurring at the bi-N sites, generating a species containing two protonated bi-N sites (**NiPc-H_2**) beyond a reduction potential of -1.5V. Continuing with the cathodic sweep observed in Figure 3.33, water concentrations starting between 0.73M and 3.47M result in two consecutive irreversible reduction events that are associated with two more PCET steps at the two remaining unprotonated bi-N sites, all curves in this concentration region contain the same events as the orange curve in Figure 3.33.

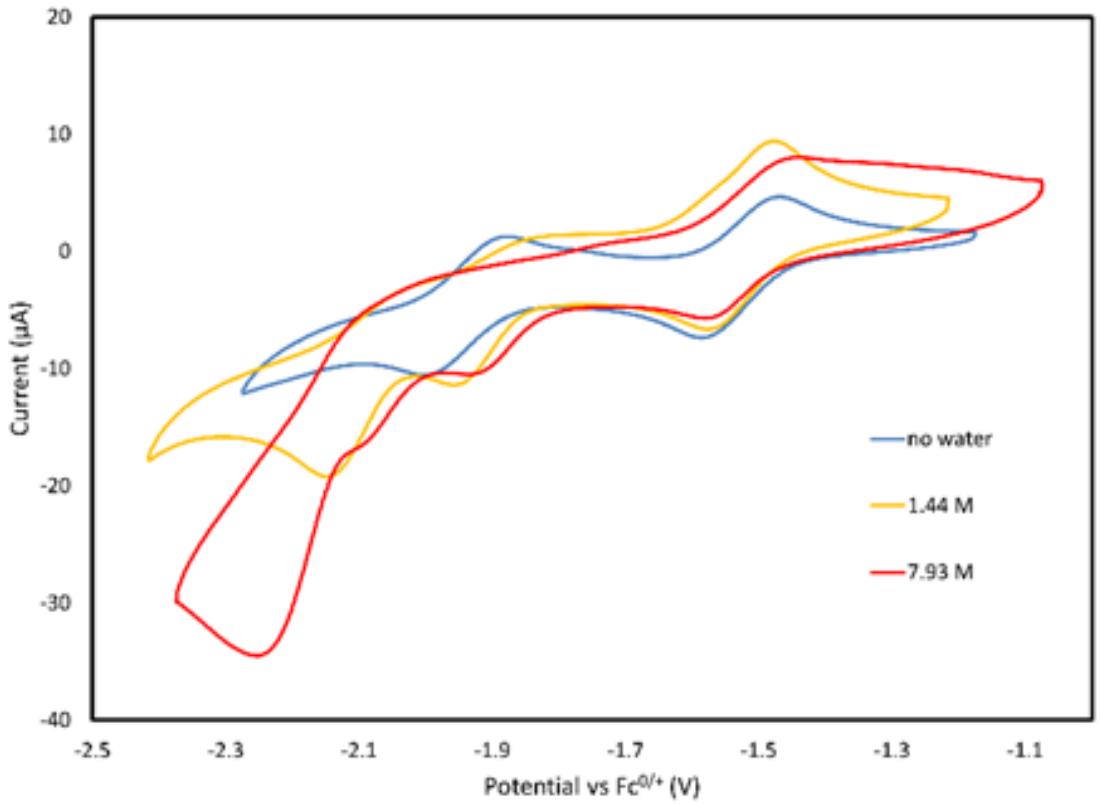

Figure 3.33: CV of 0.5mM NiPc in the presence of different concentrations of water at a scan rate of 0.1V/s with electrolyte (TBAHFP) concentration of 0.1M.

Beyond a concentration of 3.47M an additional event begins to develop at -2.17V (red curve in Figure 3.33), it increases until a saturation point at a water concentration of 7.10M. This event is associated with protonation at the coor-N site, preceding another reduction. Protonation at the coor-N site causes the isoindole unit to bend out of the plane (Figure 3.31), bringing the protonated coor-N site nearer to the protonated bi-N site, generating hydrogen in a ligand-centred manner, as illustrated in Figure 3.34.[30–32] Overall, **NiPc** undergoes 5 consecutive PCET events, leading to the evolution of H_2.

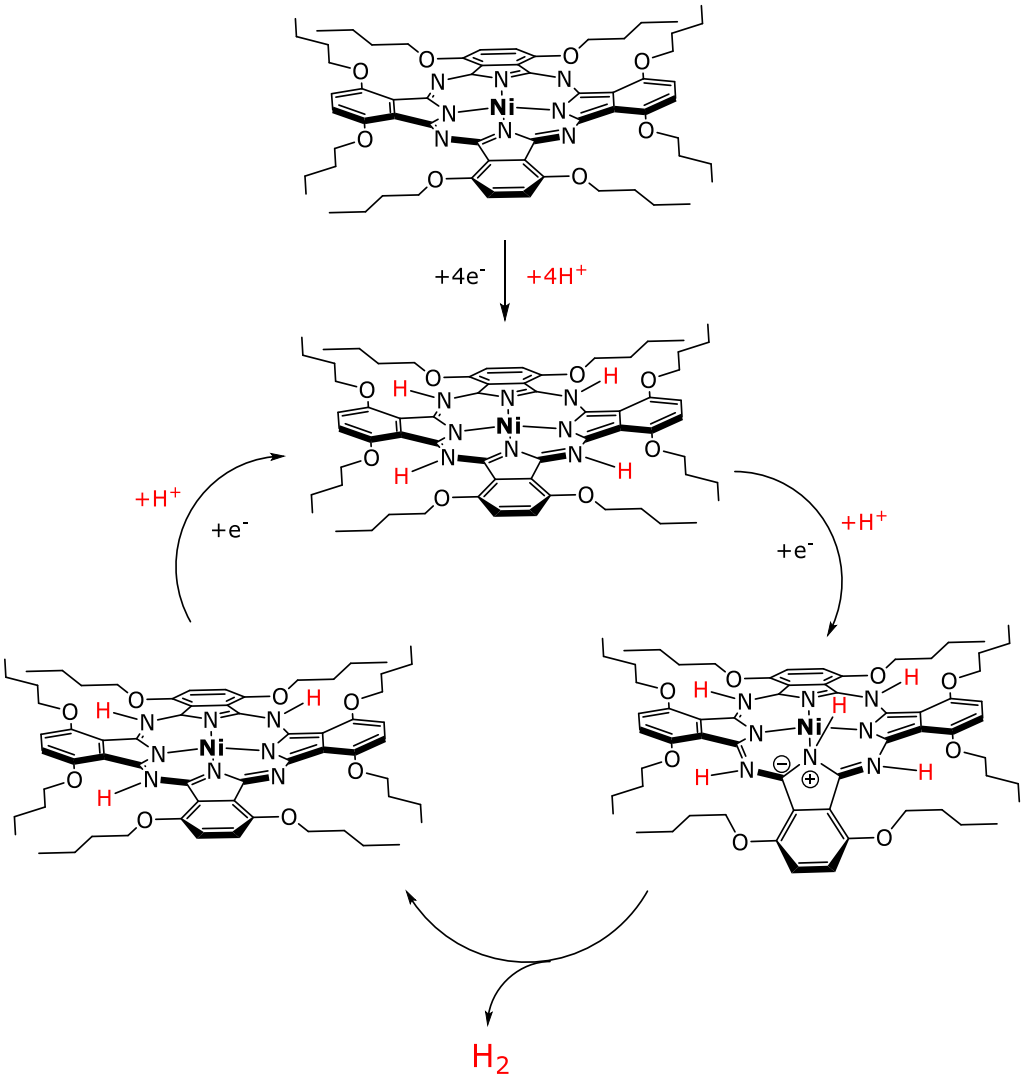

Figure 3.34. Chemdraw representation of a proposed mechanism for H_2 generation from NiPc.

In order to explore the possibility that a redox inactive metal center might display catalytic performance with this ligand platform, the complex 1,4,8,11,15,18,22,25-octabutoxyphthalocyanine Zn(II) (**ZnPc**) was prepared and the electrochemical behavior of this species was examined (Figure 3.35). These CV experiments

displayed no catalysis signatures. Furthermore, controlled potential coulometry, performed at a potential of -2.3V vs $Fc^{+/0}$, did not generate hydrogen.

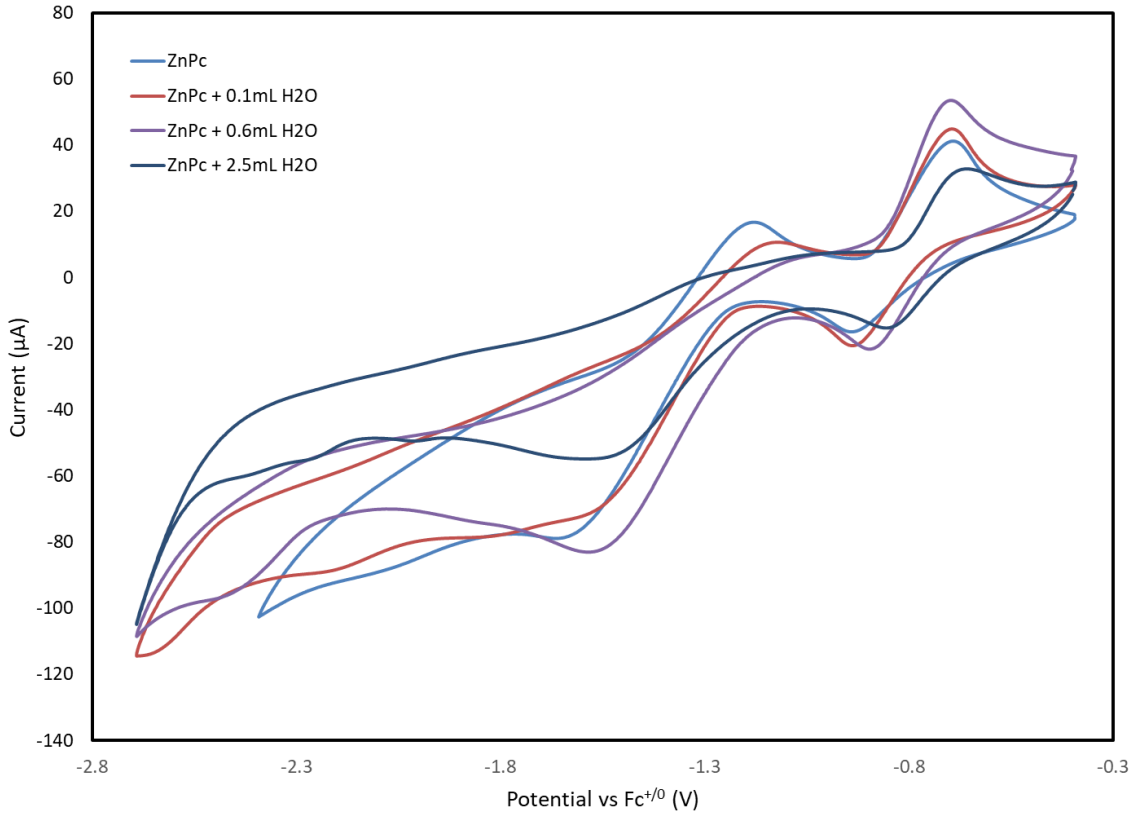

Figure 3.35: The effect of added water on the CV's of 0.5mM ZnPc in THF with 0.1M electrolyte (TBAHFP) and 0.05M TEA. The CV's were scanned between -0.4V and -2.7V with additions of water, as shown in the legend.

It appears that changes to the metal center of metal phthalocyanines has more subtle effects on the redox and acid/base chemistry of the complex and surrounding ligand. The alteration of the coordinated metal centre likely alters the basicity of the various ligand protonation sights and/or acidity of coordinated N-H, that have yet to be explored, influencing the optimal pH regions for catalysis.

3.5 – Conclusion

In conclusion, we have shown that a Ni complex of octabutoxyphthalocyanine electrocatalytically generates H_2 gas through a mechanism that is dominated by ligand-based transformations. The redox activity of **NiPc** was investigated using electro- and spectroelectrochemical analysis techniques, paired with DFT simulation. Unique interactions between the Ni-centered d-orbitals and orbitals dominated by the Pc ligand generated an electronic structure capable of stabilizing several redox events. This investigation demonstrated the reversible nature of the redox events occurring at the Pc ligand and suggested H_2 generation is directly connected to protonation sites in the ligand. Furthermore, H_2 production was unusually influenced by the acidity of the system. The presence of TEA as a base at a concentration of 0.05M demonstrated increased H_2 production relative to the system absent of TEA, suggesting that protonating the coor-N site before reduction can occur, deactivating the catalyst.

3.6 – Experimental and Analytical Details

Synthesis of Ni(II)1,4,8,11,15,18,22,25-octabutoxy-phthalocyanine

Under N_2, the ligand (purchased from Sigma-Aldrich), $H_2Pc(BuO)_8$, (300mg, 0.275mmol) and $Ni(CH_3CO_2)_2{\cdot}4H_2O$ (0.6890g, 2.77mmol) were dissolved in dimethylformamide. The mixture was refluxed for 4 hours and then cooled to room temperature. 80mL of cold water was added to the mixture causing green microcrystals of **NiPc** to crash out of solution. The crystals were filtered and washed with more water and cold ethanol with a yield of 71%. UV-vis (DCM) λ_{max}, nm (log ϵ): 734 (5.75). NMR (C_6D_6):

7.54 (s, 2,3,9,10,16,17,23,26-Ar H), 4.92 (t,OR-1 CH_2), 2.26 (m, OR-2 CH_2), 1.78 (m, OR-3 CH_2), 1.10 (t,OR-4 CH_3). Single crystals were obtained using slow diffusion; the complex was dissolved in DCM using pentane as the external solvent. The unit cell was confirmed to match through single crystal x-ray diffraction with the previously reported structure through the CCDC database.[33]

Electrochemistry:

All cyclic voltammetry (CV) experiments were carried out under nitrogen. Samples were prepared in a glovebox and sealed before removing for measurement. CV and bulk electrolysis were performed on a VersaSTAT 3 (Princeton Applied Research) potentiostat. A conventional three-electrode system was employed. A glassy carbon electrode (diameter=0.4 cm) was used as the working electrode, a Pt wire as the counter electrode, and an Ag wire was used as a pseudo-reference electrode for CV experiments. For bulk electrolysis experiments, a glassy carbon rod (diameter=0.4 cm; length 3 cm) was used as the working electrode, a coiled Pt wire as the auxiliary electrode, and an Ag wire was used as a pseudo-reference electrode. Ferrocene was added as an internal reference after purging with N_2 and measured before and after water addition. Tetra-n-butylammonium hexafluorophosphate (TBAHFP), the supporting electrolyte, was purchased directly from Sigma-Aldrich. The electrolyte solution, 0.1 m TBAHFP in THF, was saturated with N_2 by assembling the cell in the glovebox. The concentration of catalyst was 0.5mM in each experiment. For CVs and bulk, 15 mL of THF was used. First principles of the enhancements were computed to demonstrate the inflection point as a minimum value

in a similar manner to previous work.[34] Hydrogen production was measured using an Agilent 7820 A gas chromatograph equipped with a thermal conductivity detector (GC-TCD) using an Agilent select permanent gases column. The amount of H_2 was determined using a calibration curve.

UV-vis Spectroscopy:

Experiments were performed on a Cary-100 instrument using a double-beam correction. Spectra were obtained in air at a concentration of approximately 0.025mM. The spectral bandwidth of the instrument is 2nm. Scans were completed at a rate of 600nm/minute with a 1nm data interval. The cuvettes used were quartz and had a 1cm pathlength.

SEC analysis:

The potentiostat and spectrophotometer used for these experiments were the same as those described above. Consecutive controlled potential electrolysis experiments were set on the potentiostat at a stepped potential (0.05V decreases each time) and held for 90 seconds. 30 seconds after each potential change a UV-vis spectrum was obtained. The scans were completed from 850-350nm at a scan rate of 1000nm/minute with a 1.67nm data interval. The cell/cuvette used for these experiments was the Honeycomb UV/Vis SEC Cell Kit, from Pine Research. The quartz cell had a pathlength of 1.70nm. The electrochemical cell employed a 3-electrode system. The working electrode and counter electrodes were contained on a single “honeycomb electrode card.” This card has a gold honeycomb shaped working electrode that is situated directly in the beam path of the spectrophotometer. The counter electrodes are located just above the working electrode

component as 2 large, rectangular, gold bars. The Ag/AgCl reference electrode was placed inside the cell away from the beam path. Experiments were referenced to a blank that contained only the THF or DCM solvent and TBAHFP electrolyte.

Computational details:

Calculations were performed using the Gaussian 09 software package through the WebMO interface. Initial structures were established from SC-XRD coordinates and intermediates were proposed by addition of single protons and electrons, assuming singlet and doublet spin states for electron additions. All calculations were performed at the M06L level of theory.[35] Optimization and vibrational frequencies were calculated using the def2-SVP basis set. Absolute minima of the electronic structures were confirmed by verifying an absence of negative vibrational frequencies before single point energy calculations were performed.[30–32,36,37] Molecular energy single point calculations and molecular orbital isosurface simulations were performed using the def2-TZVP basis set. Molecular orbitals were visualized using Chemissian software. UV-vis spectra and excited states were simulated at the B3LYP level of theory and def2-TZVP basis set. The polarizable continuum model (PCM) was used to simulate a solvent system of THF for all optimization, molecular energy, and UV-Vis/excited state calculations. During the generation of MO figures in this document, Chemissian was also used to evaluate electron density contributions, describing the proportion localized on each group. These values are portrayed as decimal, whose summation combined with other unlisted exterior ligand

contributors totals a value of 1. Contributions are listed as; 'Ni center' = metal center, 'N-Ni' = Coor-N, 'N' = bi-N, and 'N-H' = protonated Coor-N.

Foot-of-the-wave analysis:

The foot-of-the-wave analysis (FOWA) allows for an estimate of the reaction rate for an electrocatalytic process that does not show the limiting S-curve behavior.[38,39] This analysis examines the data at the earliest points in the catalytic wave, before E_{cat}. The resulting curve is then fitted to a linear function within the region that the parent function remains linear, and the slope of this line can be used to extract the k_{FOW} of the electrocatalytic reaction of interest. The k_{FOW} is often presented as turnover frequency (TOF). Strictly speaking, this TOF is the number of moles of product produced per unit time per mole of catalyst contained in the reaction−diffusion layer at the electrode and not relative to the catalyst molecules in the bulk solvent. Furthermore, TOF is only equal to k_{FOW} when the applied potential has converted all the catalyst molecules into the active reduced form.

Following the FOWA method described in the literature[38–41], the first step is to use the applied potential, E, and the potential where the catalyst undergoes the reduction process, E_{redox}, in the following relationship:

$$\exp\left[\frac{nF}{RT}(E - E_{redox})\right] \qquad \text{(eq. 3.1)}$$

Where *R* is the universal gas constant, *T* is the temperature, *n* is the number of electrons transferred to the catalyst, and *F* is the Faraday constant. This relationship used in the

FOWA relationship given by equation 2 using the ratio of the catalytic current (i_c) divided by the non-catalytic Faradaic peak current (i_p) of a reduction wave (E_{redox}):

$$i_c/i_p = 2.24\sqrt{\left(\frac{RT}{nFv}\right)(k_{FOW})}\,\frac{1}{1+\exp\left[\frac{nF}{RT}(E-E_{redox})\right]} \quad \text{(eq.3.2)}$$

In this equation, n is the scan rate in V/s. Taking the ratio of i_c to i_p simplifies the overall analysis by avoiding the determination of catalyst diffusion coefficient and electrode surface area.

With this approach a plot ic/ip versus $\frac{1}{1+\exp\left[\frac{nF}{RT}(E-E_{redox})\right]}$ at the "foot-of-the-wave" allows for a linear extrapolation. The slope of this line, m, is given by equation 3.3.

$$m = 2.24\sqrt{(RT/nFv)(k_{FOW})} \quad \text{(eq. 3.3)}$$

and

$$k_{FOW} = 0.776\ (\text{m})^2 \quad \text{(eq. 3.4)}$$

In this set of experiments, we used n = 1, corresponding the third reduction event with a water concentration of 1.44M, as the first rate-determining chemical step. This leads to a lower limit to TOF.

For a general multielectron catalytic system, the number of unique electron-transfer processes that occur at the electrode per catalyst (n) and the catalyst equivalents used per turnover (n') are incorporated into eq. 3.2 and 3.3 , giving eq. 3.5 and 3.6.[41]

$$i_c/i_p = 2.24\sqrt{(RT/nFv)n'(k_{FOW})}\,\frac{1}{1+\exp\left[\frac{nF}{RT}(E-E_{redox})\right]} \quad \text{(eq. 3.5)}$$

$$m = 2.24\sqrt{(RT/nFv)n'(k_{FOW})} \quad \text{(eq. 3.6)}$$

In the case of water reduction to hydrogen, n'= 2 and

$$k_{FOW} = 0.388(m)^2 \quad \text{(eq. 3.7)}$$

3.7 – References

1 X. Li, L. Zhao, J. Yu, X. Liu, X. Zhang, H. Liu and W. Zhou, *Nanomicro Lett*, 2020, **12**, 1–29.

2 J. R. McKone, S. C. Marinescu, B. S. Brunschwig, J. R. Winkler and H. B. Gray, *Chem Sci*, 2014, **5**, 865–878.

3 X. Zhao, P. Wang and M. Long, *Comment Inorg Chem*, 2017, **37**, 238–270.

4 S. Sagar, R. K. Kanaparthi, M. K. Tiwari and S. Saha, in *Photophysics, Photochemical and Substitution Reactions - Recent Advances*, IntechOpen, 2021.

5 S. Sharma and S. K. Ghoshal, *Renew. Sustain. Energy Rev.*, 2015, **43**, 1151–1158.

6 S. Anwar, F. Khan, Y. Zhang and A. Djire, *Int J Hydrogen Energy*, 2021, **46**, 32284–32317.

7 O. R. Luca, J. D. Blakemore, S. J. Konezny, J. M. Praetorius, T. J. Schmeier, G. B. Hunsinger, V. S. Batista, G. W. Brudvig, N. Hazari and R. H. Crabtree, *Inorg Chem*, 2012, **51**, 8704–8709.

8 G. G. Luo, H. L. Zhang, Y. W. Tao, Q. Y. Wu, D. Tian and Q. Zhang, *Inorg Chem Front*, 2019, **6**, 343–354.

9 R. E. Adams, T. A. Grusenmeyer, A. L. Griffith and R. H. Schmehl, *Coord Chem Rev*, 2018, **362**, 44–53.

10 T. Lazarides, T. McCormick, P. Du, G. Luo, B. Lindley and R. Eisenberg, *J Am Chem Soc*, 2009, **131**, 9192–9194.

11 I. O. Shotonwa, O. Ejeromedoghene, A. O. Adesoji and S. Adewuyi, *Catal Commun*, 2023, **179**, 1-17.

12 S. Norouziyanlakvan, P. Berro, G. K. Rao, B. Gabidullin and D. Richeson, *Chem Eur J*, 2024, **30**, 1-9.

13 T. Honda, T. Kojima and S. Fukuzumi, *ChemComm*, 2011, **47**, 7986–7988.

14 G. C. Tok, A. T. S. Freiberg, H. A. Gasteiger and C. R. Hess, *ChemCatChem*, 2019, **11**, 3973–3981.

15 Ö. A. Osmanbaş, A. Koca, M. Kandaz and F. Karaca, *Int J Hydrogen Energy*, 2008, **33**, 3281–3288.

16 M. Peterson, C. Hunt, Z. Wang, S. E. Heinrich, G. Wu and G. Ménard, *Dalton Trans*, 2020, **49**, 16268–16277.

17 Y. J. Yuan, J. R. Tu, H. W. Lu, Z. T. Yu, X. X. Fan and Z. G. Zou, *Dalton Trans*, 2016, **45**, 1359–1363.

18 T. Honda, T. Kojima, N. Kobayashi and S. Fukuzumi, *Angew. Chem Int Ed*, 2011, **50**, 2725–2728.

19 İ. Özçeşmeci, A. Demir, D. Akyüz, A. Koca and A. Gül, *Inorg Chim Acta*, 2017, **466**, 591–598.

20 W. Ji, T. X. Wang, X. Ding, S. Lei and B. H. Han, *Coord Chem Rev*, 2021, 439.

21 A. B. Sorokin, *Chem Rev*, 2013, **113**, 8152–8191.

22 T. C. Gunaratne, A. V. Gusev, X. Peng, A. Rosa, G. Ricciardi, E. J. Baerends, C. Rizzoli, M. E. Kenney and M. A. J. Rodgers, *J Phys Chem A*, 2005, **109**, 2078–2089.

23 J. E. B. Randles, *J Chim Physique*, 1947, **2**, 11–19.

24 G. A. Mabbott, *J Chem Educ*, 1983, **60**, 697–702.

25 C. Costentin and J. Savéant, *ChemElectroChem*, 2014, **1**, 1226–1236.

26 E. S. Rountree, B. D. McCarthy, T. T. Eisenhart and J. L. Dempsey, *Inorg Chem*, 2014, **53**, 9983–10002.

27 B. D. McCarthy, D. J. Martin, E. S. Rountree, A. C. Ullman and J. L. Dempsey, *Inorg Chem*, 2014, **53**, 8350–8361.

28 S. Keshipour and A. Asghari, *Int J Hydrogen Energy*, 2022, **47**, 12865–12881.

29 C. G. Margarit, N. G. Asimow, C. Costentin and D. G. Nocera, *ACS Energy Lett*, 2020, **5**, 72–78.

30 J. Jiang, K. L. Materna, S. Hedström, K. R. Yang, R. H. Crabtree, V. S. Batista and G. W. Brudvig, *Angew Chem, Int Ed*, 2017, **129**, 9239–9243.

31 A. Chaturvedi, G. A. McCarver, S. Sinha, E. G. Hix, K. D. Vogiatzis and J. Jiang, *Angew Chem Int Ed*, 2022, **61**, 1-9.

32 N. Rodríguez-López, Y. Wu, Y. Ge and D. Villagrán, *J Phys Chem C*, 2020, **124**, 10265–10271.

33 T. C. Gunaratne, A. V. Gusev, X. Peng, A. Rosa, G. Ricciardi, E. J. Baerends, C. Rizzoli, M. E. Kenney and M. A. J. Rodgers, *J Phys Chem A*, 2005, **109**, 2078–2089.

34 J. Brown, J. Ovens and D. Richeson, *ChemSusChem*, 2022, **15**, 1–8.

35 D. G. Gusev, *Organometallics*, 2013, **32**, 4239–4243.

36 C. K. Williams, G. A. McCarver, A. Chaturvedi, S. Sinha, M. Ang, K. D. Vogiatzis and J. "Jimmy" Jiang, *Chem Eur J*, 2022, **28**, 1–8.

37 C. K. Williams, G. A. McCarver, A. Lashgari, K. D. Vogiatzis and J. J. Jiang, *Inorg Chem*, 2021, **60**, 4915–4923.

38 C. Costentin, M. Robert and J.-M. Savéant, *Chem Soc Rev*, 2013, **42**, 2423–36.

39 C. Costentin, S. Drouet, M. Robert and J. M. Savéant, *J Am Chem Soc*, 2012, **134**, 11235–11242.

40 E. S. Rountree and J. L. Dempsey, *J Am Chem Soc*, 2015, **137**, 13371–13380.

41 E. S. Rountree, B. D. McCarthy, T. T. Eisenhart and J. L. Dempsey, *Inorg Chem*, 2014, **53**, 9983–10002.

Chapter 4: Electrocatalytic Nitrite Reduction in Neutral Water with Ni(II) and Co(II) Macrocycle Complexes: Catalytic Evaluation and Mechanistic Elucidation

4.1 – Preamble and Statement of Contributions

The content described in this chapter was published in ChemCatChem in 2023. It can be accessed through the following link: **https://doi.org/10.1002/cctc.202301168**

Synthesis of the ligands and complexes was completed by Jonathon Ferguson. The electrochemical experiments for this investigation were completed by Jonathon Ferguson; this includes cyclic voltammetry and bulk electrolysis. Interpretation and analysis of the cyclic voltammetry data for foot-of-the-wave analysis was completed by Josh Brown. Computational data were generated and interpreted by Josh Brown. Crystallography data were processed by Jeffry Ovens. Preliminary drafts were completed by Jonathon Ferguson and Josh Brown which were further edited by Darrin Richeson, Jonathon Ferguson, and Josh Brown.

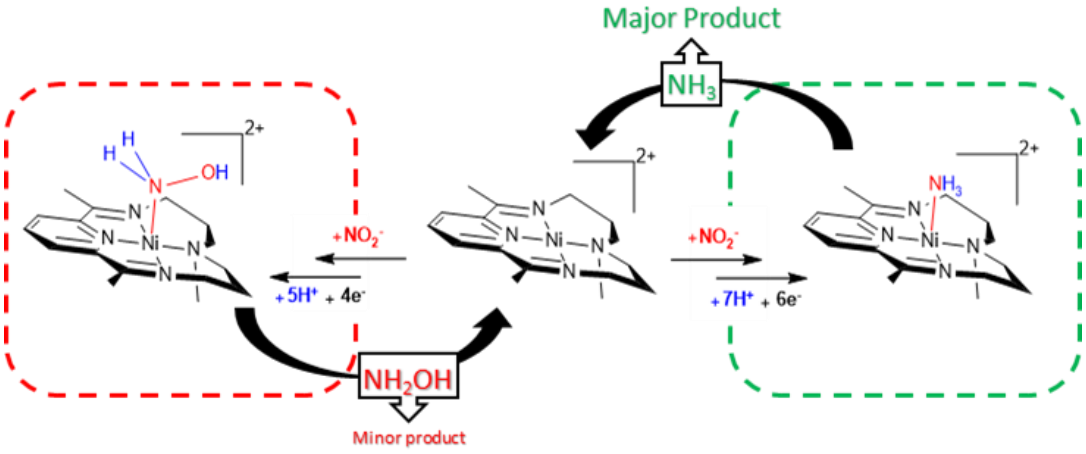

4.2 – Abstract

Nitrite anions, of anthropogenic origin, in the environment disrupt the nitrogen cycle making the electrocatalytic reduction of nitrite a significant objective. Homogeneous Ni(II) and Co(II) complexes bearing a macrocyclic supporting ligand consisting of a tridentate redox active bis(imino)pyridine moiety coupled with a tertiary amine donor site are effective and selective for the electrocatalytic reduction of nitrite to ammonium ion and hydroxylamine in buffered (pH 7) aqueous solutions. Controlled potential coulometry at potentials from -0.98 to -1.05V vs Ag/AgCl in 4-morpholinepropanesulfonic acid (MOPS) buffer yielded ammonium as the major product with Faradaic efficiencies ranging from 76-90%. A foot-of-the-wave analysis yielded calculated turn-over frequencies of 28900s^{-1} and 5410s^{-1} for the Ni and Co complexes, respectively. The Ni complex displayed a higher selectivity for NH_4^+/NH_2OH than the Co analog. A computational examination of the catalytic mechanism of the Ni complex was used to support and elucidate the proposed chemical steps, provide some energetic details of the electron and proton transfers, and present a rationale for the selectivity of this reduction.

4.3 – Introduction

The nitrogen cycle is foundational for the biosphere and critical to life on Earth. Like the carbon cycle, humanity has created a significant disturbance to this cycle; in this case, largely through the massive application of ammonia-based fertilizers. For example, greater than 50% of the nitrogen used in ammonia-based fertilizers is lost to the environment where it is converted to nitrogen oxides and oxyanions (e.g. N_2O, NO_2^-,

NO_3^-), continually increasing byproducts with negative environmental and human health effects.[1–5]

The redox transformation of nitrite plays a central position in the nitrogen cycle and as such is a significant scientific target for exploration of its electrocatalytic reduction from both an environmental and a fundamental perspective.[6] In nature, cytochrome c containing nitrite reductase (CcNiR), an iron porphyrinoid enzyme, efficiently catalyzes the reduction of nitrite to ammonia employing six electrons and seven protons.[7]

Discovering a homogeneous molecular electrocatalyst for nitrite reduction presents challenges and promise.[8] For example, nitrite reduction involves multiple electron/proton transfers and, as a result, can lead to several products including NO, N_2O, NH_3/NH_4^+, and NH_2OH. Furthermore, nitrite has a pH-dependent aqueous speciation that could result in several different electroactive forms. These features suggest that pH control is important for a successful catalytic transformation.

The search for homogeneous molecular catalysts that can electrocatalytically reduce nitrite is a growing area and is so far dominated by a focus on Fe(III), Co(III), and Cu(II) compounds (Table 4.1).[9–20] A water-soluble Fe(III) porphyrin, $[Fe(TPPS)]^{3-}$ (TPPS = (meso-tetrakis(p-sulfonatophenyl)porphyrin)), in phosphate buffered acidic aqueous solution was shown to electrocatalytically reduce NO (originating from nitrite) to ammonia with high Faradaic efficiency (FE).[9,21] Significant side products of N_2O and hydroxylamine appeared depending on the reaction conditions. A recent report described the catalytic behavior of an Fe complex supported by the macrocyclic pentadentate ligand, which incorporated a bis(imino)pyridine group in the ligand. At pH 7.2 in a buffered aqueous

solution, the Fe(III) complex gave electrocatalytic reduction of nitrite to yield hydroxylamine with high Faradaic efficiency.[10]

Table 4.1: Homogeneous nitrite reduction catalysts.

Catalyst	Metal center	Product Selectivity	Applied Potential (V) (reference)	Other comments	Ref.
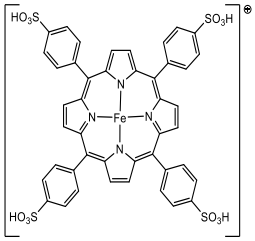	Fe(III)	NH_4^+ Up to 97%	-0.9 (SCE)	Water, pH = 6.7 phosphate buffer, Hg electrode	1
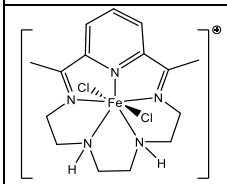	Fe(III)	NH_2OH, 91% NH_4^+, 8%	-0.98 (Ag/AgCl)	MOPS buffer pH 7.2, Hg electrode linear dependence on [MOPS], [Fe], and $[NO_2^-]$	2
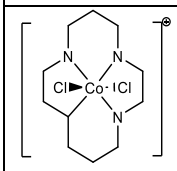	Co(III)	NH_2OH, 73% NH_4^+, 6%	-1.5 (SCE)	Hg electrode, 3M NaOH, efficiency/selectivty dependent on electrode and applied potential	3
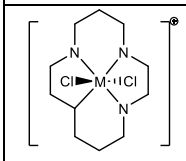 M = Co, Ni	Co(III) Ni(II)	NH_2OH	-1.5 (SCE)	Hg electrode	4
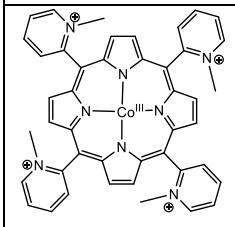	Co(III)	NH_2OH, 80% NH_4^+, 15%	-0.7 (Ag/AgCl)	pH = 5 buffer, glassy C electrode	5

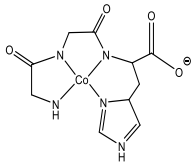	Co(III)	NH_4^+, 90%	−0.90 (Ag/AgCl)	1M MOPS buffer, pH = 7.2, Hg electrode, TON =3550 ± 420 over 5.5 h	6
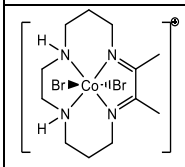	Co(III)	NH_3, 88%	-1.05V (SCE)	Aqueous	7,8
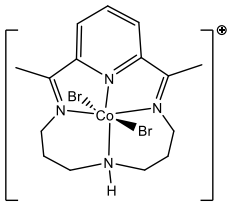	Co(III)	NH_4^+, 88%	-1.46 V (SCE)	initial pH 6.40	9
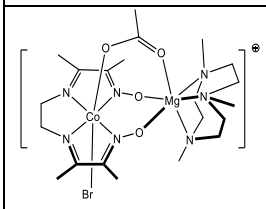	Co(III)	N_2O	-1.2V (SCE)	acetonitrile, glassy C electrode, NEt_3H^+ as proton source	10
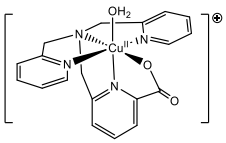	Cu(II)	NO	-0.91V ($Fc^{+/0}$)	glassy-carbon-foil electrode also contained 5 mM benzoic acid and 5 mM TBA-NO2.	11
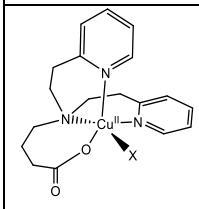	Cu(II)	NO 94-15 depending on ligand features	0.010V (Ag/AgCl)	0.1 M HEPES buffer (pH 7.4), 0.1 M NaCl, Pt disk working electrode	12

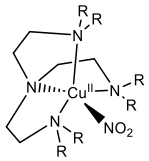	Cu(II)	NO, N_2O	Variable		13

Several cobalt (III) complexes have been reported to display activity for electrocatalytic nitrite reduction. Early reports of Co(III) cyclam catalysts yielded almost exclusively hydroxylamine at significant cathodic potentials (-1.5V vs. SCE) using Hg electrodes.[1122] The porphyrin complex, cobalt tetrakis(N-methyl-2-pyridyl)porphine (Co(2-TMPyP)) under acidic conditions (pH = 5) reduced nitrite to a 5.5:1 mixture of NH_2OH/NH_3.[12] An unusual bimetallic diimine-dioxime cobalt complex that has an outer-sphere coordinated Mg^{2+} reduces nitrite to N_2O in organic solution.[17] More recently, investigations of an analog of cyclam possessing an unsaturated α-diimine ligand framework, $[Co(DIM)Br_2]^+$ (DIM = 2,3-dimethyl-1,4,8,11-tetraazacyclotetradeca-1,3-diene) has been shown to electrocatalytically reduce nitrate to ammonia as the only detected product with 88% efficiency.[14,23] A Co(III) complex of a neutral tetraazamacrocyclic ligand containing the redox non-innocent bis(imino)pyridine moiety reacted with nitrite under electrocatalytic and acidic (pH = 6.40) conditions to yield ammonium with 88% FE. In this case, it appeared that the complex undergoes two Co-centered reduction steps to Co(I) followed by a ligand reduction to activate catalysis at −1.46 V vs. SCE.[16] An interesting Co(III) metallotripeptide complex displayed electrocatalytic reduction of nitrite at -0.90V vs. SCE with a Hg electrode in a buffered aqueous solution at pH = 7.2. The product was ammonia with a turnover number after 5.5 hours of greater than 3500.[13]

Several Cu(II) complexes supported with tripodal N-coordinating ligands have been documented to electrocatalytically reduce nitrate.[18–20] The common product from these reductions is NO and the required electrochemical potentials and Faradaic yields depend on the features of the ligand framework and solution pH.

A survey of the successful catalysts that have been documented for nitrite reduction reveals the conspicuous absence of Ni complexes.[11] We now introduce a new Ni(II) electrocatalyst for nitrite reduction to produce ammonium as the major product. Complex (**1**) was designed around a tetraazamacrocyclic supporting ligand, consisting of a tridentate redox active bis(imino)pyridine moiety coupled with a tertiary amine donor site (Scheme 4.1).[24] We also report on the electrocatalytic performance of the Co(II) analog of this species, thus providing a unique comparison of catalyst performance. Furthermore, this supplements the existing report on the catalytic behavior of the Co(III) complex with a similar tetracoordinate ligand having an NH group rather than the NMe function of **2**.[16]

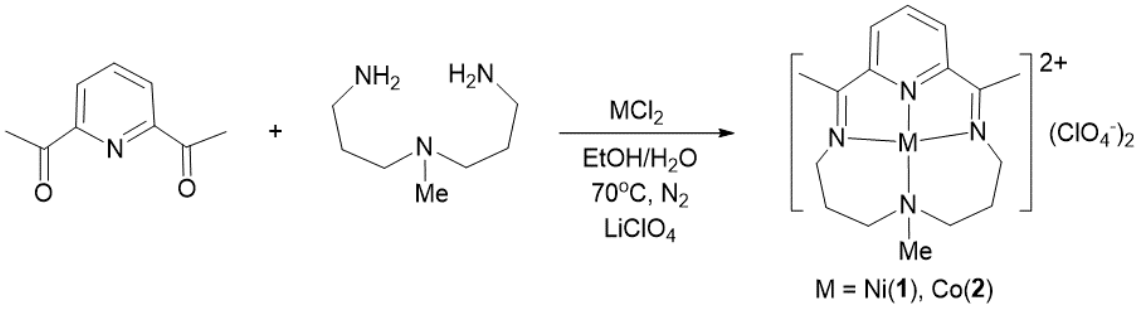

Scheme 4.1. Synthesis of Ni(II) (1) and Co(II) (2) complexes of the (2,7,12-trimethyl-3,7,11,17-tetraazabicyclo [11.3.1]heptadeca-1(17),13,15-pentaene) ligand.

4.4 – Results and Discussion

The targeted Ni(II) and Co(II) macrocyclic 2,6-diiminopyridine ligand-supported complexes were prepared using a well-established metal-templated condensation reaction between 3,3'-diamino-N-methyldipropylamine and 2,6-diacetylpyridine followed by anion exchange with perchlorate (Scheme 4.1).[25,26] The Ni complex (**1**) was crystallized from acetonitrile as bright red needle crystals, as previously reported.[27,28] Similarly, the known Co(II) complex (**2**) was isolated as red crystals.[29] The single crystal X-ray structure of **1** was reported to consist of the expected 14-membered macrocycle which adopts a planar, tetradentate distorted square planar coordination environment for the Ni(II) center.[24]

The CVs, in the cathodic region, of complexes **1** and **2** in acetonitrile are shown in Figure 4.1. The Ni complex **1**, displayed a reversible redox event at $E_{1/2}$ = -0.52 V and a reversible event at $E_{1/2}$ = -1.10 V. The electrochemistry of the analogous complex of Ni possessing the supporting tetraazamacrocycle, 2,12-dimethyl-3,7,11,17-tetraazabicyclo[11.3.1]heptadeca-1(17),2,11,13,15-pentaene, with the amino group as an NH moiety rather than the NMe group, has been thoroughly investigated.[25,27,28,30,31] The voltammogram of **1** compares very well with the "NH" analog.[32] More specifically, based on the electrochemical analysis of Wieghardt and co-workers for these $[Ni(L)]^{2+}$ species, the sequential reductions are both most likely ligand-based to produce $[Ni^{II}(L^{\bullet -})]^{+}$, and $[Ni^{II}(L^{2-})]$, respectively.[32]

Similarly, the electrochemistry of complex **2** in acetonitrile, exhibited two reversible redox events at $E_{1/2}$ = -0.4 V, -1.0 V, vs. Ag/AgCl. Again, these results compared well with the

Co(III) complexes of the NH analog.[16,33,34] In the case of these Co(III) species, $[Co(L)Br_2]^+$, three processes are observed in the CV in acetonitrile solution. The first reduction was assigned to a $Co^{III/II}$ event, which is absent in the case of this Co^{II} complex **2**. The second reduction has been assigned to $Co^{II/I}$ couple and the third to a ligand-based reduction. These correspond to the reductions observed for **2**.

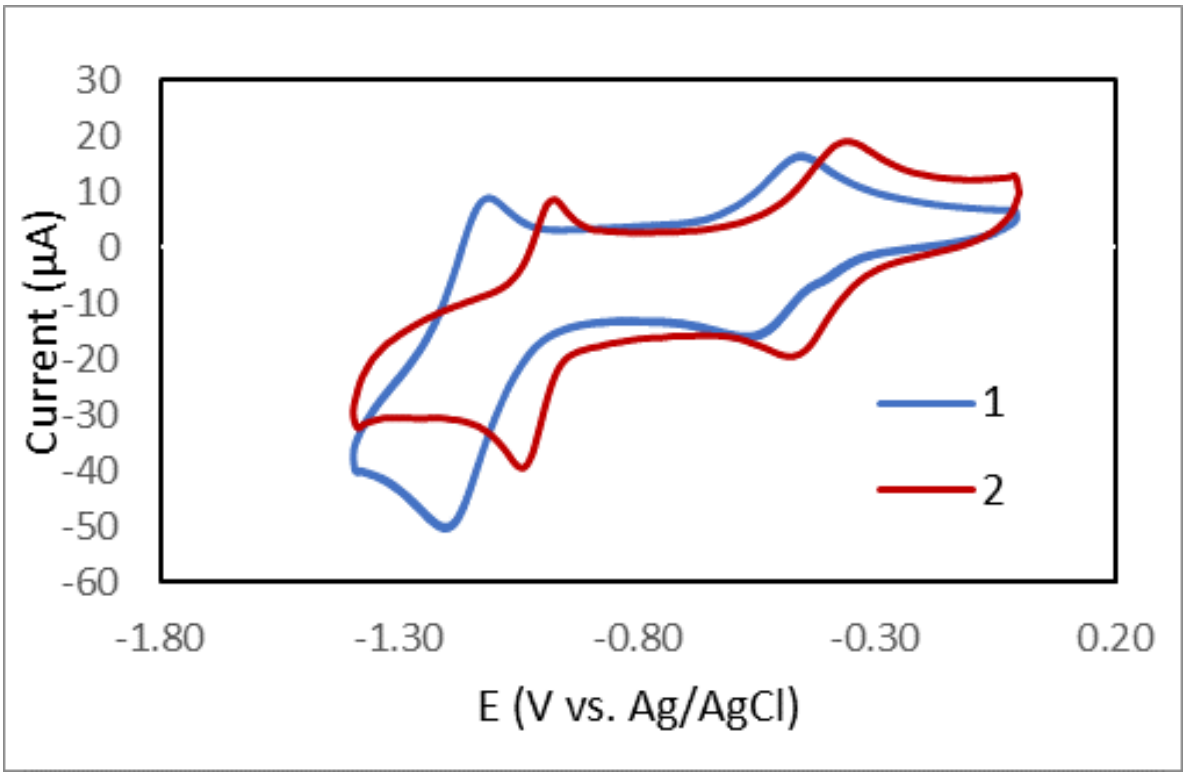

Figure 4.1. CVs of complexes 1 (blue) and 2 (red) in acetonitrile (1 mM complex) using a glassy carbon working electrode, a Pt counter electrode, and an Ag/AgCl reference electrode with 100 mM TBAHFP electrolyte and scan rate = 100mV/S.

Having confirmed the fundamental electrochemistry of complexes **1** and **2**, the electrochemical features were examined in aqueous solution, a more applicable solvent for nitrite reduction. Furthermore, given the requirement of multiple proton transfer events and the documented influence of pH on the nitrite reduction products, an aqueous buffer system was chosen to mitigate large pH changes during the catalytic transformation. The selection of the buffer was based on two criteria; the first was a buffer that was centered at pH 7 and the second was to focus on a buffer with a "non-coordinating" conjugate base to minimize interference on the catalyst. These attributes led to the selection of the "Good's buffer" derived from 4-morpholinepropanesulfonic acid (MOPS) with a pK_a of 7.20.

Cyclic voltammetry on 1 mM solutions of **1** and **2** was performed in aqueous solution with 0.1 M KCl as the supporting electrolyte. A glassy carbon working electrode (GCE) was used along with a Pt counter electrode referenced to an Ag/AgCl electrode. (Figure 4.2). Complex **1** exhibited two irreversible reduction events at E = -0.86 V and -1.03 V. These observations are similar to the recent description for the aqueous electrochemistry of $[Ni(\kappa^3\text{-}2,6\text{-}\{PhNCMe\}_2(NC_5H_3)Br_2]$.[35] The aqueous solution of **2** displayed one reversible reduction event at E = -0.70 V and one irreversible reduction event at $E_{1/2}$ = -1.05 V. Based on the non-aqueous electrochemistry and a comparison with the literature these two

reductions were assigned to a reversible $Co^{II/I}$ couple and an irreversible reduction centered on the ligand.[16]

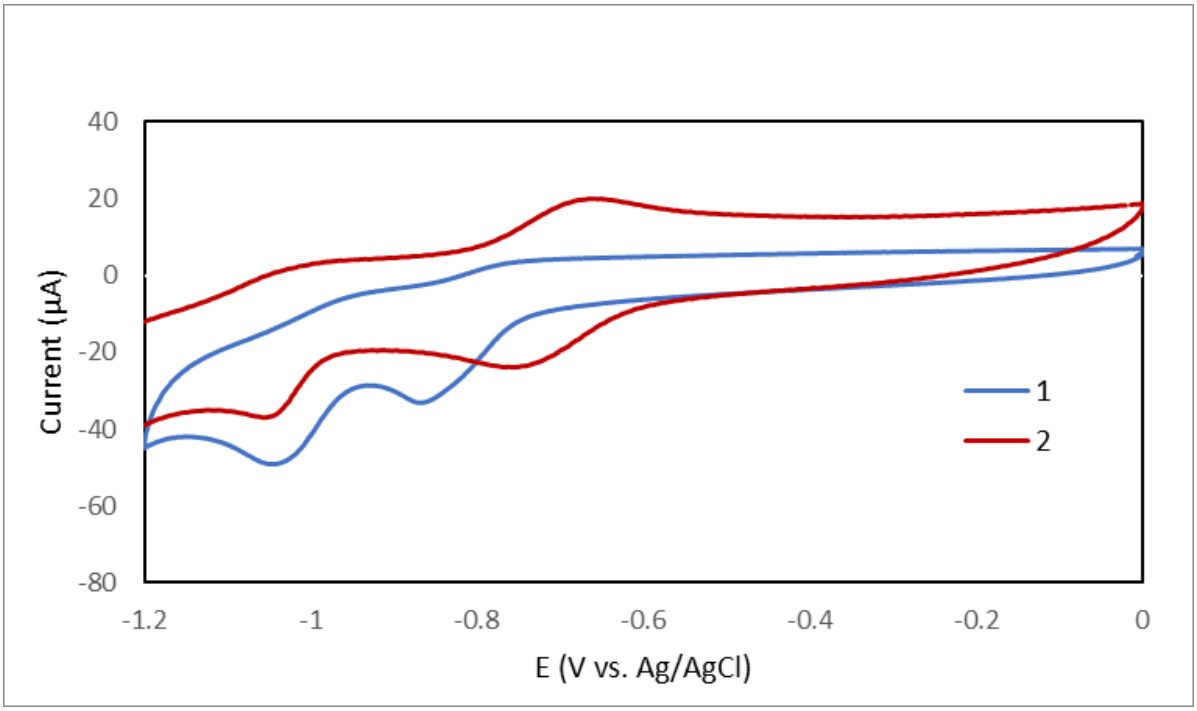

Figure 4.2: CV of 1 and 2 in aqueous solution, under N_2 with 0.1 M KCl as the supporting electrolyte.

The voltammetry of compounds **1** and **2** did not change when [MOPS] buffer (pH 7.0) was varied as demonstrated by the data shown in Figure 4.3 and Figure 4.4. This supported the innocent role of MOPS buffer in the reduction chemistry of **1** and **2.** Furthermore, the reduction events for both **1** and **2** displayed linear relationships for the $(\text{scan-rate})^{1/2}$ vs.

peak current as expected from the Randles-Ševčík equation for stable homogeneous diffusion-controlled processes (Figures 4.5-4.10).

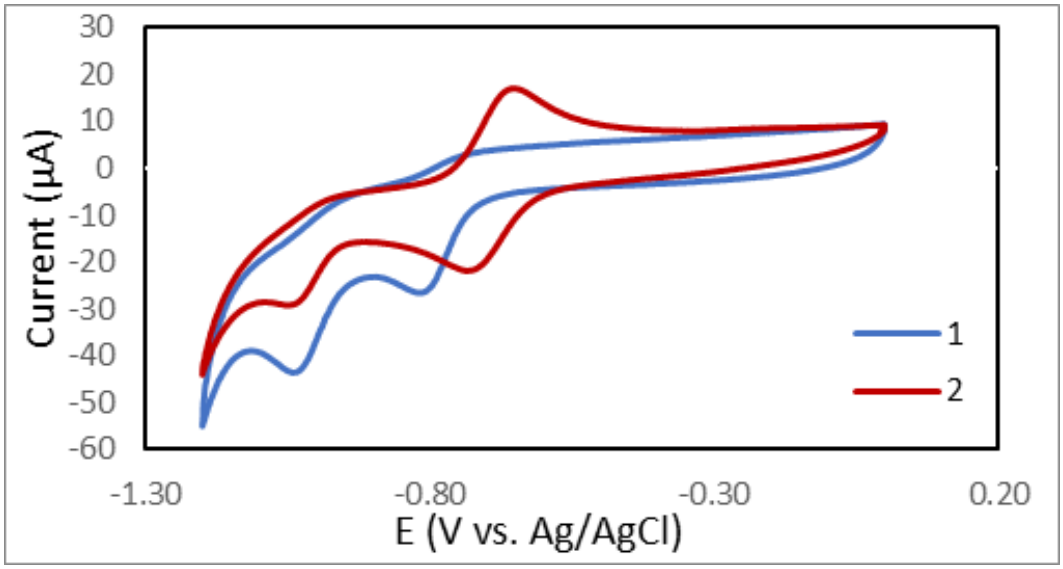

Figure 4.3. CVs of complexes 1 (blue) and 2 (red) in aqueous solution (1 mM complex) using a glassy carbon working electrode, a Pt counter electrode, and an Ag/AgCl reference electrode with 100 mM KCl electrolyte and scan rate = 100mV/S. with 100 mM MOPS.

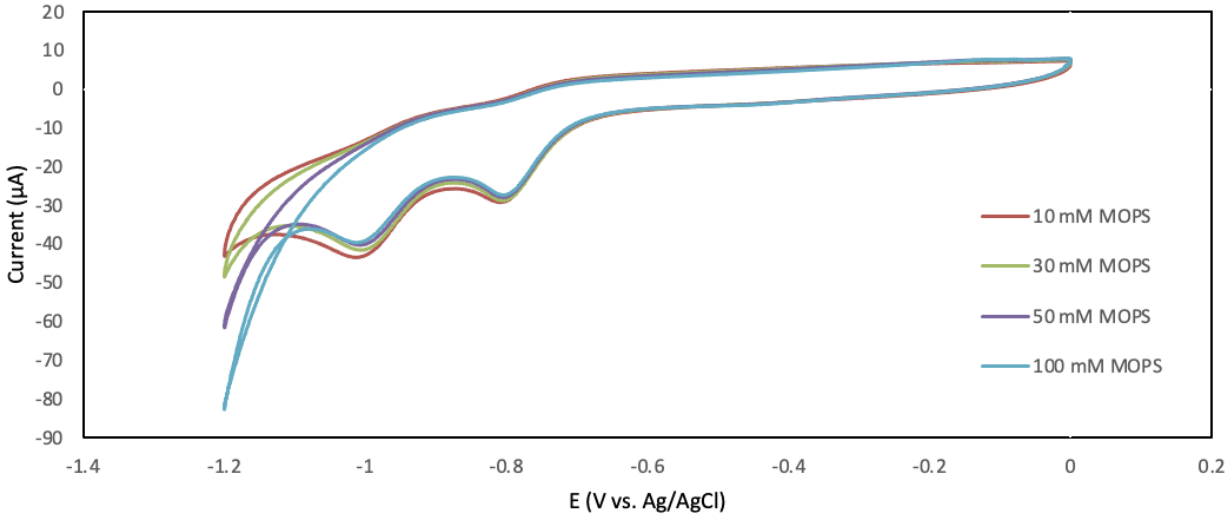

Figure 4.4: CV of 1 mM 1 in water under dinitrogen atmosphere with 0.1 M KCl as the supporting electrolyte with increasing [MOPS] in the absence of $NaNO_2$.

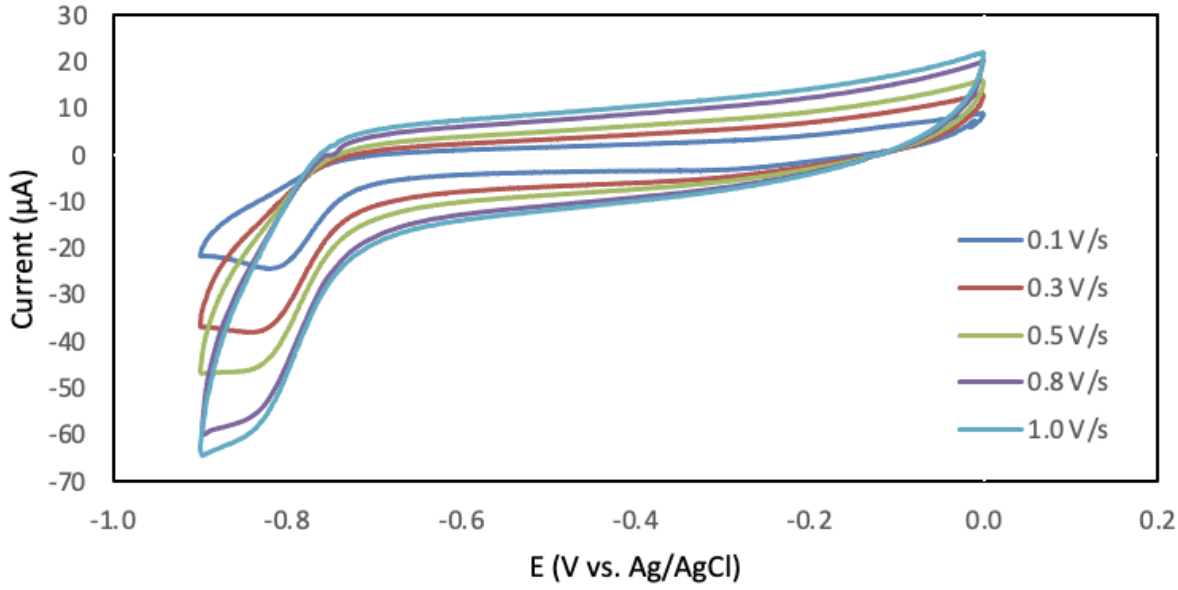

Figure 4.5: Scan rate dependence of reduction for complex 1 in 50 mM MOPS aqueous solution under N_2 with 0.1 M KCl as the supporting electrolyte.

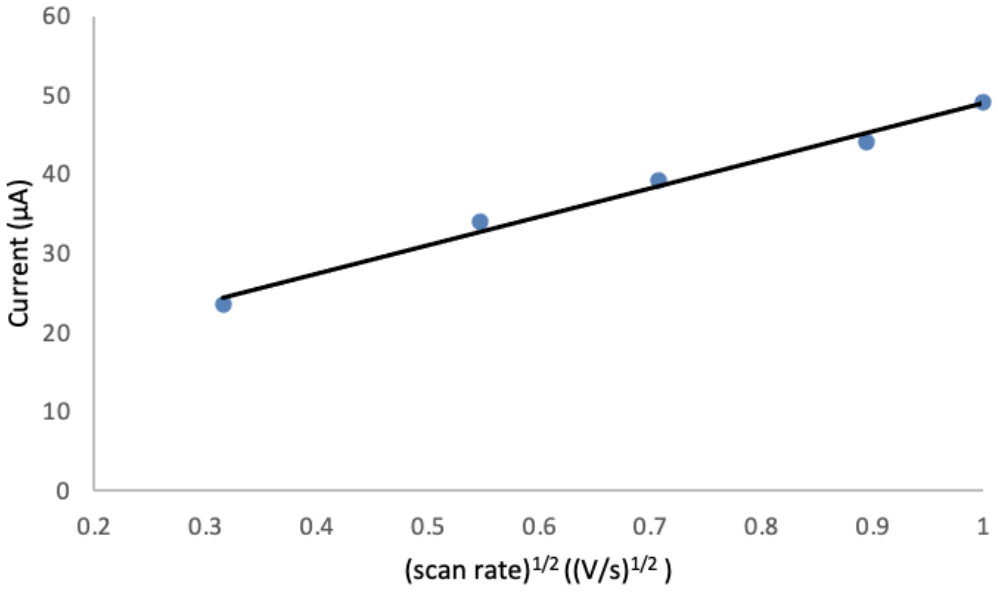

Figure 4.6: Plot of the current (mA) vs. scan rate (V/s)$^{1/2}$ for the data shown in Figure 4.5.

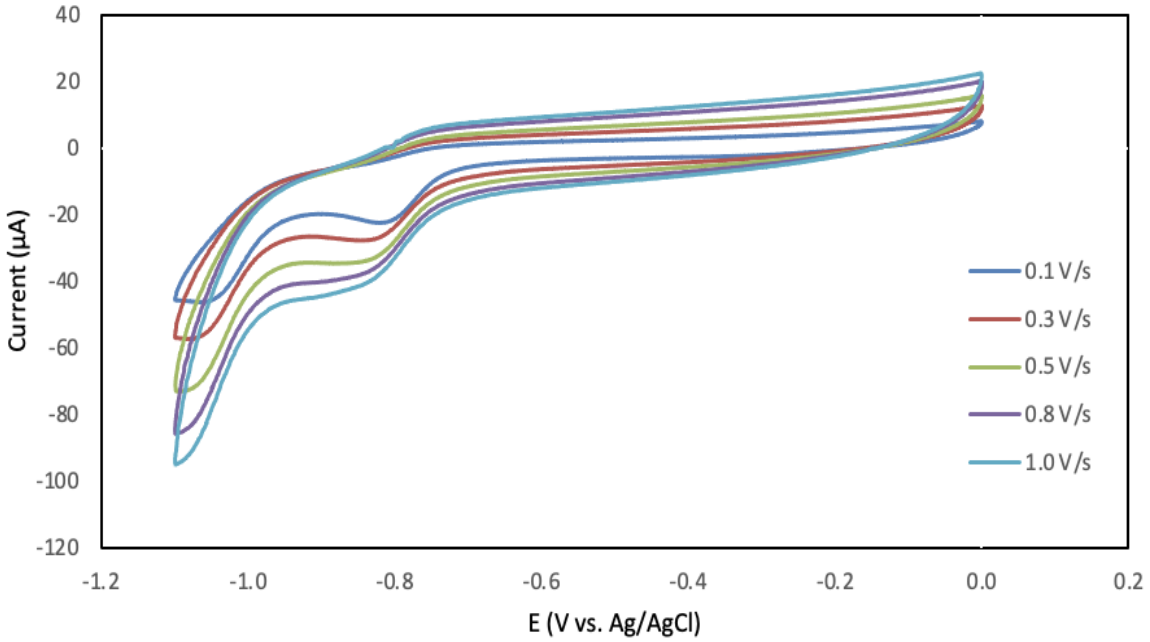

Figure 4.7: Scan rate dependence of the second reduction of complex 1 in 50 mM MOPS aqueous solution under N_2 with 0.1 M KCl as the supporting electrolyte.

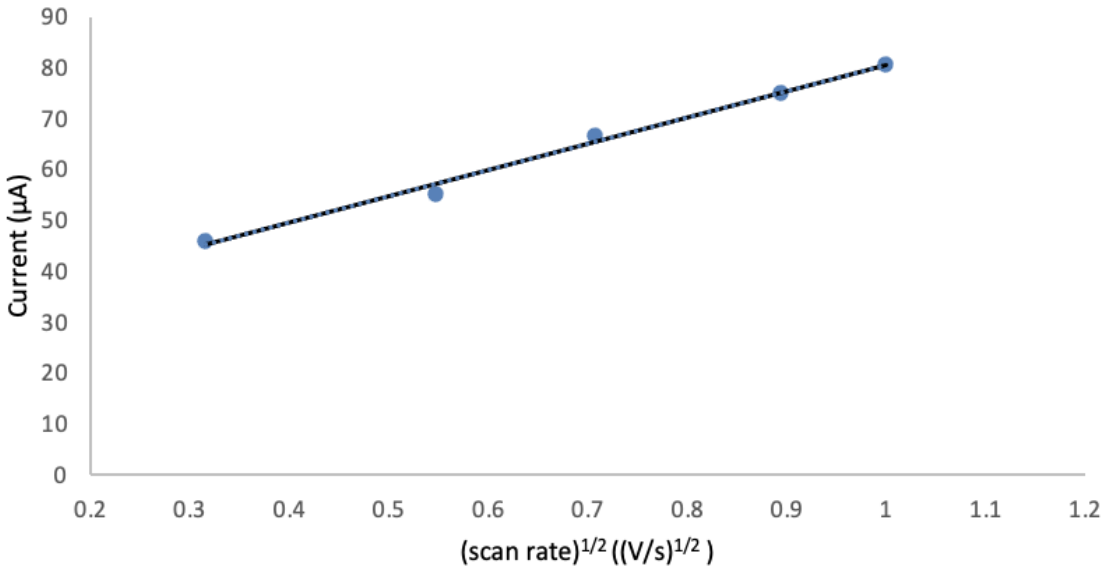

Figure 4.8: Plot of the square root of the scan rate $(V/s)^{1/2}$ for the data shown in Figure 4.7.

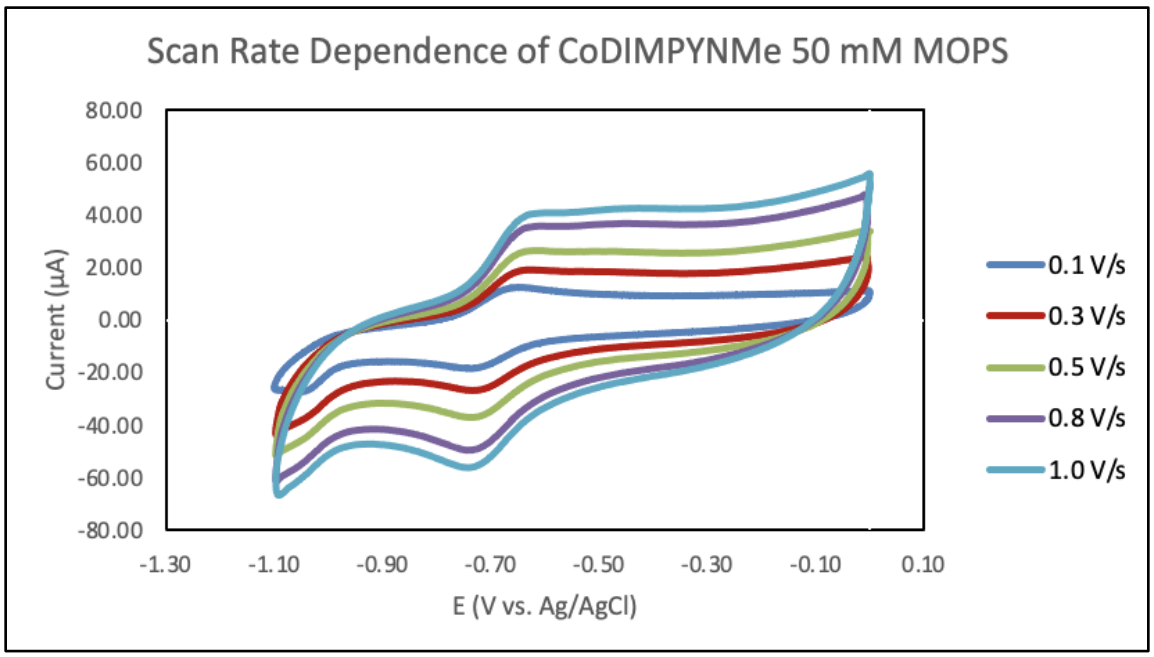

Figure 4.9: Scan rate dependence of the reduction of complex 2 in 50 mM MOPS aqueous solution under N_2 with 0.1 M KCl as the supporting electrolyte.

.

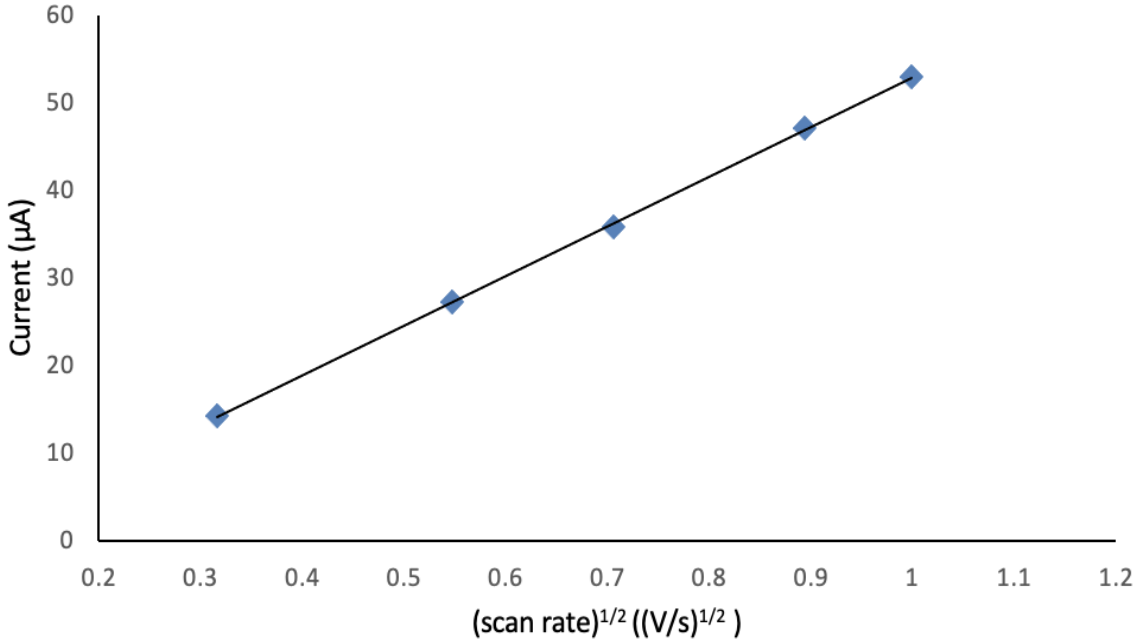

Figure 4.10: Plot of the square root of the scan rate $(V/s)^{1/2}$ for the data shown in Figure 4.9.

The voltametric behavior of **1** with nitrite in the absence of buffer was also assessed and shown in Figure 4.11. While no shifts in reduction potentials or current for the first reduction were observed, the addition of NO_2^- to solutions of **1** did generate a small current enhancement for the second reduction. This is a signature response for possible electrocatalysis and prompted an evaluation of this possibility. In addition, support for coordination of nitrite was provided by measurement of the UV-vis spectrum of **1** with addition of $NaNO_2$. The absorbances of **1** shifted slightly and two isosbestic points were observed in the presence of NO_2^- (Figure 4.12).

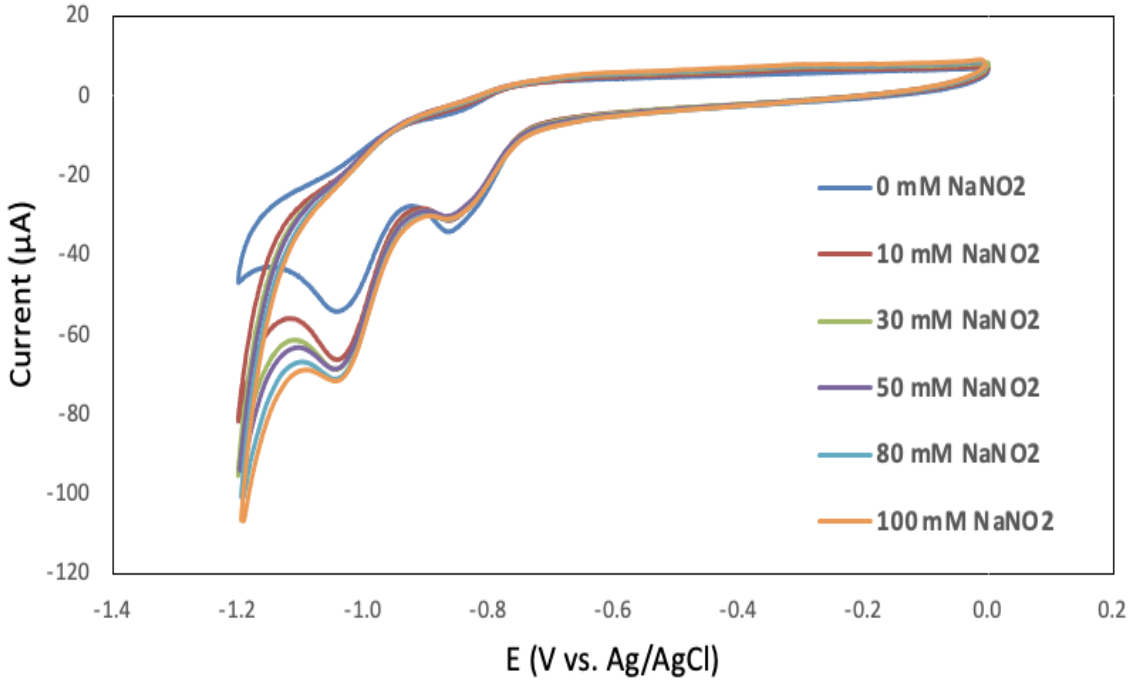

Figure 4.11: CV of 1 (1mM) in water under N_2 with 0.1 M KCl as the supporting electrolyte and varying [$NaNO_2$] in the absence of MOPS.

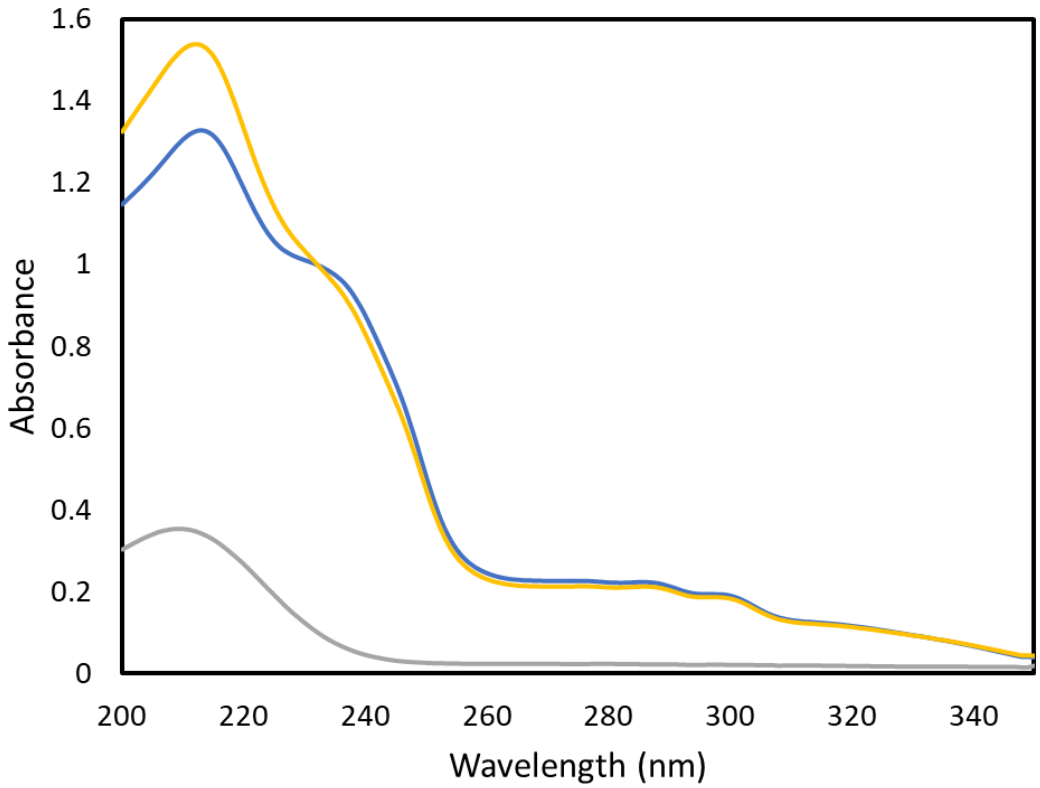

Figure 4.12. UV-vis spectra of 0.05mM solutions of $NaNO_2$ (grey), complex 1 (blue), and an equimolar mixture of 1 and $NaNO_2$. Two isosbestic points were observed at 233 nm and 325 nm (inset).

With these reactivity characteristics established, the effect of incremental addition of $NaNO_2$ to a reaction cell containing 1 mM **1**, 100 mM MOPS buffer (pH = 7), with the same electrodes was explored. From Figure 4.13 it was clear that after the initial addition of $NaNO_2$ to the reaction system, a significant current enhancement was observed indicative of a catalytic process. The increasing concentration of nitrite showed a sharp increase in the catalytic current (i_{cat}) relative to the current in the absence of substrate (i_p) and the ratio of i_{cat}/i_p began to plateau at ~0.1M NO_2^- and i_{cat}/i_p ~ 100 when the reaction shifted to saturation conditions (Figure 4.14).

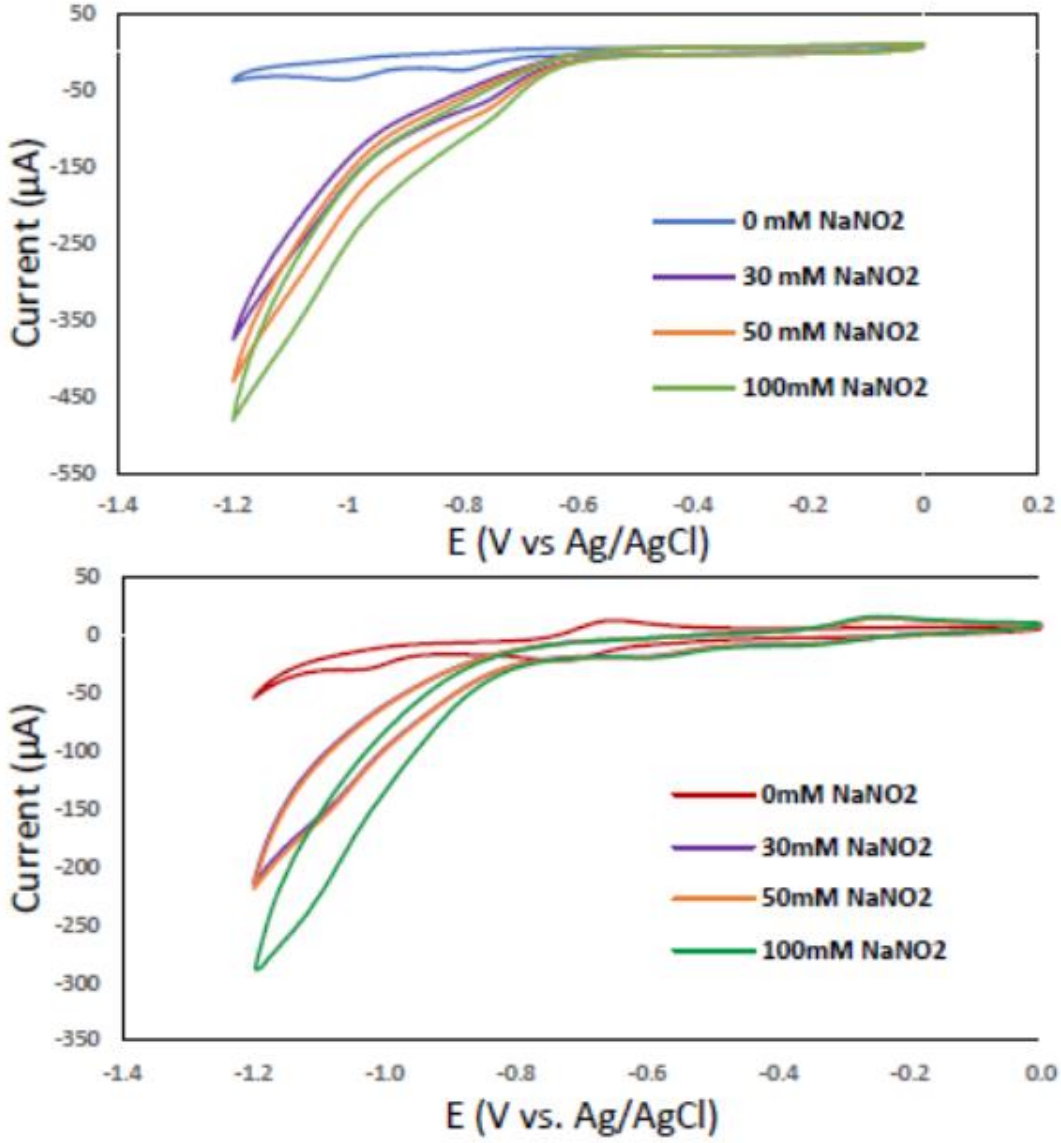

Figure 4.13. (a) CVs of aqueous 1 mM 1 and 100 mM MOPS (buffered at pH 7) under N_2 atmosphere with 0.1 M KCl as the supporting electrolyte. (b) CVs of aqueous 1 mM 2 and 100 mM MOPS (buffered at pH 7) under N_2 atmosphere with 0.1 M KCl as the supporting electrolyte. In both cases, a GC working electrode, a Pt counter electrode, and an Ag/AgCl reference electrode were used. Curves represent increasing [$NaNO_2$].

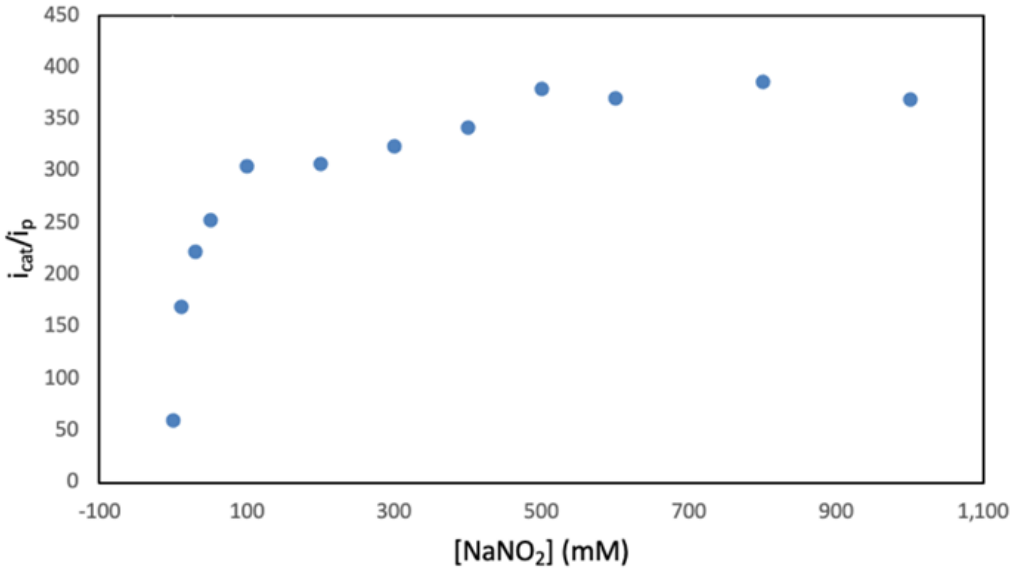

Figure 4.14. A plot of the ratio of the current under catalytic conditions (i_{cat}) to the current in the absence of substrate (i_p) versus the concentration of nitrite. Data were collected at -1.05 V vs. Ag/AgCl.

The ratio of the catalytic current (i_{cat}) and corresponding reductive peak current in the absence of a substrate (i_p) serves as a useful gauge to compare the activity of different catalysts.[36] Since ideal "S-shaped" catalytic waves were not observed in the CVs of these catalysts, a foot-of-the-wave analysis (FOWA) was applied to these systems.[37] Using eq. 4.1 the maximum TOF, under saturation conditions, was determined. With this method, the onset of the catalytic wave is analyzed for the calculation of the catalytic rate. The purpose is to avoid nonideal behavior, such as substrate depletion and catalyst deactivation. The TOF value was estimated using plots of i_{cat}/i_p versus $1/[1 + \exp\{(F/RT)(E - E_{cat})\}]$, where E_{cat} is the reduction potential of the catalyst associated with catalysis. The slopes of the linear region are given by the numerator of eq. 4.1 with

n' being the number of electrons transferred for particular reduction. The plots for complex **1** are shown in Figures 4.15, and 4.16 and the maximum TOF obtained by FOWA was 28900 s^{-1}.

$$\frac{i_{cat}}{i_p} = \frac{2.24\sqrt{\frac{RT(TOF)}{n'Fv}}}{1+\exp\left[\frac{nF}{RT}(E-E_{cat})\right]} \qquad \text{(eq. 4.1)}$$

Similarly, reactions of **2** with increasing $NaNO_2$ concentration with MOPS buffer also displayed a significant increase in current as more $NaNO_2$ was added to the system. The FOWA analysis under saturation conditions yielded a TOF for **2** of 4310 s^{-1} (Figures 4.17, 4.18)

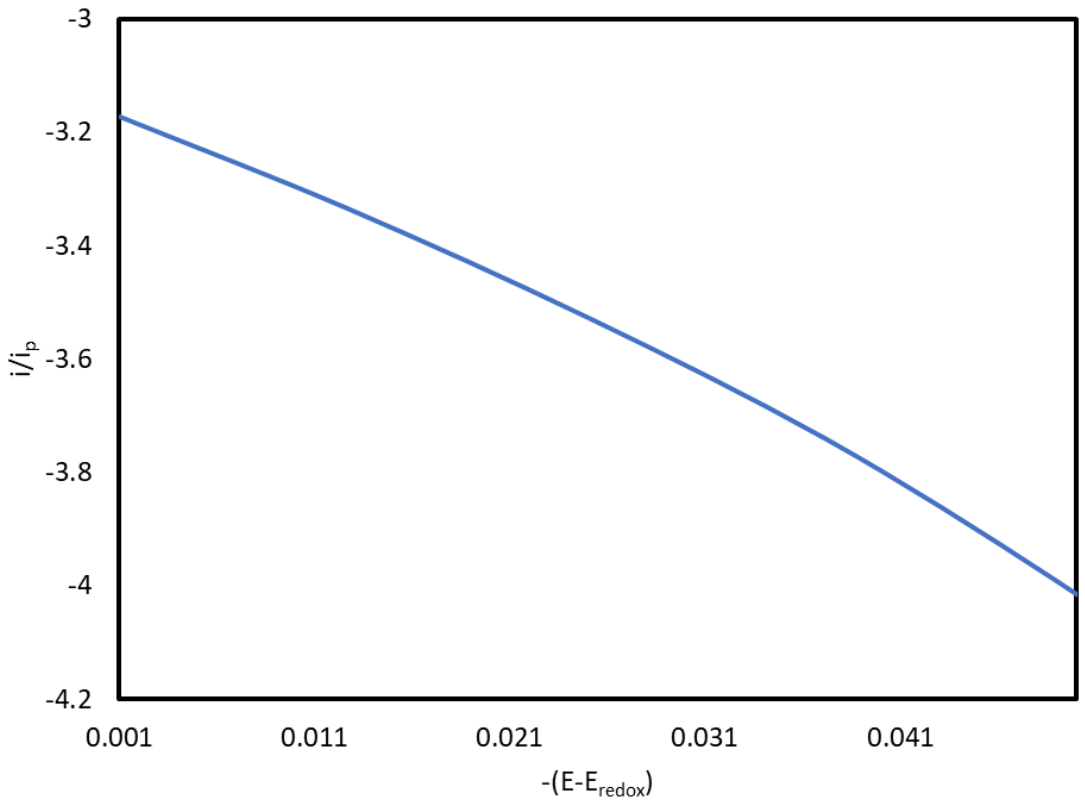

Figure 4.15. Graph of the kinetic region used for the foot-of-the-wave analysis for complex 1.

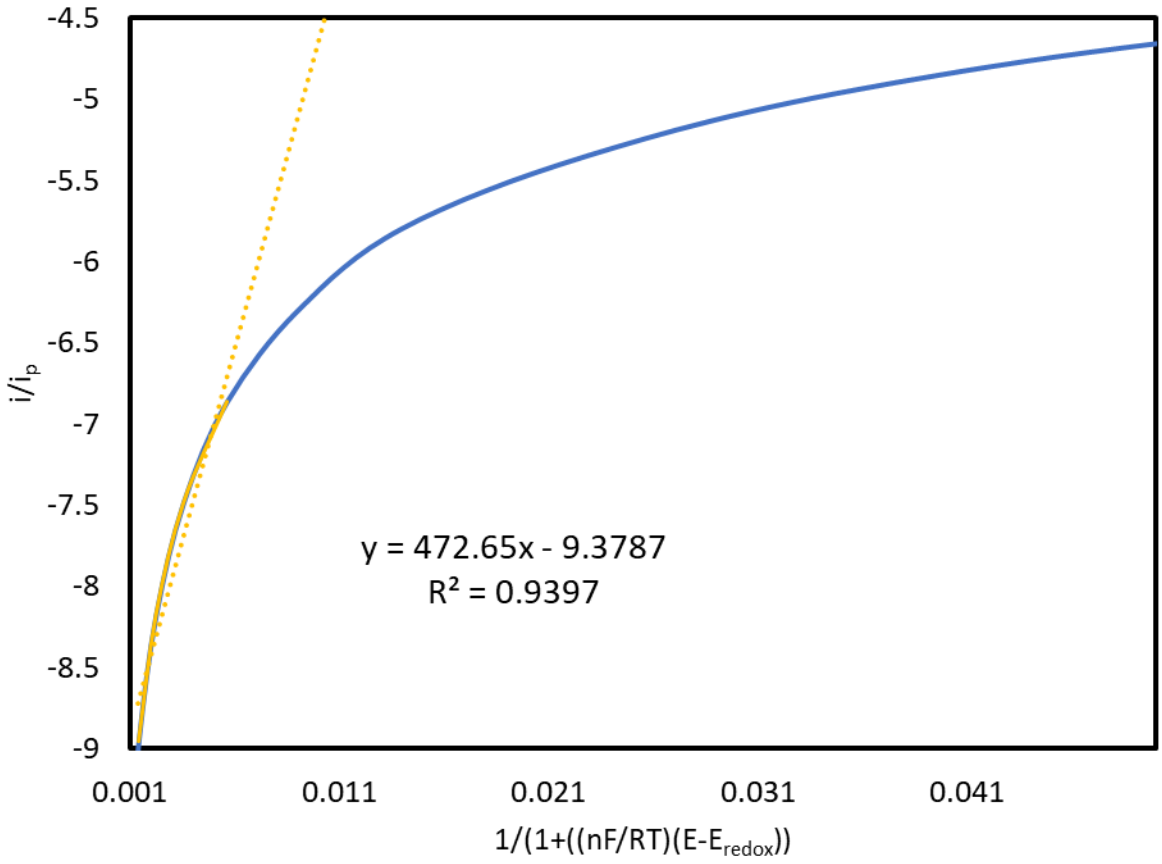

Figure 4.16. FOWA for complex 1. The yellow line represents the slope, given by $2.24\sqrt{\frac{RT(TOF)}{n'Fv}}$ ***with n' = 6 for the reduction of nitrite to ammonium. The equation for the line is given in the figure.***

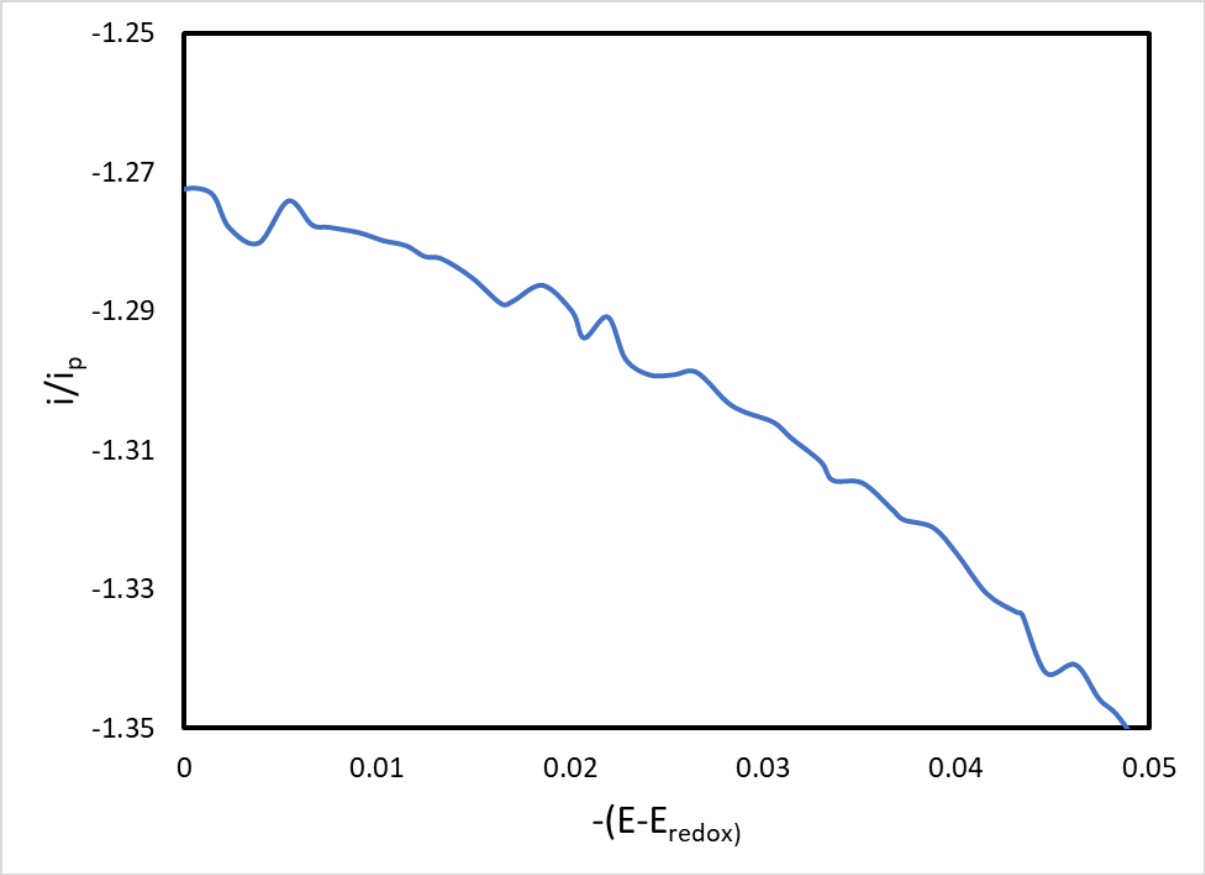

Figure 4.17. Graph of the kinetic region used for the foot-of-the-wave analysis for complex 2.

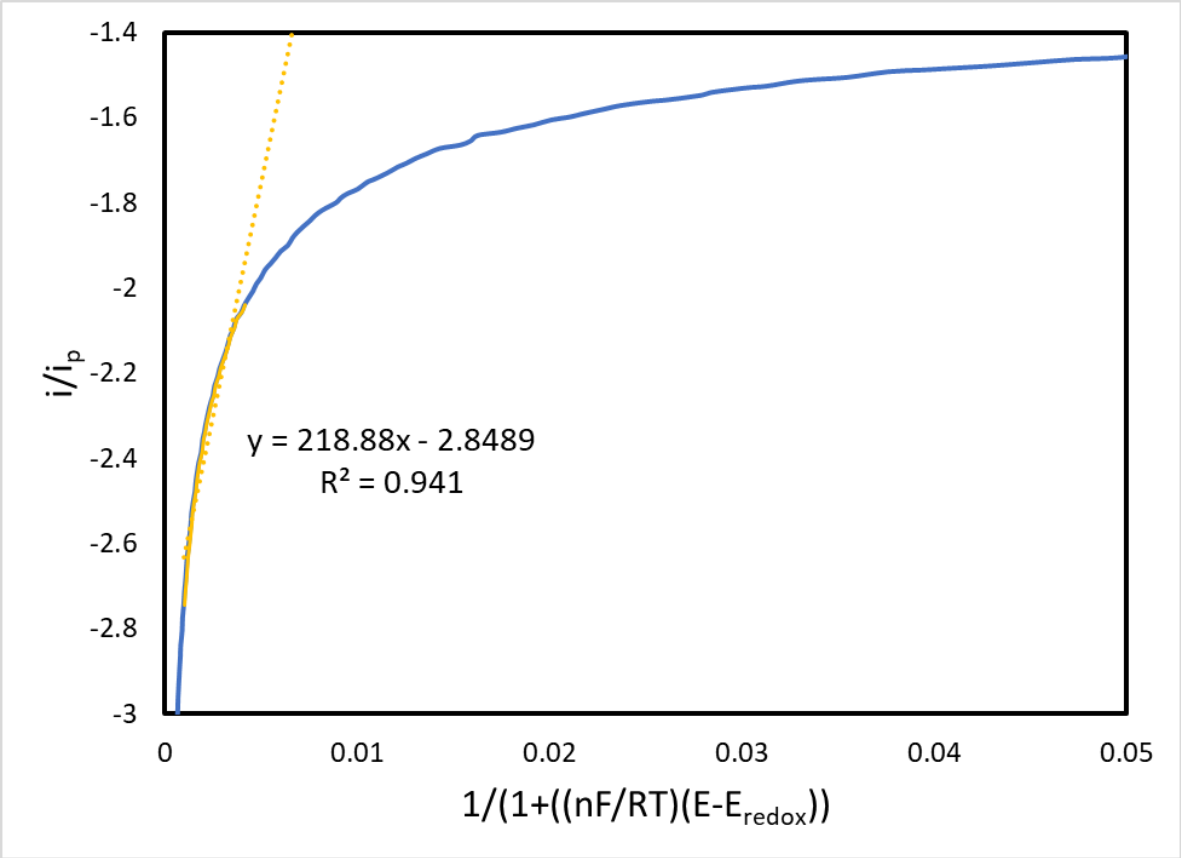

Figure 4.18. FOWA for complex 2. The yellow line represents the slope, given by $2.24\sqrt{\frac{RT(TOF)}{n'Fv}}$ ***with n' = 6 for the reduction of nitrite to ammonium. The equation for the line is given in the figure.***

A control experiment was carried out to establish the potential required to observe nitrite reduction in the absence of a catalyst. The results of cyclic voltammetry measurement of a solution with 100 mM MOPS buffer and 100 mM $NaNO_2$ are shown in Figure 4.19 and document that applied voltages exceeding -1.2V vs Ag/AgCl would be required to see the current enhancement associated with the reaction. This demonstrated the requirement of catalysts **1** and **2**.

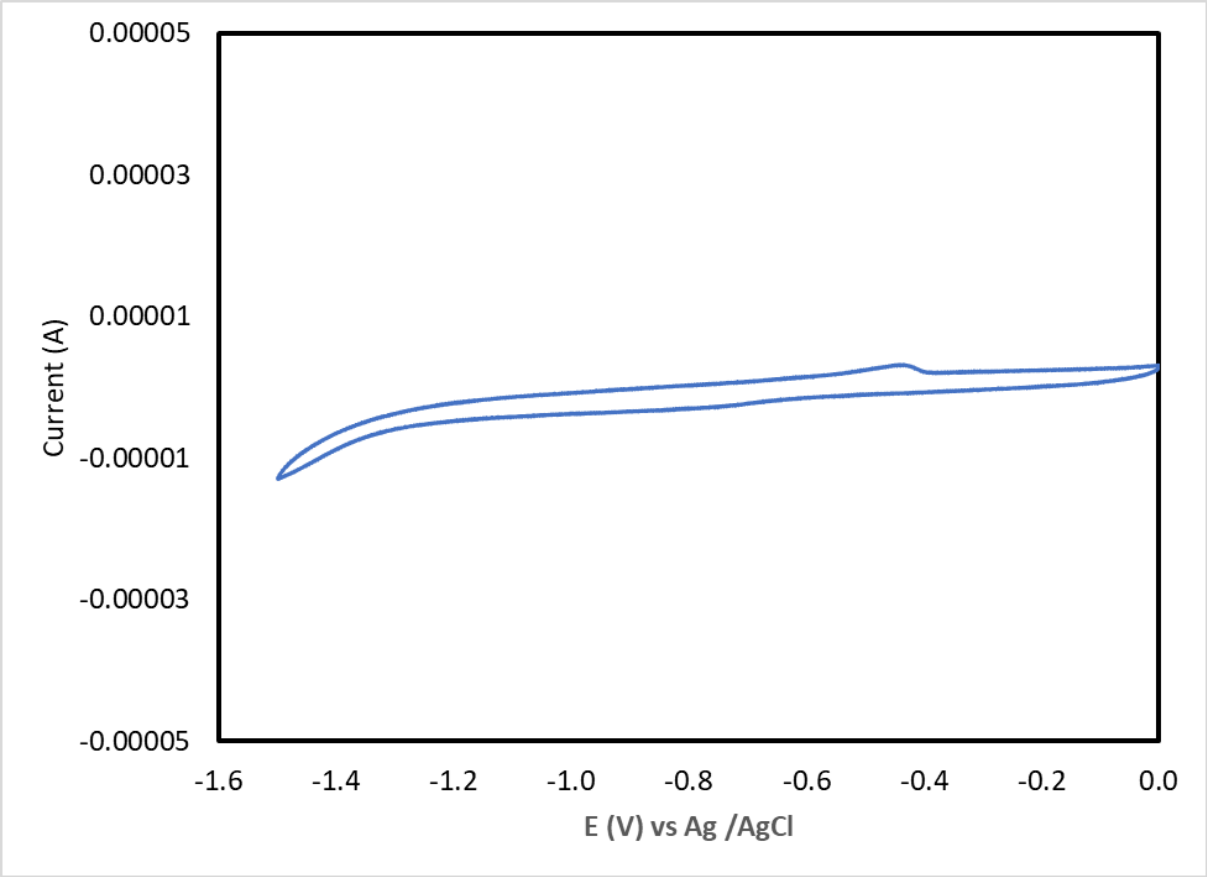

Figure 4.19: CV in the absence of catalyst of an aqueous 100 mM MOPS and 100 mM $NaNO_2$ solution with 0.1 M KCl as the supporting electrolyte, a GC working, Pt counter and Ag/AgCl reference electrode.

These electrochemical characterization experiments of **1** and **2** demonstrated significant current enhancement at -1.05V *vs.* Ag/AgCl in the presence of NO_2^- and MOPS buffer (pH 7) thus suggesting electrocatalytic reduction. To determine the product identities and selectivity as well as activity and efficiency, controlled potential electrolysis (CPE) experiments were explored. Measurements were carried out at -1.05V *vs.* Ag/AgCl. The resulting current *vs*. time profiles are shown in Figures 4.20 and 4.21. The background current in the absence of a catalyst is also shown in these Figures. The charge/time

profiles in all cases displayed a steady linear increase consistent with a stable current transfer from the catalyst to the nitrite substrate. The higher rate of charge transfer for **1** compared to **2** is consistent with the Ni complex displaying a higher rate of reaction than the Co analog.

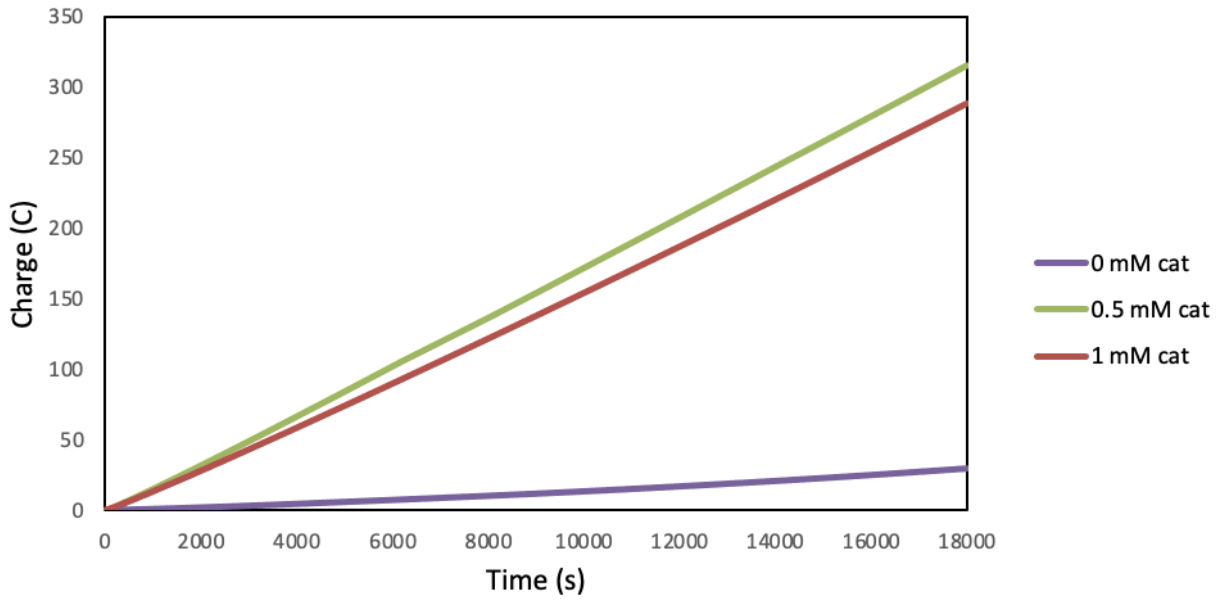

Figure 4.20: Plots showing the controlled potential coulometry measurements for compound 1 at -1.05V vs Ag/AgCl in the presence to 1M $NaNO_2$ and 1 M MOPS buffer.

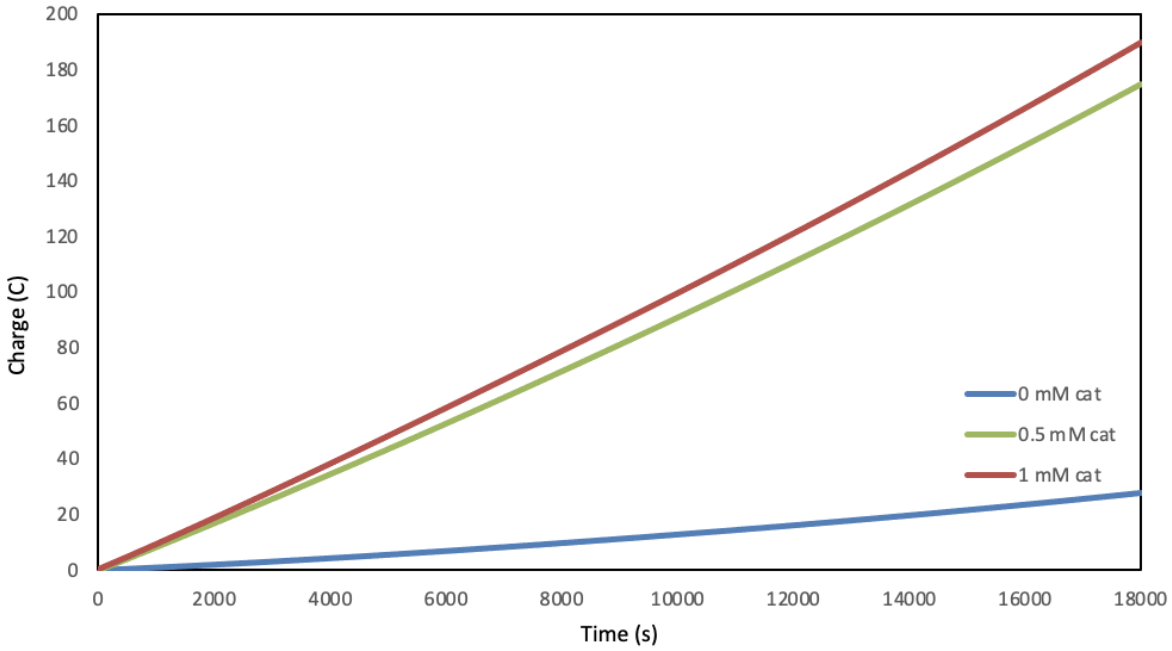

Figure 4.21: Plots showing the controlled potential coulometry measurements for compound 2 at -1.05V vs Ag/AgCl in the presence to 1M $NaNO_2$ and 1 M MOPS buffer.

Analysis of possible gas phase products, in the reaction headspace, by GC/MS confirmed the absence of NO and N_2O (Figure 4.22). Solution analysis by ^{14}N NMR confirmed the presence of ammonium and was used for quantification (Figures 4.23, 4.24). The formation of hydroxylamine was confirmed by redox titration with $[K_3Fe(CN)_6]$.[38] The results of several coulometry experiments for complexes **1** and **2** are presented in Table 4.2.

Table 4.2. Bulk results for the electrocatalytic reduction of nitrite using complex 1 and complex 2. Unless otherwise noted, all reactions were performed at -1.05V vs Ag/AgCl and contain 1.0 M MOPS buffer adjusted to pH 7.0, 1.0 M $NaNO_2$, and 0.1 M KCl as the supporting electrolyte.

Entry	Complex	[cat] (mM)	Time (hr)	µmol NH_4^+	µmol NH_2OH	Overall FE (%)
1	**1**	0.5	5	349	52	79
2	**1**	1	18	1681	12.8	76
3	**1**	1	5	314	90	81
4[a]	**1**	1	5	179	15	86
5	—	—	5	0	9	—
6[b]	**1**	1	5	0	0	—
5	**2**	0.5	5	206	54	80
6	**2**	1	5	219	108	90
7	**3**[c]	1	1	17.3	—	88

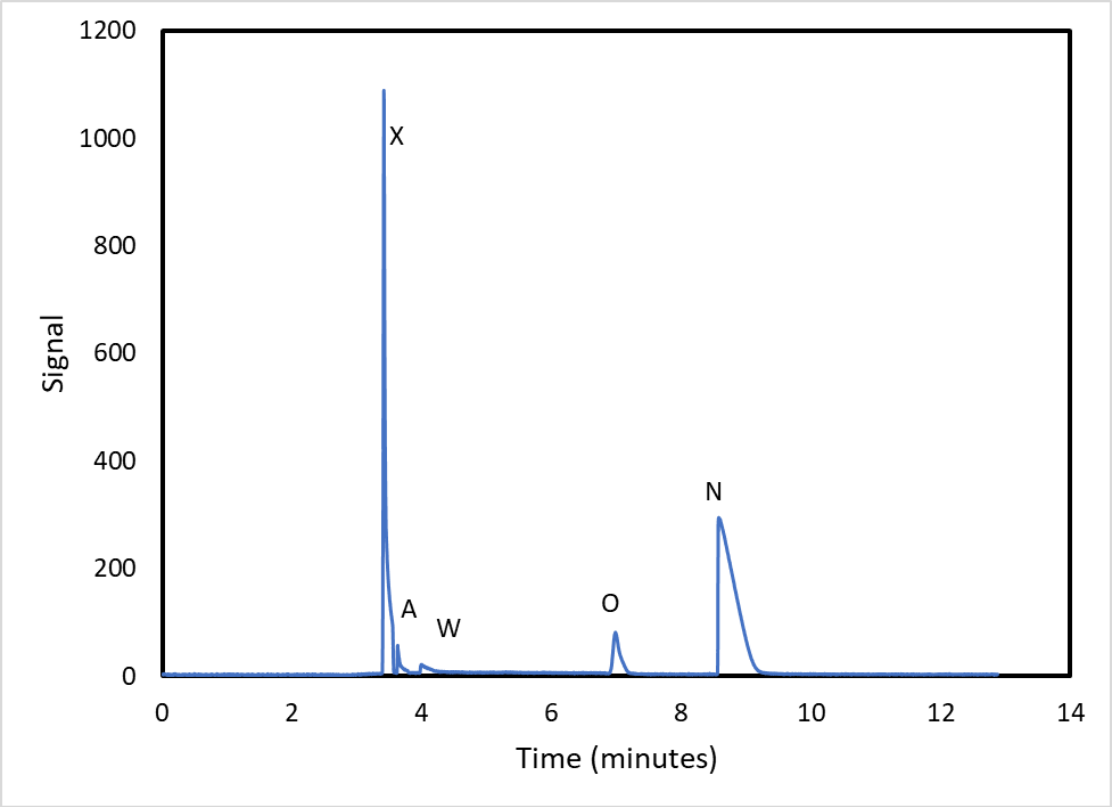

Figure 4.22: GC trace from a bulk electrocatalytic reduction of nitrite using complex 2 using an Agilent Select Permanent Gas parallel column. The peaks are labelled as follows: X is from nitrogen/oxygen passing through the parallel column; A is due to ammonia gas; W is due to water vapor; O is due to oxygen gas; N is due to nitrogen gas.

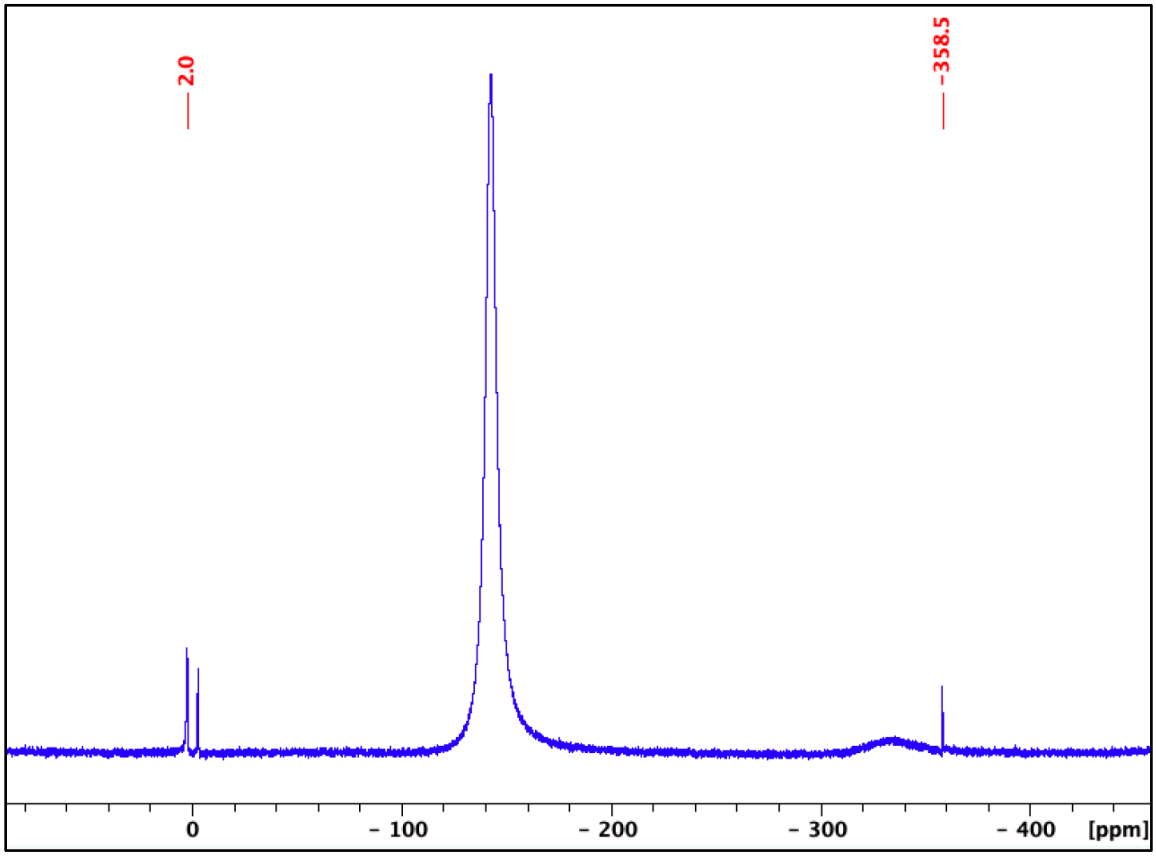

Figure 4.23: Nitrogen-14 NMR spectrum of a 0.5mL aliquot of the reaction solution and 0.2mL of acetonitrile-d3 with a 1.0M $MeNO_2$ external reference at 2.0ppm using a Bruker AVANCEIII 500MHz spectrometer with 600 scans. The broad peak at -330 ppm depicts the 1.0M MOPS buffer and the peak at -2.8 ppm depicts the nitrate anion.

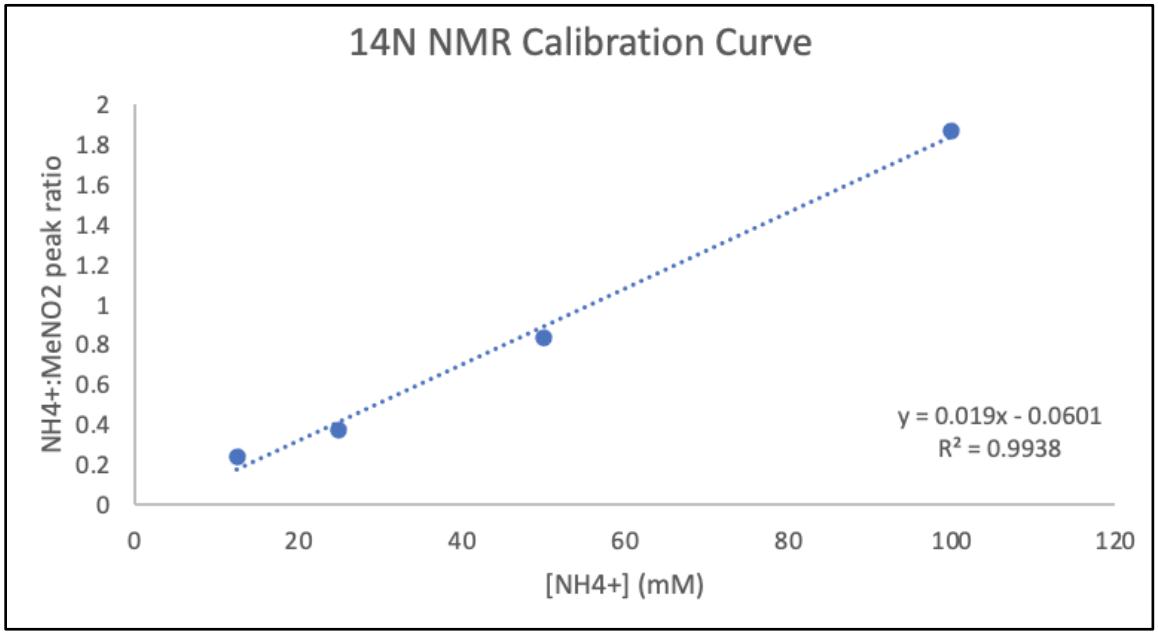

Figure 4.24: Calibration curve comparing peak areas of the external $MeNO_2$ standard with known concentrations of [NH_4^+] compared to the peak area of a 1.0 M $MeNO_2$ standard in a capillary tube.

Background coulometry measurements were conducted in the absence of catalyst and no NH_4^+ or NH_2OH were detected, thus ensuring that no product formation occurred due to the GC electrode. Furthermore, no products were detected in reactions carried out in the absence of MOPS buffer, further solidifying the observation that a buffered solution is a necessity for effective electrocatalysis. Catalyst performance was also evaluated at a slightly lower applied potential of -0.98V and presented as entry 4. Not surprisingly, the lower applied potential led to a lower conversion to ammonium and hydroxylamine. A preliminary assessment of the catalytic stability of **1** was examined by carrying out the electrocatalytic reaction for 18 hours (entry 2). This experiment produced significantly more NH_4^+ (1681 µmol) with a turnover number of 110, demonstrating catalyst durability. A comparison of the productivity of **1** with **2** revealed a lower product formation and

lower selectivity for NH_4^+/NH_2OH with the Co complex. Finally, a comparison of the performance of **2** with the reported electrocatalytic ability of the analogous Co(III) 2,12-dimethyl-3,7,11,17-tetraazabicyclo[11.3.1]heptadeca-1(17),2,11,13,15-pentaene complex **3** (figure 4.25) seemed to show that although **2** showed similar FE, the rate of product formation appeared to be higher and the selectivity for ammonium lower than for **3**.[16] However, it should be noted that a direct comparison of catalytic performance of **1** and **2** with that for **3** is complicated by the fact that the latter was investigated using unbuffered reaction conditions.

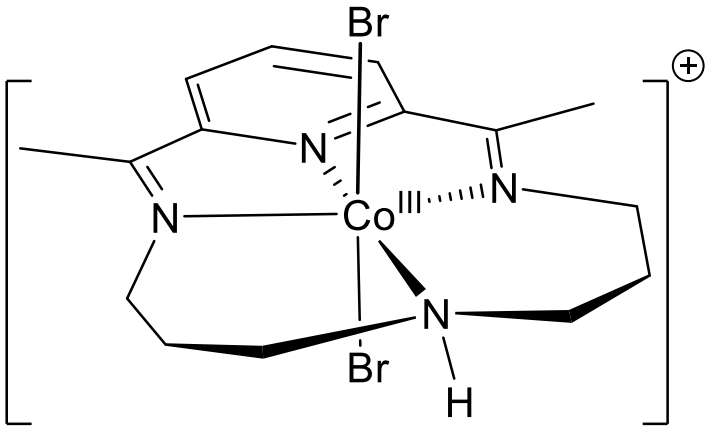

Figure 4.25: Chemical structure of 2,12-dimethyl-3,7,11,17-tetraazabicyclo[11.3.1]heptadeca-1(17),2,11,13,15-pentaene (complex 3).

4.5 – Computational Analysis & Proposed Mechanism for NO_2^- Reduction

The mechanism has been analyzed using experimental data and theory.[39] To better understand the observed redox events and to support and inform the nitrite reduction reaction mechanism, density functional theory (DFT) calculations were performed on Ni complex **1** in water, using the polarizable continuum model (PCM) at the M06L level of

theory.[40] Geometry optimization and vibrational frequency calculations were performed using def2-SVP as a basis set, followed by molecular energy computations with the def2-TZVP basis set. The results for the optimization of **1** were consistent with the experimentally determined single-crystal X-ray analysis.[24] Furthermore, the frontier molecular orbitals that displayed significant d-orbital contribution were as expected for the square planar Ni(II) geometry (Figure 4.26). In particular, the highest occupied molecular orbital (HOMO, MO87) was essentially the Ni d_z^2 and HOMO-1, HOMO-2, and HOMO-3 corresponded to the d_{yz}, d_{xz}, and d_{xy} orbitals, respectively. The lowest occupied molecular orbital (LUMO, MO88) was composed of a π^* orbital of the bis(imino)pyridine portion of the ligand. This ligand-based MO provides a means for the ligand to act as an electron reservoir for electrocatalysis. [41]

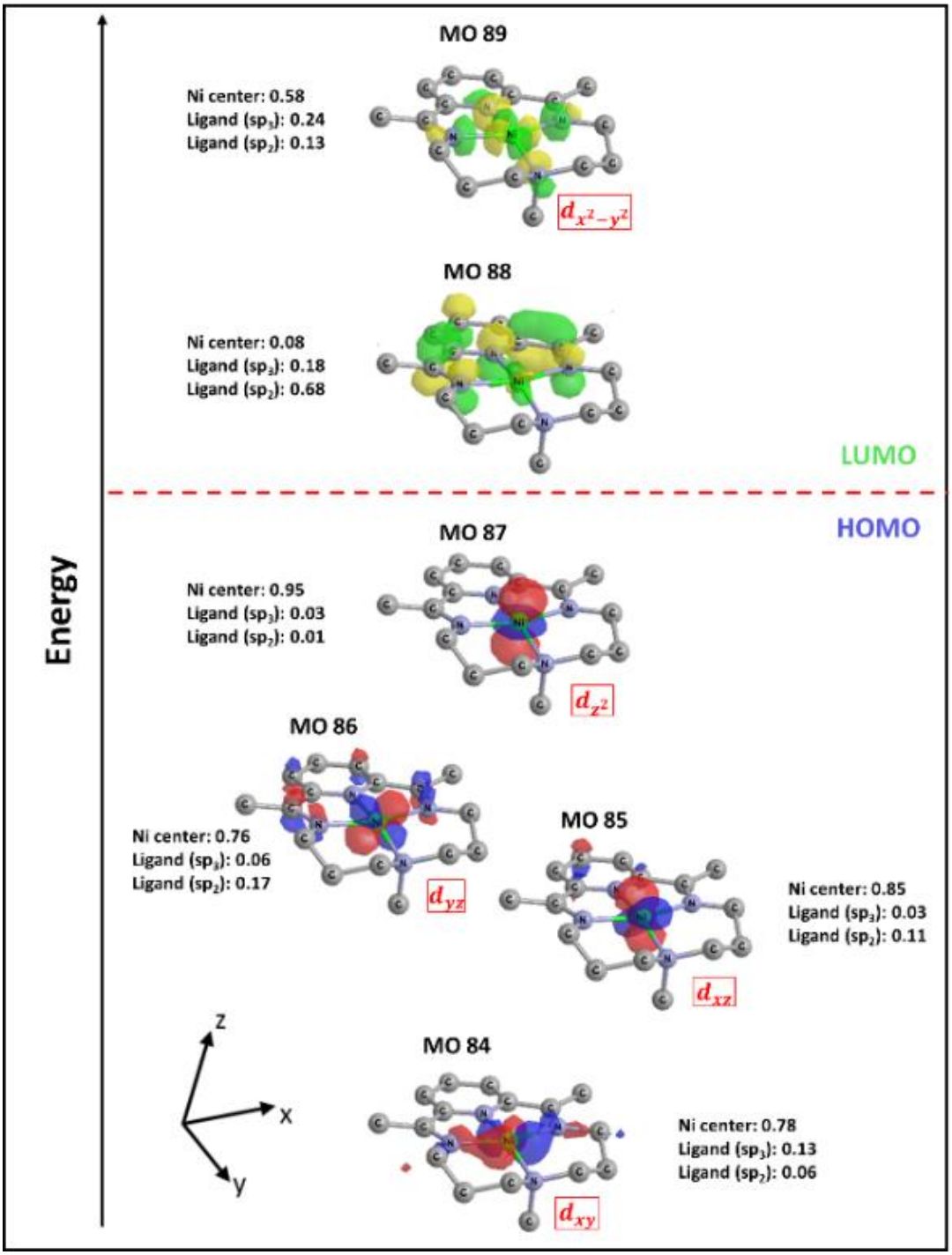

Figure 4.26: Selected molecular orbitals of complex 1 calculated using the M06L functional, the def2-TZVP basis set and using the PCM model for solvation in water.

Computational optimization on both single and double reduction products (reductions at -0.89V and -1.05V) of **1** was also completed and the resulting structures and frontier orbitals are shown in Figures 4.27-4.28. Isosurface plots for these species display similar features and vary only slightly in terms of MO contributions. The electrons added during these two reduction steps sequentially populated the π^* molecular orbital (MO88) delocalized over the pyridine and imine moieties of the ligand with little contribution from the metal center. The geometry of the simulated structures and the Ni-centered d-orbital remained essentially unchanged in this process.[32]

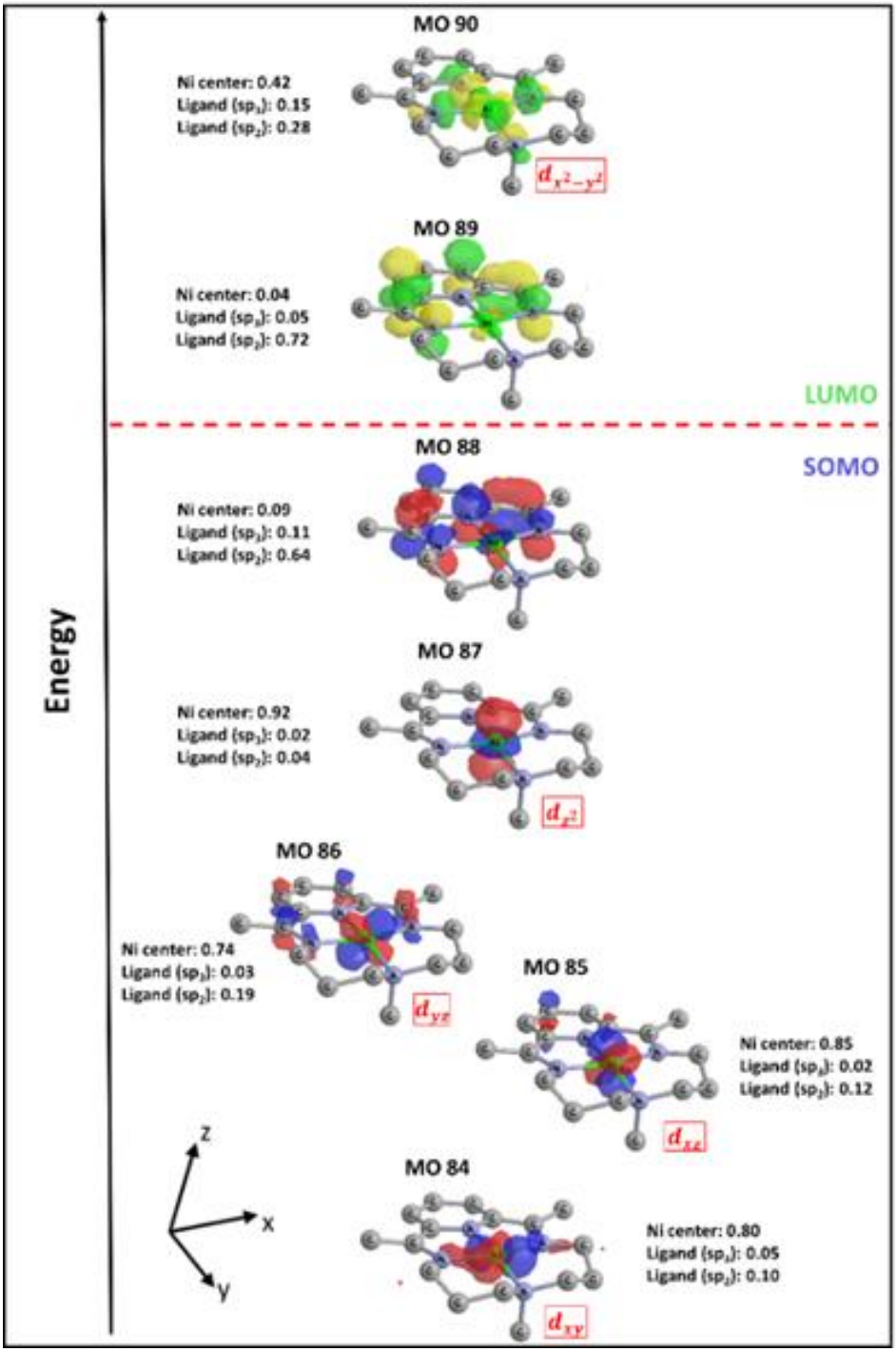

Figure 4.27: Selected molecular orbitals of 1$^-$, the complex formed after the first reduction of 1, calculated using the M06L functional, the def2-TZVP basis set and using the PCM model for solvation in water.

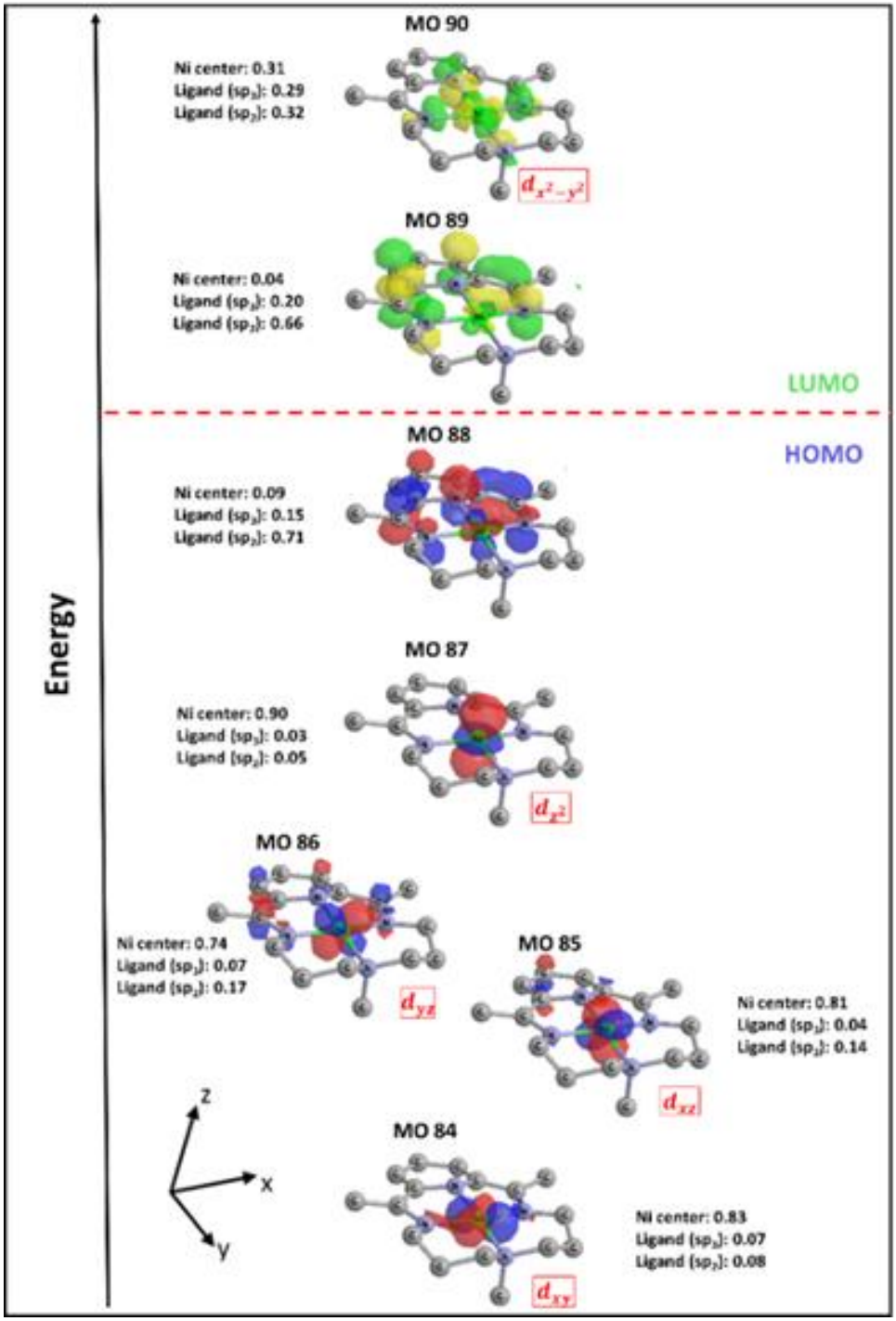

Figure 4.28: Selected molecular orbitals of complex 1^{2-} the complex formed after the second reduction of 1, calculated using the M06L functional, the def2-TZVP basis set and using the PCM model for solvation in water.

A proposed mechanism, informed by detailed DFT calculations and influenced by the reported mechanism for cytochrome c nitrite reductase[39] is presented in Scheme 4.2. The initial calculated structure of **1** forms the start of the catalytic cycle **(a)**. The first step is apical coordination of nitrite as the N-nitrito linkage isomer in an exergonic step (-7.37kcal/mol), to generate **(b)** resulting in Ni in a square-based pyramidal geometry. The Ni-NO_2 bond order was calculated to be 0.65 and the nitrite coordination led to a bend of the sp^3 nitrogen out of the bis(imino)pyridine plane.

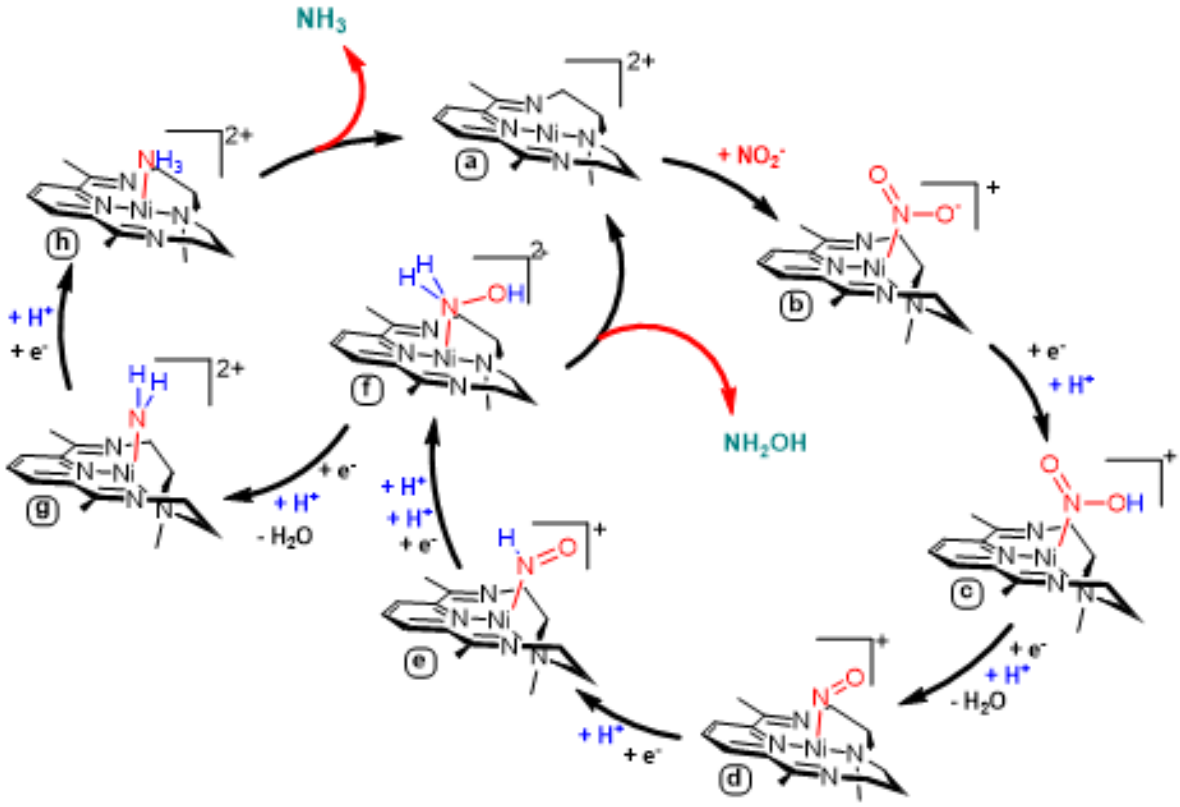

Scheme 4.2. Computationally supported proposed mechanism for the reduction of nitrite by complex 1. Calculated thermodynamic values are given in Table 4.3.

Table 4.3. Gibbs free energy values for the proposed compounds in Scheme 4.2.

Compound	M06L Energy	Gibbs Thermal Correction	Overall Gibbs Energy
$[NiN_4]^{2+}$ **(a)**	-2351.444351	0.343508	-2351.100843
$[NiN_4(NO_2)]^{+}$ **(b)**	-2556.787537	0.351578	-2556.435959
$[NiN_4(NO_2)]^{+}$ 1e-$1H^{+}$ **(c)**	-2557.379219	0.355958	-2557.023261
$[NiN_4(NO)]^{+}$ 2e-$2H^{+}$ **(d)**	-2481.529416	0.344764	-2481.184652
$[NiN_4(NHO)]^{+}$ 3e-$3H^{+}$ **(e)**	-2482.144732	0.353689	-2481.791043
$[NiN_4(NH_2OH)]^{2+}$ 4e-$5H^{+}$ **(f)**	-2483.210799	0.383731	-2482.827068
$[NiN_4(NH_2)]^{2+}$ 5e-$6H^{+}$ **(g)**	-2407.373174	0.364476	-2407.008698
$[NiN_4(NH_3)]^{2+}$ 6e-$7H^{+}$ **(h)**	-2408.034268	0.379381	-2407.654887
Nitrite	-205.3078957	-0.015468	-205.3233637
Water	-76.45040517	0.003924	-76.44648117
Ammonia	-56.57467706	0.016575	-56.55810206
Hydroxylamine	-131.7539513	0.017799	-131.7361523
Hydrogen	-1.171683505	-0.001491	-1.173174505

Addition of an electron and a proton to **(b)** proceeded to **(c)**. The reduction step proceeded through an endergonic (6.87kcal/mol) step to yield a singly occupied MO with 45% Ni-centered $d_{x^2-y^2}$ character that was antibonding with the three bis(imino)pyridine nitrogen centers. (Figure 4.29). The occupancy of this orbital led to the sp^3 nitrogen of the NMe group to bend further out of the plane (bond angle between the N_{py}-Ni-NMe 130.8°). The protonation of the nitrite oxygen was calculated to be downhill by -6.57kcal/mol and led to the N-coordinated HONO group of **(c).**

In the next step, an electron addition to **(c)** resulted in electron density forming on the coordinated HONO rather than the Ni(II) center. This also led to a more planar arrangement of the four coordinating N centers of the macrocycle ligand, which is attributed to lowering the energy of this transformation.[42] Protonation of the electron-rich oxygen center of the HONO ligand is coupled with the release of water and the formation of the nitrosyl complex **(d)**. Overall, this transformation was calculated to be exergonic by -36 kcal/mol.

Calculations on the nitrosyl complex, **(d)**, indicated a bent structure consistent with an NO^+ ligand bonded to Ni(II) with the HOMO of this proposed species localized as a lone pair on the nitrosyl. The LUMO for **(d)**, also localized on the NO ligand, can accept an electron in an endergonic step (10.26 kcal/mol). Following this reduction, protonation occurs on the nitrosyl lone pair with a release of -21.95kcal/mol and forming **(e).**[39] The magnitude of the exergonic protonation following the reduction, suggests a proton coupled electron transfer.[42,43]

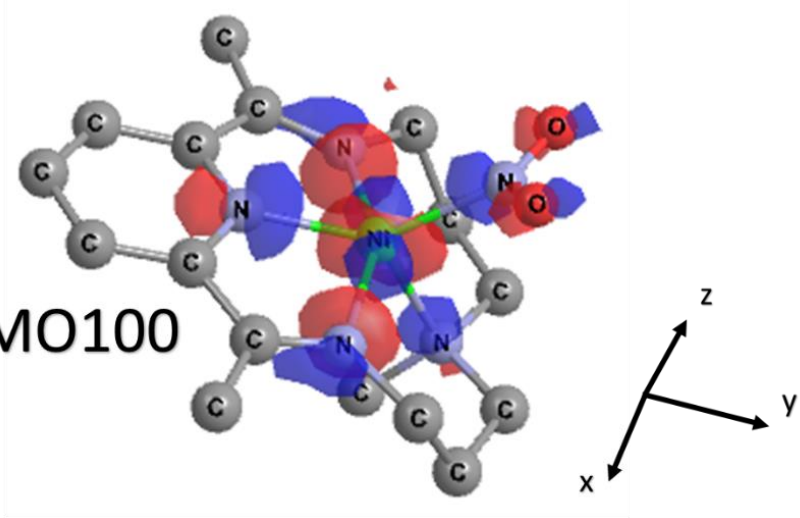

Figure 4.29: Isosurface image representing the SOMO for the species formed when (b) from Scheme 2 is singly reduced.

Proposed complex **(e)**, is an N-coordinated nitroxyl (HNO) species with a SOMO that is localized on Ni in a $d_{x^2-y^2}$ indicative of a Ni(I) species (Figure 4.30). Reduction of this species results in electron redistribution from the Ni to the di(imino)pyridyl and nitroxyl groups. The tetraazamacrocycle displayed a four-coordinate, distorted square planar coordination to what can be interpreted as a Ni(II) center. The added electron density on the nitroxyl initiates a protonation on the nitrogen in a concerted fashion with an overall endergonic transformation cost of 5.9 kcal/mol.[42] This step promotes the loss of the N=O double bond and formation of a negatively charged terminal O group. As a result, a second protonation is calculated to be energetically favored (-16.2 kcal/mol) to generate complex **(f)**. Calculations suggested that **(f)** was a d^8 Ni(II) species supported by the tetraazamacrocycle and having a coordinated hydroxylamine group. The hydroxylamine ligand appeared to be loosely bound to the metal center, having a bond order of 0.29.

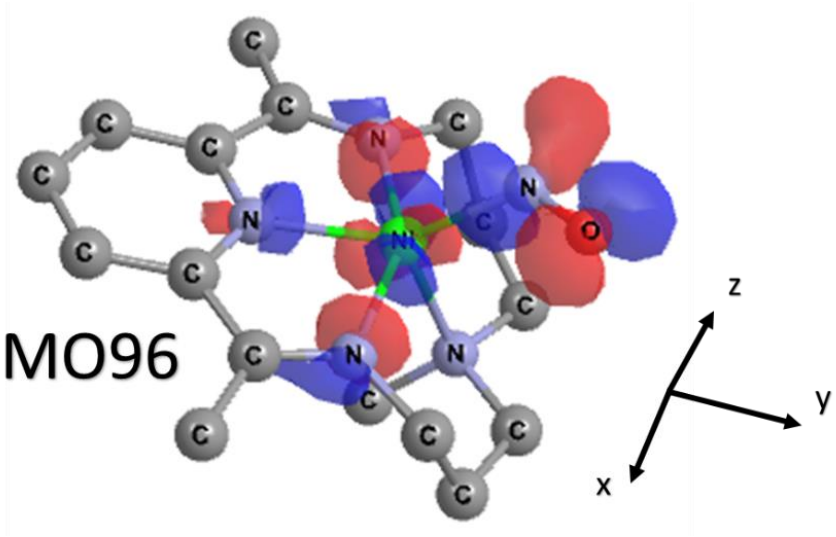

Figure 4.30: Isosurface image representing SOMO of species (e) from Scheme 2.

At this point, the proposed mechanism can bifurcate to two potential paths. In the first, hydroxylamine can be released as a free product, closing the catalytic cycle with a relative Gibbs free energy of -6.23 kcal/mol. Alternatively, **(f)** can undergo a rather low energy (3.94 kcal/mol) reduction step that bolsters the bonding interaction between the nickel and hydroxylamine, increasing the bond order to 0.43. This strengthening of the bond between hydroxylamine and Ni corroborates the experimental findings of relatively low production of hydroxylamine, compared to ammonia. It appears that the reduction step occurs more readily than the dissociation, favoring the continuation of this path in the catalytic cycle. Following this reduction, the addition of a proton to the oxygen center of the hydroxylamine occurs at a relative Gibbs free energy of -29.25kcal/mol providing water as a leaving group and yielding the amido species **(g)**.[44]

The Ni-amido can be reduced and protonated with exergonic steps of -8.60 kcal/mol and of -28.05 kcal/mol respectively. The result was a Ni(II) complex with an additional apically

coordinated amine ligand, **(h)**[45] Ammonia is weakly bound to nickel, having a calculated bond order of only 0.31. Release of ammonia from **(h)** into solution (-2.55 kcal/mol) completes this leg of the catalytic cycle and regenerated complex **(a)**. Ammonia was the major observed product and was detected as the ammonium ion by ^{14}N NMR analysis. The overall proposed cycle in Scheme 2 was completed with the addition of 6 electrons and 7 protons.

4.6 – Conclusion

Increasing nitrite levels in the environment with anthropogenic origins have become an important ecological and human health issue and make the discovery of new and creative methods for the reduction of this species, such as electrocatalysis, a topical concern. This report of two new electrocatalysts for the reduction of nitrite represents a significant addition to this field. Cobalt complex **2** provided a unique Co(II) tetraazamacrocycle that was an effective electrocatalyst for the reduction of NO_2^-. These results provide an advantageous and necessary comparison to a growing number of reported Co(III) catalysts. Significantly, the documentation of **1** as a Ni(II) nitrite reduction electrocatalyst is an exceptional contribution given the noticeable absence of Ni complexes in the armory of such catalysts.

While we focused on Ni complex **1**, both complexes **1** and **2** efficiently reduce nitrite to ammonium as the major product at applied potentials less than -1.05V vs. Ag/AgCl. Both complexes generated some hydroxylamine as a minor product, but the Ni complex provided a superior selectivity for NH_4^+ compared to the Co analog. FOWA indicated that the rate for reduction from the Ni species (TOF) was higher than for the Co complex.

In addition to the electrochemical characterization, a detailed computational examination of the catalytic mechanism of Ni complex **1** was used to illuminate the proposed chemical steps and reveal the energetic features of the electron and proton transfers. Furthermore, the calculation advanced a rationale for the selectivity of ammonium versus hydroxylamine.

Importantly, this type of investigation addresses the particular features of nitrite electrocatalytic reduction and provides information on both practical and fundamental levels to understand methods to control electrocatalysis.

4.7 – Experimental and Computational Details

General methods

Reactions were performed using standard Schlenk techniques under a flow of N_2 gas. All solvents were dried with activated molecular sieves and sparged with nitrogen. Deuterated solvents were dried using activated molecular sieves. All other chemicals were purchased from Sigma-Aldrich and used without further purification. Dried acetonitrile was purchased from Sigma-Aldrich and stored on molecular sieves in a glovebox.

Synthesis and characterization of Ni(II)(2,7,12-trimethyl-3,7,11,17-tetraazabicyclo [11.3.1]heptadeca-1(17),13,15-pentaene)$(ClO_4)_2$ (**1**) and Co(II)(2,7,12-trimethyl-3,7,11,17-tetraazabicyclo [11.3.1]heptadeca-1(17),13,15-pentaene)$(ClO_4)_2$ (**2**) followed the reported processes. [27–29]

Electrochemistry

All cyclic voltammetry experiments were carried out in a cell of approximately 50 mL volume under an atmosphere of dinitrogen. Samples were prepared in the open air, sealed, connected to a Schlenk line, and purged with a nitrogen atmosphere. Measurements were carried out using a VersaSTAT potentiostat (Princeton Applied Research). A conventional three-electrode system was employed consisting of a glassy carbon electrode (diameter = 0.4 cm), as the working electrode, a Pt wire, or a glassy carbon rod as the counter electrode, and an Ag/AgCl (3.5M KCl) electrode was used as a reference electrode. For bulk electrocatalytic experiments, a glassy carbon rod (diameter = 0.4cm; length = 2cm) was used as the working electrode, a coiled Pt wire as the counter electrode with a Ag/AgCl (3.5M KCl) as the reference electrode.

Computational methods

Calculations were performed using the Gaussian 09 software package through the WebMO interface. Initial structures were established from single crystal-XRD coordinates and intermediates were proposed by the addition of single protons and electrons, assuming singlet and doublet spin states for electron additions. All calculations were performed at the M06L functional.[40] Optimization and vibrational frequencies were calculated using the def2-SVP basis set. Absolute minima of the electronic structures were confirmed by verifying an absence of negative vibrational frequencies before single-point energy calculations were performed.[46–50] Molecular energy single-point calculations and molecular orbital isosurface simulations were performed using the def2-TZVP basis set. Molecular orbitals were visualized using Chemissian software. The polarizable continuum

model (PCM) was used to simulate a solvent system of water for all optimization and molecular energy computations. Relative Gibbs free energy calculations were completed for all coordination, dissociation, reduction, and protonation steps. Ligand structures occupying the apical site were computed in a similar manner as complexes to complete the relative Gibbs free energy calculations. Proton and electron additions were accounted for by calculating H_2 at the same level of theory as all the other structures and attributing half its energy to the joint addition of a proton and an electron. The energy for H_2 was calculated following the same protocol as all other calculations and was determined to be 31.924 eV.[47,48] . Each proton addition contributes 11.752 eV and each electron addition contributes 4.242 eV.[47,48]

Product identification & quantification

^{14}N NMR spectroscopy was used to identify and quantify ammonium ion (NH_4^+). A calibration curve with known concentrations of [NH_4^+] was prepared using an external standard of $MeNO_2$ (Figure 4.23).The analysis of NH_2OH production was performed using a redox titration with [$K_3Fe(CN)_6$].[38] The reaction vessel was also tested for the formation of NO using the qualitative myoglobin test.[10] GC-TCD also showed no formation of N_2 when CPE was performed under an argon atmosphere.

Molecular optimization coordinates for Table 4.3 and Scheme 4.2

$[NiN_4]^{2+}$ (initial) (a)
Coordinates (xyz) for optimized structures – 56368

```
28 0.379491 -0.000069 -0.125742
7 0.096032 -1.924770 -0.170729
6 -1.151630 -2.297390 -0.092874
6 -1.614227 -3.700878 -0.182971
1 -2.699472 -3.781647 -0.084056
1 -1.153715 -4.319037 0.600140
1 -1.326238 -4.142736 -1.146988
6 -2.095215 -1.179852 0.043354
7 -1.463443 0.000089 -0.049782
6 -2.095023 1.180121 0.043470
6 -3.477990 1.211879 0.227548
6 -4.163559 0.000288 0.319895
6 -3.478188 -1.211405 0.227417
1 -4.011284 -2.158672 0.301943
1 -5.243709 0.000369 0.466954
1 -4.010931 2.159225 0.302176
6 -1.151272 2.297521 -0.092729
7 0.096335 1.924730 -0.170666
6 1.126712 2.905633 -0.456161
1 0.833837 3.893736 -0.075081
1 1.179751 3.002762 -1.555577
6 2.483652 2.532772 0.092484
1 2.493566 2.618220 1.188488
1 3.196497 3.291576 -0.256004
6 3.007371 1.193497 -0.361012
7 2.324156 -0.000141 0.210424
6 2.417631 0.000146 1.684517
1 1.918991 0.882374 2.097312
1 3.472053 0.000438 2.003925
1 1.919398 -0.882176 2.097599
6 3.007340 -1.194037 -0.360508
1 4.075316 -1.111431 -0.097629
1 2.945571 -1.104013 -1.455179
6 2.483163 -2.533135 0.092991
1 3.195974 -3.292140 -0.255134
1 2.492649 -2.618448 1.189010
6 1.126340 -2.905774 -0.456089
1 1.179667 -3.002773 -1.555503
1 0.833235 -3.893885 -0.075206
1 2.945154 1.103278 -1.455646
1 4.075434 1.110722 -0.098535
6 -1.613677 3.701075 -0.182777
1 -2.698903 3.782000 -0.083787
1 -1.325691 4.142899 -1.146811
1 -1.153019 4.319163 0.600304
```

$[NiN_4(NO_2)]^+$ (b)
Coordinates (xyz) for optimized structures – 55014

```
28 -0.261269 -0.002419 0.394322
7 0.032941 -1.888283 0.257120
6 1.263545 -2.264918 0.004911
6 1.678983 -3.668772 -0.237910
1 2.764513 -3.753673 -0.340175
1 1.226383 -4.058469 -1.161038
1 1.362440 -4.328980 0.580208
6 2.200693 -1.149457 -0.052337
7 1.547062 0.030396 0.061280
6 2.172878 1.229980 0.033064
6 3.560042 1.273893 -0.119572
6 4.261153 0.072393 -0.238939
6 3.586039 -1.151538 -0.210559
1 4.134017 -2.089147 -0.308020
1 5.344959 0.088628 -0.355661
1 4.087557 2.227884 -0.143462
6 1.207106 2.312457 0.146026
7 -0.017781 1.891383 0.369959
6 -1.163534 2.770115 0.287365
1 -0.857747 3.821383 0.377915
1 -1.832745 2.544950 1.129401
6 -1.902259 2.552426 -1.030736
1 -1.215228 2.731177 -1.873767
1 -2.671471 3.333314 -1.114475
6 -2.614489 1.221761 -1.159240
7 -1.762220 0.011598 -1.181540
6 -0.970666 -0.044396 -2.414326
1 -0.346087 0.852811 -2.502236
1 -1.616724 -0.109983 -3.308113
1 -0.297948 -0.910462 -2.405230
6 -2.643588 -1.168496 -1.042739
1 -3.370250 -1.162015 -1.877474
1 -3.229200 -1.017608 -0.122303
6 -1.969020 -2.524694 -1.001995
1 -2.770210 -3.277031 -1.002599
1 -1.394994 -2.715615 -1.922344
6 -1.092532 -2.797152 0.215909
1 -1.671795 -2.659574 1.141539
1 -0.756804 -3.843294 0.204028
1 -3.308848 1.105244 -0.316953
1 -3.227182 1.229558 -2.080745
6 1.581665 3.737674 -0.030919
1 2.665507 3.859242 -0.113309
1 1.234454 4.352115 0.810285
1 1.130850 4.155336 -0.942660
7 -1.555253 -0.099721 1.895133
8 -1.227052 -0.821128 2.833315
8 -2.612606 0.529459 1.904746
```

$[NiN_4(NOOH)]^+$ 1e-$1H^+$ (c)
Coordinates (xyz) for optimized structures – 56540

```
28 0.391442 -0.014001 0.442670
7 0.031245 2.015993 0.189814
6 -1.210673 2.360961 0.044186
6 -1.682216 3.748326 -0.225492
1 -2.764884 3.849607 -0.108035
1 -1.435482 4.048514 -1.254983
1 -1.202342 4.473556 0.443260
6 -2.164160 1.231171 0.084620
7 -1.551296 0.035714 0.151237
6 -2.228235 -1.125693 0.100317
6 -3.623018 -1.119674 0.015403
6 -4.285068 0.108370 -0.023127
6 -3.557711 1.299124 -0.000486
1 -4.073475 2.258106 -0.053459
1 -5.373697 0.137388 -0.084766
1 -4.189771 -2.050058 -0.024960
6 -1.337736 -2.306538 0.081618
7 -0.080230 -2.023384 0.217252
6 0.974330 -2.989311 0.043907
1 0.605869 -4.022046 -0.056992
1 1.610685 -2.952270 0.942411
6 1.810409 -2.626429 -1.181108
1 1.199707 -2.738962 -2.091082
1 2.602648 -3.383082 -1.275717
6 2.509339 -1.278243 -1.157189
7 1.663577 -0.061370 -1.236146
6 0.844185 -0.054435 -2.449197
1 0.174477 -0.922141 -2.458636
1 1.465114 -0.076192 -3.363295
1 0.211863 0.840605 -2.475011
6 2.570250 1.112396 -1.183638
1 3.290588 1.026348 -2.020266
1 3.162074 1.014934 -0.258851
6 1.938209 2.491891 -1.239893
1 2.765637 3.206570 -1.357459
1 1.329356 2.610149 -2.150329
6 1.128976 2.927228 -0.020680
1 1.770743 2.892631 0.872617
1 0.805480 3.971181 -0.152733
1 3.108205 -1.190195 -0.236201
1 3.231814 -1.247519 -1.995687
6 -1.880066 -3.674710 -0.149839
1 -2.970169 -3.710280 -0.070420
1 -1.466685 -4.395635 0.566835
1 -1.612199 -4.033065 -1.154928
7 1.581526 -0.117367 1.949465
8 2.028208 1.113117 2.475754
1 2.746181 0.869718 3.095061
8 2.183450 -1.070560 2.398132
```

$[NiN_4(NO)]^+$ 2e-$2H^+$ (d)
Coordinates (xyz) for optimized structures – 56621

```
28 0.371687 -0.000424 0.242843
7 -0.034323 1.962889 -0.240681
6 -1.281126 2.308226 -0.009759
6 -1.725221 3.690970 0.308671
1 -2.814803 3.768352 0.379387
1 -1.374738 4.417345 -0.438948
1 -1.309561 4.015746 1.275146
6 -2.207511 1.182619 -0.046921
7 -1.597684 0.000284 0.216138
6 -2.208013 -1.181829 -0.046900
6 -3.564099 -1.209157 -0.377227
6 -4.246947 0.000815 -0.520016
6 -3.563587 1.210507 -0.377230
1 -4.071398 2.159319 -0.557648
1 -5.302198 0.001037 -0.796616
1 -4.072292 -2.157754 -0.557696
6 -1.282073 -2.307792 -0.009822
7 -0.035124 -1.962838 -0.240687
6 1.018462 -2.939584 -0.033410
1 0.731605 -3.916718 -0.456158
1 1.120144 -3.113397 1.055873
6 2.362740 -2.535683 -0.614035
1 2.329463 -2.587955 -1.712228
1 3.087084 -3.309703 -0.323386
6 2.955942 -1.212221 -0.165358
7 2.197826 -0.000253 -0.559648
6 1.906204 0.000073 -2.003356
1 1.312242 -0.880548 -2.266468
1 2.837796 0.000554 -2.592852
1 1.311662 0.880468 -2.265936
6 2.956337 1.211324 -0.164947
1 3.977113 1.122526 -0.578314
1 3.069361 1.175065 0.930304
6 2.363850 2.535057 -0.613688
1 3.088346 3.308766 -0.322582
1 2.331143 2.587485 -1.711892
6 1.019452 2.939434 -0.033601
1 1.120928 3.113844 1.055604
1 0.732917 3.916414 -0.456934
1 3.069304 -1.176156 0.929865
1 3.976661 -1.123856 -0.578976
6 -1.726646 -3.690408 0.308480
1 -2.816268 -3.767397 0.379040
1 -1.311250 -4.015392 1.274998
1 -1.376353 -4.416868 -0.439144
7 0.739744 -0.000227 2.002396
8 1.798275 -0.000302 2.516005
```

$[NiN_4(NHO)]^+$ 3e-$3H^+$ (e)
Coordinates (xyz) for optimized structures – 56696

```
28 -0.414861 -0.148921 0.605156
7 0.584691 -1.950504 0.420596
6 1.858735 -1.888072 0.185153
6 2.738102 -3.066238 -0.051590
1 3.799908 -2.806400 -0.015034
1 2.542506 -3.503044 -1.042447
1 2.558471 -3.856552 0.687826
6 2.385239 -0.509933 0.084816
7 1.417985 0.422735 0.135929
6 1.670913 1.735183 -0.008032
6 2.982675 2.177392 -0.198075
6 4.007821 1.230715 -0.237636
6 3.716478 -0.127107 -0.103224
1 4.515448 -0.867435 -0.147961
1 5.039745 1.553128 -0.382502
1 3.209019 3.237173 -0.316942
6 0.442470 2.561029 0.014183
7 -0.637203 1.887283 0.251143
6 -1.965070 2.427852 0.150797
1 -1.985114 3.522236 0.026980
1 -2.489775 2.178256 1.088489
6 -2.688004 1.762055 -1.017776
1 -2.196036 2.039592 -1.963856
1 -3.695239 2.198851 -1.079873
6 -2.881684 0.259360 -0.920405
7 -1.677754 -0.606076 -1.019570
6 -0.954789 -0.389558 -2.273453
1 -0.604123 0.647499 -2.333656
1 -1.588991 -0.601845 -3.152971
1 -0.069252 -1.034928 -2.314892
6 -2.142621 -2.011146 -0.895911
1 -2.847038 -2.212088 -1.725805
1 -2.738795 -2.064307 0.029133
6 -1.092866 -3.107612 -0.886747
1 -1.639139 -4.060237 -0.942136
1 -0.478550 -3.076035 -1.800788
6 -0.178405 -3.168641 0.334633
1 -0.792474 -3.259328 1.247091
1 0.447835 -4.072783 0.281598
1 -3.365855 0.017144 0.039140
1 -3.589145 -0.052470 -1.712444
6 0.484835 4.020702 -0.279769
1 1.504977 4.414173 -0.301326
1 -0.081640 4.594158 0.465079
1 0.029605 4.231119 -1.258902
7 -1.514882 -0.447006 2.126631
8 -2.488279 0.224412 2.535123
1 -1.476859 -1.372290 2.615954
```

$[NiN_4(NH_2OH)]^{2+}$ 4e-$5H^+$ (f)
Coordinates (xyz) for optimized structures – 56711

```
28 -0.262254 0.009265 0.063232
7 -0.011656 -1.903392 -0.025820
6 1.232731 -2.310420 -0.046849
6 1.654658 -3.730302 0.021552
1 2.740174 -3.833524 -0.055553
1 1.201456 -4.318626 -0.787645
1 1.339085 -4.188590 0.969015
6 2.195932 -1.215047 -0.114339
7 1.573512 -0.019383 -0.057321
6 2.233865 1.156058 -0.102658
6 3.625269 1.160129 -0.208043
6 4.296426 -0.062002 -0.268104
6 3.586661 -1.262637 -0.219460
1 4.108688 -2.218124 -0.267321
1 5.382829 -0.078904 -0.355627
1 4.177470 2.098896 -0.246760
6 1.307326 2.281677 -0.022968
7 0.049625 1.916997 -0.004079
6 -1.011911 2.883792 0.191353
1 -0.655793 3.899852 -0.025141
1 -1.276096 2.874188 1.264720
6 -2.240385 2.581677 -0.638988
1 -2.017878 2.711373 -1.708252
1 -2.990453 3.349745 -0.407757
6 -2.881370 1.243732 -0.361536
7 -2.101479 0.047155 -0.776741
6 -1.830750 0.077628 -2.227159
1 -1.215049 0.945378 -2.483367
1 -2.775175 0.125107 -2.794484
1 -1.278286 -0.817835 -2.528445
6 -2.924645 -1.141639 -0.427499
1 -3.874688 -1.054128 -0.982656
1 -3.167685 -1.054199 0.640545
6 -2.303566 -2.487307 -0.713387
1 -3.077678 -3.242873 -0.523432
1 -2.045381 -2.601368 -1.776518
6 -1.110421 -2.830248 0.152270
1 -1.402431 -2.798330 1.217811
1 -0.786204 -3.860345 -0.047071
1 -3.084618 1.129648 0.713192
1 -3.855260 1.194942 -0.878988
6 1.777306 3.685475 0.060757
1 2.865042 3.753492 -0.023820
1 1.484527 4.140704 1.017064
1 1.337474 4.300084 -0.736134
7 -0.803022 -0.013729 2.224017
8 -2.172049 -0.124371 2.528928
1 -2.261715 -0.130598 3.496592
1 -0.308720 -0.797550 2.662878
1 -0.435740 0.830194 2.675196
```

$[NiN_4(NH_2)]^{2+}$ 5e-$6H^+$ (g)
Coordinates (xyz) for optimized structures – 56828

```
28 -0.366138 -0.000391 -0.712492
7 -0.103900 1.922661 -0.534668
6 1.085973 2.301984 -0.156029
6 1.477823 3.707250 0.100828
1 2.558017 3.804208 0.237546
1 0.994254 4.081151 1.015090
1 1.174455 4.365734 -0.721946
6 2.013549 1.185555 0.061048
7 1.387031 0.001533 -0.045053
6 2.016133 -1.181128 0.060755
6 3.379642 -1.208708 0.356369
6 4.051862 0.004360 0.509770
6 3.377009 1.216008 0.356660
1 3.906218 2.163248 0.456542
1 5.117449 0.005493 0.739201
1 3.910853 -2.154847 0.456045
6 1.091026 -2.299555 -0.156447
7 -0.099724 -1.922818 -0.534889
6 -1.229171 -2.823758 -0.563724
1 -0.898209 -3.870679 -0.564965
1 -1.784606 -2.672256 -1.501078
6 -2.123159 -2.554226 0.640533
1 -1.567531 -2.750245 1.570769
1 -2.931800 -3.297652 0.625908
6 -2.783283 -1.194107 0.659771
7 -1.912144 -0.002073 0.835369
6 -1.250389 -0.000812 2.142288
1 -0.612855 -0.886062 2.249350
1 -1.989225 -0.001148 2.961260
1 -0.614494 0.885704 2.248553
6 -2.786254 1.187630 0.658820
1 -3.539502 1.168138 1.467000
1 -3.339009 1.035339 -0.279921
6 -2.129636 2.549444 0.639579
1 -2.940250 3.290711 0.624012
1 -1.575434 2.747222 1.570285
6 -1.235368 2.821069 -0.564006
1 -1.789809 2.668404 -1.501761
1 -0.906822 3.868754 -0.564933
1 -3.336896 -1.043596 -0.278733
1 -3.536114 -1.176216 1.468362
6 1.485994 -3.703931 0.100471
1 2.566579 -3.798648 0.235721
1 1.182741 -4.363474 -0.721477
1 1.004496 -4.078215 1.015688
7 -1.472013 -0.001828 -2.162699
1 -2.022095 -0.823044 -2.421453
1 -2.023781 0.818145 -2.421817
```

$[NiN_4(NH_3)]^{2+}$ 6e-7H^+ (h)
Coordinates (xyz) for optimized structures – 56831

```
28 -0.338890 -0.000082 0.224617
7 -0.065926 -1.909373 0.109711
6 1.180635 -2.295601 -0.003743
6 1.630022 -3.708347 0.034622
1 2.709917 -3.792601 -0.112648
1 1.136220 -4.304173 -0.744829
1 1.384185 -4.172876 0.999536
6 2.116120 -1.185486 -0.144144
7 1.476757 0.000194 -0.052819
6 2.115760 1.186056 -0.144243
6 3.496817 1.211555 -0.342254
6 4.182903 0.000581 -0.443222
6 3.497184 -1.210592 -0.342142
1 4.030286 -2.158069 -0.419178
1 5.261258 0.000739 -0.602287
1 4.029640 2.159182 -0.419354
6 1.179954 2.295905 -0.003867
7 -0.066475 1.909312 0.109854
6 -1.130163 2.860098 0.360979
1 -0.803604 3.879866 0.117414
1 -1.333166 2.855827 1.446977
6 -2.396593 2.534766 -0.400810
1 -2.229723 2.652378 -1.481445
1 -3.143177 3.297352 -0.142016
6 -3.009582 1.193099 -0.080402
7 -2.234842 -0.000173 -0.508154
6 -2.051074 0.000070 -1.971748
1 -1.483139 0.881940 -2.283443
1 -3.026876 0.000206 -2.485711
1 -1.483217 -0.881736 -2.283763
6 -3.009177 -1.193811 -0.080684
1 -4.005033 -1.127907 -0.552394
1 -3.176732 -1.101261 1.002968
6 -2.395805 -2.535232 -0.401405
1 -3.142236 -3.298074 -0.142926
1 -2.228791 -2.652501 -1.482054
6 -1.129381 -2.860526 0.360417
1 -1.332489 -2.856747 1.446400
1 -0.802527 -3.880100 0.116428
1 -3.177133 1.100258 1.003230
1 -4.005399 1.126984 -0.552162
6 1.629000 3.708761 0.034320
1 2.708609 3.793380 -0.114832
1 1.384802 4.172725 0.999938
1 1.133648 4.304869 -0.743907
7 -0.803035 -0.000480 2.370083
1 -1.765759 -0.000618 2.710369
1 -0.367769 -0.807431 2.819792
1 -0.367942 0.806535 2.819848
```

4.8 – References

1 S. Matassa, D. J. Batstone, J. Schnoor and W. Verstraete, *Environ Sci Technol*, 2005, **49**, 4247-4254.

2 P. M. Vitousek, J. D. Aber, R. W. Howarth, G. E. Likens, P. A. Matson, D. W. Schindler, W. H. Schlesinger and D. G. Tilman, *Ecol Appl*, 1997, **7**, 737–750.

3 J. Mart and J. Berbel, *Sustainability*, 2021, **13**, 5625.

4 J. G. Morrissy, M. J. Currell, S. M. Reichman, A. Surapaneni, M. Megharaj, N. D. Crosbie, D. Hirth, S. Aquilina, W. Rajendram and A. S. Ball, *Earth-Sci Rev*, 2021, **222**, 103816.

5 X. Zhang, B. B. Ward and D. M. Sigman, *Chemical Reviews*, 2020, **120**, 5308–5351.

6 L. B. Maia and J. J. G. Moura, *Chem Rev*, 2014, **114**, 5273–5357.

7 E. T. Judd, N. Stein, A. A. Pacheco and S. J. Elliott, *Biochemistry*, 2014, **53**, 5638–5646.

8 S. Amanullah, P. Saha, A. Nayek, M. E. Ahmed and A. Dey, *Chem Soc Rev*, 2021, **50**, 3755–3823.

9 M. H. Barley, K. J. Takeuchi and T. J. Meyer, *J Am Chem Soc*, 1986, **I**, 5876–5885.

10 J. R. Stroka, B. Kandemir, E. M. Matson and K. L. Bren, *ACS Catal*, 2020, **10**, 13968–13972.

11 I. Taniguchi, N. Nakashima, K. Matsushita and K. Yasukouchi, *J Electroanal Chem*, 1987, **224**, 199–209.

12 S. Cheng and Y. O. Su, *Inorg Chem*, 1994, **33**, 5847–5854.

13 Y. Guo, J. R. Stroka, B. Kandemir, C. E. Dickerson and K. L. Bren, *J Am Chem Soc*, 2018, **140**, 16888–16892.

14 S. Xu, H. Y. Kwon, D. C. Ashley, C. H. Chen, E. Jakubikova and J. M. Smith, *Inorg Chem*, 2019, **58**, 9443–9451.

15 Y. Xiang, D.-L. Zhou and J. F. Rusling, *J Electroanal Chem*, 1997, **424**, 1–3.

16 S. Partovi, Z. Xiong, K. M. Kulesa and J. M. Smith, *Inorg Chem*, 2022, **61**, 9034–9039.

17 C. Uyeda and J. C. Peters, *J Am Chem Soc*, 2013, **135**, 12023–12031.

18 G. Cioncoloni, I. Roger, P. S. Wheatley, C. Wilson, R. E. Morris, S. Sproules and M. D. Symes, *ACS Catal*, 2018, **8**, 5070–5084.

19 J. G. Woollard-Shore, J. P. Holland, M. W. Jones and J. R. Dilworth, *Dalton Trans*, 2010, **39**, 1576–1585.

20 A. P. Hunt, A. E. Batka, M. Hosseinzadeh, J. D. Gregory, H. K. Haque, H. Ren, M. E. Meyerho and N. Lehnert, *ACS Catal*, 2019, **9**, 7746–7758.

21 M. H. Barley, K. Takeuchi, W. R. Murphy and T. J. Meyer, *Chem Commun*, 1985, 507–508.

22 H.-L. Li, W. C. Anderson, J. Q. Chambers and D. T. Hobbs, *Inorg Chem*, 1989, **28**, 863–868.

23 S. Xu, D. C. Ashley, H. Y. Kwon, G. R. Ware, C. H. Chen, Y. Losovyj, X. Gao, E. Jakubikova and J. M. Smith, *Chem Sci*, 2018, **9**, 4950–4958.

24 J. Shi, W. Lan, Y. Zhou, C. Xue, Q. Liu and D. Zhang, *J Chem Sci*, 2018, **130**, 1–9.

25 J. L. Karn and D. H. Busch, *Nature*, 1966, **211**, 160–162.

26 K. M. Long and D. H. Busch, *Inorg Chem*, 1970, **9**, 505–512.

27 L. Rusnak and R. B. Jordan, *Inorg Chem*, 1971, **10**, 2199–2204.

28 J. Lewis and M. Schroder, *Dalton Trans*, 1982, 1085–1089.

29 C.-K. Poon, W.-K. Wan and S. S. T. Liao, *Dalton Trans*, 1977, 1247–1251.

30 E. K. Barefield, F. V Lovecchio, N. E. Tokel, E. Ochiai and D. H. Busch, *Inorg Chem*, 1972, **11**, 283–288.

31 F. V Lovecchio, E. S. Gore and D. H. Busch, *J Am Chem Soc*, 1974, **96**, 3109–3118.

32 M. Ghosh, T. Weyherm and K. Wieghardt, *Dalton Trans*, 2010, **39**, 1996–2007.

33 C. F. Leung, Y. Z. Chen, H. Q. Yu, S. M. Yiu, C. C. Ko and T. C. Lau, *Int J of Hydrogen Energy*, 2011, **36**, 11640–11645.

34 D. C. Lacy, C. C. L. McCcrory and J. C. Peters, *Inorg Chem*, 2014, **53**, 4980–4988.

35 S. Norouziyanlakvan, J. Ferguson and D. Richeson, *Catal Sci Technol*, 2022, **12**, 7494–7500.

36 E. S. Rountree, B. D. McCarthy, T. T. Eisenhart and J. L. Dempsey, *Inorg Chem*, 2014, **53**, 9983–10002.

37 C. Costentin, S. Drouet, M. Robert and J. M. Saveant, *J Am Chem Soc*, 2012, **134**, 11235–11242.

38 van Moesdijk C.G.M., *The catalytic reduction of nitrate and nitric oxide to hydroxylamine: kinetics and mechanism. [Phd Thesis 1 (Research TU/e / Graduation TU/e)]*, 1979, vol. 1.

39 O. Einsle, A. Messerschmidt, R. Huber, P. M. H. Kroneck and F. Neese, *J Am Chem Soc*, 2002, **124**, 11737–11745.

40 D. G. Gusev, *Organometallics*, 2013, **32**, 4239–4243.

41 P. Berro, S. Norouziyanlakvan, G. K. Rao, B. Gabidullin and D. Richeson, *Chem Commun*, 2021, **57**, 9292–9295.

42 R. Tyburski, T. Liu, S. D. Glover and L. Hammarstro, *J Am Chem Soc*, 2021, **143**, 560–576.

43 B. H. Solis and S. Hammes-Schiffer, *Inorg Chem*, 2014, **53**, 6427–6443.

44 S. E. Braley, H. Kwon, S. Xu, E. Z. Dalton, E. Jakubikova and J. M. Smith, *Inorg Chem*, 2022, **61**, 12998–13006.

45 X. Zhang, Y. Wang, Y. Wang, Y. Guo, X. Xie, Y. Yu and B. Zhang, *Chem Commun*, 2022, **58**, 2777–2787.

46 C. K. Williams, G. A. Mccarver, A. Lashgari, K. D. Vogiatzis and J. J. Jiang, *Inorg Chem*, 2021, **60**, 4915–4923.

47 A. Chaturvedi, G. A. McCarver, S. Sinha, E. G. Hix, K. D. Vogiatizis and J. Jiang, *Angew Chem Int Ed*, 2022, **61**, 1-9.

48 C. K. Williams, G. A. McCarver, A. Chaturvedi, S. Sinha, M. Ang, K. D. Vogiatzis and J. J. Jiang, *Chem Eur J*, 2022, **28**, 1-8.

49 J. Jiang, K. L. Materna, S. Hedstrçm, K. R. Yang, R. H. Crabtree, V. S. Batista and G. W. Brudvig, *Angew Chem, Int Ed*, 2017, **129**, 9239–9243.

50 N. Rodriguez-Lopez, Y. Wu, Y. Ge and D. Villagran, *J Phys Chem C*, 2020, **124**, 10265–10271.

Chapter 5: Probing Electrocatalytic Reduction for Substrates Including CO_2, $NaNO_2$, NO, and H_2O Using $M(bpca)_2$ [M = Fe^{II}, Co^{III}, Ni^{II}]

5.1 – Preamble and Statement of Contributions

The content described in this chapter is based on work describing experiments performed in the latter half of 2023 and beginning months of 2024. Selection of the complexes to be investigated, target substrates, and general research objectives were researched and established by Josh Brown. All computational data were devised, completed, and interpreted by Josh Brown. All experiments were devised and completed or directed by Josh Brown, with CVs probing nitrite reduction being performed by Eneko Gerard. Data were interpreted and presented by Josh Brown.

5.2 – Introduction: Exploring Potential Catalytic Activity for 3d M(bpca)$_2$ Complexes

Improving the utility of waste chemicals through catalytic transformations has been a central theme in the field of homogeneous electrocatalysis over the past several decades.[1,2] There are a broad host of waste targets to be utilized; CO_2 reduction is one of the most popular targets.[3–5] The overabundance of this greenhouse gas in the atmosphere has significantly decayed the health of our planet on a variety of facets, from heating the planet through the greenhouse effect, to destroying coral reefs with increased carbonic acid concentrations in oceans.[5] Determining methods to convert this chemical detriment into something useful may not directly translate to significant reduction of these chemical burdens in the atmosphere, but it will offer solutions to make use of them once they can be effectively sequestered.

Few transition metal-bpca complexes have been studied for electrocatalytic CO_2 reduction. One rhodium complex with a single coordinated bpca ligand shows enhanced current on CVs in the presence of CO_2, indicating catalytic reduction but was never fully investigated in bulk reactions.[6] Among first row transition mentals, one copper bpca complex demonstrates CO_2 fixation capabilities.[7] Other potential candidates for electrocatalytic CO_2 reduction from the 3d form a structure with two ligands, bonded in a perpendicular orientation, opposite one another (Figure 5.1). These complexes possess redox activity with voltages in the region that CO_2 and H_2O reduction are often documented in the literature.[8–10]

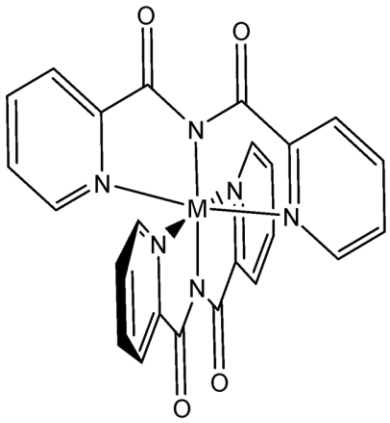

Figure 5.1: Molecular structure of 3d transition metals (M = Fe, Co, and Ni) coordinated to two bis(2-pyridylcarbonyl)amine) ligands.

The crowded coordination geometry of these complexes could cause some limitations in their electrocatalytic capabilities. Electrocatalytic reduction of CO_2 generally proceeds through a mechanism that involves coordination with the metal centre.[11] These complexes appear to have all possible coordination sites occupied, which contributes to stable and reversible redox events, but ultimately excludes interactions of substrate with the metal centre. Preventing substrate access to the metal centre could easily restrict effective catalysis.

This work intends to investigate various $M(bpca)_2$ [M = Fe^{II}, Co^{III}, and Ni^{II}] complexes as potential electrocatalysts for a variety of substrate targets, including CO_2, NO_2^-, NO, and H_2O.[12–14] In addition to simply screening these complexes with a variety of substrates, the ligand environment is modulated through the introduction of alkali metals, interacting with the carbonyl groups on the bpca ligand. Previous work has demonstrated an anodic shift in redox potentials of ruthenium-supported bpca complexes when hard Lewis acids

are introduced, having a more significant effect the harder the acid.[15] Pulling the electron density away from the metal center could weaken the metal-ligand bond of $M(bpca)_2$ compounds and encourage partial dissociation of one or more of the coordination sites, allowing substrates access to the metal center, activating the catalyst.

Many catalyst-substrate combinations were evaluated in this investigation. The most effective match was determined to be **$Fe(bpca)_2$** and $NaNO_2$ for nitrite reduction. $NaNO_2$ offered a strongly coordinating substrate (NO_2^-) along with a hard Lewis acid source (Na^+) to perturb the redox activity of **$Fe(bpca)_2$** through its interactions with the carbonyl groups of the bpca ligand. This combination addressed the absence of available coordination sites in **$Fe(bpca)_2$** by weakening the bonds of bpca to Fe, while offering a ligand with stronger binding affinity to further encourage partial dissociation of bpca.

5.3 – Synthesis of Bis(2-pyridylcarbonyl)amine) Ligand and its Complexes

Each of the following complexes was prepared according to previous literature procedures.[7–10,16,17] Extra details were added to improve the yield and purity of the described processes. All structures were confirmed by single crystal X-ray crystallography and H-NMR, when appropriate.

$[CuII(bpca)(H_2O)]^+[CuII(bpca)(SO_4)]^-$ (Cubpca): Generation of this complex was necessary to facilitate the eventual synthesis of the **Hbpca** ligand. The Cu(bpca) salt is a result of the hydrolysis of 1,3,5-tris(2-pyridyl)triazene. The copper acts to coordinate this molecule, assisting in the hydrolysis process according to the reaction displayed in Scheme 5.1. The

structure of the product was confirmed with SC-XRD to match with previous entries into the CCDC database.[17]

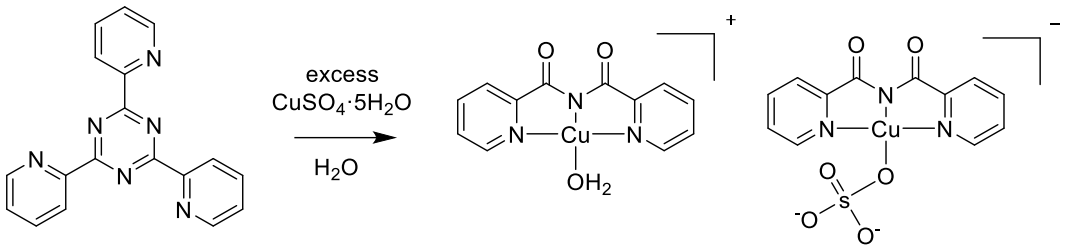

Scheme 5.1: Generation of Cu(bpca) precursor to ligand.

Hbpca ligand:[17] Removal of copper from the Cu(bpca) precursor can be accomplished through complexation with EDTA by rapidly stirring it in a mixture of water and chloroform. The two phases can be separated through a liquid-liquid extraction. The ligand is left in the organic phase, which can be dried with $MgSO_4$. Removal of the chloroform leaves behind the pure ligand. The structure was verified with SC-XRD and ^{1}H-NMR: $CDCl_3$ – δ 7.54 (2H, ddd, *J* = 7.67, 4.76, 1.18 Hz (**py3-H**)), 7.91 (2H, td, *J* = 7.68, 1.67 Hz(**py2-H**)), 8.03 (2H, dt, *J* = 7.83, 0.98 Hz (**py1-H**)), 8.72 (2H, ddd, *J* = 4.77, 1.67, 0.94 Hz (**py4-H**)) 13.01 (1H, broad, singlet (**NH**)).

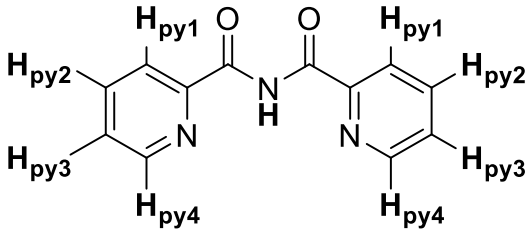

Figure 5.2: ^{1}H-NMR labeling for bis(2-pyridylcarbonyl)amine).

M(bpca)$_2$ [M=Fe(II), Ni(II), and Co(III)]: Each of the complexes can be generated with similar methods. Hydrated metal salts of each metal (according to Scheme 5.2) are dissolved in water, and mixed with 2 equivalents of the ligand, dissolved in acetone. The mixtures are vigorously stirred for an hour at room temperature. For **Ni^{II}(bpca)$_2$**, crystals immediately start to form. In the cases of **Fe^{II}(bpca)$_2$** and **[Co^{III}(bpca)$_2$]$^+$**, the solutions must be neutralized to a pH of 7 using 1M NaOH solution. Once the crystals were collected, their structures were confirmed with SC-XRD.

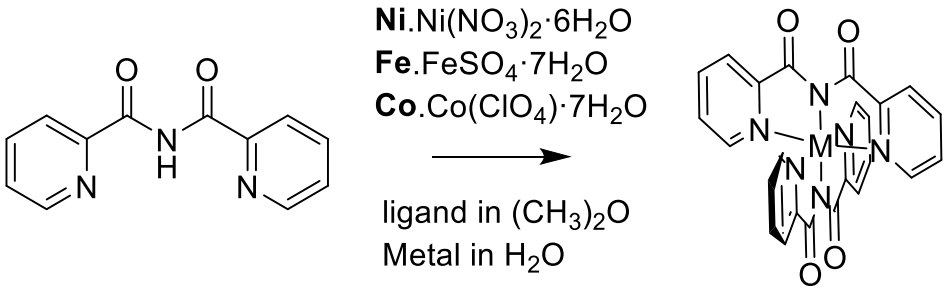

Scheme 5.2: Synthesis of M(bpca)$_2$ complexes [M=Ni, Fe, and Co].

5.4 – Electrochemical Characterization of Complexes in Organic Solvents

Understanding the electrochemical behaviour of each compound can most effectively be achieved by starting the investigation in an organic, aprotic solvent. Acetonitrile is an ideal choice, due to its large solvent potential window and favourable solubility portfolio. Each M(bpca)$_2$ complex and the free ligand were investigated for their redox activity. Cathodic scans were targeted as the intent of the investigation was to apply their reduction events to the electrocatalytic reduction of various substrates. The cell setups used for these experiments were the same as those described in Chapter 1, section 1.3.1. For the events observed during cathodic scans, accompanying DFT calculations were performed to simulate all the reduction products.

5.4.1 – Hbpca ligand

While investigating the redox behaviour of the **Hbpca** ligand (Figure 5.3), two irreversible redox events were identified with $E_{1/2}$ of -2.2V and -2.44V vs $Fc^{+/0}$. These values fit reasonably with the redox potentials calculated using DFT, which were found to be -2.04V and -2.99V vs $Fc^{+/0}$. Beyond these potentials, the solvent window was encroached upon, nullifying the possibility of identifying any other redox events. The observed events provide support for the possibility of this ligand system to act as an electron reservoir when it is complexed with metals.

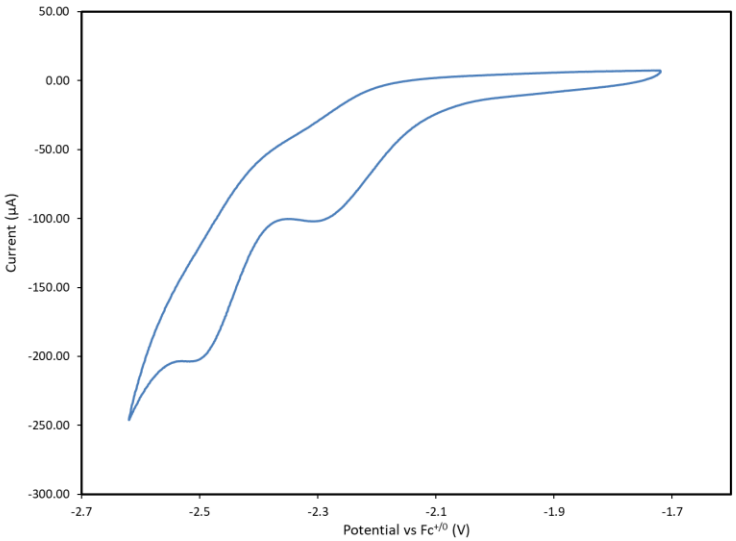

Figure 5.3: CV of 1mM Hbpca ligand in acetonitrile with a scan rate of 0.1V/s scanned between -1.7V and -2.6V using TBAHFP as the electrolyte.

Examining the MOs on the ligand structure, generated through DFT simulations helps elucidate how the electron density is stabilized through reduction events. The initial electronic structure for **Hbpca** is shown in Figure 5.4.

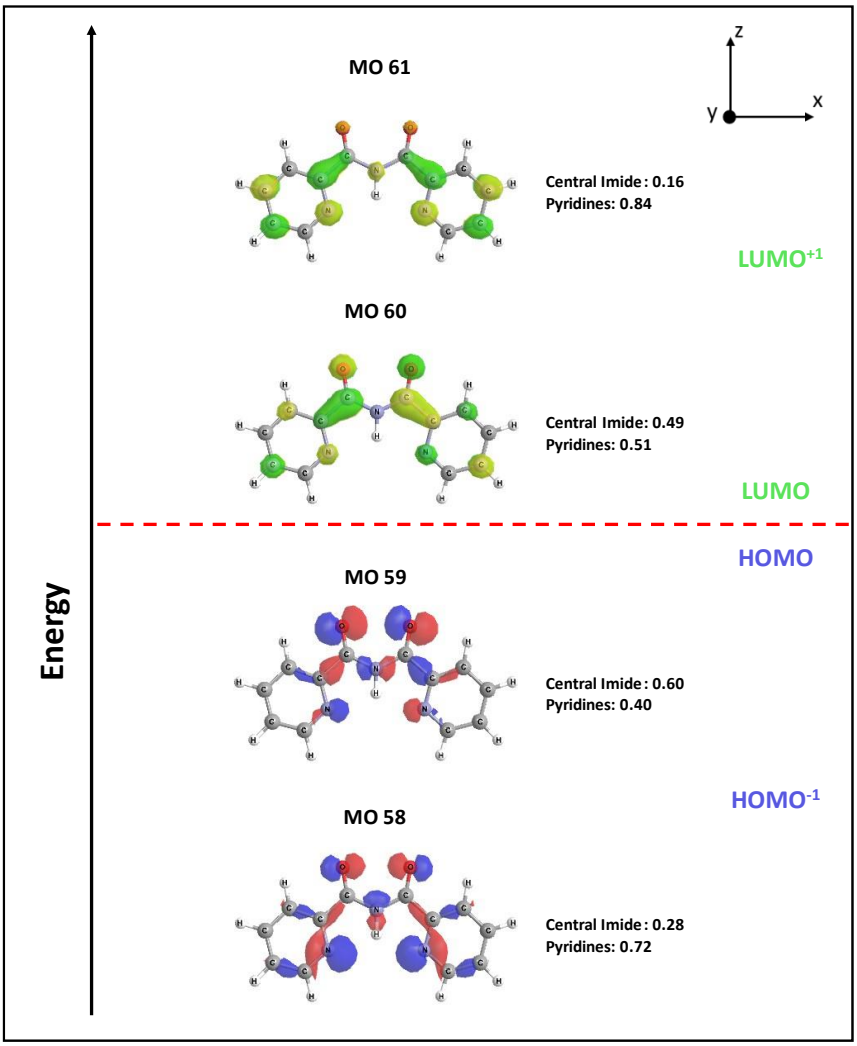

Figure 5.4: Electronic structure of Hbpca displaying the valence MOs with isosurface plots having iso-values of 0.05 calculated in acetonitrile.

The orientation of Figures 5.4-5.6 are defined relative to the Cartesian axis displayed in the top right of Figure 5.4. Groupings of atomic orbital contributions were labelled according to their location on the ligand, separating the pyridine groups from the central imine. The $HOMO^{-1}$ (MO 58) is observed to store around 72% of the electron density on the pyridine. Much of the electron density is stored in the p-orbitals of the nitrogen atom in that ring. These orbitals protrude inward with an appropriate symmetry to coordinate

to a metal center. The HOMO for this electronic structure (MO 59) places 60% of the electron density toward the center of the molecule on the imine. The LUMO (MO 60) isosurface is more evenly distributed throughout the structure, providing an accessible orbital to become occupied upon exposure to an adequate applied potential. Following the experimental reduction observed at -2.2V, **Hbpca** becomes reduced, generating **Hbpca**$^{-}$. This species was simulated using DFT calculations to generate the doublet electronic configuration displayed in Figure 5.5.

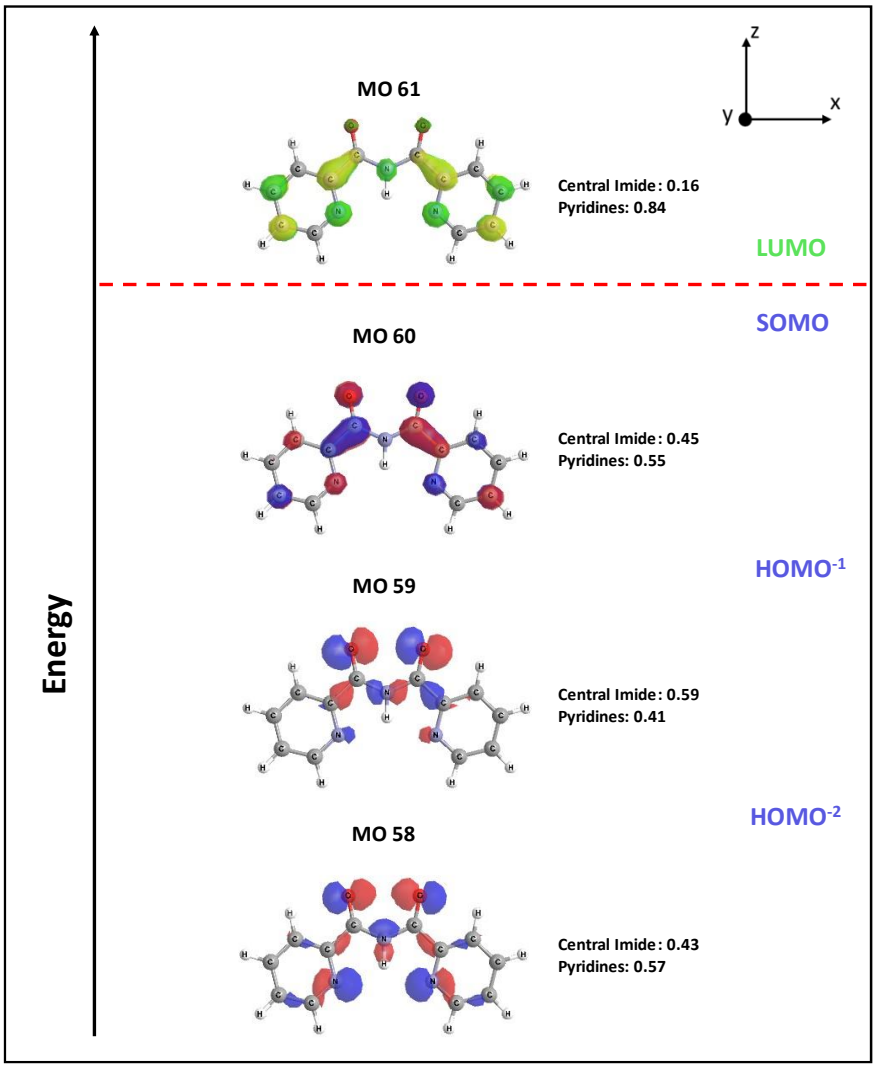

Figure 5.5: Electronic structure of Hbpca$^-$ displaying the valence MOs with isosurface plots having iso-values of 0.05 calculated in acetonitrile.

The observed molecular orbitals that make up the occupied region of this electronic structure remain similar to those observed in Figure 5.4. MO 60 in Figure 5.4 becomes singly filled to generate the SOMO observed in Figure 5.5. The orbital is reconfigured slightly in this process to store more electron density on the pyridine rings, moving from a contribution of 51% on the pyridines when it is unoccupied, to 59% when a single

electron is added. The second reduction process observed at -2.44V is associated with the filling of the SOMO to generate **Hbpca^{2-}**, having the electronic structure displayed in Figure 5.6.

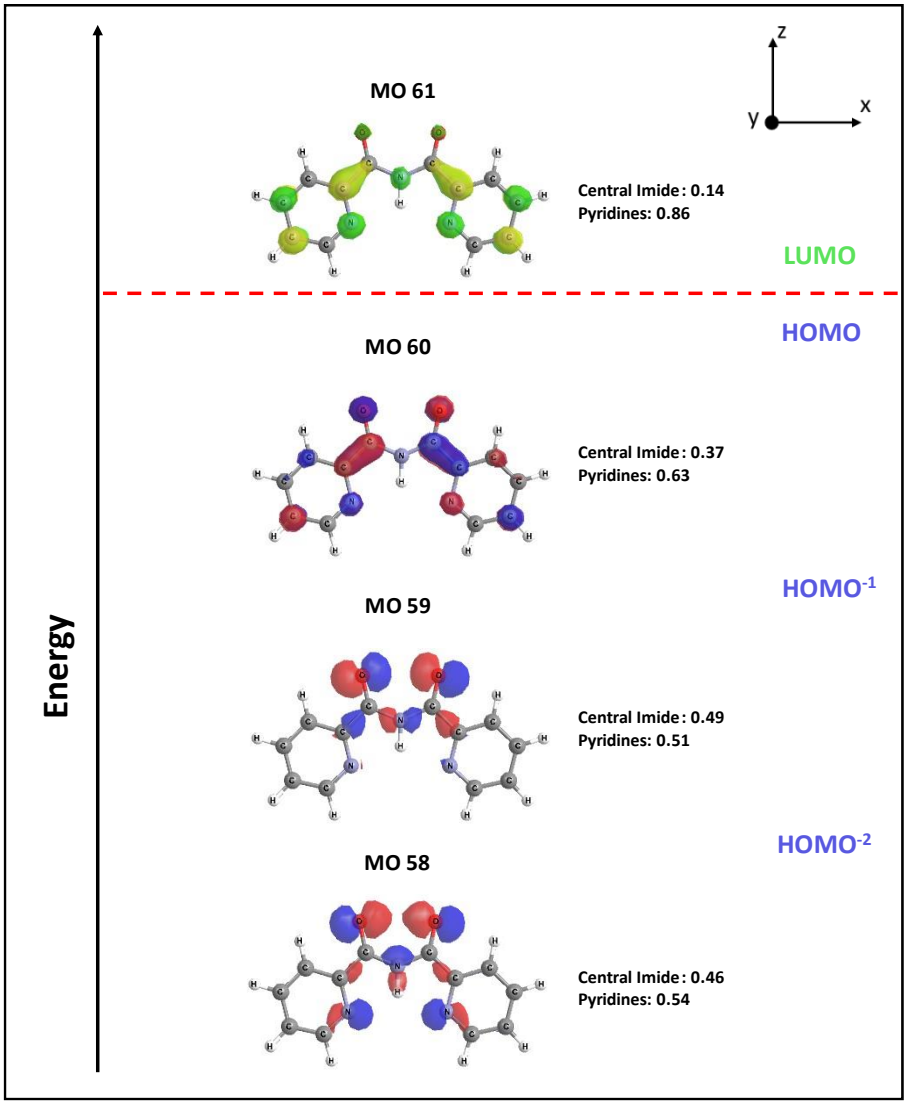

Figure 5.6: Electronic structure of Hbpca^{2-} displaying the valence MOs with isosurface plots having iso-values of 0.05 calculated in acetonitrile.

There is a similar trend observed in the partition of electron density when a second electron is added to MO 60 moving from Figure 5.5 to 5.6. The MO contributions of the pyridine are further increased, from 59% as the SOMO for $bpca^-$, to 63% as the HOMO in **$Hbpca^{2-}$**. The general form of each orbital remains largely unchanged through the reduction processes, providing further evidence for **Hbpca** being a good candidate to act as an electron reservoir when complexed with a metal. Examining selected bonds in the imine region of the **Hbpca** ligand demonstrates some variation in the ligand's structure through each observed reduction. These data can be seen in Tables 5.1-5.3 for **Hbpca**, **$Hbpca^-$**, and **$Hbpca^{2-}$** respectively. The identity of each bond is defined by the numbering scheme displayed in Figure 5.7.

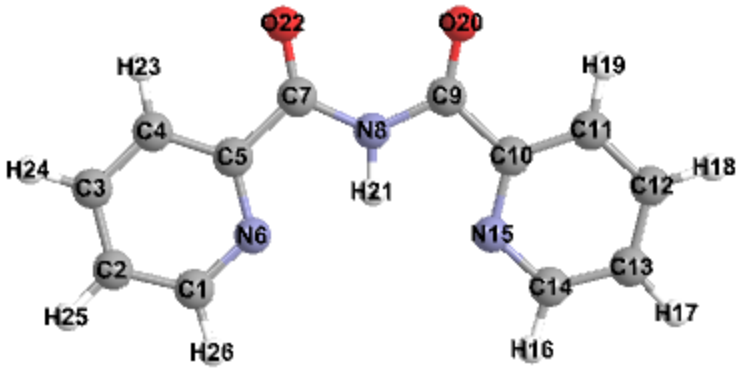

Figure 5.7: Ligand structure from Chemissian including atom number labelling covering Hbpca, $Hbpca^-$, and $Hbpca^{2-}$

Table 5.1: Descriptions of bond lengths and order for selected bonds in Hbpca.

Bond	Bond Length (Å)	Bond Order
C5-C7	1.507	1.01
C7-N8	1.377	1.08
N8-H21	1.026	0.86
C7-O22	1.211	1.66

Table 5.2: Descriptions of bond lengths and order for selected bonds in Hbpca^{-}.

Bond	Bond Length (Å)	Bond Order
C5-C7	1.475	1.11
C7-N8	1.377	1.07
N8-H21	1.025	0.86
C7-O22	1.239	1.58

Table 5.3: Descriptions of bond lengths and order for selected bonds in Hbpca^{2-}.

Bond	Bond Length (Å)	Bond Order
C5-C7	1.449	1.21
C7-N8	1.381	1.04
N8-H21	1.025	0.87
C7-O22	1.261	1.55

Overall, the calculations suggest that the ligand effectively stabilizes the added charge, without compromising the bonds responsible for connecting the two pyridyl groups together. Due to the plane of symmetry that exits about the yz-plane, occupying MO 60 from Figures 5.4-5.6 has the same effect on both sides of the plane, therefore changes that occur in bonding on one side are directly reflected on the other. The bond directly connecting the pyridyl group to the carbonyl (C5-C7) becomes stronger as electrons are added, showing an increase in bond order from 1.01, to 1.11, and finally 1.21 with consecutive electron additions. From the electronic structures in Figures 5.4-5.6, it is clear that the electrons are being added to a π-bond, justifying the decrease in bond length and increasing bond order. Bonds to the nitrogen (C7-N8, N8-H21) are minimally affected by the reduction processes. However, the carbonyl bond length (C7-O22) does increase with the added electron density, moving from 1.211 Å, to 1.239 Å, to 1.261 Å with two added electrons, which reflects in a decreased bond order. This occurrence is also predicted by

MO 60 from figures 5.4-5.6, as the carbonyl in this MO is comprised of π^* orbitals, weakening the bond when they become occupied.

5.4.2 – $Fe^{II}(bpca)_2$

Investigations into the reduction behaviour of **$Fe^{II}(bpca)_2$** were completed in a similar manner to the initial ligand structure. Figure 5.8 displays the CV collected for a cathodic sweep of the complex, beginning with its natural oxidation state. Two reversible events were observed at $E_{1/2}$ values of -1.81V and -2.01V vs $Fc^{+/0}$. The first of these reduction events matches very closely with the value calculated from DFT calculations, which was -1.86V. The second calculation was less accurate, returning a value of -2.63V for the second reduction event.

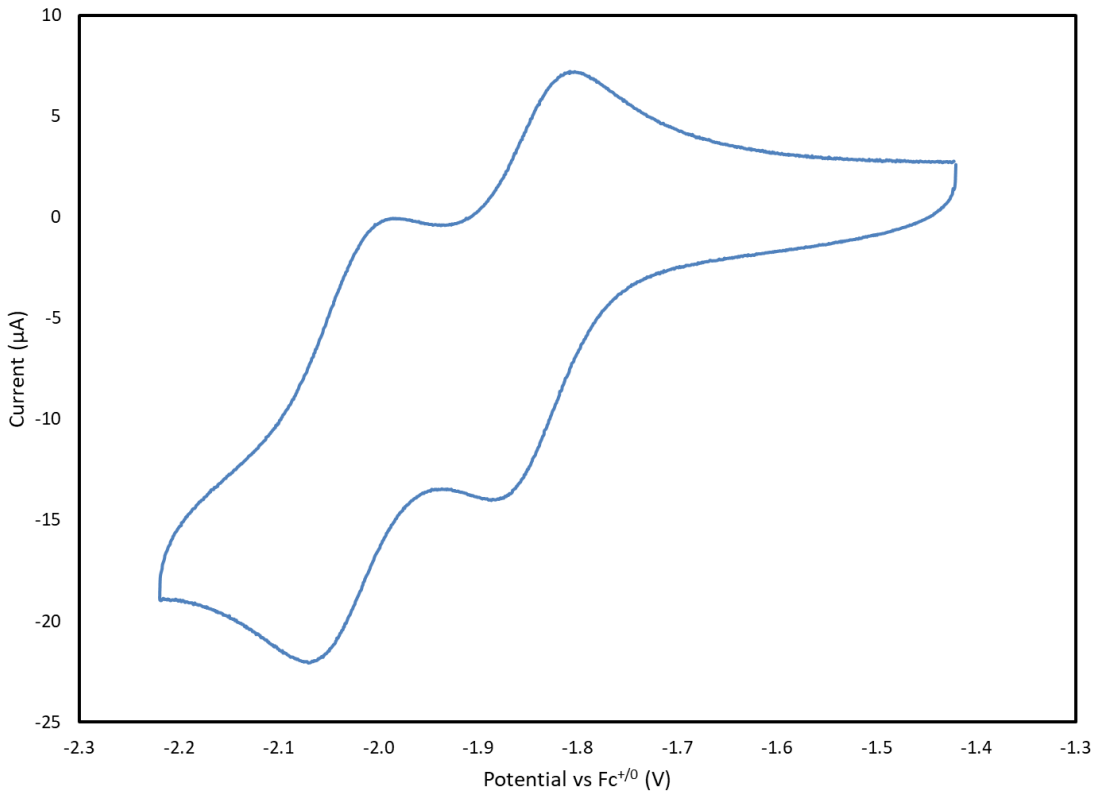

Figure 5.8: CV of 1mM $Fe^{II}(bpca)_2$ ligand in acetonitrile with a scan rate of 0.1V/s scanned between -1.7V and -2.6V using TBAHFP as the electrolyte.

Discerning the location of the added electron density following a reduction process can be achieved through DFT simulation. For organometallic complexes, added electrons are often erroneously assigned to occupying orbitals stored entirely on the metal. Our investigations into the redox behaviour of the ligands demonstrate the capacity of **Hbpca** to stabilize two added electrons with an applied potential, suggesting that the metal may not play a significant role. Figure 5.9 displays the valence electronic structure of **$Fe^{II}(bpca)_2$**, showing some select occupied orbitals, and some unoccupied orbitals that may become occupied following a reduction process.

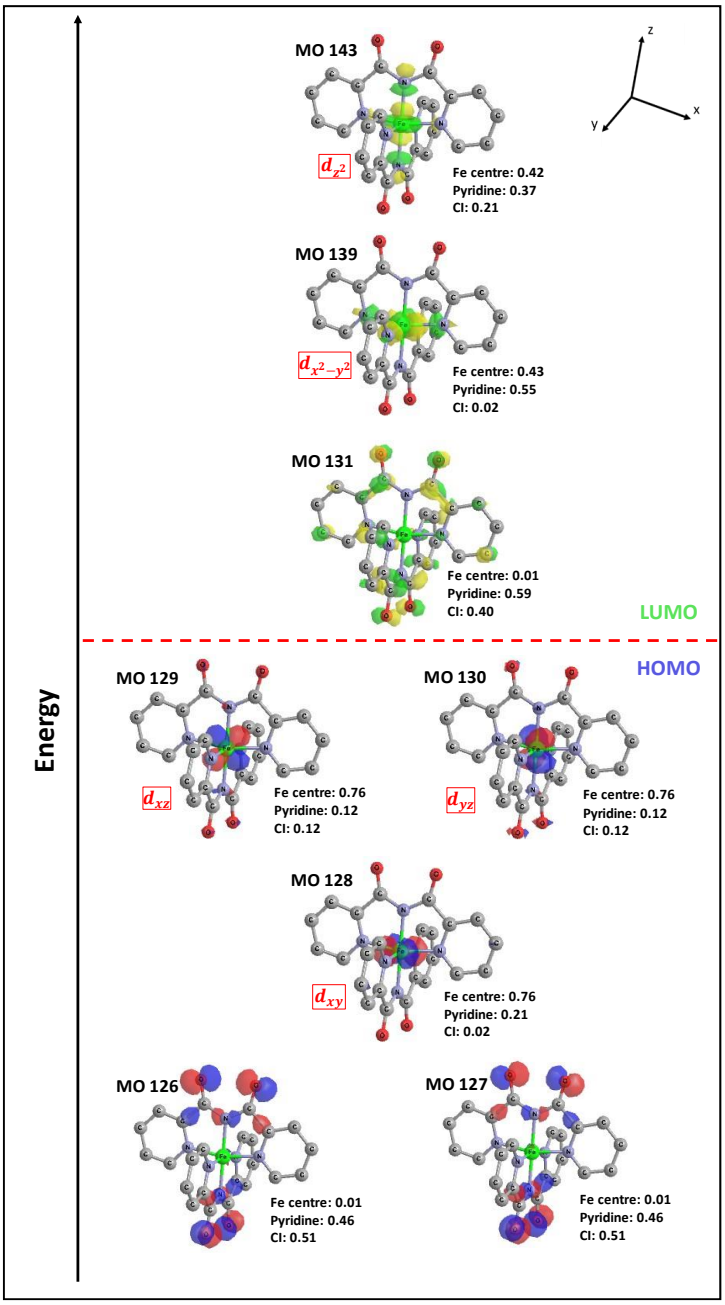

Figure 5.9: Electronic structure of $Fe^{II}(bpca)_2$ displaying selected valence MOs with isosurface plots having iso-values of 0.05 calculated in acetonitrile.

In this figure and Figures 5.10 and 5.11, electron density contributions are broken up into contributions from the metal center, the combination of all pyridine groups, and the

combination of each central imide (CI). Each MO appears to contribute equivalent densities to each of these groups, which justifies their groupings. The HOMOs (MO 129 and MO 130) for **$Fe^{II}(bpca)_2$** are most significantly comprised of the d_{xz} and d_{yz} atomic orbitals on the Fe center. These MOs are share the same symmetry and contributions from the ligands, making them degenerate in energy. MO 128 is largely comprised of the d_{xz} atomic orbital. For a low spin Fe^{II} metal center, which this complex has been shown to possess, these are the d-orbitals (t_{2g}) expected to be occupied for an octahedral coordination geometry. The $d_{x^2-y^2}$ and d_{z^2} orbitals are expected to be unoccupied in this array, as observed in MO 139 and MO 143, respectively. Both of these MOs are comprised of metal center contributions of less than 50%, leaving the majority of the MO to be comprised of ligand contributions. The LUMO for this electronic structure (MO 131) contains virtually no contributions from the metal center. 59% of the MO is comprised of contributions from the pyridines, with the remaining 40% being contributions from the CIs. No significant metal contributions are observed in any of the orbitals between MO 131 and MO 139, suggesting that added electrons will not reside in orbitals contained on the metal, assuming there is not significant structural rearrangement following a reduction process.

Following the reduction process at -1.81V, a doublet electron configuration is formed, generating **$[Fe^{II}(bpca)_2]^-$**. The electron configuration for this complex was simulated, and selected MOs are displayed in Figure 5.10. Minimal metal center contributions to the newly occupied SOMO, prompted labelling of the added charge to be attributed to the ligand system, rather than changing the oxidation state of the metal center.

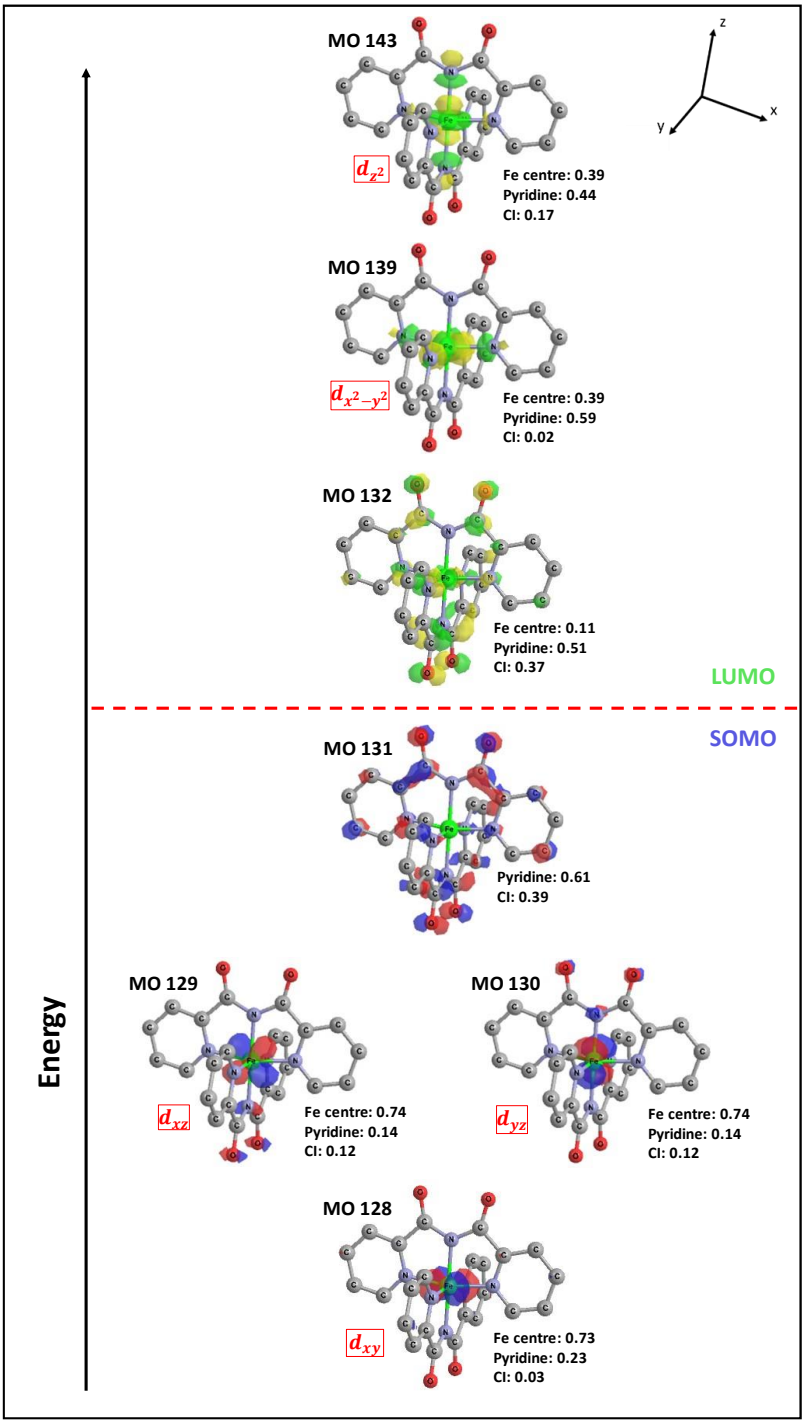

Figure 5.10: Electronic structure of $[Fe^{II}(bpca)_2]^-$ displaying selected valence MOs with isosurface plots having iso-values of 0.05 calculated in acetonitrile.

The newly occupied SOMO for **[Fe^{II}(bpca)$_2$]$^-$** very closely resembles the LUMO in Figure 5.9 for **Fe^{II}(bpca)$_2$**. The MO housing the new electron density is spread equally among both bpca ligands partitioning the density identically, meaning that the overall electronic structure of the reduced species maintains the same symmetry where both ligands continue to mirror one another. The pyridine groups in the structure contains 61% of the electron density and the remaining 49% is contained in the CI groups; the metal does not contribute. The fragment contributions for the MOs in the remainder of the occupied and unoccupied MOs remain largely unchanged and the $d_{x^2-y^2}$ *and* d_{z^2} from the metal center remain inaccessible to added electrons. Adding one more electron to the system, following the reduction process observed experimentally at -2.01V, generates **[Fe^{II}(bpca)$_2$]$^{2-}$**. The electron configuration for this species is simulated in Figure 5.11. The result of this reduction process is a diamagnetic species with a HOMO that closely resembles the SOMO from Figure 5.10. The ligand again houses the electron density from the reduction process, allowing the metal center d-electron count to remain d^6. The e_g MOs for this octahedral complex remain inaccessible to added electrons (MO 139 and 143). The occupied molecular orbitals composed of the atomic d-orbitals remain largely unchanged; the d_{xy}, d_{xz}, and d_{yz} orbitals are observed as MO 128, 129, and 130, respectively.

Further analysis into the length and bond order of certain bonds were performed to evaluate the structural effects that result in the addition of two electrons to **Fe^{II}(bpca)$_2$**. These data are displayed in tables 5.4-5.6 for **Fe^{II}(bpca)$_2$**, **[Fe^{II}(bpca)$_2$]$^-$**, and **[Fe^{II}(bpca)$_2$]$^{2-}$**

respectively. The pertinent bonds are defined by the numbering scheme displayed in Figure 5.12.

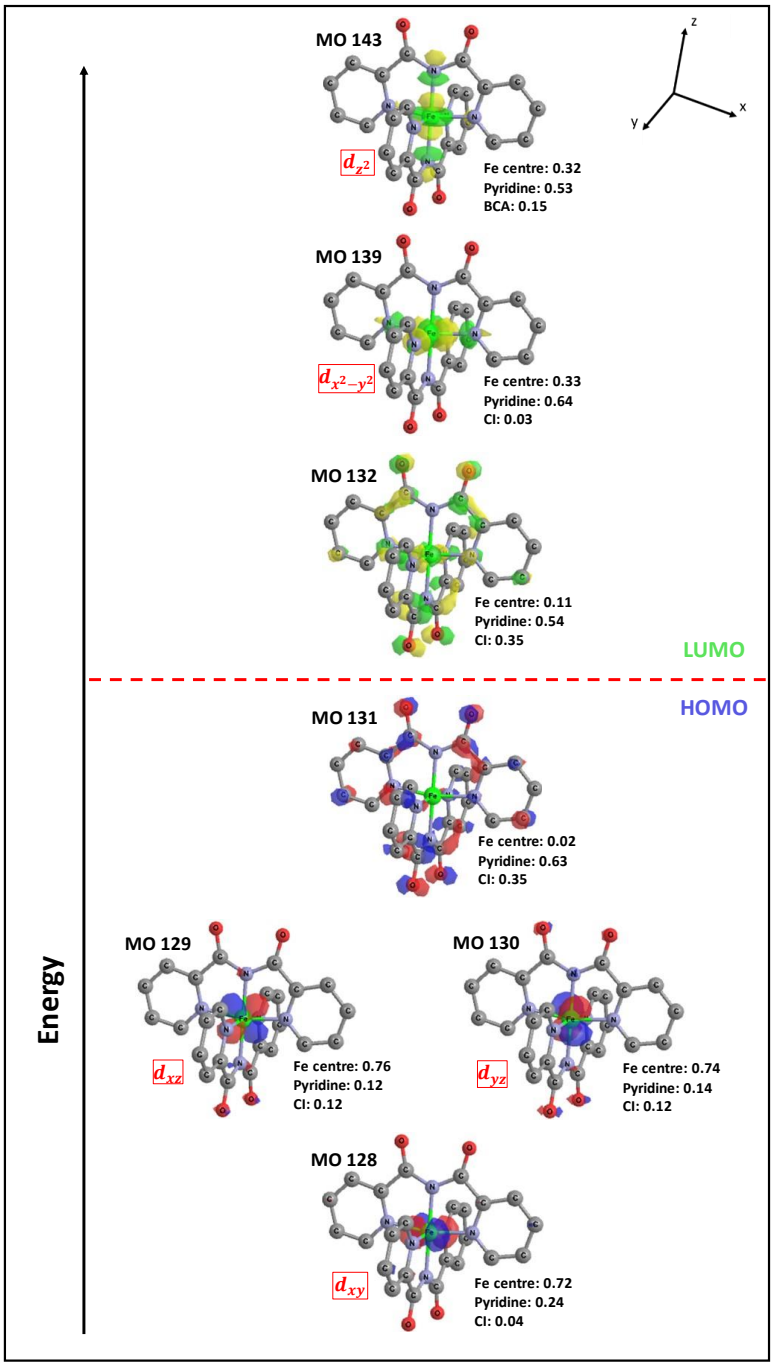

Figure 5.11: Electronic structure of $Fe^{II}(bpca)_2^{2-}$ displaying selected valence MOs with isosurface plots having iso-values of 0.05 calculated in acetonitrile.

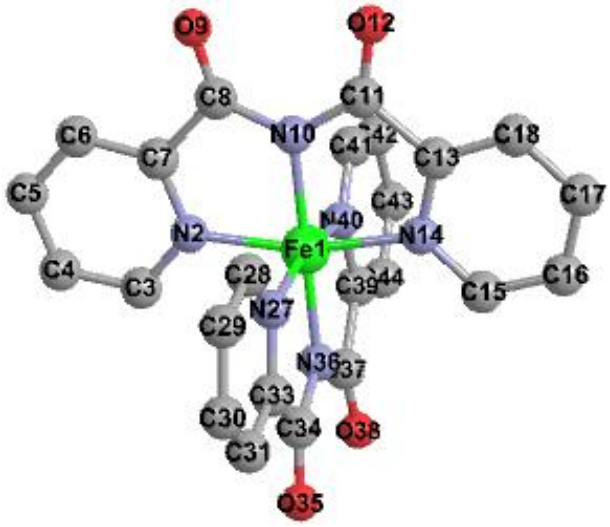

Figure 5.12: Ligand structure from Chemissian including atom number labelling covering $Fe^{II}(bpca)_2$, $[Fe^{II}(bpca)_2]^-$, and $[Fe^{II}(bpca)_2]^{2-}$.

Table 5.4: Descriptions of bond lengths and order for selected bonds in $Fe^{II}(bpca)_2$.

Bond	Bond Length (Å)	Bond Order
Fe1-N10	1.949	0.75
Fe1-N2	1.956	0.58
Fe1-N14	1.956	0.58
Fe1-N36	1.949	0.75
Fe1-N27	1.956	0.58
Fe1-N40	1.956	0.58
C7-C8	1.508	1.02
C8-N10	1.364	1.13
C8-O9	1.220	1.62
C33-C34	1.508	1.02
C34-N36	1.364	1.13
C34-O35	1.220	1.62

Table 5.5: Descriptions of bond lengths and order for selected bonds in $[Fe^{II}(bpca)_2]^-$.

Bond	Bond Length (Å)	Bond Order
Fe1-N10	1.946	0.76
Fe1-N2	1.942	0.57
Fe1-N14	1.942	0.57
Fe1-N36	1.946	0.77
Fe1-N27	1.946	0.57

Fe1-N40	1.946	0.57
C7-C8	1.496	1.07
C8-N10	1.364	1.12
C8-O9	1.231	1.60
C33-C34	1.488	1.08
C34-N36	1.365	1.12
C34-O35	1.236	1.60

Table 5.6: Descriptions of bond lengths and order for selected bonds in $[Fe^{II}(bpca)_2]^{2-}$.

Bond	Bond Length (Å)	Bond Order
Fe1-N10	1.942	0.78
Fe1-N2	1.936	0.57
Fe1-N14	1.936	0.57
Fe1-N36	1.942	0.78
Fe1-N27	1.936	0.57
Fe1-N40	1.936	0.57
C7-C8	1.479	1.12
C8-N10	1.365	1.12
C8-O9	1.246	1.60
C33-C34	1.479	1.12
C34-N36	1.365	1.12
C34-O35	1.246	1.60

Throughout each reduction process, all of the bonds coordinating each nitrogen to the Fe center become shorter. This is likely due to the accumulation of negative charge, causing the ligand to be pulled closer to the positive iron center. There is a slight disparity in the bond length in each ligand where the pyridines coordinate to the metal center for **$[Fe^{II}(bpca)_2]^{-}$**. When comparing Fe1-N2 and Fe1-N14 with Fe1-N27 and Fe1-N40 in Tables 5.4 and 5.5 it is clear that adding an electron affects these bond lengths more significantly on one ligand than the other. For one ligand, adding an electron decreases the bond length from 1.956 Å to 1.946 Å, whereas in the other ligand that same bond shrinks to 1.942 Å. This difference can be attributed to the slight variance that exists between the alpha and

beta orbitals observed during the computation of a singly filled orbital. This disparity is nullified when another electron is added, to give **$[Fe^{II}(bpca)_2]^{2-}$** as the additional electron results in a diamagnetic species.

Similar trends exist for select bond lengths of the ligand through the first reduction process as observed for metal-ligand coordination. The paramagnetic **$[Fe^{II}(bpca)_2]^{-}$** complex shows some slight structural differences between the coordinated bpca ligands but adding the final electron to generate **$[Fe^{II}(bpca)_2]^{2-}$** reinstates parity among the two ligands. Despite the actual bond lengths varying slightly between the ligands as the first electron is added, each follows a similar trend. The bond between the carbonyl carbons and amine nitrogen (C8-N10 and C34-N36) remains the same for both lengths and bond orders throughout each reduction process. The lengths of the carbonyl double bonds increase (C8-O9 and C34-O35) and the lengths of the bonds connecting the imides to the pyridines (C7-C8 and C33-C34) decrease. Both trends occur and can be explained in a similar manner to what was observed for the investigations of **Hbpca**. The carbonyl lengthens due to the occupation of a π^* orbital, and the latter bond becomes stronger due to the occupation of a σ bond.

5.4.3 – $[Co^{III}(bpca)_2]^{+}$

Completing the electrochemical analysis for **$[Co^{III}(bpca)_2]^{+}$** allows for parallels to be drawn in its redox behaviour with **$Fe^{II}(bpca)_2$**, as these species are isoelectronic to one another. The oxidation states of these two species are Fe^{II} and Co^{III}, respectively, meaning they are both d^6. The metal center in **$[Co^{III}(bpca)_2]^{+}$** contributes an overall charge of +3, meaning

the complex carries a charge of +1, with a perchlorate counter ion. For this complex, three reduction events were identified. The first event is a reversible process that occurs at an $E_{1/2}$ of -0.66V vs $Fc^{+/0}$. The computed potential was slightly more negative, having a value of -0.98V vs $Fc^{+/0}$. This redox event is isolated from the rest of the CV and displayed in Figure 5.13.

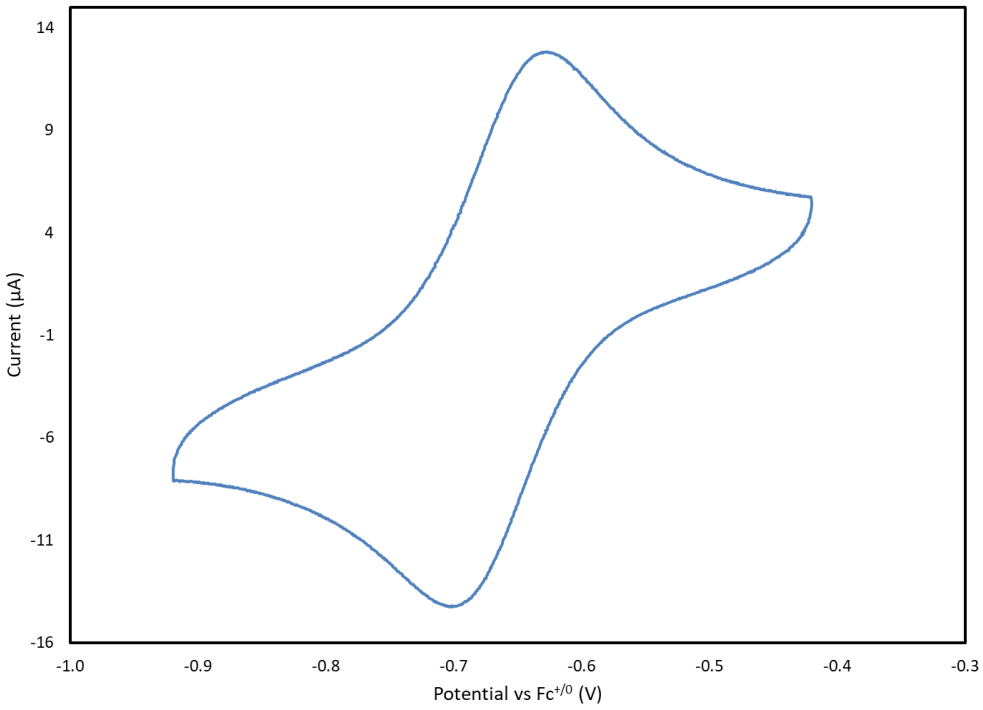

Figure 5.13: CV of 1mM $[Co^{III}(bpca)_2]^+$ ligand in acetonitrile with a scan rate of 0.1V/s scanned between -0.42V and -0.92V using TBAHFP as the electrolyte.

The second and third reduction event for **$[Co^{III}(bpca)_2]^+$** can be seen in Figure 5.14. These events appear to have some reversible characteristics, as there is a return oxidation; however, the characteristic reversible shape is disrupted due to their nearly overlapping potentials. Slowing the scan rate to 0.025V/s elucidates the separate events that are occurring during the return oxidation. Additionally, the recorded CV suggests some non-

homogeneous behaviour may be occurring at the electrode. The Gaussian-like shape of the return oxidation indicates an adsorption process may be occurring. The $E_{1/2}$ values for these events are -1.93V and -1.98V $Fc^{+/0}$. The calculated values simulating these redox events were determined to be -2.35V and -2.01V, respectively. The inaccuracy in the order of these calculated events is discussed further in section 1.4.2.

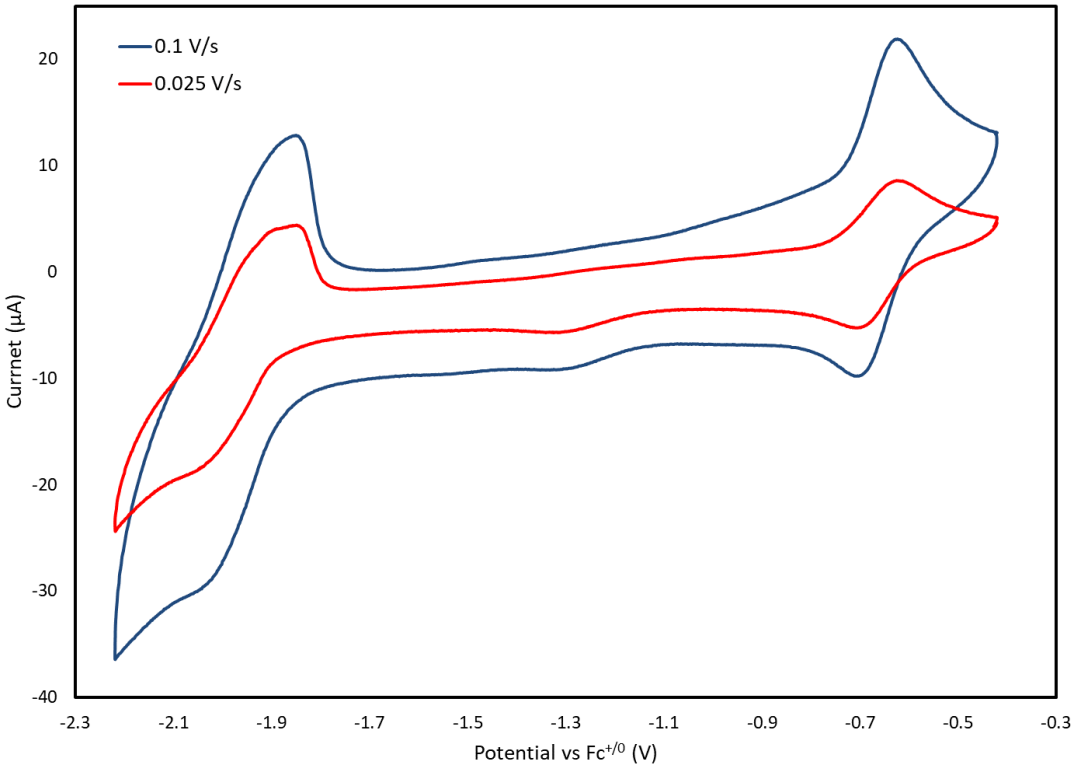

Figure 5.14: CV of 1mM $[Co^{III}(bpca)_2]^+$ ligand in acetonitrile with scan rates of 0.1V/s and 0.025V/s scanned between -0.42V and -2.25V using TBAHFP as the electrolyte.

Identifying the locations in the complex where electrons are stored following reduction processes was calculated in a similar manner to **$Fe^{II}(bpca)_2$**. The initial low spin diamagnetic **$[Co^{III}(bpca)_2]^+$** complex with some selected MOs from its valence electronic structure is displayed in Figure 5.15.

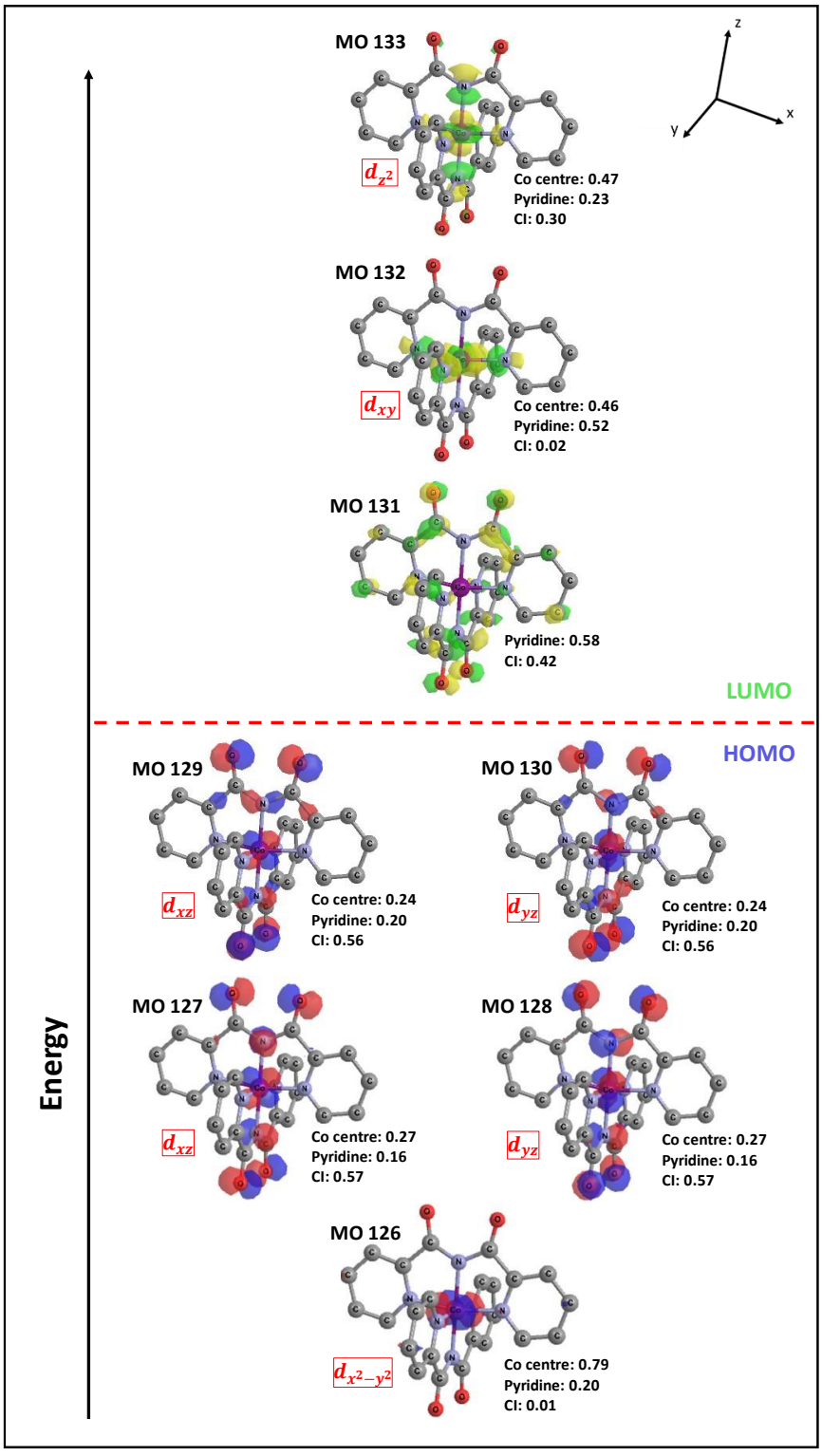

Figure 5.15: Electronic structure of $[Co^{III}(bpca)_2]^+$ displaying selected valence MOs with isosurface plots having iso-values of 0.05 calculated in acetonitrile.

Despite the isoelectronic nature of **$Fe^{II}(bpca)_2$** and **$[Co^{III}(bpca)_2]^+$**, their redox activity and accompanying electronic structures as they relate to the reduction products have some significant differences. In terms of the identity of the d-orbitals that are occupied, **$[Co^{III}(bpca)_2]^+$** maintains the expected configuration, occupying the t_{2g} orbitals while the e_g orbitals are inaccessible. The major difference for the occupied orbitals resides in the MOs that are formed between the ligands and the d_{xz} and d_{yz} orbitals. For this configuration, four MOs are generated in two sets of degenerate pairs. The HOMOs of the configuration (MO 129 and 130) contain a 24% contribution from the metal center. Lower in energy, the second set of degenerate orbitals contain 27% contribution from the metal center. The electron distributions in **$Fe^{II}(bpca)_2$** for the orbitals containing significant d_{xz} and d_{yz} character were isolated to only two occupied MOs. The unoccupied orbitals for **$[Co^{III}(bpca)_2]^+$** did not deviate far from **$Fe^{II}(bpca)_2$**, having a LUMO that is composed mostly of contributions from the pyridine groups with the remainder contained in the imine. The $d_{x^2-y^2}$ MO for **$[Co^{III}(bpca)_2]^+$** (MO 132) is far more accessible for electron occupation in this structure compared to **$Fe^{II}(bpca)_2$**; in fact, it is only slightly higher in energy than the LUMO (MO 131). Adding an electron to **$[Co^{III}(bpca)_2]^+$** generates **$Co^{II}(bpca)_2$**. The electronic structure of this species is displayed in Figure 5.16.

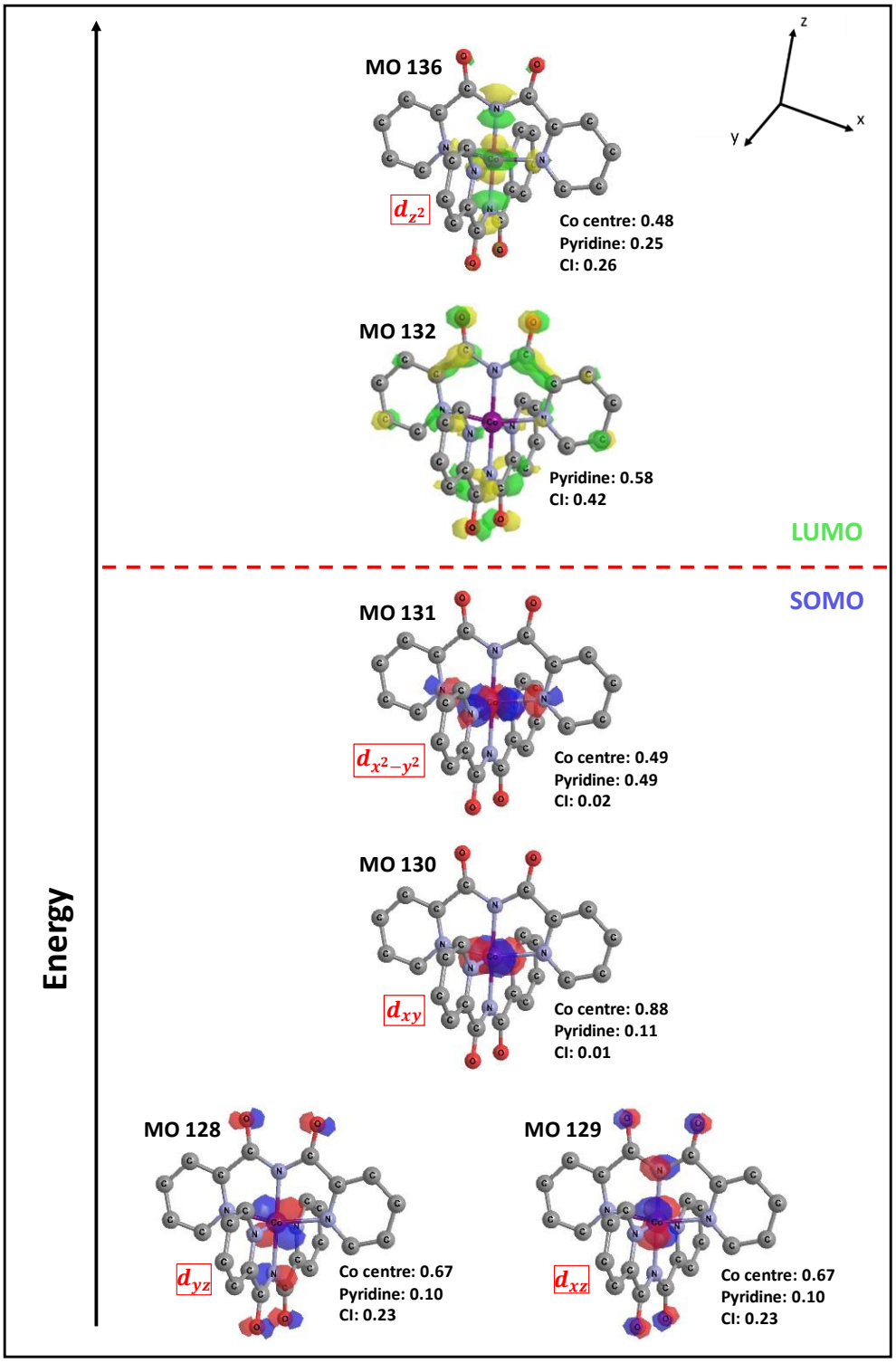

Figure 5.16: Electronic structure of $Co^{II}(bpca)_2$ displaying selected valence MOs with isosurface plots having iso-values of 0.05 calculated in acetonitrile.

During the reduction of **[Co^{III}(bpca)$_2$]$^+$**, the near degeneracy of MO 131 and MO 132 allowed for two potential reduction pathways; either reducing the ligand, or adding an electron to the metal center, respectively. The calculations for the singly reduced species (**Co^{II}(bpca)$_2$**) suggest that adding an electron to the metal center and changing the d-electron count to d^7 generates a lower energy electronic structure. The SOMO for this new structure is MO 131 in Figure 5.16. This MO contains a 49% contribution from the $d_{x^2-y^2}$ orbital. The other segments of the complex that significantly contribute to the MO are the pyridine groups, which contribute 49%. Occupying the LUMO^{+1} during the reduction process causes some of the occupied orbitals to reconfigure. Notably, the d_{xz} and d_{yz} orbitals that contribute to the formation of two sets of degenerate MOs in **[Co^{III}(bpca)$_2$]$^+$** are reconfigured to closely resemble the MOs observed for **Fe^{II}(bpca)$_2$** (MO 129 and 130 from Figure 5.9). This process appears to stabilize these MOs, elevating MO 126 from Figure 5.15 to MO 130 in Figure 5.16. The contributions from this orbital remain similar, being composed largely of the d_{xy} atomic orbital with some contributions from the pyridine groups. The d_{z^2} orbital remains inaccessible to the addition of an electron for subsequent reduction processes. Having skipped the reduction of the LUMO from the previous electronic structure, the LUMO for **Co^{II}(bpca)$_2$** remains in the same position, being comprised of by the same fragment contributions as **[Co^{III}(bpca)$_2$]$^+$**. The similar energy levels of the SOMO and LUMO continue to play an impactful role in delineating how electrons are added to the structure on subsequent reductions. Adding another electron to form **[Co^{III}(bpca)$_2$]$^-$** reverses the reconfiguration process put into motion during the first reduction, pairing the electrons in the MO analogous to the LUMO from

$[Co^{III}(bpca)_2]^+$. The diamagnetic electron configuration for the second reduction product, $[Co^{III}(bpca)_2]^-$, is displayed in Figure 5.17.

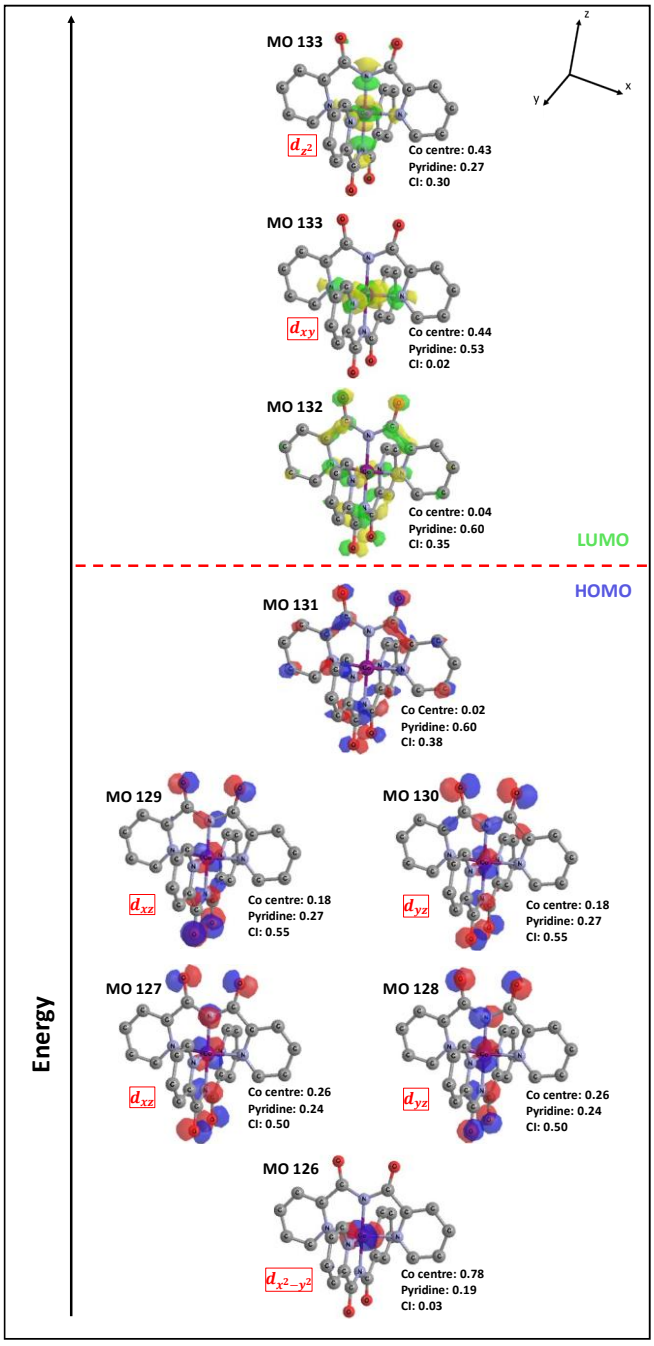

Figure 5.17: Electronic structure of $[Co^{III}(bpca)_2]^-$ displaying selected valence MOs with isosurface plots having iso-values of 0.05 calculated in acetonitrile.

As stated previously, the new electron configuration more closely resembles **[Co^{III}(bpca)$_2$]$^+$** when another electron is added. More specifically, the d_{xz} and d_{yz} orbitals contribute to two sets of degenerate orbitals again, and the MO composed largely of d_{xy} reclaims its spot lower in energy than the d_{xz} and d_{yz} orbitals. The occupied orbitals from Figure 5.15 reappear as MO 126-130 in Figure 5.17, having experienced only minor variations in their composition. The two added electrons occupy the original LUMO from Figure 5.15, which contains no contributions from the ligand, indicating that the electron count at the metal center reverts to d^6. The d_{z^2} orbital (MO 136) remains unoccupied, with several unoccupied orbitals lower in energy.

Throughout the two reduction processes completed so far on the initial **[Co^{III}(bpca)$_2$]$^+$** species, the MOs that become occupied partition their electron density in virtually the same manner spatially among the ligands, maintaining a similar symmetry profile for the complex's overall structure. Adding an additional electron to **[Co^{III}(bpca)$_2$]$^-$** to generate the third reduction product, **[Co^{I}(bpca)$_2$]$^{2-}$**, significantly deviates from this trend. This new structure represents an instance for M(bpca)$_2$ structures where one of the coordinated bpca ligands must contort its structure to stabilize the added charge. The electronic configuration for paramagnetic **[Co^{I}(bpca)$_2$]$^{2-}$** is displayed in Figure 5.18. Altering the structure of one of the ligands significantly affects the atomic d-orbital contributions for the occupied orbitals and ultimately disrupts any degeneracy present among MOs in the configuration. The relative energy levels of the MOs comprised largely of the d-orbitals rearrange for the occupied orbitals. The d_{xy} (MO 129 in Figure 5.18) orbital resides in

between the energy levels of the MOs comprised largely of d_{xz} and d_{yz} (MO 128 and 130, respectively).

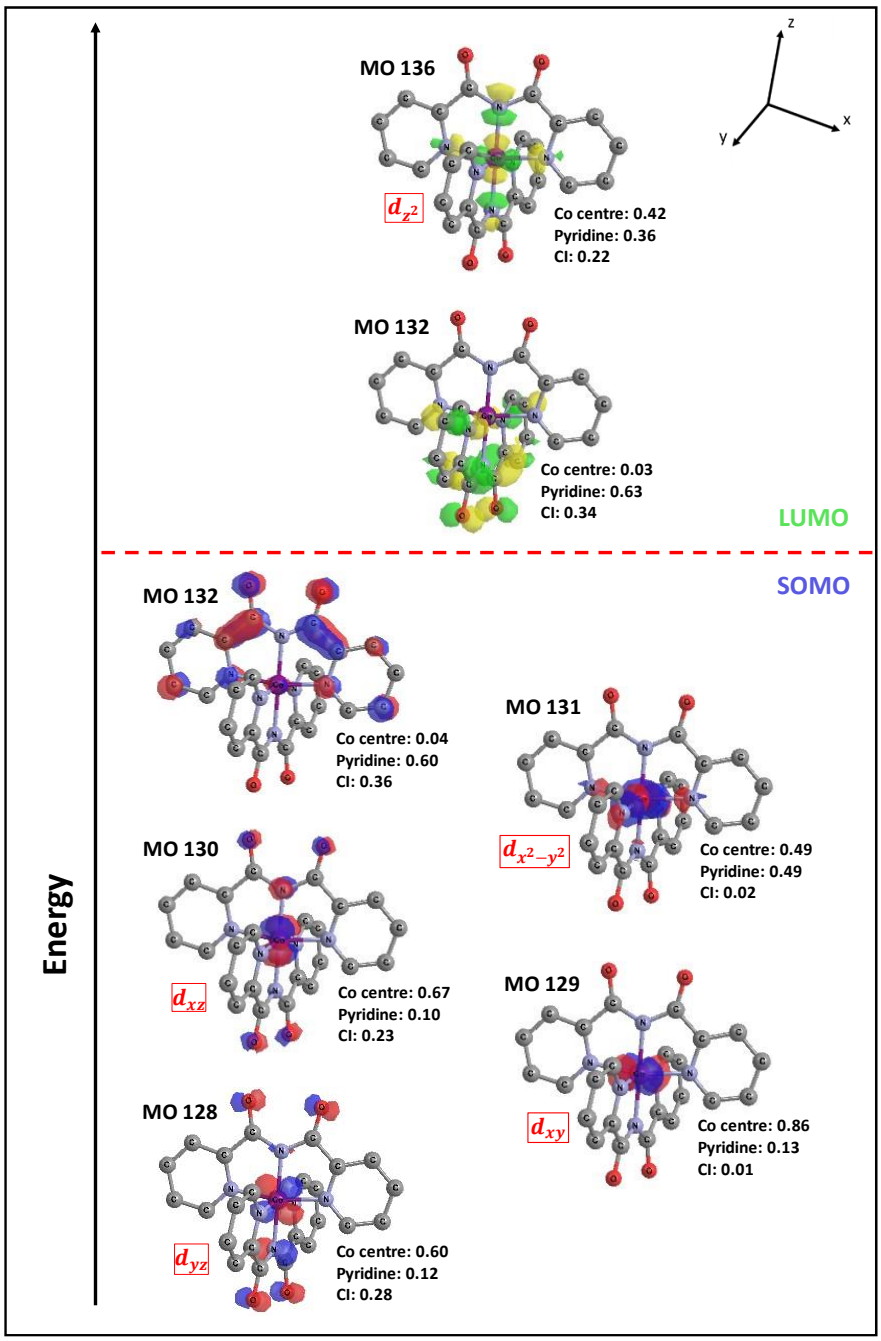

Figure 5.18: Electronic structure of $[Co^{I}(bpca)_2]^{2-}$ displaying selected valence MOs with isosurface plots having iso-values of 0.05 calculated in acetonitrile.

Following the third reduction process, MO 131 from Figure 5.18 becomes fully occupied. The final electron is added to MO 132, which places all its electron density on one of the bpca ligands forming a SOMO, causing the ligand to contort from its original structure. The planar geometry of the affected ligand twists slightly, such that the carbonyl groups are no longer in the same plane. The LUMO for this electronic structure, is the complementary MO, existing on the other ligand. The difference in the ligands can be further examined in the context of bond lengths and bond order, listed in Table 5.10.

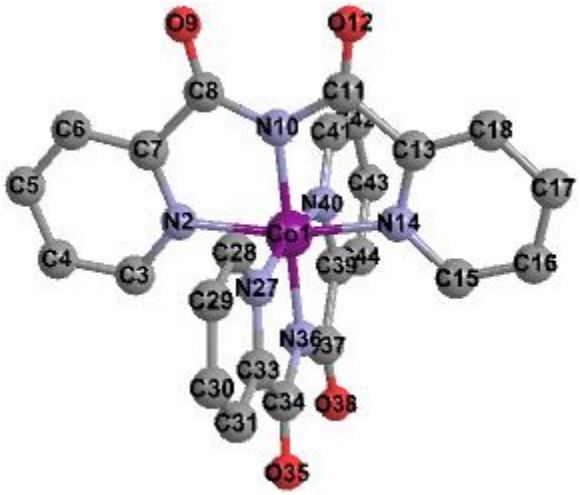

Figure 5.19: Ligand structure from Chemissian including atom number labelling covering $[Co^{III}(bpca)_2]^+$, $Co^{II}(bpca)_2$, $[Co^{III}(bpca)_2]^-$, and $[Co^{I}(bpca)_2]^{2-}$.

Table 5.7: Descriptions of bond lengths and order for selected bonds in $[Co^{III}(bpca)_2]^+$.

Bond	Bond Length (Å)	Bond Order
Co1-N10	1.895	0.91
Co1-N2	1.933	0.57
Co1-N14	1.933	0.57
Co1-N36	1.895	0.91
Co1-N27	1.933	0.57
Co1-N40	1.933	0.57
C7-C8	1.053	1.02
C8-N10	1.373	1.11

C8-O9	1.211	1.63
C33-C34	1.053	1.02
C34-N36	1.373	1.11
C34-O35	1.211	1.63

Table 5.8: Descriptions of bond lengths and order for selected bonds in $Co^{II}(bpca)_2$.

Bond	Bond Length (Å)	Bond Order
Co1-N10	1.926	0.73
Co1-N2	2.060	0.44
Co1-N14	2.060	0.44
Co1-N36	1.925	0.73
Co1-N27	2.060	0.44
Co1-N40	2.060	0.44
C7-C8	1.151	1.01
C8-N10	1.370	1.14
C8-O9	1.219	1.63
C33-C34	1.150	1.01
C34-N36	1.370	1.14
C34-O35	1.219	1.62

Table 5.9: Descriptions of bond lengths and order for selected bonds in $[Co^{III}(bpca)_2]^-$.

Bond	Bond Length (Å)	Bond Order
Co1-N10	1.889	0.94
Co1-N2	1.919	0.53
Co1-N14	1.919	0.53
Co1-N36	1.889	0.94
Co1-N27	1.919	0.53
Co1-N40	1.919	0.53
C7-C8	1.476	1.11
C8-N10	1.370	1.11
C8-O9	1.236	1.59
C33-C34	1.476	1.11
C34-N36	1.370	1.11
C34-O35	1.236	1.58

Table 5.10: Descriptions of bond lengths and order for selected bonds in $[Co^{I}(bpca)_2]^{2-}$.

Bond	Bond Length (Å)	Bond Order
Co1-N10	1.967	0.70

Co1-N2	2.142	0.31
Co1-N14	2.142	0.31
Co1-N36	1.927	0.72
Co1-N27	1.966	0.56
Co1-N40	1.965	0.56
C7-C8	1.480	1.10
C8-N10	1.371	1.14
C8-O9	1.249	1.60
C33-C34	1.474	1.12
C34-N36	1.370	1.13
C34-O35	1.247	1.59

Changes in bond lengths and order as **$[Co^{III}(bpca)_2]^+$** goes through its three reduction processes significantly deviate from the trends observed in **$Fe^{II}(bpca)_2$**. This difference can be attributed to the alternating occupation of the metal center and ligand as electrons are added. For **$Fe^{II}(bpca)_2$** both reduction processes place the electrons in MOs on the ligand, ultimately causing the coordinating bonds to shorten. In **$[Co^{III}(bpca)_2]^+$**, the first reduction process occupies the σ* MO largely comprised of $d_{x^2-y^2}$. The antibonding nature of this orbital causes the bonds to lengthen; for instance, the bonds from the ligand to the imine nitrogen (Co1-N10) extend from 1.895 Å to 1.926 Å according to Tables 5.7 and 5.8, respectively. The same trend is observed in this reduction process for all other coordination bonds. The relevant bonds in the ligand remain largely unchanged across the first reduction process.

Adding the second electron to generate **$[Co^{III}(bpca)_2]^-$** causes the coordination bonds to decrease, as the σ* MO largely comprised of $d_{x^2-y^2}$ becomes vacated. The added negative charge to the ligands causes them to be more closely attracted to the metal center. Interestingly, addition of electrons to **$[Co^{III}(bpca)_2]^+$** has the opposite effect on the bond

lengths between the carbonyl carbons and pyridine compared to **$Fe^{II}(bpca)_2$**. As shown in Tables 7-10, added electrons increase the bond lengths of (C7-C8) and decrease their bond orders. This deviation could explain the differences observed in stability for **$[Co^{III}(bpca)_2]^+$** relative to **$Fe^{II}(bpca)_2$** during catalytic trials and the tendency of the former to degrade and deposit on the electrode.

Performing the final reduction to generate **$[Co^{I}(bpca)_2]^{2-}$** causes one of the ligands to coordinate more closely, while the metal-ligand bond lengths of the other bpca increase slightly. In Table 10, bonds Co1-N10, Co1-N2, and Co1-N14 have lengths of 1.967 Å, 2.142 Å, and 2,142 Å respectively. The other ligand's analogous bonds were 1.966 Å, 1.926 Å, and 1.927 Å for bonds Co1-N36, Co1-N27, and Co1-N40, respectively. This trend was also reflected in the bond orders. The coordination site on the bicarbonylpyridine is not significantly altered, but one of the ligands disfavours coordination at the pyridine site. This occurrence could also explain how the **$[Co^{III}(bpca)_2]^+$** complex is degraded during CPE.

5.4.4 – $Ni^{II}(bpca)_2$

Electrochemical investigations of **$Ni^{II}(bpca)_2$** demonstrate the effects that varying the d-electron count could have on the redox activity of $M(bpca)_2$ complexes. The previous structures are both d^6, whereas **$Ni^{II}(bpca)_2$** has a d-electron count of d^8. Figure 5.20 displays a CV swept in the cathodic direction of **$Ni^{II}(bpca)_2$** in acetonitrile. Three reversible reduction events was observed in the scan have $E_{1/2}$ of -2.12V, -2.33V, and -2.45V vs $Fc^{+/0}$. DFT calculations predict the reduction potentials values with some inconsistency. For the first reduction potential, two different values were calculated depending on the

multiplicity of the electronic structure. Assuming a singlet state, the calculated reduction potential was -2.85V, whereas the triplet state was -1.76V. The second and third reduction potentials were calculated to be -2.52V and -2.98V, respectively.

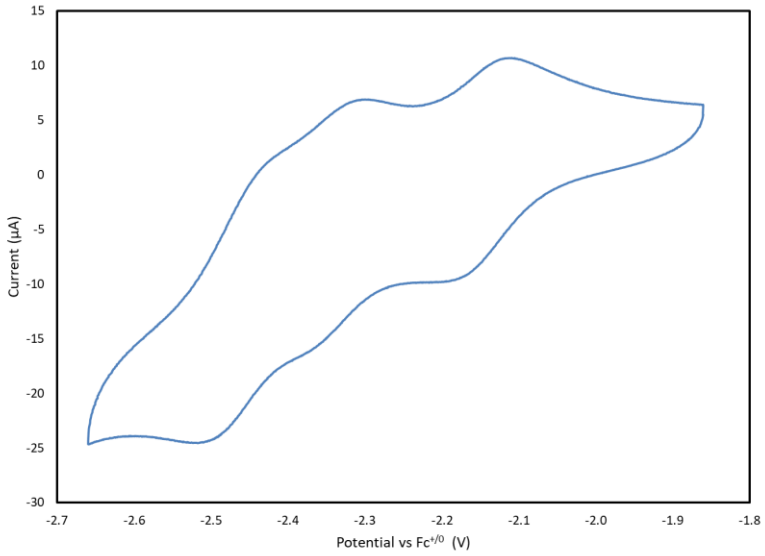

Figure 5.20: CV of 0.5mM $Ni^{II}(bpca)_2$ in acetonitrile with a scan rate of 0.1V/s scanned between -1.88V and -2.67V using TBAHFP as the electrolyte.

Forming a complex with an addition of two electrons in the d-electron count invariably results in an electron configuration with a new constitution. MOs which could have once formed to lower their energy, become irrelevant in the new electron configuration. In the case of **$Ni^{II}(bpca)_2$** and its three reduced species, the added electrons to the d-electron count result in significant structural variation. Figure 5.21 displays the triplet electronic configuration with selected MOs of **$Ni^{II}(bpca)_2$**. In general, this configuration fits well with the expected electronic configuration for an octahedral organometallic complex with a d^8 metal center. The t_{2g} orbitals are all fully occupied, and the e_g orbitals are both singly occupied, resulting in two unpaired electrons.

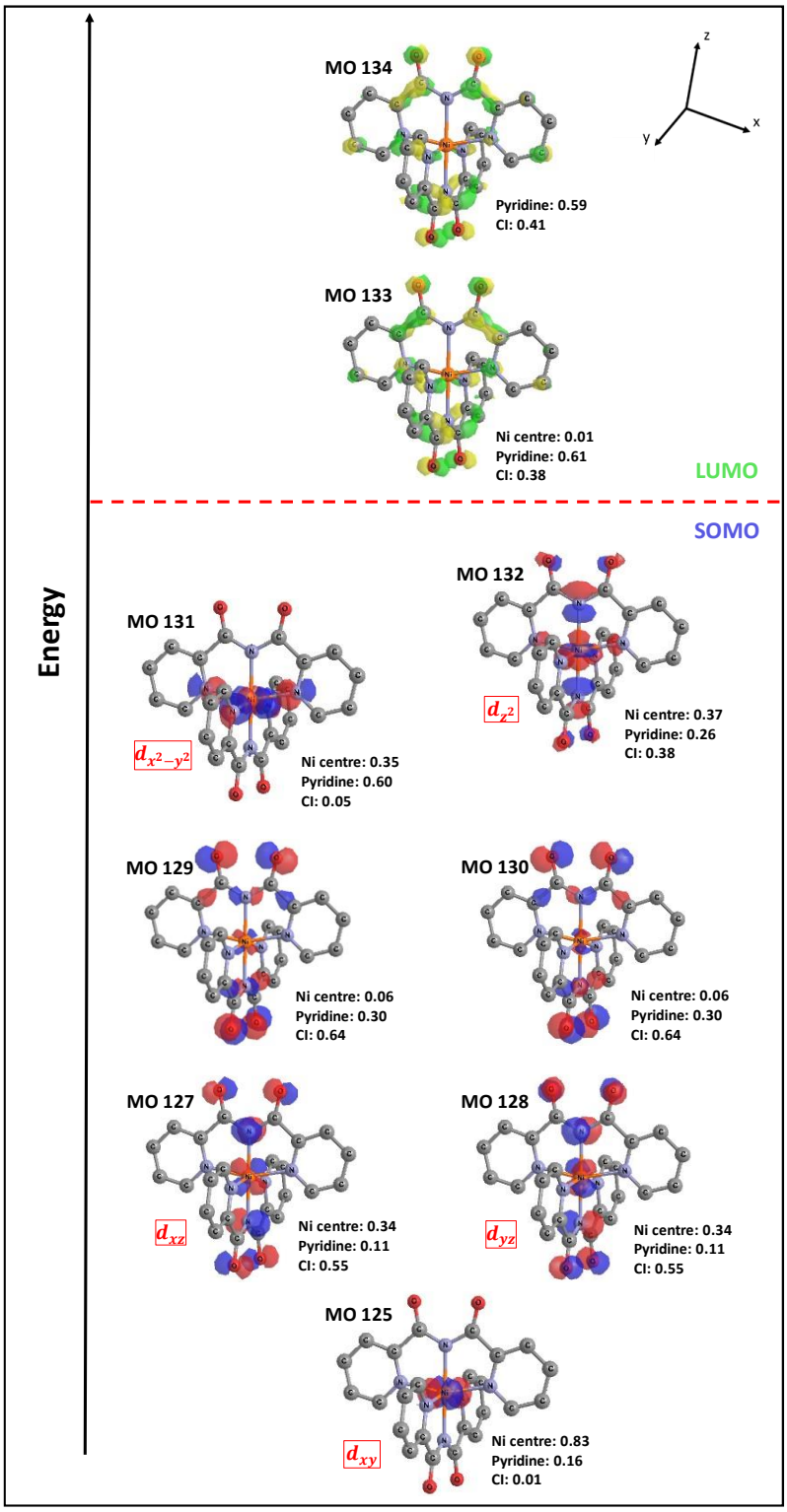

Figure 5.21: Electronic structure of $Ni^{II}(bpca)_2$ displaying selected valence MOs with isosurface plots having iso-values of 0.05 calculated in acetonitrile.

There are several similarities to be observed here, in relation to the previous complexes. Specifically, orbitals MO 127-130 from Figure 5.21 closely resemble MO 127-130 in Figure 5.15, for **$[Co^{III}(bpca)_2]^+$**. MOs 127 and 128 for each of these structures involve significant d_{xz} and d_{yz} character with ligand orbital contributions aligned with minimal overlap in a near non-bonding orientation. Higher in energy, MOs 129 and 130 display a similar structure, but with ligand contributions arranged with the symmetry to overlap in an anti-bonding capacity, raising the energy level. The disparity in contributions between each atomic component to the overall structure between the two different configurations can be attributed to the increase in energy of the electrons, moving from cobalt to nickel.

According to the electron configuration in Figure 5.21, reducing **$Ni^{II}(bpca)_2$** is expected to place another electron in MO 131, fully occupying that orbital and generating an electron configuration with a doublet multiplicity. The atomic orbitals that contribute to the formation of MO 131 consist of the $d_{x^2-y^2}$ atomic orbital from the metal center anti-bonding with p-orbitals from each of the nitrogen on all the coordinated pyridines. Fully occupying these σ^* bonds would disfavour the interaction and result in some significant alteration to the overall molecular structure. Ultimately, occupying the orbital causes a shift in the overall orientation used to visualize the structure, as the bonding interaction is disrupted for both pyridines on one of the bpca ligands. The octahedral d_8 electronic configuration is disrupted, leaving behind an electronic configuration that has a d-electron count of d^8 with a square planar geometry, storing the added electron in an orbital composed of major contributions from the fully coordinated bpca ligand (MO 132 in Figure 5.22).

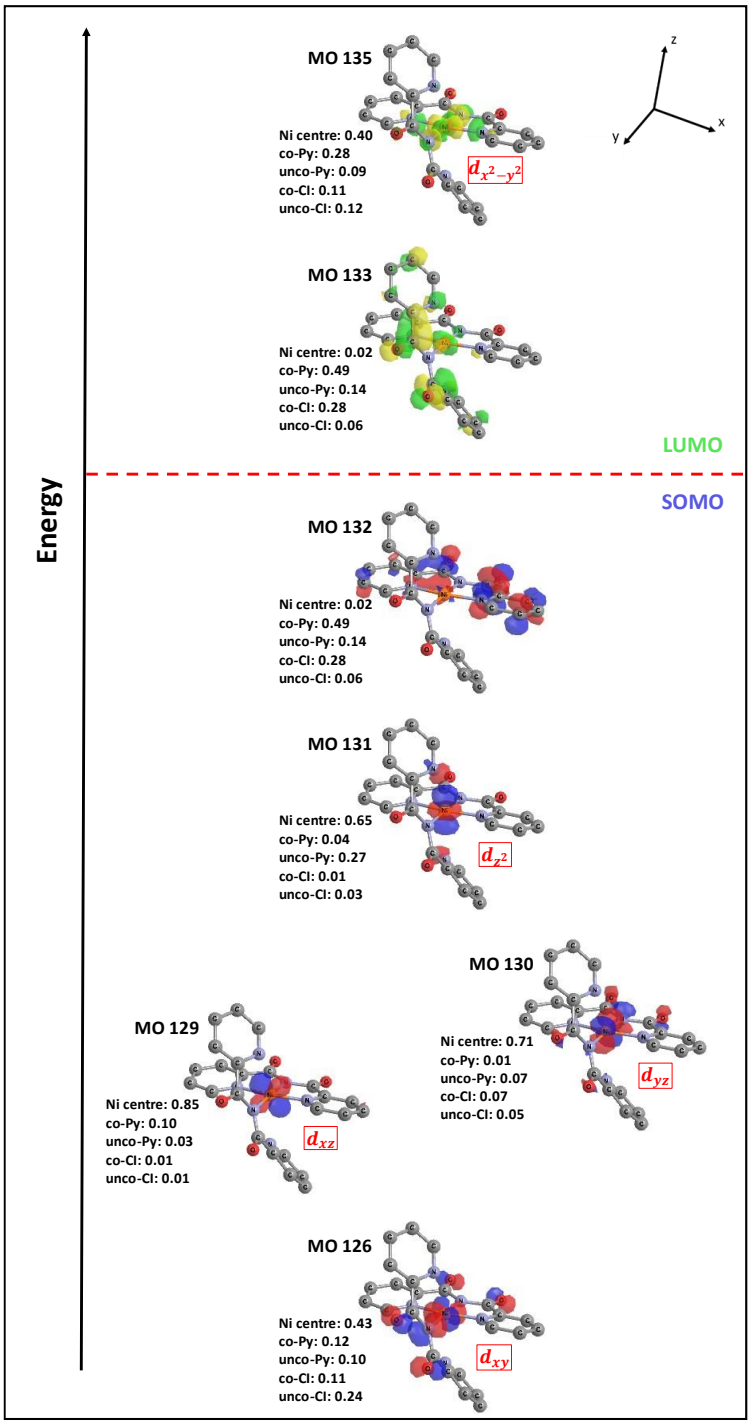

Figure 5.22: Electronic structure of $[Ni^{II}(bpca)_2]^-$ displaying selected valence MOs with isosurface plots having iso-values of 0.05 calculated in acetonitrile.

Due to the significant departure from the typical $M(bpca)_2$ structure with nearly identical bpca structure observed in Figure 5.22, the labeling system used to designate each fragment contributions to the overall MO was adjusted. Co-Py and Co-CI denote orbital contributions from the pyridine groups and CI, respectively, contained on the bpca ligand that is functioning as a tridentate ligand. Unco-Py and Unco-CI represent the same structures, but on the ligand coordinating only through one site.

Altering the coordination of the pyridine groups for one of the bpca ligands removes any degeneracy that was once present for the valence electronic configuration. Specifically, MO 129 and 130 from Figure 5.22 are no longer comprised of the same contributions from each fragment. In previous structures these orbitals were analogously constructed of the same ratio of fragment contributions from the d_{xz} and d_{xy} atomic orbitals from the metal centers paired with the same percentage from the CI and pyridine groups. For this configuration, MO 129 and 130 are comprised of 85% and 71% d-orbitals on the metal center respectively, removing the degeneracy and placing MO 130 at a higher energy level.

The orbital comprised largely of $d_{x^2-y^2}$ (MO 135) becomes unoccupied and inaccessible to added electrons. The d_{z^2} orbital is doubly occupied in this electronic structure (MO 131). This MO is stabilized relative to the analogous MO in the previous structure (MO 131 from Figure 5.21) by the increased bond length, mitigating the antibonding character featured in the previous MO. The SOMO and LUMO (MO 132 and 133) are comprised of orbitals that reside almost entirely on the ligands. MO 132 resides on the tridentate bpca, whereas MO 133 resides on the monodentate bpca ligand. Adding another electron to

this structure generates **[Ni^{II}(bpca)$_2$]$^{2-}$**, as seen in Figure 5.23. This complex is diamagnetic with a d-electron count of d^8.

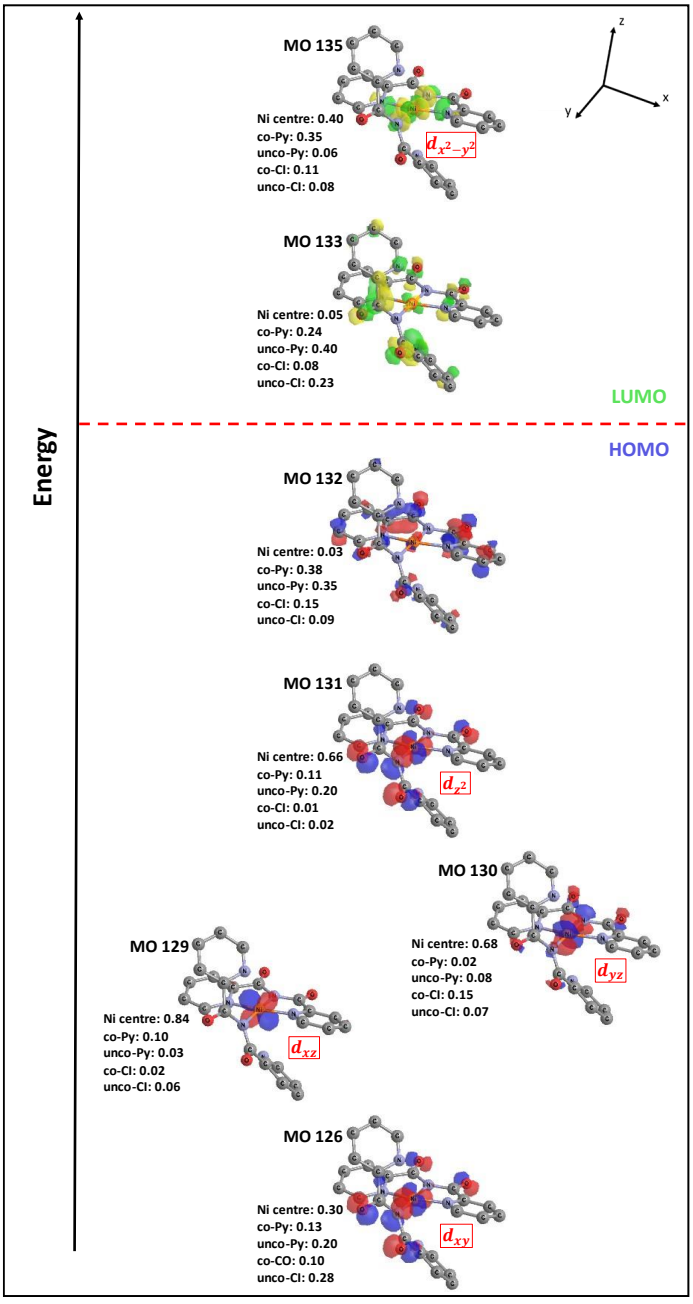

Figure 5.23: Electronic structure of [Ni^{II}(bpca)$_2$]$^{2-}$ displaying selected valence MOs with isosurface plots having iso-values of 0.05 calculated in acetonitrile.

Reducing **[Ni^{II}(bpca)$_2$]$^-$** to generate **[Ni^{II}(bpca)$_2$]$^{2-}$** proceeds as would be expected through simple inspection of the electronic configuration of **[Ni^{II}(bpca)$_2$]$^-$** (Figure 5.22). The added electron is placed in the SOMO, fully occupying it to become the HOMO of the new electron configuration. There are some minor changes to the MO structure of the newly formed HOMO. In its previous form, MO 132 (Figure 5.22) is comprised almost entirely of orbitals contained on the tridentate bpca. When another electron is added (Figure 5.23) some significant contributions from the monodentate bpca are present. The contributions from the unco-CI and unco-Py change from 6% to 9% and 14% to 35%, respectively. The LUMO undergoes a similar change. The occupied MOs remain largely unaltered following the electron addition.

Simulating the final reduction process, one more electron was added the system to generate **[Ni^{II}(bpca)$_2$]$^{3-}$**, as displayed in Figure 5.24. The new system is paramagnetic with a doublet multiplicity. The SOMO for the system (MO 133) is comprised largely of atomic orbitals on the tridentate bpca ligand, having switched the energy levels of MO 133 and MO 132 from the previous structure. The MO comprised largely of the $d_{x^2-y^2}$ atomic orbital from the metal center remains unoccupied, implying that the d^8 electron count remains unaltered. The ligand system appears to distribute the electron density from all added electrons on the ligands.

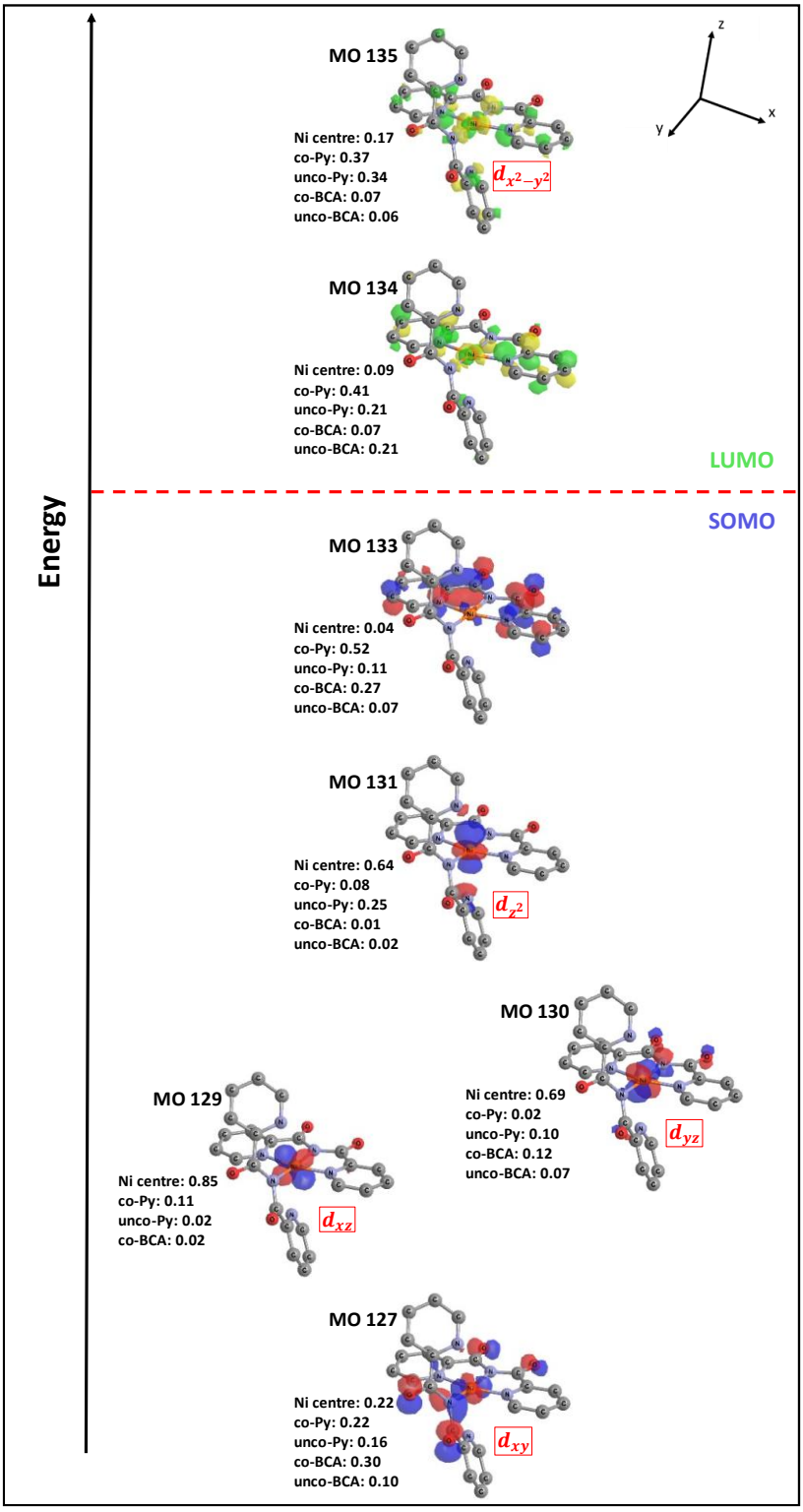

Figure 5.24: Electronic structure of $[Ni^{II}(bpca)_2]^{3-}$ displaying selected valence MOs with isosurface plots having iso-values of 0.05 calculated in acetonitrile.

Significant alterations in bonding interactions are observed through the three reduction processes that can occur for ***$Ni^{II}(bpca)_2$***. Some selected bonds are displayed in Tables 5.11-5.14. Each bond is described based on the atom number system displayed in Figure 5.25.

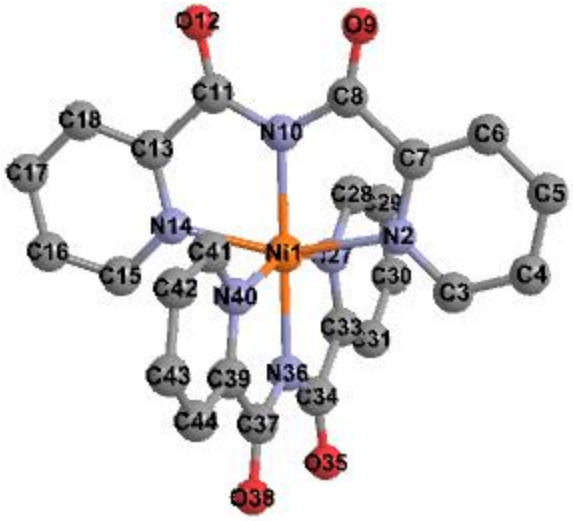

Figure 5.25: Ligand structure from Chemissian including atom number labelling covering $Ni^{II}(bpca)_2$, $[Ni^{II}(bpca)_2]^-$, $[Ni^{II}(bpca)_2]^{2-}$, and $[Ni^{II}(bpca)_2]^{3-}$.

Table 5.11: Descriptions of bond lengths and order for selected bonds in $Ni^{II}(bpca)_2$.

Bond	Bond Length (Å)	Bond Order
Ni1-N10	2.040	0.47
Ni1-N2	2.088	0.43
Ni1-N14	2.088	0.43
Ni1-N36	2.040	0.47
Ni1-N27	2.088	0.43
Ni1-N40	2.088	0.43
C7-C8	1.518	0.99
C8-N10	1.361	1.14
C8-O9	1.221	1.62
C33-C34	1.518	0.99
C34-N36	1.361	1.14
C34-O35	1.221	1.62

Table 5.12: Descriptions of bond lengths and order for selected bonds in $[Ni^{II}(bpca)_2]^-$.

Bond	Bond Length (Å)	Bond Order
Ni1-N10	1.960	0.60
Ni1-N2	2.469	0.13
Ni1-N14	2.476	0.12
Ni1-N36	1.876	0.74
Ni1-N27	1.934	0.65
Ni1-N40	1.913	0.68
C7-C8	1.514	0.99
C8-N10	1.371	1.13
C8-O9	1.223	1.65
C33-C34	1.491	1.06
C34-N36	1.356	1.15
C34-O35	1.235	1.59

Table 5.13: Descriptions of bond lengths and order for selected bonds in $[Ni^{II}(bpca)_2]^{2-}$.

Bond	Bond Length (Å)	Bond Order
Ni1-N10	1.932	0.63
Ni1-N2	2.523	0.11
Ni1-N14	2.550	0.11
Ni1-N36	1.878	0.70
Ni1-N27	1.923	0.65
Ni1-N40	1.924	0.65
C7-C8	1.499	1.02
C8-N10	1.372	1.14
C8-O9	1.235	1.64
C33-C34	1.458	1.15
C34-N36	1.374	1.11
C34-O35	1.249	1.59

Table 5.14: Descriptions of bond lengths and order for selected bonds in $[Ni^{II}(bpca)_2]^{3-}$.

Bond	Bond Length (Å)	Bond Order
Ni1-N10	1.976	0.60
Ni1-N2	2.788	0.07
Ni1-N14	2.389	0.16
Ni1-N36	1.928	0.68
Ni1-N27	1.948	0.65
Ni1-N40	1.952	0.63
C7-C8	1.509	0.98

C8-N10	1.346	1.24
C8-O9	1.246	1.66
C33-C34	1.444	1.23
C34-N36	1.379	1.10
C34-O35	1.263	1.57

Throughout each reduction process, some similarities in bond length and order trends are present for **$Ni^{II}(bpca)_2$** as were observed for **$Fe^{II}(bpca)_2$** and **$Co^{III}(bpca)_2$**. In some instances, bond lengths were altered in a manner not observed in the other complexes. One observation unique to **$Ni^{II}(bpca)_2$** occurred directly following the first reduction. The ligand coordinated in the top position in Figure 5.25 significantly elongates along bonds Ni1-Ni2 and Ni1-Ni14. Initially these bonds are both 2.088 Å with bond orders of 0.43 (table 5.11). After the reduction (table 5.12), Ni1-N2 grows to 2.469 Å with a bond order of 0.13, while Ni1-N14 increases to 2.476 Å with a bond order of 0.12, essentially generating a monodentate ligand. The other bpca ligand exhibits the opposite, decreasing the analogous bond lengths and increasing bond order over this reduction process. Adding another electron to generate **$[Ni^{II}(bpca)_2]^{2-}$**, further increases the bond lengths of the top ligand to 2.523 Å and 2.550 Å for bonds Ni1-N2 and Ni1-N14, respectively as seen in table 5.13. For the bottom bpca ligand, the lengths of the analogous bonds stay nearly the same. During the final reduction process to generate **$[Ni^{II}(bpca)_2]^{3-}$**, the relative bond strengths of Ni1-N2 and Ni1-N14 significantly diverge as seen in Table 5.14, having bond orders of 0.07 and 0.16, respectively. During the third reduction process of **$[Co^{III}(bpca)_2]^{+}$**, some slight structural differences were observed differentiating the bpca ligands, but the effect was not as pronounced as what was observed here for **$Ni^{II}(bpca)_2$**.

When examining some select bonds on the pyridine ligands, some familiar trends are observed. For the bpca ligand that remains tridentate throughout the reduction processes, the bonds between the pyridine carbon and carbonyl carbon (C33-C34) decrease with added electrons. For the other bpca ligand, the decrease is also observed, but to a lesser degree and during the final electron addition the bond length increases.

5.5 – Describing the DFT Calculations in Acetonitrile

5.5.1 – General computational protocol

Calculations were completed for the bpca ligand and each $M(bpca)_2$ complex to elucidate details of their redox behaviour. The general method involves a 2-step process; optimization in acetonitrile using the polarizable continuum model (PCM) paired with vibrational frequency calculations followed by molecular energy point calculations.[18,19] For each structure, the optimization was validated by the absence of negative vibrational frequencies.[20] The molecular energy computations can be used for multiple purposes. Firstly, they are used to generate MOs to visualize the atomic orbital contributions from each fragment of the molecule. Secondly, they can be used to generate Gibbs free energy values for added electrons. DFT calculations were completed using the Gaussian 09 software package through the WebMO interface. The MO diagrams were constructed using Chemissian. Structures were obtained for each initial molecule through the CCDC database.

5.5.2 – Designing the computational strategy

Selection of the optimal functional and basis set combination for this investigation, like all DFT investigations, required a careful balance of accuracy and efficiency.[21,22] The software package (Gaussian 09), total number of processors, and time constraints were limiting factors that prevented the use of high-powered double hybrid methodologies that often prove to be needlessly overpowered. Basis set selection can be variable for a sequence of jobs. For instance, a smaller basis set can be employed to optimize a molecular structure than is used to compute the molecular energy.[23] This process reduces the computational burden implicit in the job type. Optimization must make iterative energy level computations followed by incremental structural alteration until the global minimum is achieved. Relative to a single point molecular energy calculation, this process requires a great deal of computational power, resulting in long run times. Overall, the size of the molecule being studied, goal of the experiment, and time constraints all must be considered when selecting the functional and basis set.[23,24]

Initial DFT calculations for the $M(bpca)_2$ project were performed using the hybrid functional PBE0 with the D3 Grimmes dispersion correlation correction.[25–28] Many hybrid orbitals, including PBE0 and B3LYP, tend to overestimate the stability of medium to large molecules, falling victim to self-interaction error.[23] Increasing Hartree Fock (HF) contributions to a functional can reduce this error. PBE0 has 25% HF exchange, making it more accurate in this context than B3LYP, which has 20% HF exchange.[23] Adding the D3 Grimmes correction further reduces the error associated with self-interaction. The first computational attempts utilized too large of a basis set, resulting in run-times that took

over a week. In the initial trails optimizing **Fe(bpca)$_2$**, def2-TZVP was the basis set used. In order to reduce the run-times, the triple zeta basis set was exchanged with a split-valence basis set (def2-SVP). This basis set reduced the run-time to acceptable levels, but the method struggled to optimize the **[Fe^{II}(bpca)$_2$]$^-$** and **[Fe^{II}(bpca)]$^{2-}$**. These runs tended to bifurcate into two energy levels, alternating back and forth, never settling on a minimum energy. The proximity of components of the ligands could be to blame for this occurrence. Presumably, the larger polarizable function present on atoms at the extremity of each ligand could be the victim of self interaction. This interaction can be circumvented by removing the larger polarization function on the hydrogens by selected def2-sv(p) as the new basis set. Switching to this basis set allowed each of the target complexes to be optimized with minimal computational burden. The overall optimization and vibrational frequencies methodology used, was PBE0-D3/def2-SV(P). When calculating the molecular energy, the original basis set, def2-TZVP was used.

5.5.3 – Computing reduction values versus Fc$^{+/0}$

Approximations for the reduction potentials of the ligand and each M(bpca)$_2$ complex were calculated using the ferrocene/ferrocenium (Fc$^{+/0}$) couple as an isodesmic reaction couple.[29] This technique avoids the need to approximate the dissolution energy of an electron in acetonitrile. Reduction potentials can be calculated from the free energies of isodesmic reactions composed of the target process and another similar process with an experimental value for the reduction potential. Scheme 5.3 displays an example for the assembly of an isodesmic redox equation used in the first reduction of **Fe^{II}(bpca)$_2$**.

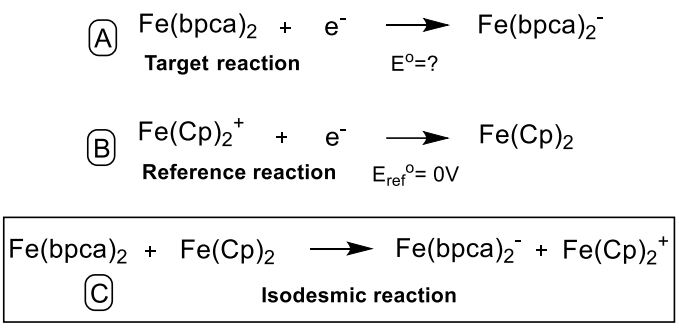

Scheme 5.3: A) Single electron process for the first reduction of $Fe^{II}(bpca)_2$. B) Single electron process for the $Fc^{+/0}$ redox couple as the reference reaction. C) combined reaction of A and B making the isodesmic reaction.

Similar schemes were prepared to simulate all the redox processes discussed in section 1.3. There exists a varying degree of computational error for each of the processes. Isodesmic pairing are most effectively constructed when the reference reaction closely mimics the chemistry of the target process. For instance, if a redox process is associated with the dissociation of a solvent ligand, using a reference reaction that undergoes a similar process negates any errors that may be associated with the re-configuration process. For this investigation, significant error is likely introduced for the instances where one of the bpca ligands begins to dissociate from the metal center. The lack of correction for these errors leaves these calculations as only an approximate value. Calculations approximating the redox potential of **$Fe^{II}(bpca)_2$** are described in eq. 5.1.

$$E^{o}_{Fe/Fe^{-}} = \frac{\Delta G_C}{F} - E^{o}_{Fc^{+/0}} \qquad \text{(Eq. 5.1)}$$

For the above equation, ΔG_C = Gibbs free energy of isodesmic process from scheme 5.1 (kcal/mol). F = Faraday constant (kcal/Vg). $E^{o}_{Fc^{+/0}}$ = Experimental $E_{1/2}$ of $Fc^{+/0}$ (V).

Overall, the calculated reactions ranged in their accuracy from the lowest disparity of 0.05V for the first reduction of **$Fe^{II}(bpca)_2$** to the least accurate approximation found for the third reduction of **$Ni^{II}(bpca)_2$** with a disparity of 0.53V. The first reduction process of **$Ni^{II}(bpca)_2$** resulted in two different potentials, depending on the initial multiplicity of the structure. When calculating the neutral structure in acetonitrile, the multiplicity could either be a singlet or a triplet. Previous work demonstrates that **$Ni^{II}(bpca)_2$** exists as a triplet as a solid. The computed value for the singlet structure in solution was lower in energy than the triplet structure. However, the structure of the singlet implies that one of the ligands must break away from the metal center, which could have a high energy transition state. Additionally, the computed value for the first reduction potential of **$Ni^{II}(bpca)_2$** starting in the triplet state (-1.76V) more closely resembles the experimental value (-2.12V) compared to the singlet state (-2.85V). The rearrangement of the ligand could also add some error to the calculation, exacerbating the inaccurate approximation. Another example of potential added error for these computations occurs for the final reduction of **$[Co^{III}(bpca)_2]^+$**. This series of computations suggests that the third reduction occurs before the second. Slight rearrangement of one bpca ligand for the triple reduced species could explain this inaccuracy.

5.6 – Screening Redox Catalysis Capabilities of Complexes

Having explored the reduction behaviour of **$Fe^{II}(bpca)_2$**, **$[Co^{III}(bpca)_2]^+$** and **$Ni^{II}(bpca)_2$**, a variety of potential electrocatalytically active redox events can be explored for several substrate targets. This class of compound has already been suggested as a CO_2 reducing catalyst hopeful, but none of the complexes investigated here have been proven in this

capacity. Neutral H_2O, NO_2^-, and NO are some of the other substrates explored as targets for electrocatalytic reduction herein.

5.6.1 – Evaluating diffusion control for each complex

Before the catalytic environment can be applied to each complex, homogeneous kinetics must be established. Investigating the rate dependence on the peak current can establish this. According to the Randles-Sevcik equation, the square root of the scan rate should be proportional to the peak current for a homogeneous process.[30] Therefore, each process must be investigated. The scan rate dependence CV and accompanying linear relationships between peak current and square root of the scan rate for **$Fe^{II}(bpca)_2$** are presented in Figure 5.26. Similar figures are presented for **$[Co^{III}(bpca)_2]^+$** and **$Ni^{II}(bpca)_2$** in Figures 5.27 and 5.28, respectively.

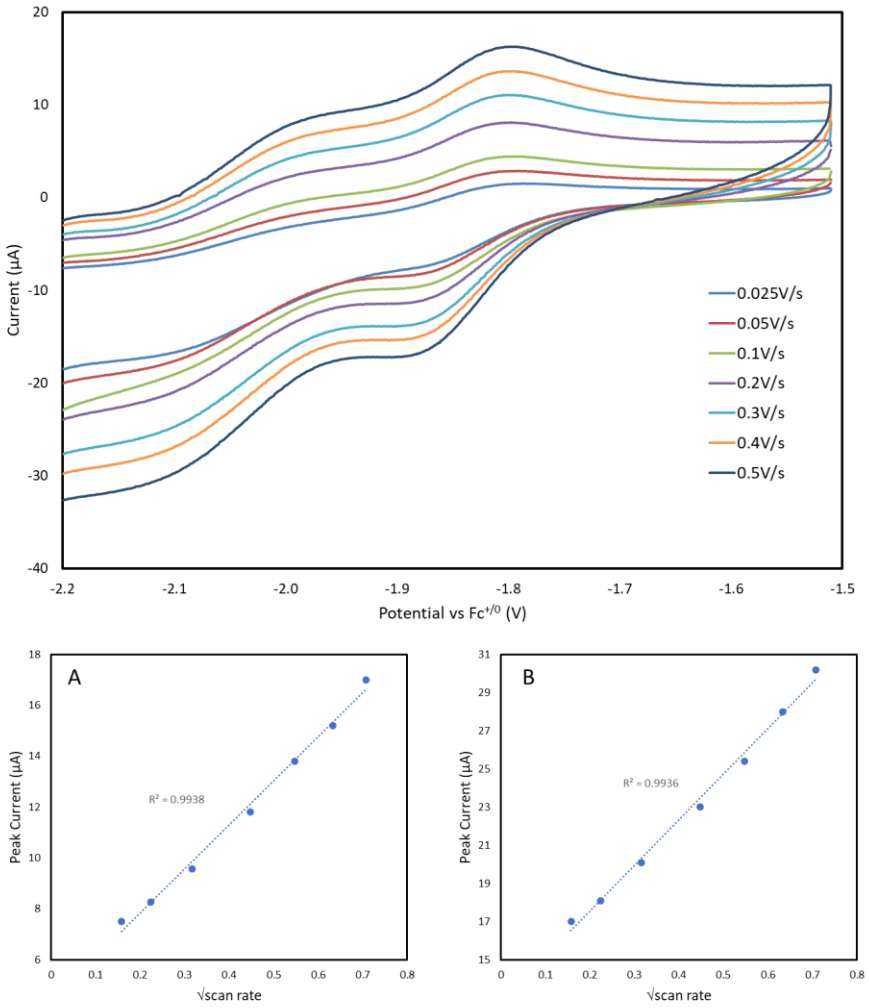

Figure 5.26: <u>Top</u> – CV of 0.5mM $Fe^{II}(bpca)_2$ in acetonitrile with varied scan rates scanned between -1.5V and -2.5V with TBAHFP as an electrolyte. <u>Bottom</u> – peak current as a function of scan rate for each of the reduction events observed in top figure. A) first reduction event B) second reduction event.

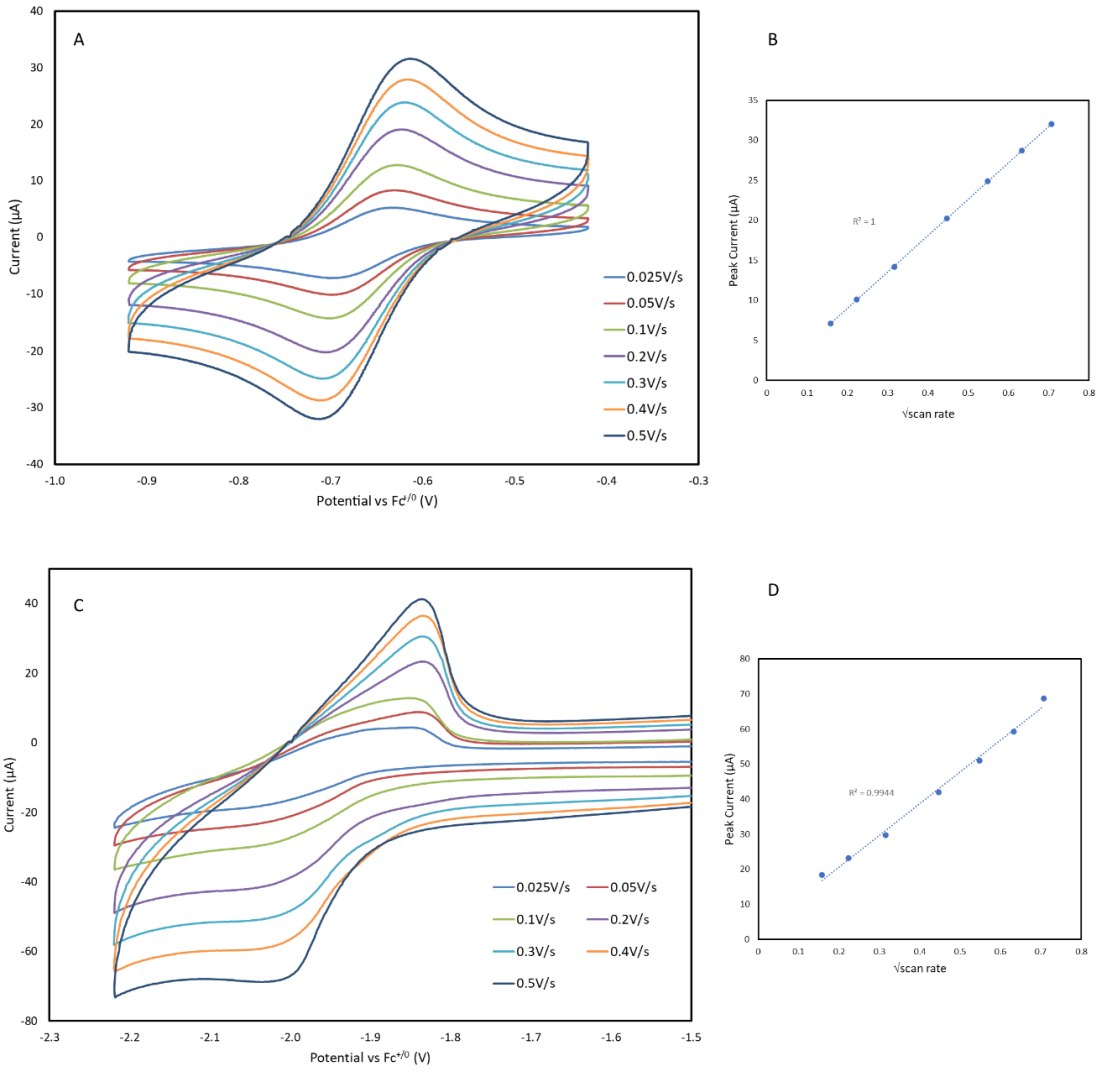

Figure 5.27: A) CV of 0.5mM $[Co^{III}(bpca)_2]^+$ in acetonitrile with varied scan rates scanned between -0.45V and -0.95V with TBAHFP as an electrolyte. B) peak current as a function of scan rate for the reduction event observed in A. C) CV of 0.5mM $[Co^{III}(bpca)_2]^+$ in acetonitrile with varied scan rates scanned between -0.45V and -2.23V with TBAHFP as an electrolyte. B) peak current as a function of scan rate for the reduction event observed in A.

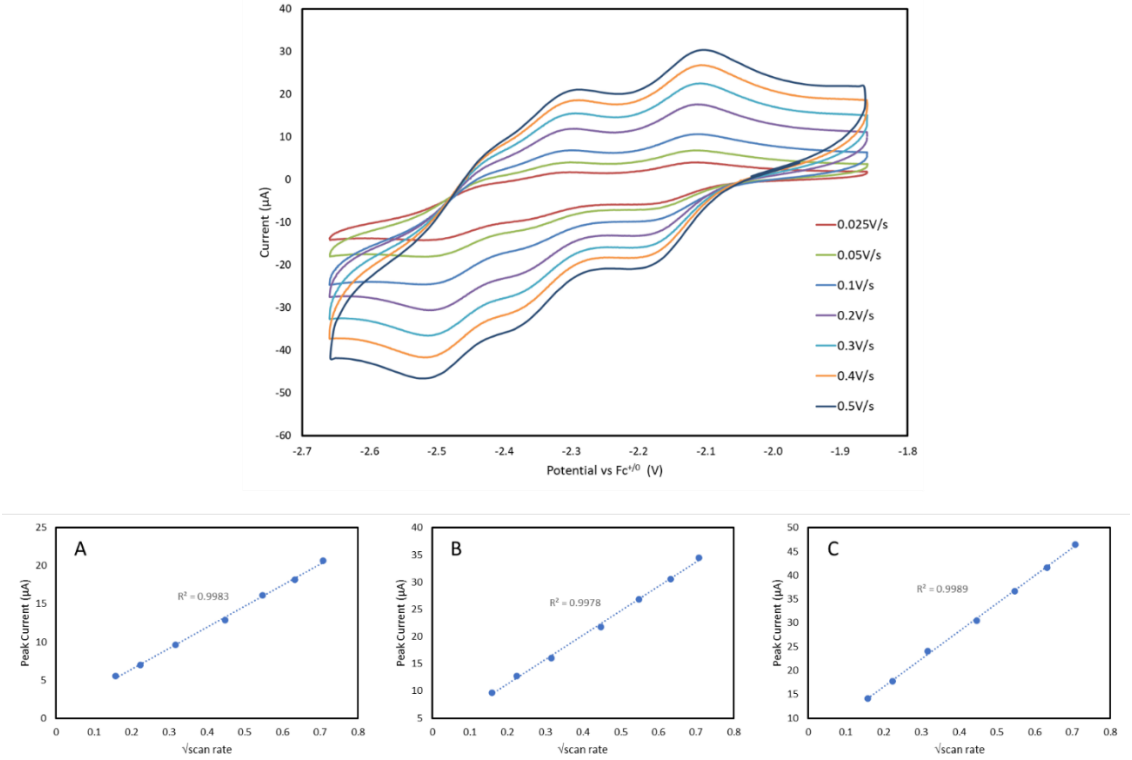

Figure 5.28: <u>Top</u> – CV of 0.5mM $Ni^{II}(bpca)_2$ in acetonitrile with varied scan rates scanned between -1.88V and -2.67V with TBAHFP as an electrolyte. <u>Bottom</u> – peak current as a function of scan rate for each of the reduction events observed in top figure. A) first reduction event B) second reduction event C) third reduction event.

Each of the investigated redox events for all complexes adhere to the conditions that describe a diffusion-controlled process, indicating that the complexes are undergoing reduction events homogeneously. For **$[Co^{III}(bpca)_2]^+$**, the second and third reduction events seem to overlap. As the scan rate increases, the overlap becomes more pronounced. Despite this observation, the scan square root of the scan rate is still proportional to the combined peak current, indicating a diffusion-controlled process.

5.6.2 – Water reduction

Screening a potential reduction electrocatalyst targeting any substrate involves following a set of criteria which would initially label a complex as a potential candidate. Firstly, the complex must have a reduction event that exists within a specified voltage region that pertains to the specific substrate and solvent. The bottom limit of the range is zero overpotential, the maximum voltage is the potential at which the substrate is reduced at the electrode.[31] Each of the complexes investigated here have reduction events that exist in this region. Initial catalytic screening involves exposing the catalyst to water and performing a CV. These experiments must be performed in a solvent that is miscible with water, like acetonitrile. Destruction of the return oxidation (for reversible processes) and development of enhanced currents at the reduction events can indicate the presence of an electrocatalytic process.[32,33] Sequential addition of water should increase the enhancement process until the saturation concentration.

Performing CVs of **$Fe^{II}(bpca)_2$** with added water demonstrates some modulation of the initial CV compared to when water is excluded, as demonstrated in Figure 5.29. the presence of water removes the reversible qualities of the CV and appears to shift the potential of the reduction event to a slightly more anodic potential. There does not appear to be a significant enhancement in the reduction current, however, suggesting that no catalysis has been detected. Disappearance of the return oxidation could be attributed to some protonation steps associated with the reduction processes. The shift in reduction potential also supports a protonation step occurring for **$Fe^{II}(bpca)_2$**, as protonation events

generally result in less negative reduction potential. Evidently, the complex appears to interact with water but does not catalyze its reduction.

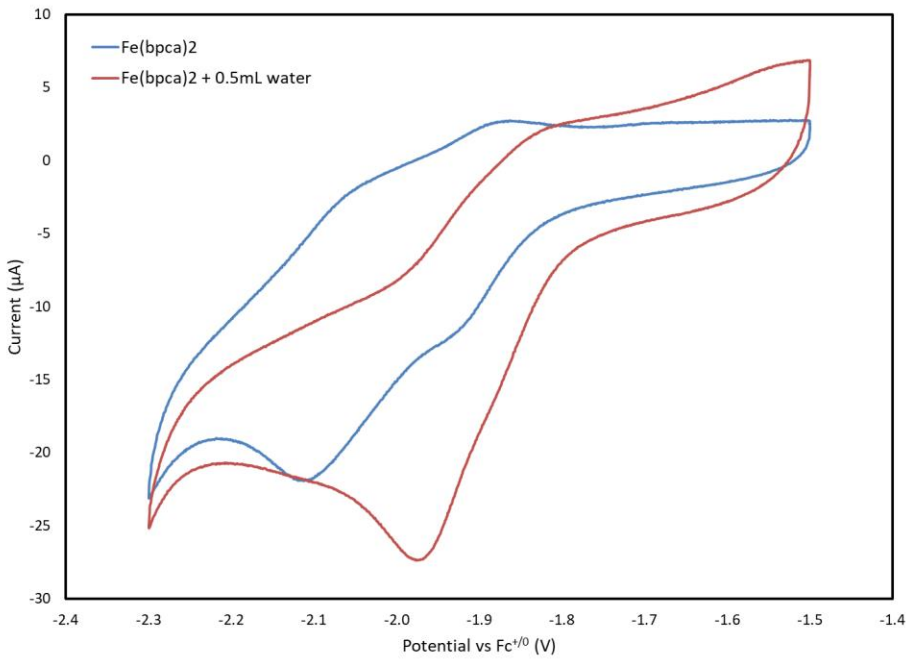

Figure 5.29: CV of 0.5mM $Fe^{II}(bpca)_2$ in acetonitrile with added water scanned between -1.5V and -2.3V with TBAHFP as an electrolyte at a scan rate of 0.1V/s.

The interactions of the redox events for **$[Co^{III}(bpca)_2]^+$** with water are displayed in Figure 5.30. The initial reversible event at -0.66V vs $Fc^{+/0}$ appears to be unaffected when water is added. Similar effects for **$Fe^{II}(bpca)_2$** are observed at the subsequent reduction potentials with added water. The reduction potential shifts in a similar manner and the return oxidation is disrupted. There is a slight enhancement associated with the added water, but the enhancement does not increase with water concentration. Also, there is some indication of a heterogeneous process present in the series of curves. Namely, when 0.5mL of water is added, a Gaussian shaped event occurs during the return, anodic scan.

This shape is often associated with an adsorption process to the working electrode. Similarly to **$Fe^{II}(bpca)_2$**, **$[Co^{III}(bpca)_2]^+$** appears to interact with water, suggesting some protonation processes, but not necessarily catalysis.

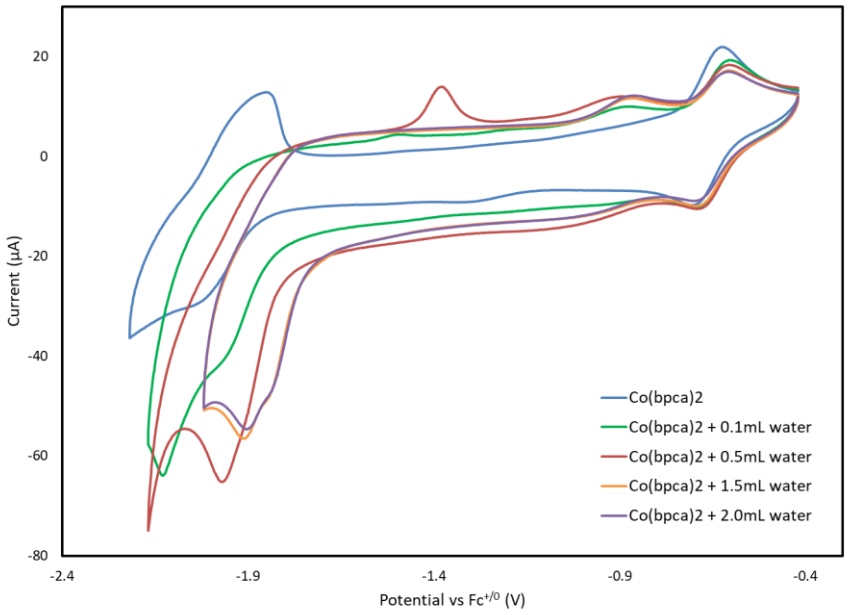

Figure 5.30: CV of 0.5mM $[Co^{III}(bpca)_2]^+$ in acetonitrile with added water scanned between -0.4V and -2.3V with TBAHFP as an electrolyte at a scan rate of 0.1V/s.

Introducing water to the redox events of **$Ni^{II}(bpca)_2$** results in no significant enhancements indicating the complex does not catalyze the reduction of water (Figure 5.31). Similarly to the other complexes, the CV is altered, again removing the return oxidation and destroying the reversibility of each process. All three events are affected in this case. The first reduction event at -2.12V is not shifted significantly, but the return oxidation is removed. The following two reduction processes were again combined into one but was shifted in the opposite direction of the events observed in **$Fe^{II}(bpca)_2$** and **$[Co^{III}(bpca)_2]^+$**,

moving to a more negative potential. Again, the complex appears to interact with water but does not reduce it.

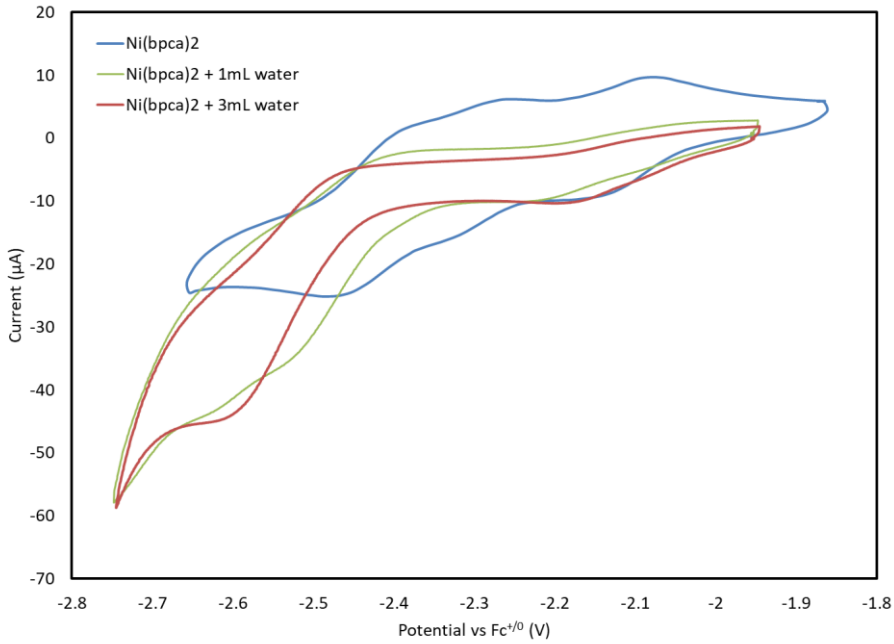

Figure 5.31: CV of 0.5mM $Ni^{II}(bpca)_2$ in acetonitrile with added water scanned between -1.9V and -2.76V with TBAHFP as an electrolyte at a scan rate of 0.1V/s.

Each of the complexes investigated for water reduction seem to become protonated when introduced to water around their reduction events, however no indication of catalysis is detected. It is possible that the two tridentate ligands sterically hinder access to the metal center, thus preventing the formation of a metal-hydride that could ultimately evolve hydrogen. Opening a coordination site for protons to access the metal center could enable catalysis from these complexes. Adding a positively charged species that can interact with the carbonyl groups could decrease the bonding interaction of the bpca ligands enough to allow access to one of the occupied sites, acting as a sort of co-catalyst.

5.6.3 – CO_2 reduction

Previous investigations have suggested that transition metal complexes with coordinated bpca ligand show some potential as effective CO_2 reduction catalysts. These claims were explored herein, by sparging the solution containing our catalysts with CO_2, to generate an atmosphere of CO_2 and then completing CVs. CO_2 reduction mechanisms require the presence of a proton source, so some water was added during these trials. During the synthesis of the ligand, a Cu(bpca) salt was generated, which was the first complex probed for potential CO_2 reduction. Enhancements can be observed for this complex in Figure 5.32, that suggest catalytic activity. Unfortunately, the complex appeared to deposit on the electrode when CPE experiments were performed for 1 hour at a potential of -2.17V vs $Fc^{+/0}$. Additionally, these bulk reactions produced no reduction products of CO_2 or hydrogen. Therefore, it can be inferred that the observed enhancements are likely a result of the plating process.

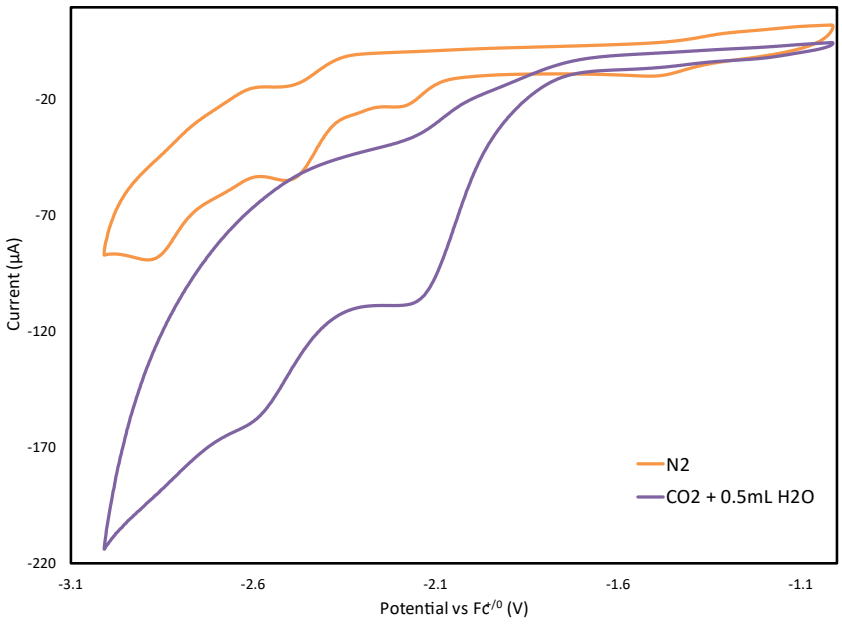

Figure 5.32: CV of 1mM Cu(bpca) precursor in acetonitrile with added water scanned between -1V and -3.08V with TBAHFP as an electrolyte at a scan rate of 0.1V/s.

Similar investigations for CO_2 reduction were conducted for **$Fe^{II}(bpca)_2$**. Figure 5.33 displays the CV of **$Fe^{II}(bpca)_2$** when placed under a CO_2 atmosphere. Previously, it was demonstrated that **$Fe^{II}(bpca)_2$** displays no significant enhancements when exposed to water. This experiment was performed by simply sparging the cell used for the water additions in Figure 5.29, then running another CV. Adding CO_2 similarly has no effect, seemingly suggesting that **$Fe^{II}(bpca)_2$** is not catalytically active for either substrate. Alterations could be made to encourage catalysis, but in the simple environment using acetonitrile as the solvent with small amounts of water to act as a proton source, no catalysis can be detected. The enhancement that tails off following the redox events is likely caused by the decreased pH associated with dissolved CO_2.

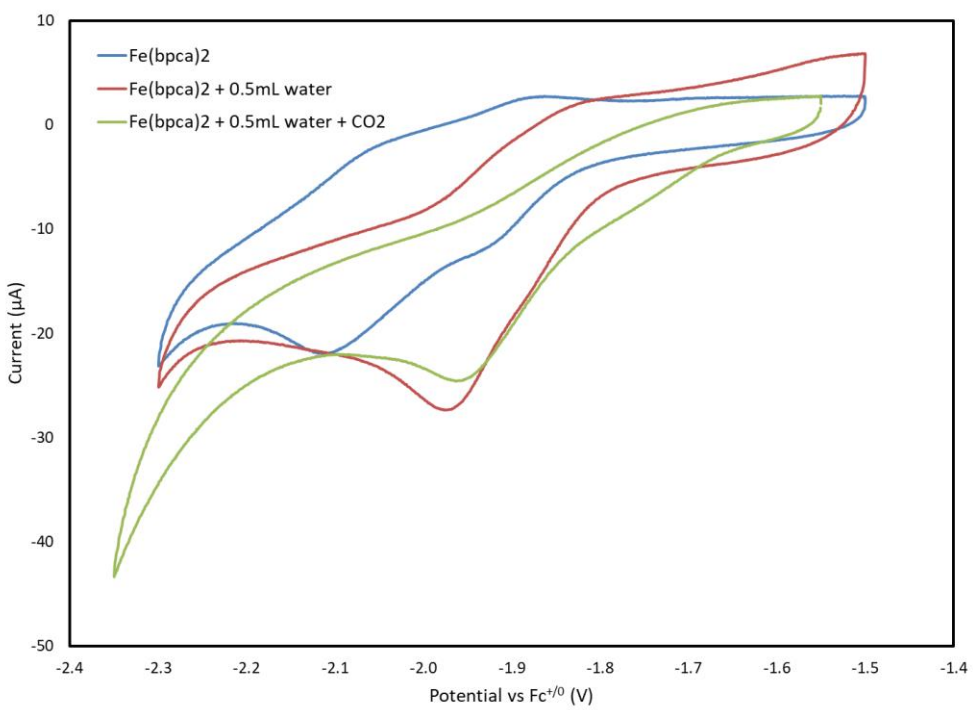

Figure 5.33: CV of 0.5mM $Fe^{II}(bpca)_2$ in acetonitrile with added water scanned between -1.5V and -2.3V at a scan rate of 0.1V/s with TBAHFP as an electrolyte. Cell was sparged with CO_2 following water additions.

5.6.4 – Modulation of redox potential with alkali metals to activate catalysts

Modulation of the coordination environment could encourage parts of the bpca ligand to dissociate from the metal center, ultimately allowing access to substrate, facilitating catalysis. Introducing various alkali metals as hard Lewis acids to interact with the carbonyl groups from the imides on the bpca ligands could enable such a process to occur. Attempting to reproduce the reduction shift observed by Nagao et al. on their Ru-bpca complex for $M(bpca)_2$ complexes was hindered by solubility limitations. In essence, the experiments are relatively simple to perform. Sequential CVs are performed with added alkali metal salts. Selecting the solvent system to allow the $M(bpca)_2$ complex, alkali metal

salt, and the complex formed when the alkali metal interacts with $M(bpca)_2$ to remain in solution proved to be challenging. Initial trials for **$Fe^{II}(bpca)_2$** used $NaPF_6$ as the alkali metal source in acetonitrile. The CVs for these trials immediately showed decreased current with added salt, as the sodium would interact with the carbonyl groups, generating a complex that was not soluble in acetonitrile. To counter this effect, a mixed solvent system was used with a 2:1 ratio of ACN:H_2O. The CV of **$Fe^{II}(bpca)_2$** with sequential $NaPF_6$ additions is presented in Figure 5.34. The presence of the alkali metal in this figure results in the reduction process becoming shifted to a less negative potential, similar to the effect demonstrated by Nagao et al.[15]

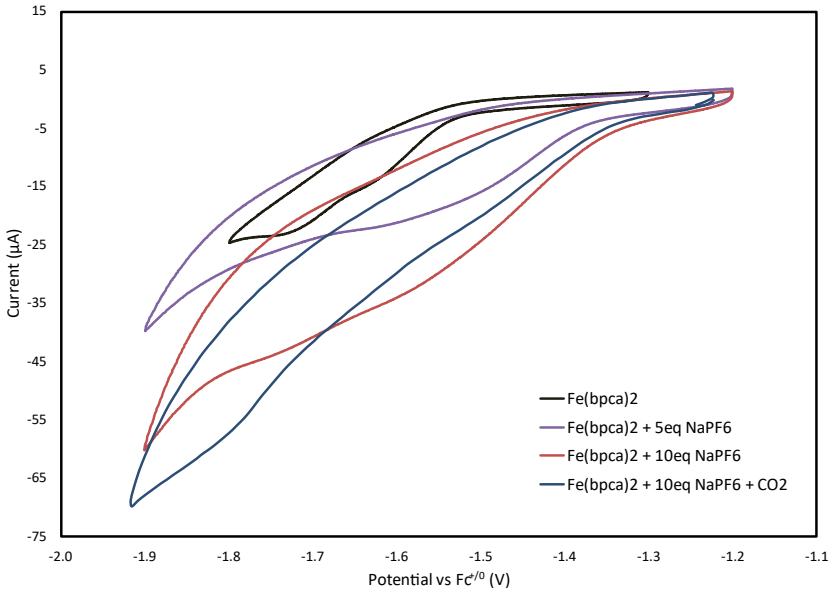

Figure 5.34: CVs of 0.5mM $Fe^{II}(bpca)_2$ performed in 2:1 ACN:H_2O solvent with added $NaPF_6$ followed by introduction of a CO_2 atmosphere using TBAHFP as the electrolyte with a scan rate of 0.1V/s.

In addition to the shift in redox potential, there appears to be some slight enhancements present when $NaPF_6$ is added. These effects could be a result of water reduction, induced by the presence of the alkali metal reducing the bonding of bpca ligand to the metal and allowing increased access of water. When CO_2 is introduced as the atmosphere for the CV, slightly more enhancement was observed. These enhancements were both explored as potential signs of catalysis. One hour CPE experiments were performed with 10 equivalents of $NaPF_6$. The first experiment was performed with an atmosphere of N_2 at -1.8V vs $Fc^{+/0}$. The second was sparged with CO_2 and set to react at a potential of -2.1V vs $Fc^{+/0}$. Each of these runs returned only trace amounts of H_2, which was accounted for by the electrode in follow-up trials excluding any **$Fe^{II}(bpca)_2$** The head space and solvent were investigated for the CO_2 trials and no CO, methanol, or formate was detected, again demonstrating that no catalysis was observed for water reduction or CO_2 reduction.

Having observed notable shifts in reduction potential caused by the addition of an alkali metal paired with some enhancements in the presence of water and CO_2 without identifying any catalysis, the investigation shifted to new substrate, NO and NO_2^-. Figure 5.35 displays the effect of adding $NaNO_2$ to a CV of **$Fe^{II}(bpca)_2$** in a 1:1 mixture of water and acetonitrile. This substrate is ideal, since it acts as an alkali metal salt, while incorporating a potential substrate target in NO_2^- with favourable ligand coordination strength, relative to CO_2 or water.

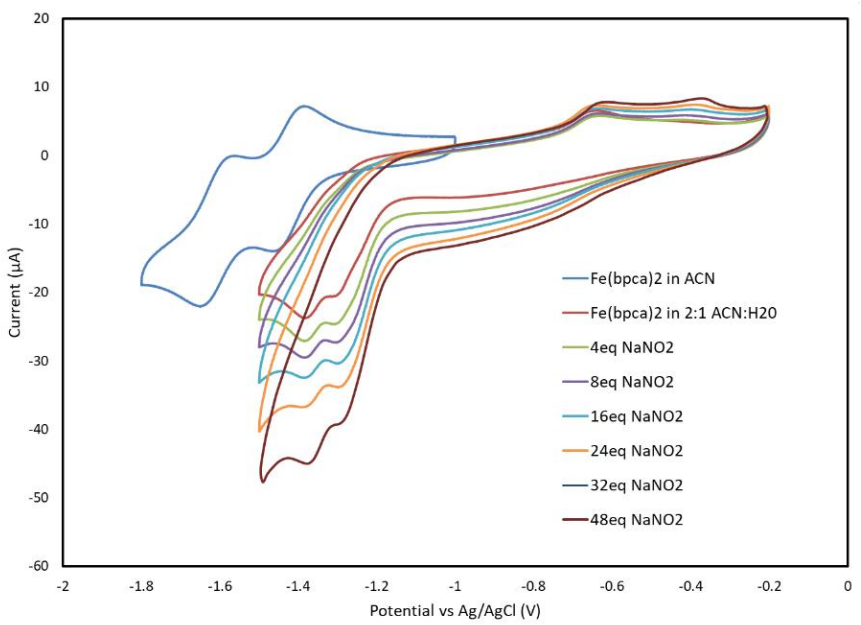

Figure 5.35: CVs of 0.5mM $Fe^{II}(bpca)_2$ performed initially in acetonitrile followed by added $NaNO_2$ in 2:1 ACN:H_2O using TBAHFP as the electrolyte with a scan rate of 0.1V/s.

Initial water addition to the complex shifts the reduction events by 0.3V to a less negative potential and removes the reversibility of the redox events. Additionally, the sequential events occur in a smaller potential window. As previously mentioned, the shift is likely associated with protonation events occurring at the ligand, resulting in a lower potential required to reduce the complex. As equivalents of $NaNO_2$ are added, the redox events shift slightly further in the anodic direction and enhance. These observations point to a similar effect as observed in Figure 5.34, with more significant enhancements that continue to grow as more substrate is added. Electrocatalytic reduction of $NaNO_2$ is further explored for **$[Co^{III}(bpca)_2]^+$** and **$Fe^{II}(bpca)_2$** in Section 5.7.

5.6.5 – NO reduction

Along the multiple reduction pathway transforming nitrite to ammonia, several other substrate targets exist for electrocatalytic reductions. NO is one of these potential targets. The first reduction event observed in **$[Co^{III}(bpca)_2]^+$** occurs at -0.66V vs $Fc^{+/0}$ which is an appropriate voltage that has the potential to catalyze the reduction of NO to generate hydroxylamine or ammonia.[34] Screening for this reaction involves a similar protocol as was used for CO_2 reduction. An initial CV is performed under N_2, then the cell is sparged with NO gas, displayed in Figure 5.36.

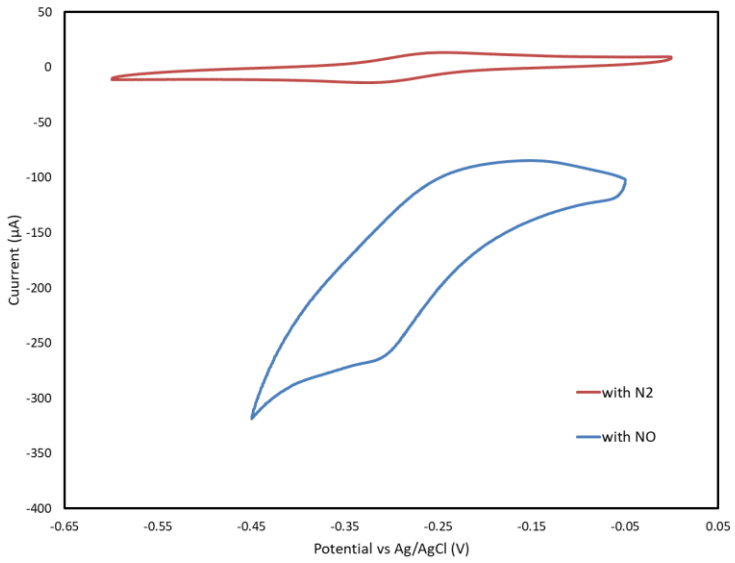

Figure 5.36: CVs of 0.5mM $Fe^{II}(bpca)_2$ performed initially in acetonitrile under N_2 followed by sparging with NO in water using KCl as the electrolyte with 50mM MOPS buffer with pH=7 with a scan rate of 0.1V/s.

The first reduction event of **$[Co^{III}(bpca)_2]^+$** remains reversible when replacing the acetonitrile solvent with an aqueous environment. When NO is introduced to the system,

both characteristic traits of a catalytic process are observed. The reduction event is enhanced, and the return oxidation is removed. CPE experiments were performed to further explore possible catalysis at a potential of -0.45V vs Ag/AgCl for a run time of 1 hour. No gaseous or liquid products were detected through GC-TCD analysis, titration with ferricyanide for hydroxylamine, and ^{14}N-NMR for ammonium. Overload issues due to bubble formation on the electrode paired with the failure to detect any catalytic products from NO shifted the focus of the investigation towards NO_2^- reduction.

5.7 – Exploring Nitrite Reduction Electrocatalysis for $[Co^{III}(bpca)_2]^+$ and $Fe^{II}(bpca)_2$

Experiments probing catalytic NO_2^- reduction were performed in aqueous environments with Ag/AgCl as the reference electrode. **$Ni^{II}(bpca)_2$** was found to have poor solubility in water and was therefore excluded from further exploration. **$[Co^{III}(bpca)_2]^+$** and **$Fe^{II}(bpca)_2$** both displayed indications of their capacity to catalytically reduce NO_2^- in CVs and were confirmed to generate hydroxylamine and ammonium as catalytic products in CPE experiments.

5.7.1 – Initial electrocatalytic detection

Sequential additions of $NaNO_2$ were completed for **$[Co^{III}(bpca)_2]^+$** and **$Fe^{II}(bpca)_2$** followed by CVs in aqueous environments with MOPS concentrations of 50mM and KCl concentration of 0.1M. The buffered solutions were normalized to a pH of 7, mimicking a neutral water environment. Figures 5.37 and 5.38 display these experiments for **$[Co^{III}(bpca)_2]^+$** and **$Fe^{II}(bpca)_2$**, respectively.

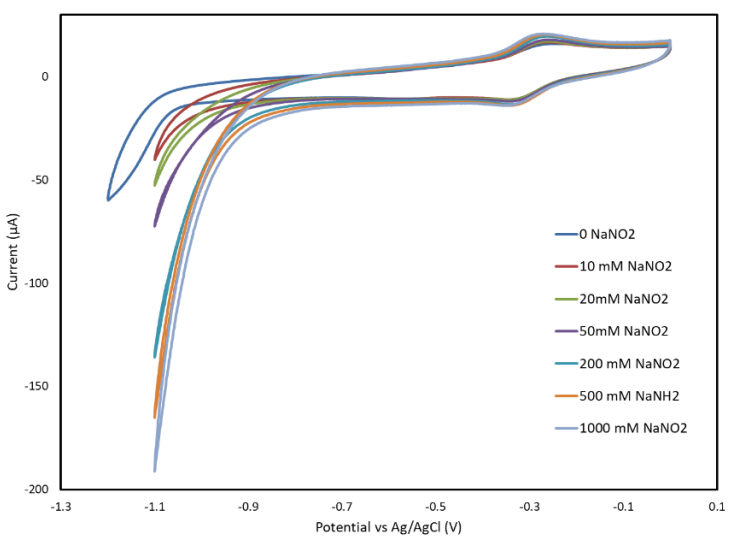

Figure 5.37: CVs of 0.5mM $[Co^{III}(bpca)_2]^+$ performed in water under N_2 with $NaNO_2$ additions using KCl as the electrolyte with 50mM MOPS buffer with pH=7 with a scan rate of 0.1V/s.

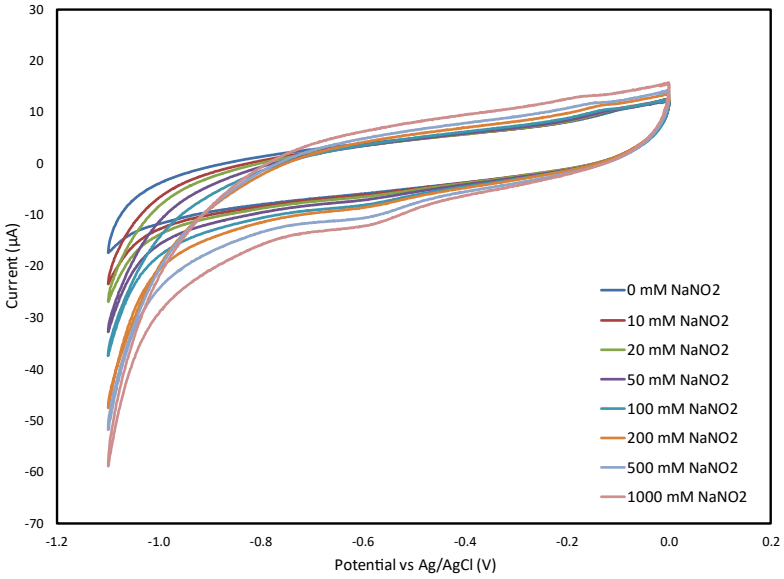

Figure 5.38: CVs of 0.5mM $Fe^{II}(bpca)_2$ performed in water under N_2 with $NaNO_2$ additions using KCl as the electrolyte with 50mM MOPS buffer with pH=7 with a scan rate of 0.1V/s.

Based on the CVs displayed in Figures 5.36 and 5.37, both complexes appear to display some enhancements with sequential addition of $NaNO_2$. The enhancement is significantly more pronounced for **$[Co^{III}(bpca)_2]^+$** compared to **$Fe^{II}(bpca)_2$**. At the highest concentration of $NaNO_2$, **$[Co^{III}(bpca)_2]^+$** reaches a maximum current value of -180μA at a potential of -1.1V vs Ag/AgCl. This is triple the current reached for **$Fe^{II}(bpca)_2$** under the same conditions. Blank CV experiments excluding catalyst were previously reported in Chapter 4, Figure 4.19 demonstrating the necessity of these complexes in generating an increased current in this potential range. Following the detection process, some CPE experiments were performed to quantify the catalytic production.

5.7.2 – Generation of bulk catalytic product

Bulk experiments were completed at a potential of -1.05V for a variety of time periods. Ammonia and hydroxylamine were both detected as products for the catalytic reduction. Additionally, small amounts of hydrogen were also generated as background. Similar amounts of hydrogen were generated, regardless of the presence of catalyst. Results for the CPE experiments are summarized in Table 5.15.

Table 5.15: Results of 2-hour CPE experiments run at a potential of -1.05V vs Ag/AgCl.

Trial #	Catalyst	Concentration (mM)	Hydroxylamine (μmol)	Ammonium (μmol)
1	**$[Co^{III}(bpca)_2]^+$**	0.5	20	130
2	**$[Co^{III}(bpca)_2]^+$**	1	4	212
3	**$Fe^{II}(bpca)_2$**	0.5	24	140
4	**$Fe^{II}(bpca)_2$**	1	48	162
5	-	-	0	0

For each catalytic trial, ammonium was the most abundant product generated. Hydroxylamine was also produced, to a lesser degree. Increasing the concentration of catalyst resulted in an increase of ammonium generation for both complexes. There is a marked difference in production of hydroxylamine for **$[Co^{III}(bpca)_2]^+$** when the concentration is increased, much less was generated. This difference can be attributed to an unintended heterogeneous product that is generated more extensively when the **$[Co^{III}(bpca)_2]^+$** concentration is increased. While some solid formed in trial one, a thick, orange film is present at the end of trial two. The film appears to have catalytic capabilities, as it boosts the output of ammonium significantly. It is possible that the film also converts hydroxylamine into ammonium more efficiently than the glassy carbon electrode. Investigating the catalytic performance of an unintended solid product formed from the decomposition of **$[Co^{III}(bpca)_2]^+$** is outside of the scope for this investigation and disqualifies **$[Co^{III}(bpca)_2]^+$** as a viable homogeneous catalyst in this context. The extra electrons stored on the bpca ligand for **$[Co^{III}(bpca)_2]^+$** compared to **$Fe^{II}(bpca)_2$** could explain the disparity in stability. The simulated structure for the reduction products of **$[Co^{III}(bpca)_2]^+$** suggest elongation of the bond between the carbon on the pyridine and the carbonyl carbon (C7-C8 in Tables 5.7-5.10) which could result in the destruction of the bond and degradation of the complex. For this reason, **$Fe^{II}(bpca)_2$** became the focal point of catalytic studies. **$Fe^{II}(bpca)_2$** did not show any indication of decomposition throughout the duration of the catalytic trials. Further experiments were performed to demonstrate the stability of **$Fe^{II}(bpca)_2$** and elucidate some details on how it could function during NO_2^- reduction.

5.7.3 – Evaluating the catalytic function of $Fe^{II}(bpca)_2$

Elucidating details regarding the functionality of **$Fe^{II}(bpca)_2$** can be achieved through the combination of electrochemical and spectroscopic methods paired with details of the DFT computations. Figure 5.38 displays the effect added MOPS buffer has on the CV of **$Fe^{II}(bpca)_2$**. These series of CVs were performed prior to the dip test displayed in Figure 5.40. Added MOPS appears to overlap the redox events of **$Fe^{II}(bpca)_2$**, this could either be attributed to a reduction process associated with MOPs alone, or a chemical change made to **$Fe^{II}(bpca)_2$**.

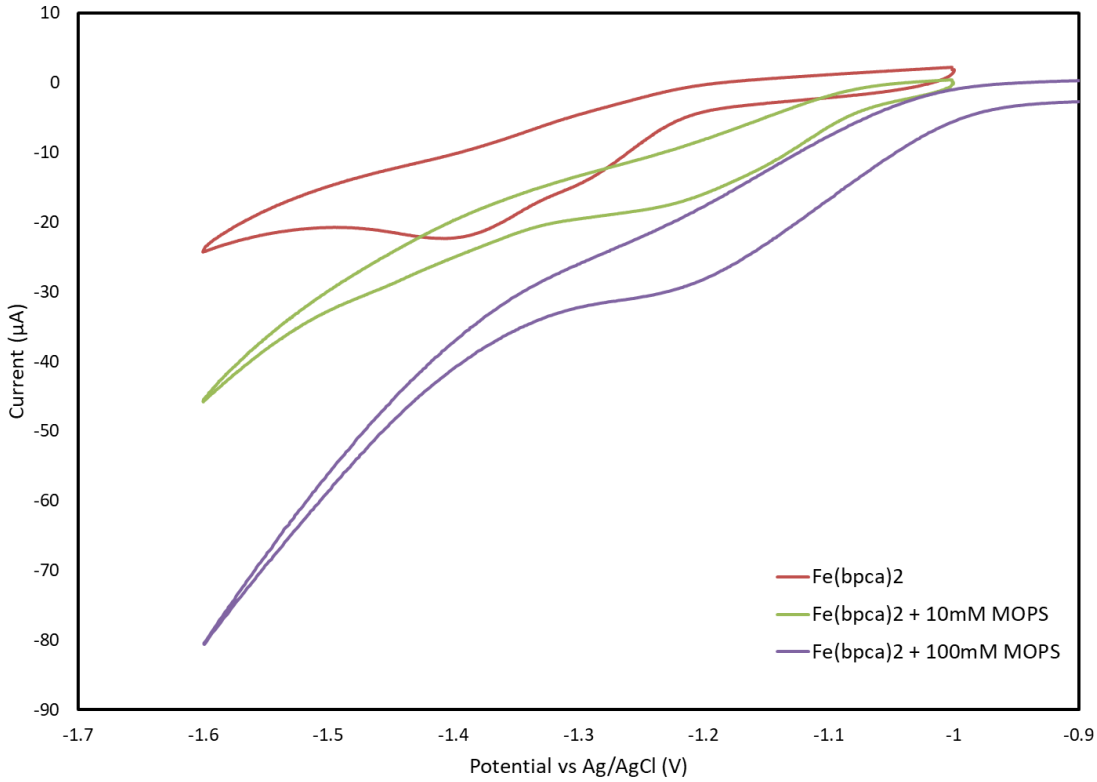

Figure 5.39: CVs of 0.5mM $Fe^{II}(bpca)_2$ performed in 1:1 ACN:H_2O with added MOPS using 0.1M TBAHFP as the electrolyte with a scan rate of 0.1V/s.

The “post-wash” scans observed in Figure 5.40 suggest the latter of these proposals. The features observed in the CVs with added MOPs in Figure 5.39 are not observed in the “post wash” LSV scans from Figure 5.40. This suggests that MOPS must affect some chemical change on **$Fe^{II}(bpca)_2$** to produce these curves. Protonation of the bpca ligands by MOPs can likely be blamed for the observed shift in potentials.

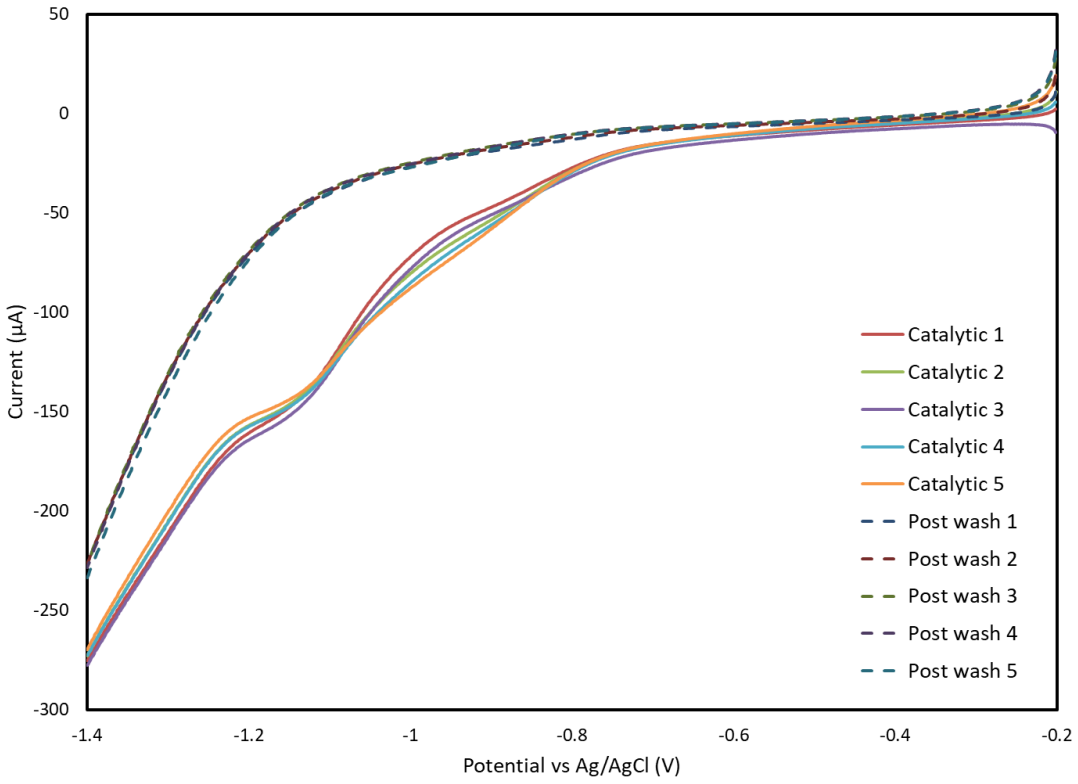

Figure 5.40: LSV dip test performed in 1:1 ACN:H_2O initially with 0.5mM $Fe^{II}(bpca)_2$ and 500mM $NaNO_2$ followed by a solvent rinse and reintroduction of the electrode into a solution excluding $Fe^{II}(bpca)_2$. 0.1M TBAHFP was used as the electrolyte with a scan rate of 0.1V/s.

Performance of the dip-test in Figure 5.40 provides further support for the homogeneous nature of the catalytic reduction of NO_2^-. The initial scans labeled as catalytic 1 to catalytic 5 display the redox events associated with **$Fe^{II}(bpca)_2$** interacting with $NaNO_2$. After lightly rinsing the electrode used for the catalytic scans with some solvent containing no catalyst and placing the electrode back in an environment with no **$Fe^{II}(bpca)_2$** all the redox features associated with **$Fe^{II}(bpca)_2$** disappear, suggesting that it did not deposit onto the electrode.

Determining the order in which nitrite chemically interacts with **$Fe^{II}(bpca)_2$** in the overall mechanism can be established through some spectroscopic experiments. Monitoring UV-vis absorption of **$Fe^{II}(bpca)_2$** in the presence of $NaNO_2$ can validate whether nitrite interacts with **$Fe^{II}(bpca)_2$** before or after any reduction steps occur. In the absence of interaction, added $NaNO_2$ should appear to additively contribute to the observed absorption events. The gray curve and blue curve from Figure 5.41 representing **$Fe^{II}(bpca)_2$** and **$Fe^{II}(bpca)_2$** with added nitrite, respectively, appear to perfectly trace one another apart from the region between 200nm and 250nm, which directly overlaps with the absorption peak of $NaNO_2$ on its own (red curve). The lack of any significant wavelength shift in absorption peaks when nitrite is added suggests that there is no chemical interaction between **$Fe^{II}(bpca)_2$** and $NaNO_2$ prior to a reduction process.[35]

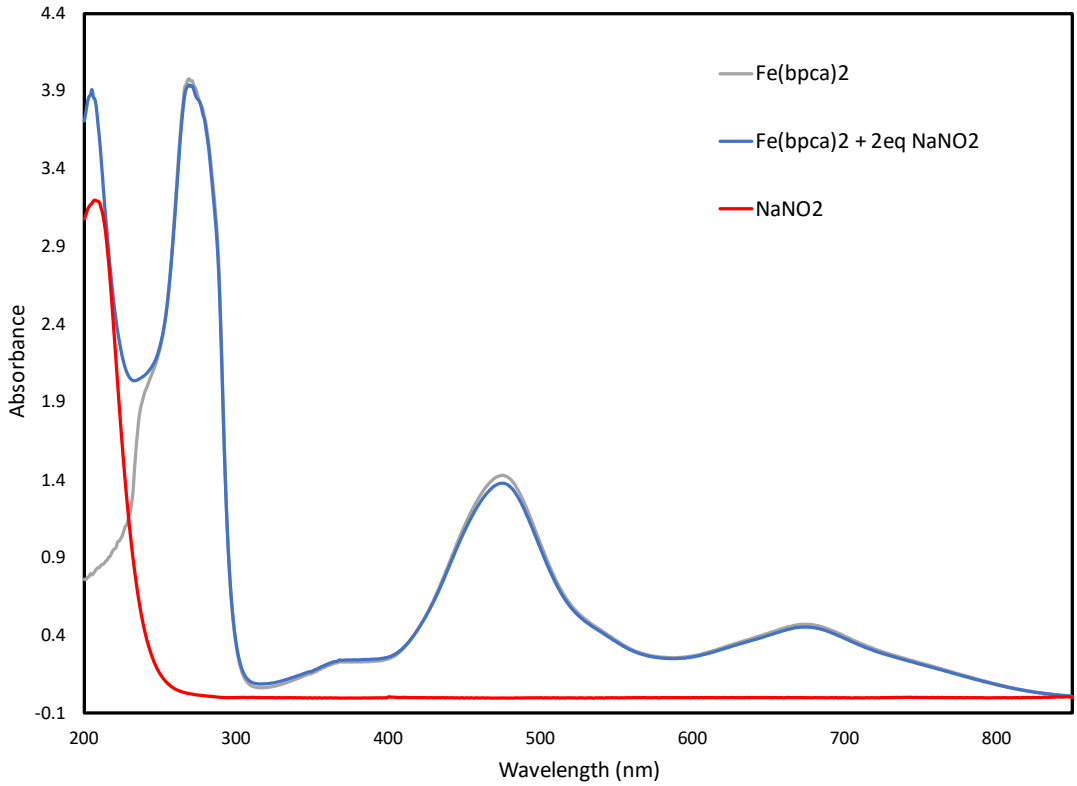

Figure 5.41: Absorption spectra of $Fe^{II}(bpca)_2$ with added $NaNO_2$ at a concentration of 0.2mM in a 1:1 mixture of ACN:H_2O.

Based on the shift in reduction potential in the presence of $NaNO_2$ observed in Figure 5.35 paired with the absence of spectroscopic changes when $NaNO_2$ is introduced, it is likely that nitrite does not coordinate with the metal center until after the reduction process. Alteration of the CV observed moving from ACN to water suggests protonation processes must occur on the ligand, likely as PCETs. In order to better understand how the ligand might dissociate following a reduction process in a catalytic environment, a SEC experiment was completed to observe if permanent changes occur to the complex follow brief CPE experiments. The changing spectroscopic absorption peaks with an applied potential of -1.4V vs Ag/AgCl in 1:1 ACN:H_2O solution are displayed in Figure 5.42.

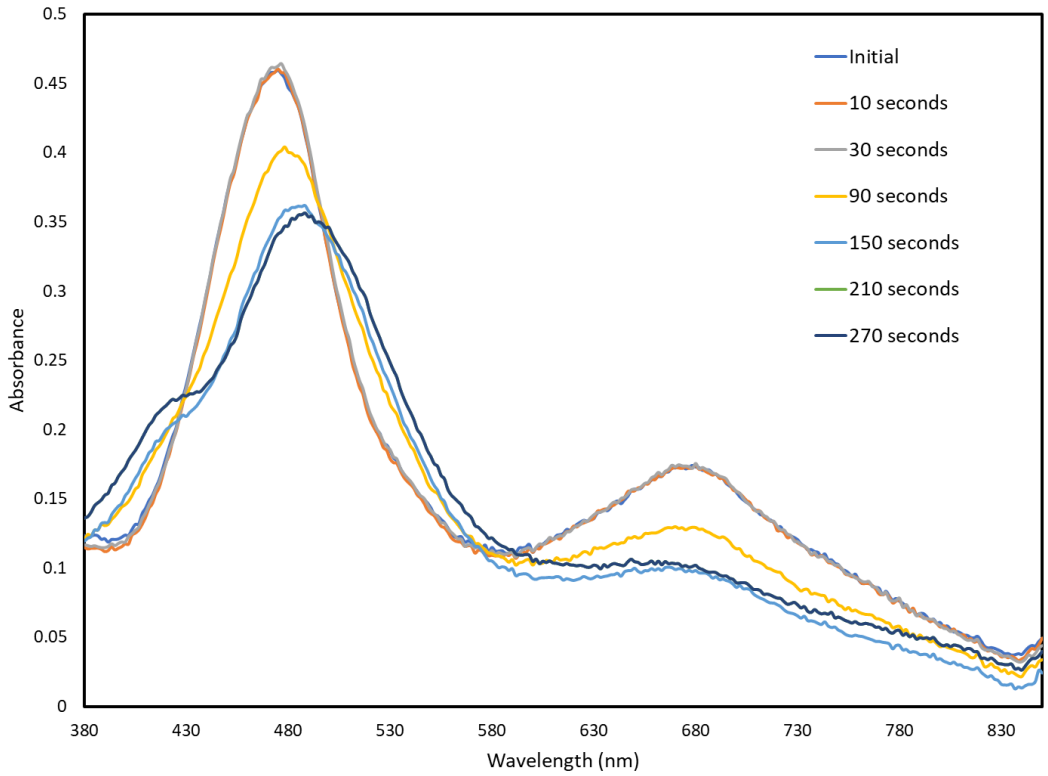

Figure 5.42: Spectroelectrochemical absorption spectra for $Fe^{II}(bpca)_2$ performed following sequential CPE experiments run at -1.4V vs Ag/AgCl with 0.1M $LiClO_4$ electrolyte.

Some clear spectroscopic changes occur following CPE experiments after a time-period of 90 seconds. In these experiments, 30 seconds was allowed to pass before the absorbance scan was completed indicated a structural change to the ligand. This structural change likely opens a coordination site and allows nitrite access to the metal center. Scheme 5.4 displays a possible pathway to activating the catalyst.

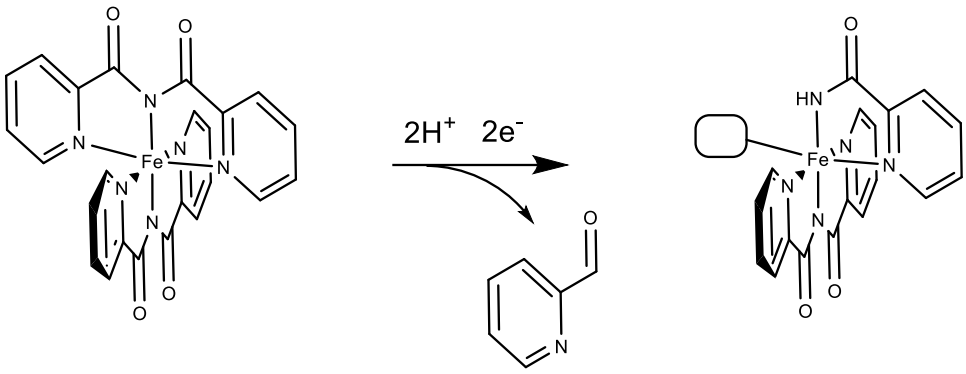

***Scheme 5.4: Proposed decomposition pathway for $Fe^{II}(bpca)_2$* with added protons and electrons.**

Opening the catalytic site in the structure on the right of Scheme 5.4 allows the opportunity for NO_2^- to coordinate the metal center and proceed through a catalytic cycle similar to that displayed in Chapter 4, Scheme 4.2. The adjacent proton on nitrogen could also act as a proton-shuttle facilitating the generation of ammonia.

5.8 – Conclusion

Overall, the $M(bpca)_2$ complexes investigated in this work displayed robust and reversible redox activity in organic solvents. The DFT simulations completed on these complexes portrays organometallic processes stabilized in molecular orbitals largely comprised of atomic orbitals on the ligand structures. Added electrons were effectively stabilized within the ligand structure, acting as an electron reservoir to potentially be utilized in catalytic cycles. **$[Co^{III}(bpca)_2]^+$** and **$Fe^{II}(bpca)_2$** both showed early promise as electrocatalysts for H_2O and CO_2 reduction but failed to generate any catalytic product. Addition of alkali metals during CVs for **$Fe^{II}(bpca)_2$** was able to modulate the redox events, causing an anodic shift in the potentials. This modulation failed to activate catalytic turnover for CO_2 and

H_2O reduction but successfully reduced $NaNO_2$ for both **$Fe^{II}(bpca)_2$** and **$[Co^{III}(bpca)_2]^+$**. Upon further investigation of CPE experiments for **$[Co^{III}(bpca)_2]^+$**, significant generation of a heterogeneous product was detected, excluding it as a candidate for homogeneous catalysis. **$Fe^{II}(bpca)_2$** emerged as the best candidate for NO_2^- reduction. The major product generated during CPE experiments was ammonium, with small amounts of hydroxylamine. In order to complete the catalytic cycle, part of the ligand likely breaks up and dissociates from the metal center, opening up a coordination site. The close proximity of the coordinated amine observed in Scheme 5.2 helps to facilitate turnover of the catalytic cycle by acting as a proton shuttle. Further experiments optimizing the catalytic environment and probing the mechanism should be performed to better understand the functionality of **$Fe^{II}(bpca)_2$**.

5.9 – Experimental Methods

All experiments were performed according to the protocols specified in section 4.7, from Chapter 4, with some slight variation in the CPE experiments where a different electrochemical cell was used. The new cell was slightly larger, requiring 20mL of sample. The counter electrode was separated from the bulk solution by a 5mm agarose layer doped with 1M KCl. This layer was formed by boiling 0.126g of agar in 10mL of 1M KCl solution. Once the solution is clear, a 5mm layer is poured on top of the frit which is allowed to cool and solidify. From there, the cell is assembled and purged with N_2.

The spectroelectrochemical experiment was performed in a slightly modified manner to what is described in section 3.6 of Chapter 3. Rather than gradually stepping the potential

to a more negative value, the same potential was applied with increasing time periods, as specified in Figure 5.41.

5.10 – References

1 J. H. Yang, M. Peng, D. D. Zhai, D. Xiao, Z. J. Shi, S. Yao and D. Ma, *ACS Catal*, 2022, **12**, 2898–2906.

2 G. Wang, J. Chen, Y. Ding, P. Cai, L. Yi, Y. Li, C. Tu, Y. Hou, Z. Wen and L. Dai, *Chem Soc Rev*, 2021, **50**, 4993–5061.

3 X. Tan, C. Yu, Y. Ren, S. Cui, W. Li and J. Qiu, *Energy Environ Sci*, 2021, **14**, 765–780.

4 S. Zhang, Q. Fan, R. Xia and T. J. Meyer, *Acc Chem Res*, 2020, **53**, 255–264.

5 M. N. Anwar, A. Fayyaz, N. F. Sohail, M. F. Khokhar, M. Baqar, A. Yasar, K. Rasool, A. Nazir, M. U. F. Raja, M. Rehan, M. Aghbashlo, M. Tabatabaei and A. S. Nizami, *J Environ Manage*, 2020, **260**, 1-14.

6 P. Paul, B. Tyagi, A. K. Bilakhiya, M. M. Bhadbhade, E. Suresh and G. Ramachandraiah, *Inorg Chem*, 1998, **37**, 5733–5742.

7 R. M. R. da Silva, I. M. L. Rosa, W. X. C. Oliveira, O. C. Alves, E. C. S. Santos, F. Garcia, H. C. Silva Junior, G. B. Ferreira, G. P. Guedes, W. D. do Pim, M. Julve and M. V. Marinho, *New J Chem*, 2022, **47**, 1066–1075.

8 T. Kajiwara, R. Sensui, T. Noguchi, A. Kamiyama and T. Ito, *Inorg Chim Acta*, 2002, **337**, 299–307.

9 D. Marcos, J. Folgado, D. Beltran-Porter, S. H. Pulcinelli and R. H. De Almeida-Santos, *Polyhedron*, 1990, **9**, 2699–2704.

10 S. Wocadlo, W. Massa and J.-V. Folgado, *Inorg Chim Acta*, 1993, **207**, 199-206.

11 K. A. Grice, *Coord Chem Rev*, 2017, **336**, 78–95.

12 R. Deeba, F. Molton, S. Chardon-Noblat and C. Costentin, *ACS Catal*, 2021, **11**, 6099–6103.

13 J. R. Stroka, B. Kandemir, E. M. Matson and K. L. Bren, *ACS Catal*, 2020, **10**, 13968–13972.

14 S. Anwar, F. Khan, Y. Zhang and A. Djire, *Int J Hydrogen Energy*, 2021, **46**, 32284–32317.

15 T. Misawa-Suzuki, M. Etoh and H. Nagao, *Bull Chem Soc Jpn*, 2020, **93**, 1412–1418.

16 A. M. Madalan, K. Bernot, F. Pointillart, M. Andruh and A. Caneschi, *Eur J Inorg Chem*, 2007, 5533–5540.

17 A. Kamiyama, T. Noguchi, T. Kajiwara and T. Ito, *Inorg Chem*, 2002, **41**, 507–512.

18 N. Rodríguez-López, Y. Wu, Y. Ge and D. Villagrán, *J Phys Chem C*, 2020, **124**, 10265–10271.

19 C. K. Williams, G. A. McCarver, A. Chaturvedi, S. Sinha, M. Ang, K. D. Vogiatzis and J. "Jimmy" Jiang, *Chem Eur J*, **28**, 1-8.

20 A. Chaturvedi, G. A. McCarver, S. Sinha, E. G. Hix, K. D. Vogiatzis and J. Jiang, *Angew Chem Int Ed*, 2022, **61**, 1-9.

21 A. M. Teale, T. Helgaker, A. Savin, C. Adamo, B. Aradi, A. V. Arbuznikov, P. W. Ayers, E. J. Baerends, V. Barone, P. Calaminici, E. Cancès, E. A. Carter, P. K. Chattaraj, H. Chermette, I. Ciofini, T. D. Crawford, F. De Proft, J. F. Dobson, C. Draxl, T. Frauenheim, E. Fromager, P. Fuentealba, L. Gagliardi, G. Galli, J. Gao, P. Geerlings, N. Gidopoulos, P. M. W. Gill, P. Gori-Giorgi, A. Görling, T. Gould, S. Grimme, O. Gritsenko, H. J. A. Jensen, E. R. Johnson, R. O. Jones, M. Kaupp, A. M. Köster, L. Kronik, A. I. Krylov, S. Kvaal, A. Laestadius, M. Levy, M. Lewin, S. Liu, P. F. Loos, N. T. Maitra, F. Neese, J. P. Perdew, K. Pernal, P. Pernot, P. Piecuch, E. Rebolini, L. Reining, P. Romaniello, A. Ruzsinszky, D. R. Salahub, M. Scheffler, P. Schwerdtfeger, V. N. Staroverov, J. Sun, E. Tellgren, D. J. Tozer, S. B. Trickey, C. A. Ullrich, A. Vela, G. Vignale, T. A. Wesolowski, X. Xu and W. Yang, *PhysChemChemPhys*, 2022, **24**, 28700–28781.

22 K. I. Ramachandran, G. Deepa and K. Namboori, *Computational chemistry and molecular modeling: Principles and applications*, Springer Berlin Heidelberg, 2008.

23 M. Bursch, J.-M. Mewes, A. Hansen and S. Grimme, *Angew Chem Int Ed*, 2022, **61**, 1–27.

24 N. Mardirossian and M. Head-Gordon, *Mol Phys*, 2017, **115**, 2315–2372.

25 B. A. Shiekh, *ACS Omega*, 2019, **4**, 15435–15443.

26 D. Coskun, S. V. Jerome and R. A. Friesner, *J Chem Theory Comput*, 2016, **12**, 1121–1128.

27 L. R. Maurer, M. Bursch, S. Grimme and A. Hansen, *J Chem Theory Comput*, 2021, **17**, 6134–6151.

28 P. Petrović, J. P. Djukic, A. Hansen, C. Bannwarth and S. Grimme, "Non-covalent Stabilization in Transition Metal Coordination and Organometallic Complexes", *Non-covalent Interactions in the Synthesis and Design of New Compounds*, A. M. Mähärrämov, K. T. Mahmudov, M. N. Kopylovich and A. J. L. Pombeiro, First Ed, John Wiley & Sons, 2016, 115-143.

29 B. H. Solis and S. Hammes-Schiffer, *Inorg Chem*, 2011, **50**, 11252–11262.

30 J. E. B. Randles, *J. Chim. Physique*, 1947, **2**, 11–19.

31 A. M. Appel and M. L. Helm, *ACS Catal*, 2014, **4**, 630–633.

32 V. Fourmond, P. A. Jacques, M. Fontecave and V. Artero, *Inorg Chem*, 2010, **49**, 10338–10347.

33 P. Banoth, C. Kandula and P. Kollu, in *ACS Symposium Series*, American Chemical Society, 2022, vol. 1432, pp. 1–37.

34 S.-H. Cheng and Y. O. Su, *Inorg. Chem*, 1994, **33**, 5847–5854.

35 Z. N. Nilsson, B. L. Mandella, K. Sen, D. Kekilli, M. A. Hough, P. Moënne-Loccoz, R. W. Strange and C. R. Andrew, *Inorg Chem*, 2017, **56**, 13205–13213.

Chapter 6: Conclusions from Completed Investigations and Opportunities to Extend and Expand Future Research

6.1 – Summary of Research Contributions Advancing the Field

Overall, the investigations completed in this thesis placed a large emphasis on understanding the form and function relationship for each catalyst; therefore, many of the significant contributions to advancing the field of electrocatalysis involved mechanistic elucidation. Combining electrochemical and spectroscopic analysis techniques with support from DFT calculations helped identify an array of ligand contributions influencing catalytic activity. Many of these attributes were determined to be heavily affected by the identity of the solvent and pH of the environment.

Probing the H_2 evolution mechanism of CoPN3RP in chapter 2 lead to the establishment of two possible catalytic pathways for one catalyst. This work demonstrated the versatility of the PN3RP ligand to operate in a range of pH's, using TFA (pK_a=12.7), AA (pK_a=22.3) , and TFE (pK_a=35.4) as proton sources in acetonitrile. The ligand support allows CoPN3RP to reach two active oxidation states for hydrogen generation of Co(I) and Co(0). Achieving the low oxidation state of Co(0) allows CoPN3RP to react with weaker acids (TFE). CoPN3HP demonstrated impressive catalytic activity for TFA reduction releasing H_2, boasting a TOF of 2740s^{-1}.

Chapter 3 explores the ligand centred water reduction activity of **NiPc**. This complex possesses two reversible two-electron redox events which distribute their charge on the Pc ligand. This study highlights the relationship between the redox activity of the ligand and the effect on it's acid/base chemistry. Redox processes directly influence the pK_a of the coor-N and bi-N protonation sites, favoring protonation of the bi-N sites following a

reduction. Ultimately, water reduction is achieved following a mechanism that excludes direct interaction with the Ni centre.

Homogeneous ammonia generation from Co(II) and Ni(II) heterocyclic complexes was presented in Chapter 4. This investigation marks a rare demonstration of electrocatalytic NO_2^- reduction from a homogeneous Ni(II) complex. The performance of Ni(II) catalyst is impressive, having a TOF of 28900s^{-1} calculated from FOWA, with a Faradaic efficiency of 86%. DFT calculations supported the proposition for the electron storage capacity of the bis(imino)pyridine moiety of the heterocyclic ligand. The Ni(II) complex demonstrated significant selectivity of ammonia over hydroxylamine, which was supported by the DFT analysis. These calculations suggest increased bond order to hydroxylamine with added electrons, preventing its release during the catalytic cycle.

Chapter 5 probed $M(bpca)_2$ [M=Fe,Co,Ni] complexes for their homogeneous electrocatalytic reduction activity targeting H_2O, CO_2, CO, and NO_2^-. DFT calculations were performed on the free ligand and all $M(bpca)_2$ complexes, noting the change in their bonding behaviour with added electrons. These calculations indicated that the bpca ligand was able to stabilize two added electrons as a free ligand or as part of a complex. Alkali metals were employed as an attempt to interact with the imide moieties of the bpca ligand to modulate the redox behaviour of the complex and coordination of the ligand to the metal. A positive shift in potential was demonstrated with added Na^+, however no electrocatalytic reductions could be induced for H_2O, CO_2, or CO. Ultimately, **$Fe(bpca)_2$** was found to reduce $NaNO_2$ to ammonia due to the combined affect of the alkali metal influence and strongly coordinating nitrite substrate.

Overall, the catalysts studied in this thesis demonstrate the range of ligand function during catalysis that can occur across the ligand contribution continuum. With minimal ligand contributions, CoPN3RP can electrocatalytically reduce protons to generate water. Chapters 4 and 5 present examples of catalysts that store electron density in the ligand and have accessible protonation sites, but still function through the metal centre. The most extensive ligand contributions come from **NiPc**, which acts as the site for catalysis.

6.2 – Preamble Describing Premise of Future Research Projects

Each of the compounds researched during this thesis possesses the capability of meaningfully contributing to other catalytic endeavors or improving on their current trajectory. Exploring different mechanistic pathways can involve redirecting the trajectory of a catalytically active complex or perturbing its functionality. For each complex, both or either of these directives will be applied. The following sub-section will discuss outlines of potential research projects that could be explored using some of the same structures discussed in this thesis. Specifically, the frameworks of structures to be explored will be CoPN3RP, MPc, and $M(bpca)_2$.

6.3 – Summary of Future Research Opportunities

6.3.1 – Exploring a variety of substituents to establish an electrocatalytic continuum of redox potentials capable of reducing proton sources varying in pK_a using CoPN3RP

Identifying a viable redox catalyst for one pathway, often suggests it is capable of similar catalytic processes. For instance, neutral H_2O reduction catalysts are often proficient at CO_2 reduction. These substrate targets happen to fall within a similar potential window, meaning significant redox tuning is not needed. Shifting the pH of a catalytic system, however, can alter the potential required to effectively perform catalytic reduction. Redox events can be shifted by varying substituents in the ligand system in terms of their ability to push or pull electron density. Establishing a class of ligands which offers an array of functional groups ranging from electron withdrawing to electron donating could result in a catalogue of complexes specialized for substrates that exist within each complex's redox window. Proceeding with this research pathway, selection of ideal ligand targets can be considered based on two main criteria. i) do complexes with this ligand perform electrocatalytic reductions? ii) is the potential of the active redox event influenced easily by the identity of the varied EWG or EDG substituent?

Based on these simple criteria, the PN3RP ligand system represents an ideal candidate for this research pathway. Firstly, as in Chapter 2, CoPN3RP demonstrates proton reduction capabilities at a variety of potentials, reducing substrates varying in pK_a. Secondly, the identity of the R group was shown to alter the potential of the redox events with only small changes in the EWG/EDG character of the substituents.[1] Varying the R group from a methyl group to a hydrogen resulted in a slight shift in the redox potentials. These

substituents vary only slightly in their EWG/EDG character yet display a notable shift; it stands to reason that varying the EWG/EDG character more significantly will result in a more significant shift. Additionally, the functional group connected to the phosphorus (R') could be varied in a similar manner.

Several ligand structures are already known that demonstrate clear differences in EWG/EDG character. Based on the syntheses of the known structures, some procedural adjustments could be made to establish a larger variety of redox potentials, as portrayed in Figure 6.1.[2–5]

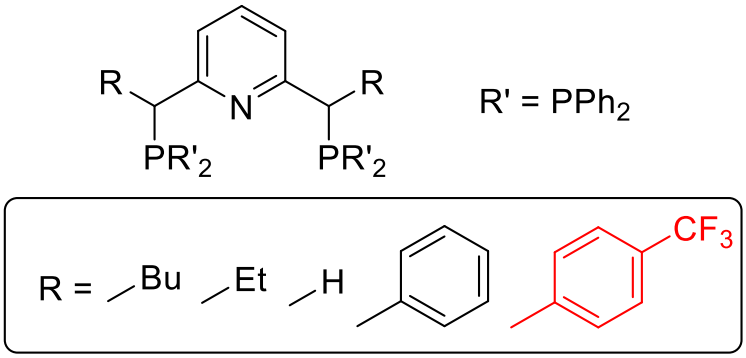

Figure 6.1: Proposed PN3RP ligand systems with varied R-groups designed to generate a range of redox potentials.

The functional groups shown in black in Figure 6.1 generate PN3RP frameworks that are known in the literature. The 4-(trifluoromethyl)phenyl group, in red, would result in a new structure, but could likely be synthesized with a similar protocol as the phenyl group. Each PN3RP ligand can be refluxed with MBr_2 [M = Fe, Co, Ni, Cu, and Zn] to generate the complexes. Each newly formed complex can then have CVs performed on them to examine their redox activity, ultimately establishing a catalogue of complexes

with a continuum of redox events. Having established catalytic activity previously for CoPN3P, these newly identified redox events could prove to be catalytically active and be fruitful areas of research following screening from a variety of substrates.

6.3.2 – Applying MPc ligand complexes as a combined catalyst and photosensitizer performing redox catalysis on a collection of waste chemicals to generate value-added products

Photocatalytic redox systems targeting substrate like CO_2 and H_2O generally require a photosensitizer, redox catalyst, and sacrificial electron donor to function.[6] In these systems, the photosensitizer absorbs the incoming photon, which is either quenched by the electron donor or the catalyst. The active species in these systems is usually the reduced catalyst, similarly to what would be observed in an electrocatalytic system. Requiring several chemical components to achieve the active catalyst is emblematic of poor atom economy, especially when photosensitizers are often composed of expensive metals like ruthenium or iridium. In an ideal system, one complex would absorb and utilize the photon for a catalytic process. MPc complexes may be good candidates to function in this capacity.[7,8]

Several Pc ligand variations can be purchased from chemical providers, allowing for quick generation of several MPc complexes with known redox and absorbance characteristics. Establishing potential targets for these systems requires an MPc that absorbs in the visual range and displays electrocatalytic activity. The investigation completed for **NiPc** in Chapter 3 portrays a catalyst with potential to act as its own photosensitizer, with a source that emits red light (~750nm), based on the absorbance spectra in Figure 3.9. Identifying

a catalytic process that occurs at the first reduction event of **NiPc** (-1.46V vs $Fc^{+/0}$) would give the system its best chance for success. Reduction of NO_2^- could be a potential target for such a process, as the first reduction of **NiPc** occurs close to the region where NO_2^- reduction has been documented. Establishing such a catalytic system would first involve demonstrating activity electrochemically at the first reduction event. Following the successful detection of catalytic activity, the photocatalytic system can be designed. Several electron donors could be attempted, including TEA or TEOA. Additionally, trials could be completed using an applied potential as the electron donor. Exploring this system would initially entail multiple photocatalytic trials in which samples are irradiated with 750nm light for varying periods of time. Product detection would require ^{14}N-NMR for ammonium, ferricyanide titration for hydroxylamine, and GC-TCD to detect gaseous products. Beyond **NiPc**, other 3d metal centers should also be explored, which can be synthesized following a similar procedure as **NiPc**.

6.3.3 – Investigating the heterogeneous product generated during CPE of $[Co^{III}(bpca)_2]^+$ and its catalytic capacity for nitrite reduction

Initial CVs and short-term CPE experiments for **$[Co^{III}(bpca)_2]^+$** seemed to indicate some promise for the complex as a homogeneous NO_2^- reduction catalyst. Upon further evaluation, the complex appeared to significantly degrade and deposit on the electrode. After a two-hour experiment, the layer that formed was orange in colour and exceptionally uniform in its deposition for the section of the electrode submerged in solution. This deposition process is worth further exploration, as the newly formed layer appears to display some catalytic capacity and was exceptionally difficult to remove from the

electrode. Characterization of the formed layer is necessary to elucidate the functionality of the heterogeneous catalyst. XPS analysis, PXRD analysis, SEM imaging, and TEM imaging, should all be completed on the film to define its composition and structure.[9–11]

Assessing the influence of varying **$[Co^{III}(bpca)_2]^+$** concentration, $NaNO_2$ concentration, run time, and applied potential could result in coatings varying in thickness, uniformity, or even composition. These variables can be configured to generate the optimized structure for heterogeneous electrocatalytic NO_2^- reduction. Catalytic experiments for this heterogeneous catalyst closely resemble homogeneous trials. Both CVs and CPE experiments must be completed to examine the kinetics of the experiment, evaluate product generation, and assess the robustness of the structure. Following CPE experiments, the solution must be examined to identify products and potential leaching from the surface. This work aims to characterise the structure of the film, document its catalytic ability, elucidate its functionality, and establish a reliable and reproducible protocol to generate the optimized heterogeneous catalyst.

6.4 – Conclusion

Exploring catalytic pathways for the generation of value-added products from environmental detriments has become an important and significant area of study using homogeneous organometallic complexes for electrocatalytic systems, in recent decades. Studying the functionality of these complexes has led to the establishment of many unique mechanisms, pointing to a range of ligand contributions for completion of catalytic

cycles. This investigation targeted proton and nitrite reduction, with a focus on mechanistic elucidation.

Each of the complexes investigated in this work were electrochemically studied and further analyzed using DFT simulation. For each identified redox event, the electronic structure was investigated. The results of the DFT simulations were displayed as valence electronic structures to gain insight into MO makeup and how different fragments may contribute to electron storage. Ligand contributions spanned from playing a minimal role for water reduction using CoPN3RP (Chapter 2), to acting as an electron reservoir for NO_2^- reduction in Chapter 4, to a ligand-centred role for H_2O reduction from **NiPc** in Chapter 3. Chapter 5 examined **$Fe^{II}(bpca)_2$** for NO_2^- reduction, identifying a likely change in ligand structure to open a coordination site and activate the catalyst. Overall, this work has displayed and evaluated catalytic activity from several 3d transition metal complexes with a variety of multidentate ligands for proton and NO_2^- reduction, highlighting the vast range in mechanistic functionality.

6.5 – References

1 X. Li, X. Zhao, L. Zhang, A. Mathur, Y. Xu, Z. Fang, L. Gu, Y. Liu and Y. Liu, *Nat Commun*, 2024, **15**, 1175–1188.

2 Z. Fei, E. Păunescu, W. H. Ang, R. Scopelliti and P. J. Dyson, *Eur J Inorg Chem*, 2014, 1745–1750.

3 G. K. Rao, I. Korobkov, B. Gabidullin and D. Richeson, *Polyhedron*, 2018, **143**, 62–69.

4 N. W. Kinzel, D. Demirbas, E. Bill, T. Weyhermüller, C. Werlé, N. Kaeffer and W. Leitner, *Inorg Chem*, 2021, **60**, 19062–19078.

5 M. Montag and D. Milstein, *Isr J Chem*, 2023, 63.

6 C. Michelin and N. Hoffmann, *ACS Catal*, 2018, **8**, 12046–12055.

7 T. C. Gunaratne, A. V. Gusev, X. Peng, A. Rosa, G. Ricciardi, E. J. Baerends, C. Rizzoli, M. E. Kenney and M. A. J. Rodgers, *J. Phys. Chem. A*, 2005, **109**, 2078–2089.

8 M. Peterson, C. Hunt, Z. Wang, S. E. Heinrich, G. Wu and G. Ménard, *Dalton Trans.*, 2020, **49**, 16268–16277.

9 Z. Wang, D. Richards and N. Singh, *Catal Sci Technol*, 2021, **11**, 705–725.

10 S. Zhang, Q. Fan, R. Xia and T. J. Meyer, *Acc Chem Res*, 2020, **53**, 255–264.

11 G. Yang, P. Zhou, J. Liang, H. Li and F. Wang, *Inorg Chem Front*, 2023, **10**, 4610–4631.